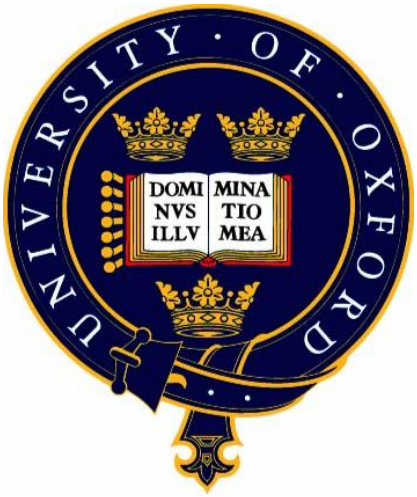
THE DEVELOPMENT OF AN AMPEROMETRIC AMMONIA GAS SENSOR



XIAOBO JI

ST JOHN'S COLLEGE

OXFORD UNIVERSITY

TRINITY TERM 2007

A THESIS FOR THE

DEGREE OF DOCTOR OF PHILOSOPHY

IN CHEMISTRY

The Development of An Amperometric Ammonia Gas Sensor

Abstract of a thesis submitted for the degree of Doctor of Philosophy in Chemistry
by Xiaobo Ji, St John's College, Oxford University, Trinity Term 2006.

In this thesis electrochemical techniques are employed towards the development of an amperometric ammonia gas sensor. In chapters 1 to 3 the fundamental principles which underlie electrochemical techniques employed are described. We overview the role of carbon nanotubes in electro-analysis and seen how crucial edge plane pyrolytic graphite electrodes are, not only is sensing, but for understanding the fundamental properties of carbon nanotubes.

Chapters 4 to 8 investigate the fundamental electrochemistry of carbon based electrodes. It is found that the presence of oxygenated species on different carbon electrodes influences the heterogeneous electron transfer. Moreover, metal nanowires and nano-particles grown on different carbon electrodes via electrochemical deposition are presented, with Atomic Force Microscopy used to study the growth of these nano-materials, and the dopants used as electrocatalysis.

Finally in chapters 9 to 12 the electrochemical oxidation of ammonia is studied in both aqueous and non-aqueous systems, all indicating analytical utility for ammonia sensing. First, in aqueous solution the direct oxidation of ammonia at boron-doped diamond electrode provides the basis for the sensitive, direct detection of ammonia using Clark cell type gas sensors in conjugation with aqueous electrolyte. Proof-of-concept is also shown for an amperometric sensor which is constructed where the working electrode consists of conductive boron-doped diamond particles supported on a PTFE gas-porous hydrophobic support. Next, the indirect electrochemical oxidation of ammonia has been studied by cyclic voltammetry at glassy carbon electrodes in propylene carbonate. Its analytical utility of indirect for ammonia sensing was examined by measuring the peak current of new wave resulting from reaction between ammonia and the hydroquinone, as function of ammonia concentration. Further, the direct oxidation of ammonia has been investigated in several room temperature ionic liquids and the mechanism is explored further.

Acknowledgements

I would like to thank Professor Richard Compton for giving me the opportunity to undertake my DPhil as part of his group and for his guidance and encouragement throughout.

I am indebted to a number of individuals who made this work possible. Many thanks to all the group members over the years who make the Compton group a fun and social place to be. In particular Craig for teaching my “nice” English word, and remembering me forever with squash; Marisa for being a patient guider, and for all her help; Andy Wain for his theory of electrochemistry, impressing me a lot; Biljana for being a nice girl with various postcards; Francois, Rodrigo and Chris for the credible football competition in our free time to enjoy the England grass pitch; Andy Simm for his “Lost”, and a large amount of MP3; Nicole for her earnest and positive attitude to life; Xuan for her extra free life; Greg for endless paper passion; Ian for his continuous exercise with rolling; Behzad for his patriotism, and support for me; Abiman for the caring of his family, especially the second baby coming; Deb for her teaching with proper English slam, particularly Essex girls stories; Tessa for a funny face in my mind ever; Yun for the knowledge of the growing of CCP; Lei for his beers passion, and Japanese porn cartoon; Elicia Wong for her excellent presentation; Leonardo for being a Brazil man while not to play footie.

Also thanks to my mates Wang chao, Hao tong, Yungtai, Wang Zhengyu, Shao Lidong, Hu Gang, Wang Xiaowei, Ouyang Bin for keeping me sane over the last three years with regular weekends of lair.

Finally, I would like to thank my fiancée, Binghan Qiao, my parents, and sister for their continuous support behind me.

CONTENTS

ABSTRACT……i

ACKNOWLEDGEMENTS ……ii

CONTENTS……iii

GLOSSARY……viii

CHAPTER 1: INTRODUCTION TO ELECTROCHEMISTRY....1

1.1 Dynamic Electrochemistry....1

1.1.1 Structure of the Electrode-Solution Interface....2
1.1.1.1 The Double Layer....2

1.1.2 Mass Transport....4
1.1.2.1 Diffusion....4
1.1.2.2 Migration....5
1.1.2.3 Convection....6

1.1.3 Electrode Kinetics....7
1.1.3.1 Tafel Analysis....6

1.1.4 Mechanistic Electrochemistry....10
1.1.4.1 CE Reactions....10
1.1.4.2 EC Reactions....10
1.1.4.3 ECE Reactions....11
1.1.4.4 CE Reactions....13

1.2 Voltammetric methods....13

1.2.1 Linear Sweep Voltammetry....14
1.2.2 Cyclic Voltammetry....15
1.2.3 Potential Step Chronoamperometry....18
1.2.4 Square Wave voltammetry....19

1.3 Electrochemical Cell....22

1.3.1 Working Electrode....23
1.3.1.1 Microelectrodess....23
1.3.1.2 Rotating Disk Electrodes....24

1.3.2 Reference Electrode....23
1.3.2.1 The Saturated Calomel Electrode....25
1.3.2.2 Quasi Reference Electrodes....25

1.4 References....26

CHAPTER 2: INSTRUMENTATION AND EXPERIMENTAL METHODS....28

2.1 Electrodes....28

2.1.1 Microelectrodes....28
2.1.2 Macroelectrodes....29
2.1.3 Reference Electrodes....29

2.2 Electrochemical Cell....30

2.3 Instrumentation....31

2.3.1 Potentiostat....31
2.3.2 Atomic Force Microscopy....31
2.3.3 Electrochemical Electron Spin Resonance....34

2.4 References....35

CHAPTER 3: CARBON BASED ELECTRODES IN LECTROANALYSIS....36

3.1 Pyrolytic Graphite....36

3.2 Carbon nanotubes....38

3.2.1 Carbon Nanotubes in Electrochemistry: Modifiying the Nanotubes....42
3.2.1.1 Covalent Functionalization of CNTs and Their Applications....42
3.2.1.2 CNTs oxidation and Subsequent Modifications....43
3.2.1.3 Fluorinated Nanotubes and their Electrochemical Applications....46
3.2.1.4 Electrochemical Activation of CNTs and their Applications....47

3.2.2 The Applications of Un-functionalized CNTs in Electroanalysis....51

3.2.3 Fundamental Understanding of the Electroactive Sites of Carbon Nanotubes....53

3.2.4 The Role of Metal Oxide Impurities in Carbon Nanotubes....56

3.3 Edge Plane Pyrolytic Graphite Electrodes....58

3.3.1 Utilising Edge Plane Pyrolytic Graphite Electrodes in Electroanalysis....59
3.3.1.1 Thiol Dection: Replacing MWCNT Modified Electrodes in Routine Sensing....58
3.3.1.2 NADH Detection....60
3.3.1.3 Utilising Edge Plane Pyrolytic Graphite Electrodes: Other Examples....69

3.4 References....70

CHAPTER 4: OXYGENATED SPECIES AT TUBE ENDS DOES NOT IMPROVE ELECTRON TRANSFER KINETICS ECTRODES IN LECTROANALYSIS....77

4.1 Introduction....77

4.2 Experimental....79

4.2.1 Chemicals....79

4.2.2 Instrumentation 79

4.3 Results and Discussion 81

4.3.1 TEM and XPS Analysis 81
4.3.2 Voltammetric Characterisation of Various CNTs. 84

4.4 Conclusion 86

4.5 References 87

CHAPTER 5: MULTI-WALLED CARBON NANOTUBES RESIST INTERCALATION WHEREAS PYROLYTIC GRAPHITE CAN EXFOLIATE IN PROPYLENE CARBONATE 89

5.1 Introduction 89

5.2 Experimental 92

5.2.1 Chemicals 92
5.2.2 Instrumentation 92

5.3 Results and Dicussion 94

5.3.1 Voltammetric Response of Ammonia in Propylene Carbonate 94
5.3.2 Electrochemical Behavior of MWCNTs in Propylene Carbonate 99

5.4 Conclusion 100

5.5 References 102

CHAPTER 6: 'OXYGENATED' EDGE PLANE SITES SLOW THE ELECTRON TRANSFER KINETICS OF THE FERROCYANIDE / FERRICYANIDE REDOX COUPLE AT GRAPHITE ELECTRODES 104

6.1 Introduction 104

6.2 Experimental 106

6.2.1 Chemicals 106
6.2.2 Instrumentation 106

6.3 Results and Dicussion 108

6.3.1 Electrochemical Behaviour of Pyrolytic Graphite Electrodes 108
6.3.2 The Influences of Exposure time of Oxygen to Electrochemical Behaviour of Pyrolytic Graphite Electrodes 111
6.3.3 Electrochemical Behaviour of CNTs 118

6.4 Conclusion 123

6.5 References 124

CHAPTER 7: EDGE PLANE SITES ON HIGHLY ORDERED PYROLYTIC GRAPHITE AS TEMPLATES FOR MAKING PALLADIUM NANOWIRES VIA ELECTROCHEMICAL DECORATION....126

7.1 Introduction....126

7.2 Experimental....128

7.2.1 Chemicals....128
7.2.2 Instrumentation....129

7.3 Results and Dicussion....129

7.3.1 Fabrication of Palladium Wires Produced by Electrochemical Decoration....129
7.3.2 Investigation of Decoration with Atomic Force Microscopy....131
7.3.3 Investigation of Decoration with Scanning Tunneling Microscopy....134
7.3.4 Voltammetric Responses of Hydrazine on Pd Nanowires....137

7.4 Conclusion....138

7.5 References....139

CHAPTER 8: "INSTANTANEOUS" GROWTH OF COBALT NANOPARTICLES ON BORON-DOPED DIAMOND ELECTRODES....141

8.1 Introduction....141

8.2 Experimental....144

8.2.1 Chemicals....144
8.2.2 Instrumentation....144

8.3 RESULTS AND DISCUSSION....145

8.3.1 Voltammetric Response of Cobalt(II) at a BDD Electrode....145
8.3.2 *In situ* AFM....148
8.3.3 Growth Rate of Individual Nuclei....151

8.4 Conclusion....156

8.5 References....156

CHAPTER 9: THE ELECTROCHEMICAL REDUCTION OF AQUEOUS HEXAMMINECOBALT(III)....158

9.1 Introduction....158

9.2 Numerical Simulation....163

9.2.1 Model....163

9.3 Experimental....167

9.3.1 Chemicals 167
9.3.2 Instrumentation 168

9.4 RESULTS AND DISCUSSION 169

9.4.1 Cyclic Voltammetry at Macro and Micro Gold Electrodes 169
9.4.2 Fast Scan Cyclic Voltammetry 171
9.4.3 Theoretical Results 173

9.5 Conclusion 177

9.6 References 178

CHAPTER 10: THE ELECTROCHEMICAL OXIDATION OF AMMONIA AT BORON-DOPED DIAMOND ELECTRODES 181

10.1 Introduction 181

10.2 Experimental 183

10.2.1 Chemicals 183
10.2.2 Instrumentation 183

10.3 RESULTS AND DISCUSION 184

10.3.1 Electrochemical oxidation of NH_3 184
10.3.2 A Miniature Amperometric Sensor 189

10.4 Conclusion 192

10.5 References 192

CHAPTER 11: ELECTRODE KINETIC STUDIES OF HYDROQUINONE AND BENZOQUINONE IN PROPYLENE CARBONATE 194

11.1 Introduction 194

11.2 Experimental 197

11.2.1 Chemicals 197
11.2.2 Instrumentation 197

11.3 RESULTS AND DISCUSION 199

11.3.1 Electrochemical Study of Hydroquinone 199
11.3.1.1 Cyclic Voltammetry of Hydroquinone in PC 199
11.3.1.2 Simulating the Oxidation of Hydroquinone 203

11.3.2 Electrochemical Study of Benzoquinone 206
11.3.2.1 Voltammetric Responses and ESR Behavior of Benzoquinone in PC 206
11.3.2.2 Simulating the Reduction of Benzoquinone 210

11.3.3 Kinetic Analysis of Hydroquinone in the Presence of Ammonia in PC.....217

11.3.4 Analytical ability of this Reaction between Hydroquinone and Ammonia.....219

11.4 Conclusions.....221

11.5 References.....223

CHAPTER 12: ELECTRODE KINETIC STUDIES OF HYDROQUINONE AND BENZOQUINONE IN PROPYLENE CARBONATE.....226

12.1 Introduction.....226

12.2 Experimental.....230

12.2.1 Chemicals.....230
12.2.2 Instrumentation.....230
12.2.3 Chronoamperometric Transients.....232

12.3 RESULTS AND DISCUSION.....233

12.3.1 A Mechanistic Electrochemical Study of Ammonia in [C_4mim][BF_4].....233
12.3.1.1 Voltammetry of Ammonia in [C_4mim][BF_4].....233
12.3.1.2 Reduction of Ammonium Nitrate in [C_4mim][BF_4].....237
12.3.1.3 The Addition of Hydrogen Gas and Electrode "Activation".....239
12.3.1.4 Using Cobaltocenium Hexafluorophosphate as An Internal Reference Couple 240

12.3.2 Electrochemical Study of Ammonia in Different RTILs.....243
12.3.2.1 Voltammetry of Ammonia in [C_4mim][OTf].....243
12.3.2.2 Voltammetry of Ammonia in [C_2mim][NTf_2].....245
12.3.2.3 Voltammetry of Ammonia in [C_4mim][NTf_2].....247
12.3.2.4 Voltammetry of Ammonia in [C_4mim][PF_6].....248

12.3.3 Effect of Electrode Activation on the Relative Ratios of Peaks i and ii.....250

12.3.4 Comparison of Results Obtained in All Five RTILs.....252

12.4 Conclusions.....255

12.5 References.....256

Glossary

Below is a list of abbreviations and symbols employed throughout this work.

Term	Meaning	Units
Å	Angström, atomic dimension	10^{-10} m
A	Area of electrode	cm^2
AAS	Atomic absorption spectroscopy	
AFS	Atomic fluoresce spectroscopy	
AFM	Atomic force microscopy	
ASV	Anodic stripping voltammetry	
BDD	Boron doped diamond	
c_A	Concentration of A	mol cm^{-3}
CM	Contact mode (AFM)	
CSV	Cathodic stripping voltammetry	
CV	Cyclic voltammogram	
CVD	Chemical vapour deposition	
D_A	Diffusion coefficient of A	cm^2 s^{-1}
e^-	Electron	
E	Electrode potential	V
$E^ø$	Standard potential	V
E_e	Equilibrium potential	V
$E_f{}^0$	Formal potential	V
E_{SW}	Square wave amplitude	V
ΔE_S	Square wave step	V
F	The faraday constant	C mol^{-1}
f	Frequency	Hz
G	Gibbs free energy	J mol^{-1}
ΔG	Gibbs free energy change	J mol^{-1}
I	Current	A
ICP-MS	Inductively coupled plasma mass spectrometry	
IHP	Inner Helmholtz plane	IHP
J	Flux	mol cm^{-2} s^{-1}
k_0	Standard rate constant	s^{-1}
LOD	Limit of detection	

LSV	Linear sweep voltammogram	
m	Sensitivity of LOD calibration chart	AM^{-1}
M	Molarity	mol dm^{-3}
n	Number of electrons transferred	
OHP	Outer helmholtz plane	
Q	Charge	C
r	Correlation coefficient of LOD calibration chart	
R	Universal gas constant	J K^{-1} mol^{-1}
RDE	Rotating disc electrode	
Re	Reynolds number	
SCE	Saturated calomel electrode	
SEM	Scanning electron microscope	
SPM	Scanning probe microscope	
SWV	Square wave voltammetry	
TM	Tapping mode (AFM)	
WHO	World health organisation	
δ	Diffusion layer thickness	cm
η	Overpotential	V
ν	Kinematic viscosity	cm^2 s^{-1}
σ	Standard Deviation	

CHAPTER 1

Introduction to Electrochemistry

The work presented in this thesis is broadly concerned with the changes observed in various electrochemical systems. The fundamental principles which underlie the electrochemical techniques employed will be described in this introductory chapter.

1.1 Dynamic Electrochemistry

Dynamic electrochemistry involves the application of a potential which can result in the transfer of electrons across a solution-electrode surface in an electrolytic solution. The processes taking place at electrode which contribute to the currents comprise two distinct categories: Faraday and non-Faraday currents.[1] Faraday currents arise from the electron transfer across the interface between the electrode and solution surface. This process is governed by Faraday's law, which states that the amount of substance converted by the flow of the current is proportional to the amount of charge passed. Non-Faraday processes include adsorption / desorption but generally refer to capacitative charging currents. This component arises from the reorganisation of both ions and dipoles in the electric double layer immediately adjacent to the surface of the electrode; there is in effect a capacitative component in an electrochemical cell which charges and discharges whenever the electrode potential is changed.[1,2]

Many factors have been found to influence the current response observed in voltammetric experiments, namely, the electrode – solution interface, mass transport to and from the electrode surface and heterogeneous charge transfer, and electrode processes We will begin with a description of the interfacial region that is established when a metal electrode is immersed in a solution, a thorough understanding of which is crucial to probing electrochemical reactions and mechanisms.

1.1.1 Structure of the Electrode – Solution Interface

1.1.1.1 The Double Layer

When an electrode is placed in an electrolyte solution, an immediate redistribution of ions and reorientation of dipoles in solvent molecules occurs, which acts to restore charge neutrality at the electrode surface. At the interfacial region, this double layer,[3] as it is commonly termed, differs significantly in composition to the bulk solution and several models have been proposed over the years. The simplest model is that of Helmholtz,[4,5] in which the charge neutralization is complete and the double layer acts as a capacitor, confined to a region known as the Outer Helmholz Plane, or OHP.

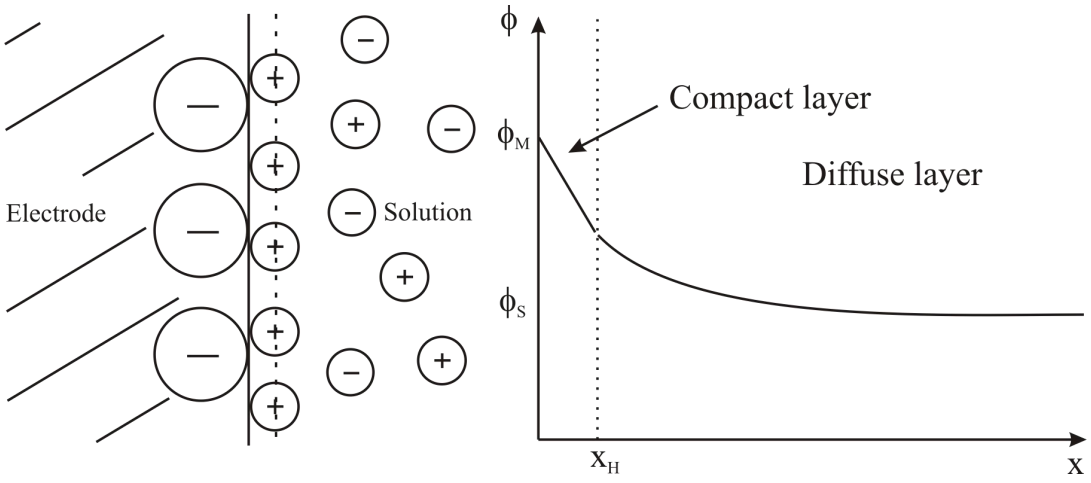


Figure 1.1 Diagrams of the Stern double-layer models

However, this is incompatible with experimental observations since it neglected these following two factors: (1) influences of concentrations of supporting electrolyte; (2) interactions occurring further from the electrode surface. Next a more realistic model was proposed independently by Gouy[6]and Chapman[7] called as the "diffuse" double layer. It includes the thermal motion of ions in solution and uses a Boltzman distribution term to define the spread of ions into the solution within the diffuse layer close to the electrode surface. In this diffuse layer the charge density decreases with distance away from the phase boundary. In the following, Stern[8] built up this approach further by combining ideas from those previous models. The result indicates the net charge is balanced by a compact layer of ions close to the electrode surface in the OHP and a diffuse layer which extends into the bulk solution, as depicted in Figure 1.1. For the potential distribution, a sharp drop exists between the electrode surface and OHP, and then approximately exponentially across the diffuse layer.

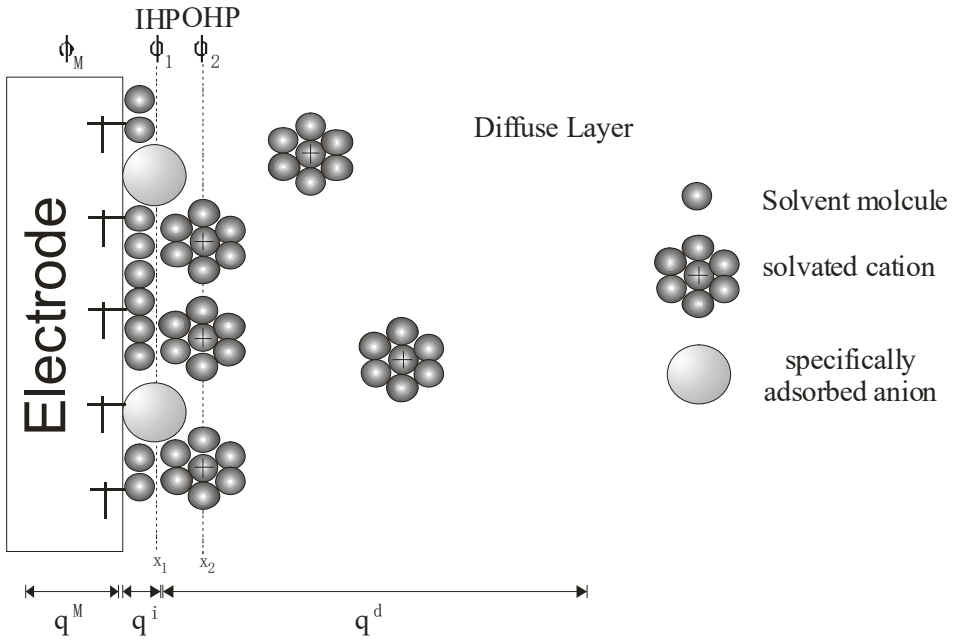


Figure 1.2 Schematic representation of Grahame double layer

Later on, Grahame[9] proposed a model comprising of three layers: the Inner Helmholtz Plane (IHP), the Outer Helmholtz Plane, and the diffuse layer, as illustrated

schematically in Figure 1.2. IHP is closest to the electrode surface and is defined as the distance x_1. It consists of specifically absorbed species, such as solvent molecules or ions, which can compensate the charge on the electrode. In terms of OHP, the plane, x_2, can be drawn through the centre of solvated and non-specifically absorbed ions. The interaction of the solvated ions with the electrode surface involves only long-range electrostatic forces and is independent of the chemical properties of the ions.

1.1.2 Mass Transport

The overall reaction rate may be limited by the slowest step; either the rate of electron transfer, or the rate at which the electro-active species are brought to the electrode from the bulk solution. Mass transport describes the movement of electro-active species to the electrode surface from the bulk solution. Generally three main types of mass transport of species to the electrode surface are diffusion, migration and convention.

1.1.2.1 Diffusion

Diffusion is the movement of species in solution as a result of concentration gradient. For electrode processes the concentration distribution occurs at a region close to the electrode surface in which the solution is depleted of electro-active species, known as the diffuse layer so as diffusion acts to remove this gradient. This is quantified by Fick's first law,[10,11] expressed here as:

$$j = -D \frac{\partial [A]}{\partial x} \tag{1.1}$$

where j is the flux for species A in mol cm^{-2} s^{-1}, $[A]$ is the concentration of the species, $\frac{\partial [A]}{\partial x}$ is the concentration gradient in the direction x, and D is the diffusion coefficient

in $cm^2\ s^{-1}$. Also D is function of solvent viscosity, temperature and electrolyte. Fick's second law describes changes in concentration of the electro-active species with time:

$$\frac{\partial[A]}{\partial t} = D\frac{\partial^2[A]}{\partial x^2} \tag{1.2}$$

1.1.2.2 Migration

Migration[12] is motion of species due to the electrostatic force on a charged particle in the electric field that exists at the interfacial region between the electrode and the solution. The migratory flux due to electric effects is given by:

$$j = -\frac{zF}{RT}Dc\frac{\partial\phi}{\partial x} \tag{1.3}$$

where c is the solution concentration, ø is the potential gradient, R is the molar gas constant, T is the absolute temperature and z is the charge on the ion under consideration. The overall rate of migration might be different for the cation and anion, resulting in a liquid junction potential. In fact, this mode of mass transport has undesirable effects as on voltammetric experiments by varying the potential at the electrode, altering the rate of migration and thus making the interpretation of voltammetric data difficult. Hence, by adding an excess of electrolytically inert ions[13] these effects can be rendered negligible in dynamic electrochemical experiments. This is known as a supporting electrolyte and is typically added to be 100 times more concentrated than the concentration of the species of interest. The electrolyte can act by to eliminate the effect that migration of the reactants would have on the current at the electrode, and it also reduces the 'ohmic drop' by increasing the solution conductivity. A further result of adding supporting electrolyte is that the electrical double layer is extremely narrow effectively shielding the bulk solution from the charged surface of the electrode so that very little migration occurs within the bulk solution; consequently

the full electrode potential is available to an electro-active specie that has diffused to the surface of the electrode to drive electron transfer. Finally in the presence of high concentrations of supporting electrolyte the ionic strength of the solution remains effectively constant in the electrochemical process, and thus the activity coefficients of the electro-active species are unchanged over the experimental scale, allowing the formal electrode potentials, $E f^{o}$, to be used and treated as constant.

1.1.2.3 Convection

Convection concerns transport of the solution caused by mechanical forces. There are two different types of convection that can occur, natural convection and forced convection. Natural convection usually arises from the differences in density or thermal gradients in solution, and is undesirable as it is difficult to quantify.[14] Natural convection may be minimized, or overcame by shortening the time-scale of the electrochemical experiment or applying a method of forced convection. Forced convection is achieved by the intentional agitation of a solution by means such as stirring, bubbling or hydrodynamic flow which can then swamp the irreproducible and unpredictable effects of natural convection, allowing for the establishment of consistent reaction conditions and the obtainment of reliable data.[3,13,15] For cases where forces convection is used the convective flux in one dimension is then given by:

$$j = cv \tag{1.4}$$

where j is the flux of species, v is velocity of the solution, and c is the solute concentration. Forced convection may be employed to greatly increase the flux of material arriving at the electrode surface, which is of particular interest in electroanalytical chemistry.

1.1.3 Electrode Kinetics

Electron transfer between the electrode and electro-active species is the main factor other than the transport of electro-active species to the electrode surface. As an illustration of the principles involved, we begin by considering the simple reversible heterogeneous one electron transfer:

$$A + e^- \rightleftharpoons B \tag{1.5}$$

At a given potential the overall current can be expressed in terms of the oxidative and reductive currents:

$$I = FA\left(k_b[B]_0 - k_f[A]_0\right) \tag{1.6}$$

where A is the electrode area, F is the Faraday constant, $[B]_0$ and $[A]_0$ are the concentrations of B and A at the electrode surface, and k_f and k_b (units cm s^{-1}) are the rate constants for the forward and backward rates, respectively. Using transition state theory, the two rate constants can then be expressed as a function of two parameters: α, the charge transfer coefficient, a dimensionless parameter which is measure of where the tranisiton state for electrochemical reaction lies and k_0, the standard heterogeneous charge transfer coefficient at E_f^0, where E_f^0 is the formal potential of the system, defined by:

$$E_f^{\,o} = E^0 + \frac{RT}{F} In\left(\frac{\gamma_A}{\gamma_B}\right) \tag{1.7}$$

where E_0 is the standard potential of the system. The formal potential is used here instead of the standard potential to reflect that real experiments are rarely performed under standard conditions. Equation 1.6 may be used to predict the effect of potential on the induced current by relating, k_0, E_f^0, and α. The value of α is commonly close to 0.5, indicating the transition state lies midway between reactants and products along the reaction coordinate in terms of its electrical behaviour. The resulting expressions are:

$$k_f = k_0 \exp\left(-\frac{\alpha F\left(E - E_f^0\right)}{RT}\right) \tag{1.8}$$

$$k_b = k_0 \exp\left(\frac{(1-\alpha) F\left(E - E_f^0\right)}{RT}\right) \tag{1.9}$$

The net current flowing at an electrode at any given potential is the sum of the cathodic and anodic components, $I = I_c + I_a$, where:

$$I_c = -FAk_f[A]_0 \tag{1.10}$$

$$I_a = FAk_b[B]_0 \tag{1.11}$$

and $[A]_{x=0}$ and $[B]_{x=0}$ are the concentrations of the species at the electrode surface. Thus,

$$I = FA\left(k_b[B]_{x=0} - k_f[A]_{x=0}\right) \tag{1.12}$$

These can then be substituted into equation 1.6 to give the Butler-Volmer equation[16,17] which describes electrode kinetics taking place:

$$I = FAk_0\left[[B]_0\left(\exp\frac{(1-\alpha) F\eta}{RT}\right) - [A]_0 \exp\left(-\frac{\alpha F\eta}{RT}\right)\right] \tag{1.13}$$

where the term η is the overpotential and given by $\eta = \left(E - E_f^0\right)$. This expression allows variation of the total current with potential and the transfer coefficient, α, to be predicted.

The faradaic current is subject to the rate of mass transport of the electroactive species to the surface of the electrode and the rate of the electron transfer between the electrode and the electroactive species. It can be seen that there will be two limiting cases. If the rate of electron transfer in the heterogeneous step is much faster than the rate of diffusion then the equilibrium is reached. This is referred to as a reversible reaction. Conversely if the electrode kinetics are much slower than the rates of mass

transport this is known as an irreversible reaction. Reactions which lie in between these two extremes are known as quasi-reversible reactions.

1.1.3.1 Tafel Analysis

At values close to E_f^0, there exists a range of potentials over which the current depends exponentially on the potential. This is known as the Tafel region and the resulting so-called Tafel equations allow for an assessment of electrode kinetics, specifically through the determination of α or β, where β = (1-α).[18] For a one-electron reduction process,

$$\ln|I| = \text{constant} - \frac{\alpha \mathrm{F}}{RT} E \tag{1.14}$$

and for an oxidative process,

$$\ln|I| = \text{constant}' + \frac{(1-\alpha)\mathrm{F}}{RT} E \tag{1.15}$$

Hence, plots of ln|*I*| vs. *E* (Tafel plots) give slopes of α and β.

If the limiting current has been measured, the effects of mass transport can be corrected and the Tafel equations are modified as shown below for a simple, one-electron reduction and oxidation ($\mathrm{A} \pm e^- \rightleftharpoons \mathrm{B}$), respectively:[1,18]

$$\ln\left|\frac{1}{I_{\text{lim,red}}} - \frac{1}{I}\right| = \text{constant} - \frac{\alpha \mathrm{F}}{RT} E \tag{1.16}$$

$$\ln\left|\frac{1}{I_{\text{lim,ox}}} - \frac{1}{I}\right| = \text{constant}' + \frac{(1-\alpha)\mathrm{F}}{RT} E \tag{1.17}$$

1.1.4 Mechanistic Electrochemistry

In this section we will consider the case when the electron transfer is coupled with a homogeneous chemical step. It is convenient to classify the reaction schemes by using letters in the order that the steps occur. '**E**' is used to represent the heterogeneous electron transfer step and '**C**' to represent the homogeneous chemical step.[19] For example an electron transfer followed by a chemical reaction of the product would be termed an **EC** reaction. The following are a selection of commonly encountered and interesting mechanisms.

1.1.4.1 CE Reactions

In this case the electro-active species is generated by a chemical reaction that precedes the reaction, depicted by these equations. An example of the CE mechanism is the reduction of formaldehyde at a mercury electrode in aqueous solution.[1] In solution formaldehyde exists mainly in the non-reducible hydrated form $H_2C(OH)_2$ but in equilibrium with the reducible H_2CO form. Under some condtions the current is controlled by the kinetics of the equilibrium giving rise to what is termed a kinetic current.

$$Y \rightleftharpoons O \tag{1.18}$$

$$O + ne^- \rightleftharpoons R \tag{1.19}$$

1.1.4.2 EC Reactions

In an EC process, the species generated by the electron-transfer step undergoes a homogeneous chemical reaction to give an electrochemically inert product.

$$O + ne^- \rightleftharpoons R \tag{1.20}$$

$$R \rightleftarrows X \tag{1.21}$$

An example of this is the oxidation of *p*-aminophenol at platinum electrode in acidic media.[20] The *p*-aminophenol is oxidized to the quinine imine and this undergoes a hydrolysis reaction to form benzoquinone which is neither oxidized nor reduced at the potential required fro the first electron transfer (Figure 1.3). The mechanism is very common as the electrochemical oxidation or reduction will often produce a very reactive species. A usual example of this is the one electron reduction of suitable organic compounds in aprotic solvents such as acetonitrile, which produces radicals or radical ions.

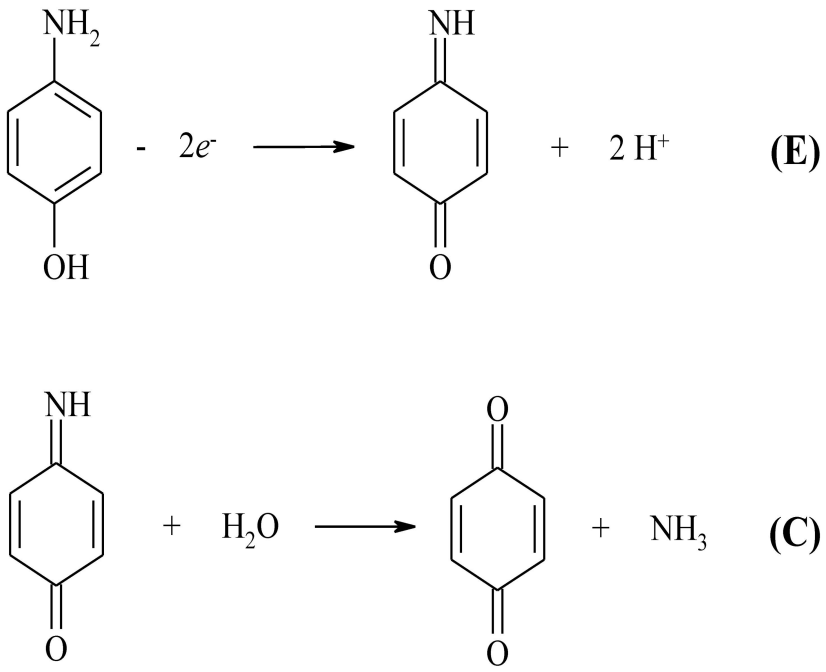


Figure 1.3 An example of an EC mechanism: oxidation of *p*-aminophenol.

1.1.4.3 ECE Reactions

In this category of mechanisms, the chemical step that follows the electron-transfer generates an electro-active species, which itself can then undergo either a reduction or oxidation thus:

$$O + n_1 e^- \rightleftharpoons R_1 \quad (1.22)$$

$$R_1 \overset{+Y}{\rightleftharpoons} O_2 \quad (1.23)$$

$$O_2 + n_2 e^- \rightleftharpoons R_2 \quad (1.24)$$

One example of this is the reduction of *p*-halonitrobenzene in an aprotic solvent.[21] The reaction proceeds in the manner shown in Figure 1.4. The assignment of the ECE mechanism is not as easy as it appears from the mechanism as the second E step occurs at a much higher potential and the species R_1 is capable of reducing O_2 whilst diffusing away in solution and thus another reaction can occur. These pathways are characterized depending on whether or not the chemical reaction or the disproportionation step is rate-determining

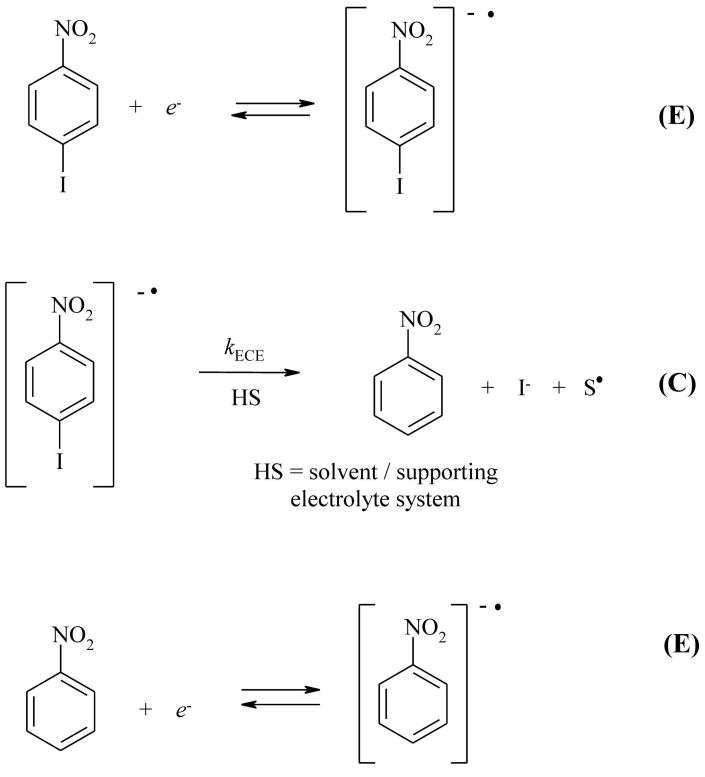


Figure 1.4 An example of an ECE mechanism: reduction of *p*-iodonitrobenzene.

1.1.4.4 ECE Reactions

If the product formed in the homogeneous step regenerates the electroactive starting material, it is labeled EC', where C' denotes the catalytic step. In the example shown, ferrocyanide[22] is electrochemically oxidised to ferricyanide in basic aqueous/ethanolic mixtures, which can oxidise aniline with the regeneration of ferrocyanide thus establishing a catalytic cycle such that the latter can undergo further oxidation at the electrode.

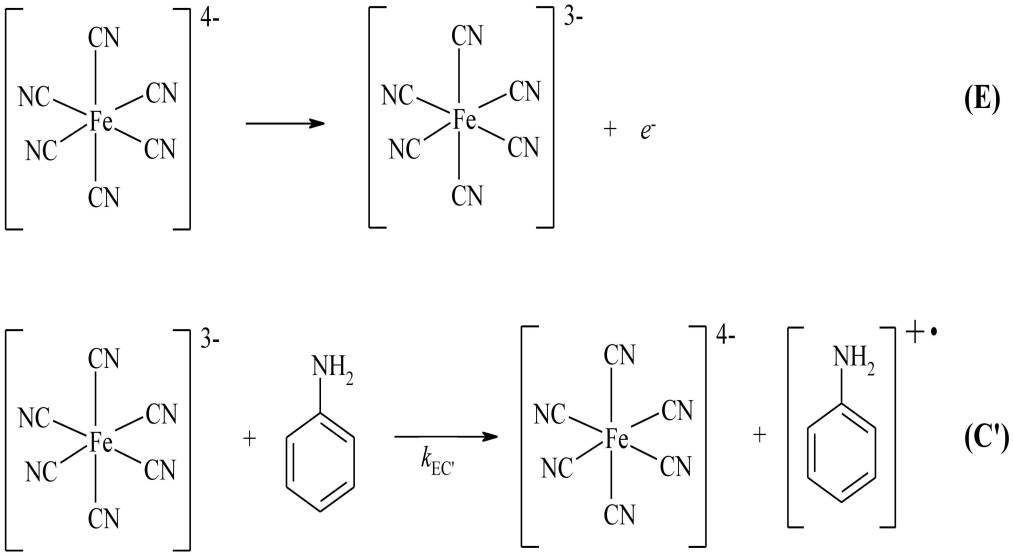


Figure 1.5 An example of an EC' mechanism: oxidation of ferrocyanide in the presence of aniline in aqueous /ethanolic mixtures.

1.2 Voltammetric Methods

Voltammetry involves the application of a potential to an electrode and the measurement of electrode currents which is plotted as a function of voltage in a linear sweep or as a function of time in a potential step experiment. Two main analysis methods are considered: linear sweep voltammery / cyclic voltammery and potential step chronoamperometry. Each of these techniques will be explored in the following parts.

1.2.1 Linear Sweep Voltammetry

In linear sweep voltammtry (LSV) experiments the potential at the working electrode is scanned from a potential E_1 to E_2 and simultaneous measurement of the current response as function of applied potential at a sweep rate. The sweep rate or "scan rate" is defined as, v;

$$v = \frac{dE}{dt} \tag{1.25}$$

Consider the example of a general n-electron reduction:

$$A + ne^- \rightleftharpoons B \tag{1.26}$$

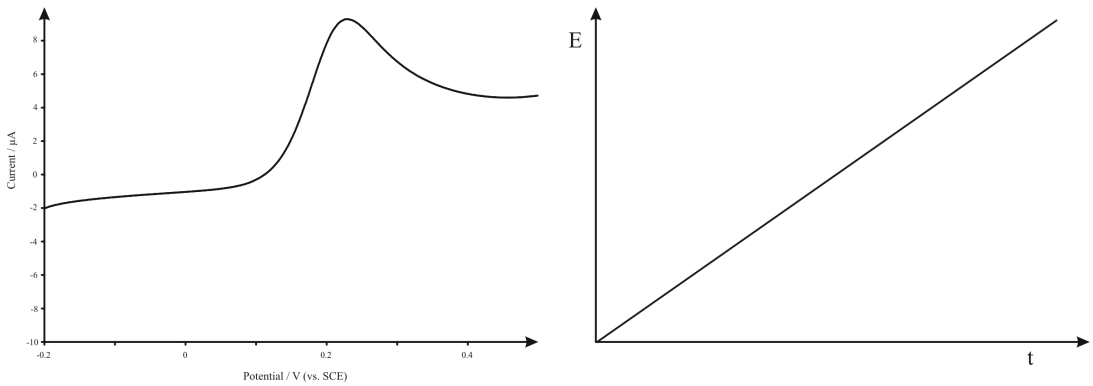


Figure 1.6 (left) a linear sweep voltamogram depicting the characteristic asymmetric peak-shaped response and (right) graph showing the variation of applied potential with time.

Initially no current flows since the applied potential is not sufficient to induce an electron transfer. As the potential is swept negative, to more reducing potentials, the reduction more favorable and current begins to flow exponentially in line with the Butler-Volmer equation as the activation overpotential to electron transfer is overcome. Eventually, at higher overpotentials the rate of electron transfer is much faster than the rate of mass transport resulting in the current reaching a maximum, where the current diminishes as the flux of *A* decreases. This produces the characteristic asymmetric peak-shaped response, as depicted in Figure 1.6. The combination of rising current in

the early part of the voltammogram due to potential activation control and the decaying current in the latter part corresponding to mass transport control means that the linear sweep voltammogram allows the determination of factors such standard rate constants for electron transfer (k^o) and the diffusion coefficients of the species undergoing electron transfer (D) which may be extracted from the rising and decaying portions of the voltammogram.

1.2.2 Cyclic Voltammetry

Cyclic voltammetry (CV) is an extension of linear sweep voltammetry where the direction of sweep is revered when a desired potential is reached and the electrode potential is cycled back to the original value, giving a triangular waveform of potential cycle. Thus the first part of the cyclic voltammogram is exactly the same as that of a linear sweep voltammogram with the interplay of electrode kinetics and the same factors influence the characteristic peak shape observed. At the end point of the linear sweep the potential is reversed and cycled back to its starting point re-oxidising or reducing the products formed in the first cycle, Figure 1.7.

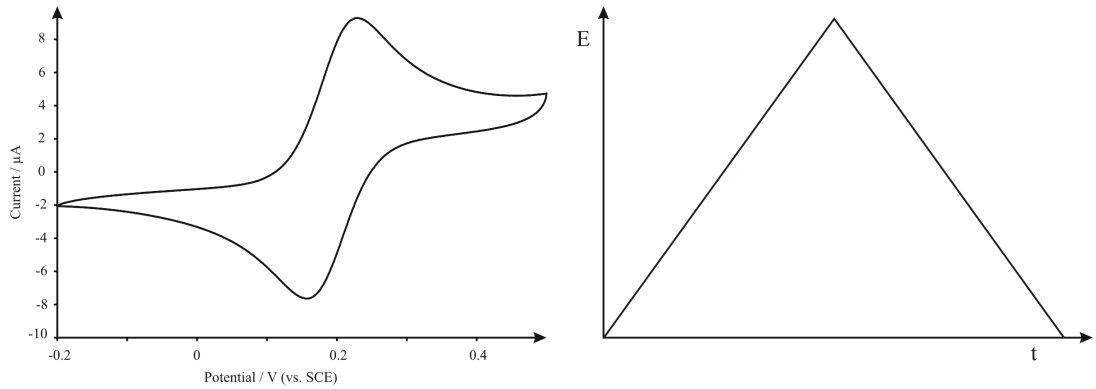


Figure 1.7 (left) A cyclic voltammogram depicting the characteristic asymmetric peak-shapes response and (right) graph showing the variation of applied potential with time

The shape of the cyclic voltammetry mainly depends on the reversibility of the redox couple being studied. The characteristic features of cyclic voltammetry observed

at macro electrodes where planar diffusion is dominant mode of mass transport are depicted below in Figure 1.8.

The response is illustrated for both electrochemically reversible, quasi-reversible, and irresverible processes wherein the species formed at the electrode is chemically stable. For a reversible species the current peak height in a linear sweep voltammetry experiment, or in the forward sweep of a cyclic voltammogram, is given by the relationship:

$$I_p = (2.69\times10^5)n^{3/2}AD^{1/2}C_0v^{1/2} \tag{1.27}$$

where D is the diffusion coefficient and C_0 is the bulk solution concentration and n is the number of electrons transferred.

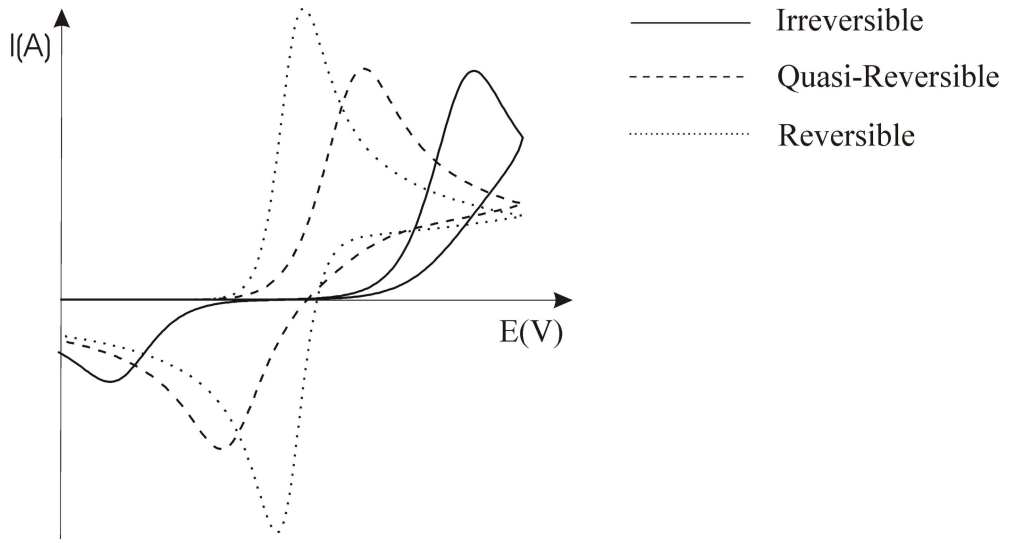


Figure 1.8 Cyclic voltammetry for reversible, quasi-reverisible, irrverisble electrode process when planar diffusion dominates.

Accordingly the dependence of peak current, i_p on scan rate, v, follows a characteristic square root law providing a telltale sign of the presence of a process in which the electron transfer is to a solution phase species; for a surface bound species, i_p depends directly on v . This relationship is particularly useful because by measuring i_p *vs.*

$v^{1/2}$ we can obtain an experimental value for the diffusion coefficient. When the system is fully reversible, the forward and the reverse peaks are separated by $2.3RT/nF$ ($59/n$ mV at 298 K) and the peak potentials are independent of the scan rate.

In the case of irreversible systems, the observed voltammogram is typically broadened and a reverse peak is not seen since the electron transfer kinetics are slow relative to mass transport unless a significant overpotential is applied. Unlike in the reversible limit, the peak potentials vary with scan rate and the separation of peaks is greater than $120/n$ mV. The current maximum observed under these conditions is given by the following equation:

$$I_p = (2.99\times10^5)n(\alpha n_a)^{1/2} AD^{1/2} C_0 v^{1/2} \qquad (1.28)$$

where n_a is the number of electrons transferred in the rate-determining step.

There exists an intermediate case known as quasi-reversible behaviour. As the scan rate is increased the kinetics of the electron transfer are not fast enough to maintain equilibrium. The separation of the forward and reverse peak is larger than $59/n$ mV at 298 K, with the peak-to-peak separation increasing with increasing scan rates. The peaks also become broader as the scan rate is increased with the peak current below the expected value for a reversible electron-transfer process.

Cyclic Voltammetry is probably the most widely used electrochemical method and also usually the first technique that is used to investigate a new electrochemical system. The reasons for its popularity are because cyclic voltammetry is a very fast way of obtaining information about an unknown electrochemical process. It is able to rapidly provide information on the thermodynamics of redox processes, the kinetics of heterogeneous electron-transfer reactions and on coupled chemical reactions or absorption processes. In an electroanalytical context its value is that it allows the rapid

determination of the redox potentials of the electroactive species and also allows for the fast evaluation of the effect of different solution media on the redox process.

1.2.3 Potential Step Chronoamperometry

In this method, the applied potential is stepped from a value at which no Faradaic processes occur to a potential that lies in the diffusion-controlled regime of the system under investigation. The current is measured as a function of time and when recorded on a macrodisk, can be described by the Cottrell equation:

$$I(t) = \frac{nFAc\sqrt{D}}{\sqrt{\pi t}} \tag{1.29}$$

Figure 1.9 illustrates the chronoamperogram that results from a potential step experiment measured at a disk electrode of micrometre dimensions.

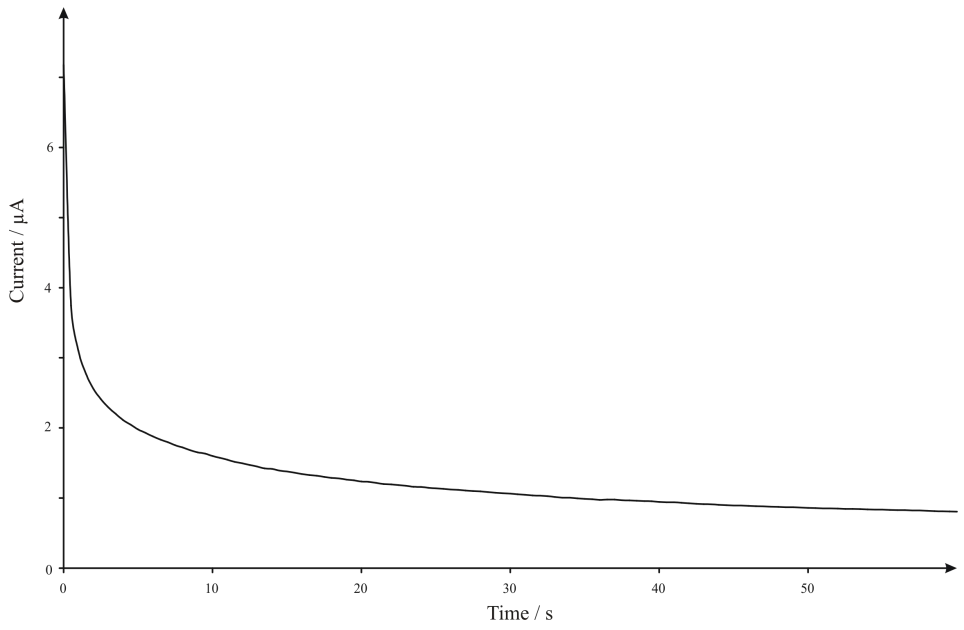


Figure 1.9 Schematic diagram of a chronoamperogram recorded at a microdisk electrode.

At the start of the potential step the current instantly reaches a high value and then decays proportionally to $\frac{1}{\sqrt{t}}$. This is because initially the potential is not sufficiently

negative to drive electrons from the electrode to the solution phase and hence no current flows. When the potential is stepped a sufficiently negative potential is applied in order to overcome this activation barrier and a large current flows instantly. This current can then be seen to decay because the reactants at the electrode surface are being depleted and the process is relying on transport of fresh reactants from the bulk solution, thus the process has become diffusion limited.

Several analytical techniques have been developed to describe the current observed by this technique at microelectrodes, which can be expressed by the following equation,

$$I = 4nFr_eDcf(\tau) \tag{1.30}$$

where n is the number of electrons transferred, F is the Faraday constant, r_e is the radius of the microdisk, D the diffusion coefficient of the electroactive species, c the concentration of the electroactive species, and the dimensional parameter, $\tau = 4Dt/r_e^2$, becomes an index of time, t. The Shoup and Szabo model gives one single relationship that is accurate with in 0.6% of all times:

$$f(\tau) = 0.7854 + 0.8862\tau^{-1/2} + 0.2416e^{-0.7823\tau^{-1/2}} \tag{1.31}$$

At this point, the recorded transients were fitted using nonlinear curve fitting function available in ORIGIN 6.0 (Microcal Software Inc.) with equation. With the fixed value of the radius of electrode it is possible to obtain the value for diffusion coefficient, D, of the species and the result of the concentration multiplied with the number of electrons, nC transferred by fitting the experiment data over an appropriate time period.

1.2.4 Square Wave voltammetry

Square-wave voltammetry (SWV)[23,24] is a pulse voltammetric technique which is commonly used in electroanalytical procedures to further enhance the sensitivity of a process that uses linear sweep voltammetry. Hence it is regularly used as the stripping

step in stripping analysis in order to reduce the detection limit even further, it is generally able to reduce the detection limit by an order of magnitude over a given process utilising linear sweep voltammetry to attain the analytical signal.

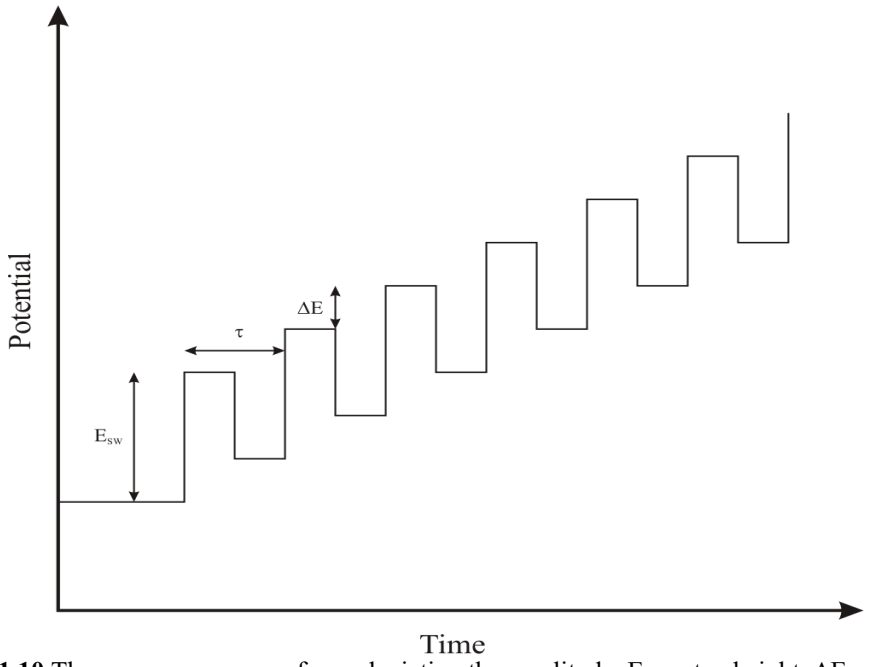


Figure 1.10 The square-wave waveform, depicting the amplitude, E_{SW}; step height, ΔE and square wave period τ.

The increase in sensitivity is attained by superimposing a waveform composed of a symmetrical square wave on the base staircase (linear sweep) potential, Figure 1.10. The current is sampled twice during each square wave, at the ends of both the forward and reverse pulses. As the square-wave amplitude is very large the reverse pulses cause the reverse reaction of the product of the forward pulse**,** Figure 1.11. Thus a square wave voltammogram consists of both a forward and a reverse component, the difference between the two measurements is plotted against the base staircase potential. The increase in sensitivity over a linear sweep voltammogram is due to the fact that the net current obtained from a square wave voltammogram is larger than either the forward or the reverse components because it is the difference between them.

Square-wave voltammetry has further advantages over linear sweep voltammogram, first the square wave itself effectively reduces charging background current. However

the major advantage of square-wave voltammetry is its speed. The effective scan rate to compare with a linear sweep voltammogram is given by $f \Delta E$ where f is the square-wave frequency and ΔE is the step height. The amplitude is given as $E_{SW,}$ reasonable square-wave amplitudes are in the range of 5-25 mV, larger amplitudes yield a larger response, but faradaic peaks will get broader and potential resolution will be lost at very large amplitudes. A proper choice of frequency is important as the influence of capacitive current is larger at high frequencies. Normally, the useful frequency range is 8-250Hz. It can be seen using these ranges that effective scan rates in the order of 1 Vs^{-1} can be achieved meaning that using square-wave voltammetry rather than linear sweep voltammetry not only results in a significant increase in sensitivity but also a significant decrease in the time taken to analyse a sample.

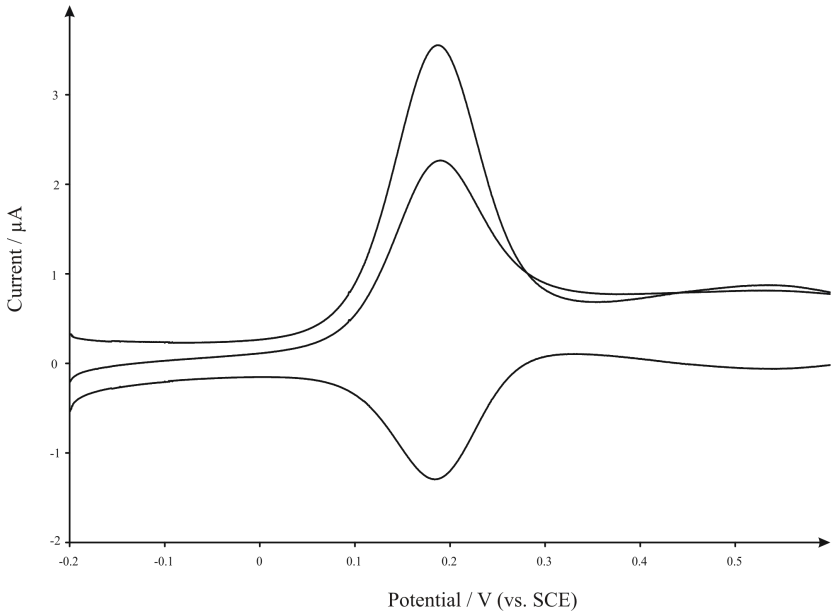


Figure 1.11 A square-wave voltammogram for the oxidation of 1 mM Ferrocyanide in 0.1 M KCl at a gold electrode, showing both the forward and reverse components of the net current

1.3 Electrochemical Cells

Having described above the factors which influence a current-voltage response, we shall now consider the practical arrangement of this system in the form of an electrochemical cell. In such a set-up, the reaction of interest occurs at the working electrode and a reference electrode produces a constant potential so that the potential drop between the two remains precisely defined. The applied voltage, E, can be expressed as

$$E = \left(\phi_m - \phi_s\right) + IR_s + \left(\phi_s - \phi_{ref}\right) \tag{1.32}$$

where ϕ_m, ϕ_{ref} and ϕ_s are the potentials for the working electrode, reference electrode and solution, respectively, R_s the solution resistance and I the current flowing between the two electrodes. The third term, ($\phi_s - \phi_{ref}$), is a measure of the potential drop at the reference electrode – solution interface and should be a fixed constant. The aim of the voltammetric measurement is to measure the potential drop between the working electrode and the solution interface, ($\phi_m - \phi_s$).

Under certain conditions, for example experiments conducted at microelectrodes, contribution of the IR_s term is negligible and can be ignored and thus the expression for the voltage is simplified to

$$E = \left(\phi_m - \phi_s\right) + \text{constant} \tag{1.33}$$

and changes in the applied potential are then directly reflected in the driving force, ($\phi_m - \phi_s$). At larger electrodes, however, where a much greater current is passed through the system, the IR_s term can no longer be ignored and ($\phi_s - \phi_{ref}$) is not necessarily a constant. A third, auxiliary electrode must be introduced to the system, typically referred to as the *counter* electrode. In this arrangement, the potential of the working

electrode is held relative to the reference electrode and an external potentiostat ensures that current only flows between the working and counter electrodes.

1.3.1 Working Electrodes

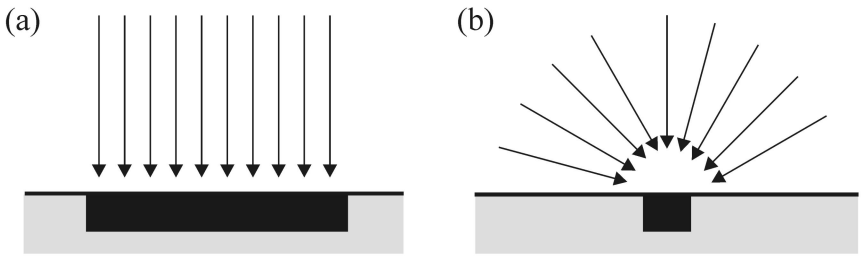
1.3.1.1 Microelectrodes

A microelectrode can be strictly defined as one whose critical dimension is smaller than the length of the diffusion layer developed over the experimental timescale. This typically translates to a disk with a diameter of less than 25 μm in conventional solvents.[25,26] The various geometries of these small electrodes, which includes discs, hemicylinders, rings and bands,[26,27] result in important differences in the voltammetric responses they produce as well as the electrochemical data they make accessible.[14,28-30] As the current measured at an electrode is a function of its area, those measured at microelectrodes are relatively small. However, convergent (non planar) diffusion is known to occur at electrodes of such small dimensions and thus, contributions to the current are received from both planar and radial diffusion, resulting in an increased current density as compared to a macroelectrode. Figure 1.12 illustrates the difference between planar diffusion, typically observed at a macroelectrode, and the hemispherical diffusion seen at a microdisk electrode, whereby the 'edge effects' serve to increase the current density.

Convergent diffusion also results in faster mass transport to these electrodes as compared to those of macrometere size, which enables the measurement of fast kinetics and allows for steady-state currents to be obtained at modestly attainable scan rates, where

$$I_{ss} = 4nFrDc_{\text{bulk}} \tag{1.34}$$

The ohmic drop caused by uncompensated solution resistance is considerably reduced at microelectrodes and, under certain experimental conditions, eliminates the need for added supporting electrolyte. Last, microelectrodes allow for a simpler two-electrode arrangement to be employed since the potential of the reference electrode is not expected to shift significantly with the passing of such tiny currents.



Firgure 1.12 Schematic representation of (a) linear diffusion observed at a macrodisk electrode and (b) convergent diffusion to a microdisk electrode surface

1.3.1.2 Rotating Disk Electrodes

The rotating disk electrode is one example of a hydrodynamic electrode, whereby forced convection is employed to dominate and enhance the rate of mass transport. In the case of the rotating disk electrode, the actual electrode itself, comprised of a disk electrode

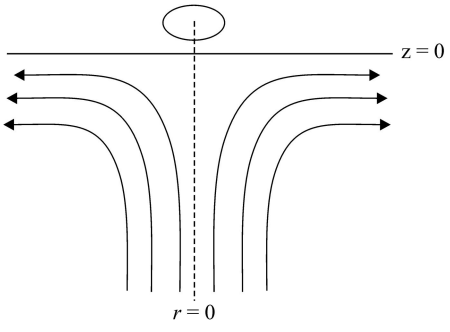


Figure 1.13 Laminar flow towards an RDE (z is the coordinate perpendicular to the electrode surface and r is the radius of the electrode).

surrounding by an insulating sheath, imposes the motion as the name implies; the disk is rotated around the axis perpendicular to its plane with an angular velocity, ω. As with most hydrodynamic systems, a laminar flow is established as the rotation forces solution out from the outer sheath in a radial direction, pulling fresh material towards the working surface (see Figure 1.13). The limiting currents observed at these electrodes with one electron transfer can by expressed by the Levich equation:[18,31]

$$I_{\text{lim}} = 0.62FAc_{\text{bulk}}D^{2/3}\nu^{-1/6}\omega^{1/2} \qquad (1.35)$$

where the kinematic viscosity, ν, is defined as $\nu = \eta / \rho$ and given in units of $cm^2\ s^{-1}$ and the angular velocity, ω, in units of Hertz (s^{-1}).

1.3.2 Reference Electrodes

For a reference electrode to be suitable for use in electrochemical experiments, it is requirement that the relevant half cell provide a stable potential, relative to which the voltage of the working electrode may be measured. A range of the reference electrodes are available, though their suitability is usually dependent on exponential conditions, particually the solvent. Aqueous electrochemistry is undertaken using a saturated calomel reference electrode whereas non-aqueous studies normally involve the use of quasi-reference electrodes.

1.3.2.1 The Saturated Calomel Electrode

The saturated calomel electrode (SCE) comprises mercurous chloride, mixed with liquid mercury in contact with saturated aqueous potassium chloride. These components are typically contained within a tube and separated from the bulk solution of interest by a porous frit. Since the solution is saturated in chloride ions, the activity

of chloride is constant, provided the temperature is invariant and so the Nernstian equilibrium is held fixed, providing a stable reference potential.

1.3.2.2 Quasi Reference Electrode

Quasi references are commonly used in non-aqueous systems, and are usually just a metal wire, such as platinum or silver. The potential determining equilibrium of such electrode is ill-defined, but if the wire is situated in bulk solution where few changes in electrode composition occur, the electrode potential, although unknown, will usually remain constant during the course of an electrochemical experiment. There electrode may be calibrated if necessary by measuring the voltammetry of a standard redox couple of known potential against the quasi reference under investigation. Alternatively, if more accurate potential measurements are required, this standard redox couple may be used in-situ, as long as it does not interfere with the electrochemical system studied.

1.4 References

(1) Bard, A. J.; Faulkner, L. R. *In Electrochemical Methods: Fundamentals and Applications.*, 2nd ed ed.; Wiley & Sons, Inc.: New York., 2001.

(2) Eklund, J. C.; Bond, A. M.; Alden, J. A.; Compton, R. G. *Adv. Phys. Org. Chem.* **1999**, *32*, 1.

(3) Brett, C. M. A.; Brett, A. M. O. *Electrochemistry: Principles, Methods and Applications;*; Oxford University Press: Oxford 1993.

(4) Helmholtz, H. L. F. v. *Ann. Physik* **1853**, *89*, 211.

(5) Helmholtz, H. L. F. v. *Ann. Physik* **1879**, *7*, 337.

(6) Gouy, G. *Compt. Rend.* **1910**, *149*, 654.

(7) Chapman, D. L. *Phil. Mag.* **1913**, *25*, 475.

(8) Stern, O. *Z. Elektrochem.* **1924**, *30*, 508.

(9) Grahame, D. C. *Chem. Rev.* **1947**, *41*, 441.

(10) Fick, A. *Phil. Mag.* **1855**, *10*, 30.

(11) Fick, A. *Poggendorff's Annel. Phsyik.* **1855**, *94*, 59.

(12) Rieger, P. H. *Electrochemistry.*, 2nd ed ed.; Chapman and Hall: New York, 1994.

(13) Fisher, A. C. *Electrode Dynamics*; Oxford University Press: Oxford, 1996.

(14) Oldham, K. B.; Zoski, C. G. *Comprehensive Chemical Kinetics* **1986**, *26*, 79.

(15) Bond, A. M. *Broadening Electrochemical Horizons*; Oxford Unversity Press: Oxford, 2002.

(16) Butler, J. A. V. *Trans. Faraday Soc.* **1924**, *19*, 734.

(17) Erdey; Gutz, T.; Volmer, M. *Z. Phys. Chem.* **1930**, *150A*, 203.

(18) Albery, J. *Electrode Kinetics*; Clarendon Press: Oxford, 1975.

(19) Testa, A. C.; Reinmuth, W. H. *Anal. Chem.* **1961**, *33*, 1320.

(20) Conant, J. B.; Pratt, M. F. *J. Am. Chem. Soc.* **1926**, *48*, 3178.

(21) Lawless, J. G.; Hawley, M. D. *J. Electroanal. Chem.* **1969**, *21*, 365.

(22) Rashid, A.; Kalvoda, R. *J. Electroanal. Chem.* **1970**, *28*, 245.

(23) Brett, C. M. A.; Brett, A. M. O. *Electroanalysis*; Oxford University Press: Oxford, 1998.

(24) Wang, J. *Analytical Electrochemistry*, 2nd ed ed.; Wiley: New York, 2000.

(25) Fleischman, M.; Lassere, F.; Robinson, J. *J. Electroanal. Chem.* **1984**, *177*, 115.

(26) Montenegro, M. I. *Res. Chem. Kin.* **1994**, *2*, 1.

(27) Aoki, K. *J. Electroanal. Chem.* **1981**, *122*, 19.

(28) Aoki, K. *Electroanalysis* **1993**, *5*, 627.

(29) Heinze, J. *Angew. Chem. Int. Ed.* **1993**, *32*, 1268.

(30) Stulik, K.; Amatore, C.; Holub, K.; Marecek, V.; Kutner, W. *Pure Appl. Chem.* **2000**, *72*, 1483.

(31) Levich, V. G. *Physiochemical Hydrodynamics*; Prentice Hall: Englewood Cliffs, 1962.

CHAPTER 2

Instrumentation and Experimental Methods

This chapter covers fundamental aspects of the instrumentation and experimental techniques that are commonly employed throughout the work presented in this thesis. More details on each experiment and how it s performed will be given in the relevant chapters.

2.1 Electrodes

2.1.1 Microelectrodes

All microelectrodes, with the exception of the platinum microdisks employed, were purchased from Cypress Systems (Kansas City, Kansas, USA). The following polishing routine was used prior to experimentation: microelectrodes were first carefully polished using a 1.0 μm alumina slurry (Kent, U.K.), followed by a 0.3 μm alumina suspension (Buehler, Lake Bluff, IL, USA) and on a clean, damp cloth (Microcloth, Buehler, Lake Bluff, IL, USA). In some cases, the electrode was then immersed in 10 % nitric acid solution to remove any adsorbates. The electrode was always rinsed with an aprotic solvent before introducing it to the solution. The diameter of the microdisk electrodes was calibrated electrochemically using 2 mM Cp_2Fe in 0.1 M TBAP / MeCN, using a value for the diffusion coefficient of 2.3 x 10^{-5} cm^2 s^{-1} at 295 K.[1]

2.1.2 Macroelectrodes

The following macrodisk electrodes have been employed: gold (Au, 1 mm diameter), platinum (Pt, 1 mm diameter), boron-doped diamond, (BDD, 3 mm diameter, Windsor Scientific Ltd, U.K.), edge and basal plane pyrolytic graphite electrodes, (EPPG, BPPG, 4.9 mm diameter, Le Carbone, Ltd. Sussex, U.K.)[2,3] glassy carbon (GC, 3 mm diameter, BAS Technicol, USA), and highly oriented pyrolytic graphite electrode (HOPG, 4.9mm diameter, SPI supplies). The gold and platinum electrodes were polished on 1.0 μm alumina slurry, whilst the later was polished on diamond pastes of decreasing particle size (6 μm to 1 μm, Kemet, Kent, UK). The EPPG and BDD electrodes were polished on alumina lapping compound of decreasing sizes (0.1–5 μm) on soft lapping pads. The BPPG electrode surface was renewed using cellotape. This procedure involves polishing the BPPG electrode surface on carborundum paper and then pressing cellotape on the cleaned BBPG surface before removing along with general attached graphite layers. After repeating several times, the electrode was then cleaned in acetone to remove any adhesive. The basal plane HOPG electrode was prepared by first disassembling the electrode housing and taking the HOPG slab out. The slab was renewed by pressing cellotape on the slab surface to get rid of general attached graphite layers. This was repeated several times until a shiny and smooth electrode surface was observed.

2.1.3 Reference Electrodes

Different reference electrodes were used according to the solvent employed. For aqueous studies a saturated calomel reference electrode was used (SCE, Radiometer, Copenhagen, Denmark). Generally experiments based in non-aqueous media were

carried out using a 0.5 mm diameter silver wire aqueous quasi-reference electrode (Goodfellow).

2.2 Electrochemical Cell

For all electrochemical experiments carried out in large volumes, a standard three-electrode configuration was used within a three-arm electrochemical cell. A platinum wire wound into a spiral provided the counter electrode and a platinum or silver (Ag, 0.5 mm diameter, 99.99%, Advent Research Materials Ltd, Oxford, UK) wire pseudo reference electrode completed the cell assembly (see Figure 2.1). The system was purged with nitrogen prior to any experimentation

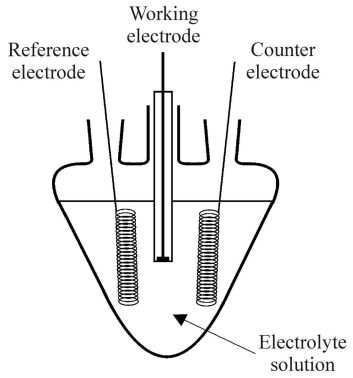


Figure 2.1 Cross section of the cell

For those electrochemical experiments involving the ionic liquid in small volumes, the working electrode was modified with either a trimmed disposable micropipette tip or a short piece of heat-shrink tubing so as to provide a cavity into which a small sample of ionic liquid (20 - 40 μL) could be delivered by micropipette. A conventional two-electrode set-up was utilised with a silver wire (0.5 mm diameter, 99.99%, Advent Research Materials Ltd, Oxford, UK

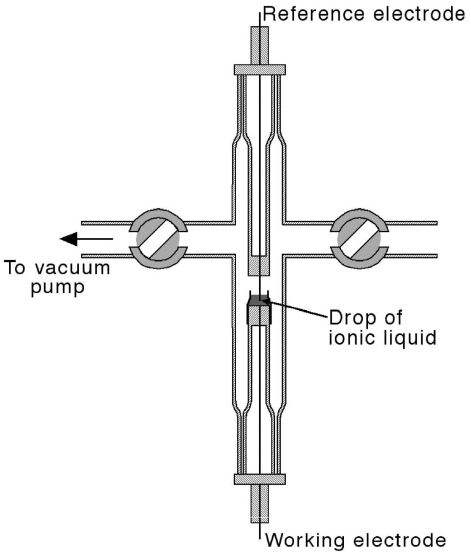


Figure 2.2 Cross section of the cell used with microlitre samples of ionic liquids.

acting as the quasi-reference electrode. All experiments were carried out in an electrochemical cell designed to sustain vacuum conditions at a temperature of 298 K, (see Figure 2.2). Prior to the addition of any gaseous analyte, the sample of ionic liquid was either placed under vacuum (Edwards High Vacuum Pump, Model ES 50) for forty minutes or purged with nitrogen until the baseline showed little trace of atmospheric oxygen. Those experiments that employed a microelectrode were conducted inside a Faraday cage so as to minimize external noise.

2.3 Instrumentations

2.3.1 Potentiostat

A commercial potentiostat, PGSTAT 20 (Eco Chemie, Utrecht, Netherlands), was used for all electrochemical experiments in conjunction with a Pentium-based PC running the General Purpose Electrochemical System (GPES) software, version 4.7 (Eco Chemie).

2.3.2 Atomic Force Microscopy

The Atomic Force Microscope (AFM) is a form of Scanning Probe Microscopy (SPM), which allows a samples surface topography to be imaged on the nanometer scale.[4] It is therefore the ideal tool for use in viewing and characterising electrochemically grown nanoparticle deposits. Unlike traditional microscopes, scanning probe systems do not use lenses to acquire an image. Instead a tiny probe attached to the end of a cantilever is traced across the sample surface measuring a specific property – in this case height, so their resolution is limited by the size of the probe rather than diffraction effects. It operates by measuring repulsive forces between a tip and the sample, the instrument lightly touches a tip at the end of a leaf spring or

"cantilever" to the sample. As a raster-scan drags the tip over the sample, a laser beam aimed precisely at the cantilever measures its vertical deflection recorded on a photodetector grid which indicates the local sample height. Unlike electron microscopes, AFM does not require any form of sample pre-treatment and can generally image samples in air and under liquids. As a height profile of the surface is acquired an atomic force microscope effectively images the sample surface in 3D, the image analysis software then allows the size, volume and surface density of particles to be accurately measured. An important feature of AFM imaging is the ability to image an electrode surface in-situ under solution while electrochemical processes are carried out, in this case nucleation and growth of nanoparticles can be monitored almost in real time. Figure 2.3 shows some example AFM images taken of bare commonly used electrode surfaces.

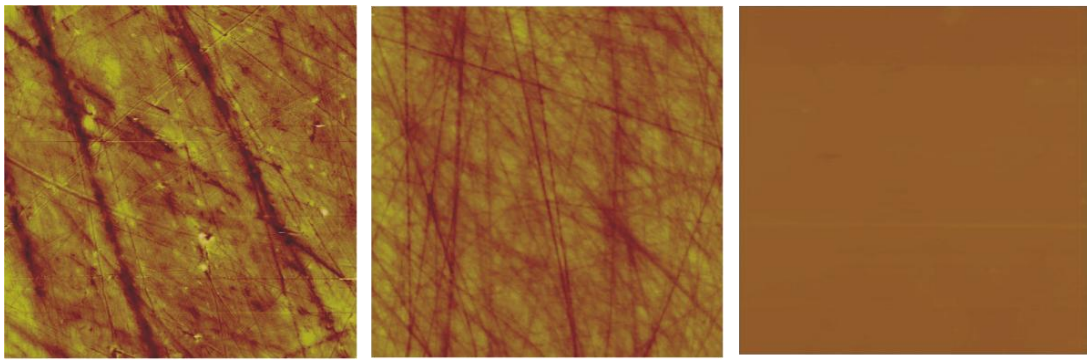


Figure 18 Typical AFM images of bare commonly used electrode surfaces. (10 μm x 10 μm)

AFM is based around the ability to be able to move a sample under a small stationary tip (or tip over a stationary sample) over the scale on nanometres. To do this a piezoelectric crystal is used, a piezoelectric crystal is a material which expands and contracts proportionally to an applied voltage, it forms the basis for the construction of the AFM scanner head. A typical piezoelectric material will expand by about 1 nm per

applied volt. In order to get larger motions it is necessary to make piezoelectric transducers with hundreds of layers of piezoelectric materials.

There are two forms of AFM which are commonly used when looking at deposits on electrode surfaces, these are known as tapping mode (TM) and contact mode (CM), each having its own advantages and disadvantages for use in a particular experiment. Contact mode is the simplest form of AFM available, it operates by scanning a tip attached to the end of a cantilever across the sample surface while monitoring the change in cantilever deflection with a laser beam reflected off the cantilever onto a photodiode detector. The primary advantage of contact mode is its simplicity and high scan speed, it is also the only AFM technique which can obtain "atomic resolution" images. The main disadvantages with contact mode are that as the tip is in direct contact with the surface it exerts a force on the surface which may distort features in the image but more seriously actually remove electrode deposits that are not well adhered to he surface. To reduce the interaction between the tip and surface, less invasive imaging modes have been developed. The most useful of these is tapping mode.

Tapping mode employs a relatively rigid cantilever attached to a piezoelectric oscillator. The oscillator is tuned to the resonant frequency of the cantilever usually 300 kHz in air or 20 kHz in a liquid. As with contact mode the laser beam is reflected off the back of the cantilever onto a photodetector this time the detector receives an oscillating signal. The RMS amplitude of the signal is a measure of the distance the cantilever is moving. As the distance between the tip and the sample is reduced the oscillation of the cantilever is damped by the interactions between the tip and the sample surface the output RMS amplitude is therefore proportional to the distance between the tip and the sample surface. As the tip is not in direct contact with the

surface as with contact mode AFM, the forces applied to the surface are much smaller. This makes tapping mode a useful imaging tool for soft samples, or those with poorly attached features which may be dislodged by contact mode imaging. The drawbacks to using tapping mode AFM however are a reduced resolution and a much slower scan rate must be employed to obtain good quality images.

2.3.3 Electrochemical Electron Spin Resonance

Electron spin resonance (ESR) is a spectroscopic technique used to detect species which posses unpaired electrons such as free radicals, radical ions and transition metal complexes.[5-7] Such substances are referred to as paramagnetic because of their interaction with magnetic fields. Free radicals and radical ions are ubiquitous throughout electrochemistry since single electron transfer reaction are very commonly associated with electrode processes, and so ESR is an idea tool to study electrochemical systems. Mechanistic features of electrode reactions may be elucidated by identification of paramagnetic intermediates and, since the ESR signal intensity is a quantitative measure of the number of paramagnetic centers, this technique may be used to determine the kinetics of their decay. Due to some fundamental incompatibilities and limitations, using ESR in conjunction with electrochemistry is by no means trivial, but significant advances have been made, particularly in the field of electrochemical cell design, which have circumvented these problems and allowed electrolytic processes to be studied in-situ, making this a very powerful methodology indeed.

ESR spectra were measured using a JEOL JES-FA 100 X-band spectrometer operating at 9.5 GHz (336 mT centre field), equipped with cylindrical TE011 resonant cavity. Cavity tuning was achieved using the JEOL spectrometer software (A-SYSTEM v. 1. 100, FA-MANAGER v. 1. 0. 1). In order to account for variations in cavity Q

throughout the course of an experiment, integrated signal intensities were typically measured relative to a standard marker consisting of solid MgO dispersed with paramagnetic Mn^{2+}, inserted into the cavity at the time of measurement. In the experiments a microwave power of 1 mW was used, and regular tests were carried out to check that increasing the microwave power increased the ESR signal, thus ensuring the system was not power saturated. In addition to allowing to the control of experimental condition relevant to the acquisition of ESR spectra, the JEOL spectrometer software package permits the simulation of isotropic spectra based upon selected hyperfine coupling constants and line-width parameters. This software was used in order to aid the identification of species rescored spectra.

2.4 References

(1) Sharp, M. *Electrochim. Acta* **1983**, *28*, 301.

(2) Bowler, R.; Davies, T. J.; Hyde, M. E.; Compton, R. G. *Anal. Chem.* **2005**, *77*, 1916.

(3) Moore, R. R.; Banks, C. E.; Compton, R. G. *Anal. Chem.* **2004**, *76*, 2677.

(4) Cohen, C.; Bray, S. H. *Atomic Force Microscopy/Scanning Tunneling Microscopy*; Springer, 1995.

(5) Alger, R. A. *Electron Paramagnetic Resonance: Techniques and Applications*; Wiley: New York, 1968.

(6) Symons, M. C. R. *Chemical and Biochemical Aspects of Electron-Spin Resonance Spectroscopy*; Van Norstrand Reinhold: New York, 1978.

(7) Weil, J. A.; Bolton, J. R.; Wertz, J. E. *Electron Paramagnetic Resonance: Elementary Theory and Practical Applications*; Wiley: New Yok, 1994.

CHAPTER 3

Carbon Based Electrodes in Electroanalysis

This chapter reviews recent investigations of carbon nanotube modified electrodes in electroanalysis, as well as reporting on fundamental advances in understanding the electrochemical reactivity of carbon nanotubes.

3.1 Pyrolytic Graphite

Carbon is one of the most abundant elements found in the earth. It is well known that a variety of bulk carbon structures exist, which have different forms such as diamond and graphite. A diamond crystal consisting of sp^3-hybridised carbon atoms is cubic with the atoms arranged in a tetrahedral configuration, and represents one of the hardest substances known. Graphite on the other hand has a hexagonal structure with sp^2-carbon atoms where the C-C bond length is around 1.42 Å arranged in hexagonal layered planes.[1-3] A large variety of graphite products which have been used as working electrodes, such as amorphous carbon, glassy carbon, carbon black, carbon fibres, powdered graphite, pyrolytic graphite (PG) and highly ordered pyrolytic graphite (HOPG), each with different chemical and physical properties. Whilst all being products of graphite, they all have a key structural factor which leads to an assortment of different materials. This is the average graphite microcrystallite size, *viz* lateral grain

size, the average size of the hexagonal lattices that make up the macro structure. The smallest lateral grain sizes are found in amorphous carbon, glassy carbon and carbon black and can be as low as 10 Å. In the intermediate range are carbon fibres and pyrolytic graphite with lateral grain sizes around 100 Å and 1000 Å respectively. In contrast, the highest grade of HOPG (ZYA and SPI 1 grade) can have lateral grain sizes of 1–10 μm.

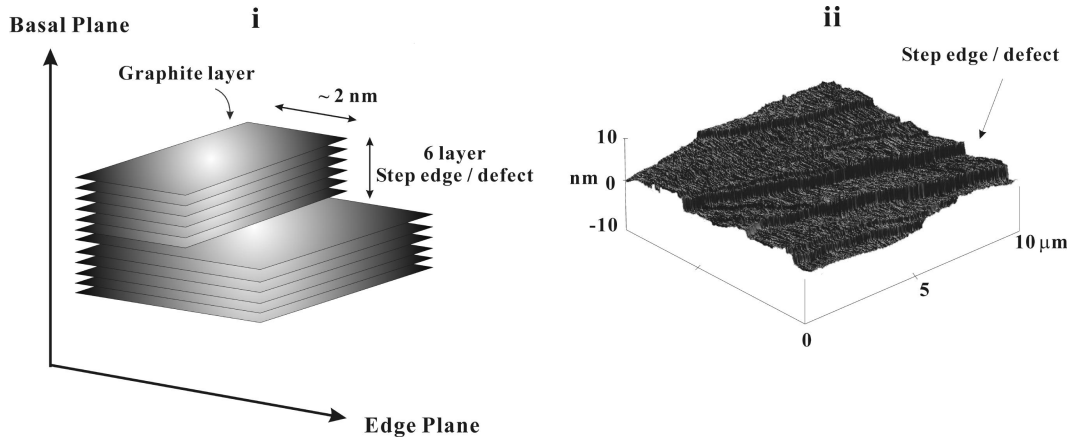


Figure 3.1 (i) Schematic representation of 6 layers HOPG and (ii) AFM image of a pieceof HOPG. Note that the interlayer spacing between graphite sheets is ~ 3.35Å.

From a slab of HOPG, edge plane pyrolytic graphite (EPPG) and basal plane pyrolytic graphite (BPPG) electrodes can be readily fabricated. Figure 3.1 shows a schematic representation of a slab of HOPG. If the graphite crystal is cut, as shown, perpendicular to these sheets an ‘edge plane’ electrode is formed whereas if the crystal is cut parallel to the sheets then a ‘basal plane’ electrode is formed. In the latter case the surface should not be thought of as perfect but rather as illustrated (Figure 3.1), there will be surface defects in the form of steps exposing the edges of the graphite layer. Such steps are typically 1 – 4 sheets of graphite in height; Figure 3.1 also shows an AFM image detailing edge steps. In carefully prepared samples of basal plane HOPG the distance between the edge steps can be as much as 1 – 10 μm. Due to the nature of the chemical bonding, the two phases, edge and basal exhibit completely different

electrochemical properties (see later). For voltammetry, the edge plane very often exhibits considerably faster electrode kinetics in comparison with the basal plane. This means that of an electrode consisting entirely of edge plane, an 'edge plane pyrolytic graphite electrode' may show a nearly reversible voltammogram whilst an electrode consisting mainly of basal plane can show irreversible behaviour but, crucially, depending on the number of edge plane step defects on the surface. For this reason, as discussed below, edge plane electrodes are often preferable to basal plane or other electrode for electroanalytical purposes.

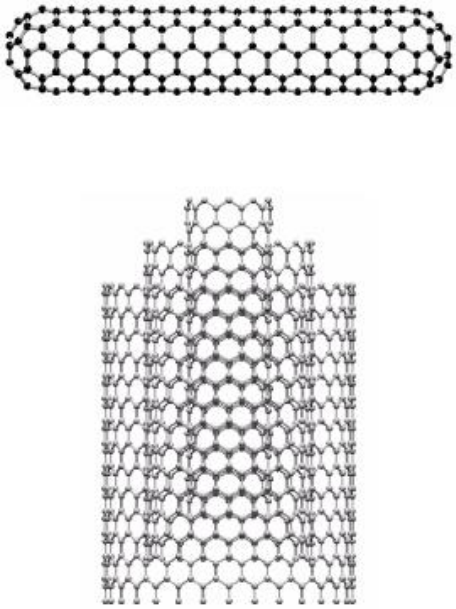


Figure 3.2 Structure of single walled and multi walled carbon nanotubes

3.2 Carbon Nanotubes

Carbon nanotubes (CNTs), as relatively a new form of carbon material, have attracted enormous attention around the world since their re-discovery in 1991 by Iijima.[4] CNTs are assigned into two classes: single walled (SWCNTs) and multi-wall carbon nanotubes (MWCNTs); Figure 3.2 shows a schematic representation of SWCNTs and MWCNTS. SWNCTs possess the simplest geometry, consisting of a single graphite sheet rolled flawless producing a tube diameter of 0.4 - 2 nm with the

length of the nanotube up to 20 cm.[5] Note that the ratio of the length against diameter is about 1000, so these hollow cylinders can be considered as a "one dimensional" structure. Since the formation of SWCNTs is based on the rolling of the graphite sheet, the cylinder structure of a SWCNT can exhibit different characteristics if the graphite sheet is wrapped in different directions as shown in Figure3.3.[6] This is explained by the chiral vector (C_h) which is denoted by (n,m). Hence the armchair (n=m) and zig-zag (m=0) configurations both have a mirror plane and thus are achiral. Nanotubes with (n≠m) are chiral (Figure 3.4). It is clear that SWCNTs with different chiral vectors might exhibit different chemical reactivity, electrical conductivity and mechanical strength. Additionally two different parts are apparent in SWCNTs: one is the side wall of the tube which is basal plane like and the other is the cap or end of the tube. These two different sites have different physical and chemical properties.

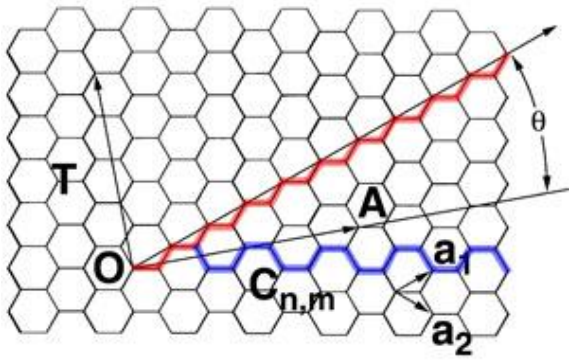


Figure 3.3 Roll-up of a graphite sheet

MWCNTs comprise several concentric tubes fitted one inside the other and their diameter can reach up to 100 nm.[6] There are a number of morphological variations of the MWCNTs including "hollow-tube", "herringbone" or "bamboo-like" MWCNTs (Figure 3.5).[7,8] A proportionally higher number of "edge-plane-like" defect sites occur on herringbone and bamboo MWCNTs because in these two cases the plane of the graphite sheets is at an angle to the axis of the tube resulting in a high proportion of the

graphite sheets terminating at the surface of the tube. The different structures of MWCNTs give different properties compared with those of SWCNTs

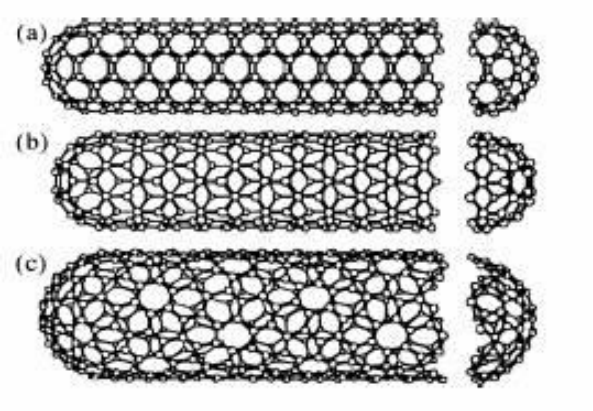


Figure 3.4 Different structures of SWCNTs: (a) armchair (b) zig-zag (c) chiral

The carbonaceous materials as described above, have many desirable properties such as high electrical conductivity, good chemical stability, and dimensional and mechanical stability, and as a result, are highly attractive for fundamental research and commercial applications.[9-21] One major use is in electrochemistry as electrodes as well as use in cell components for batteries and fuel cells, field emission materials and electronic devices; due to their unique size and properties carbon nanotubes are becoming increasingly used in such applications.

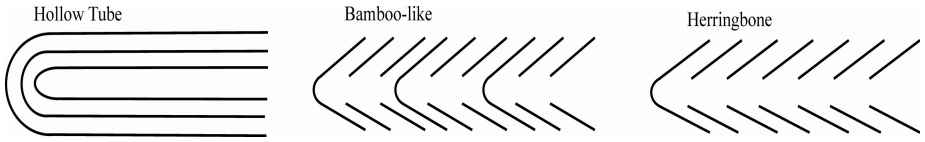


Figure 3.5 Schematic representation of the different structures of MWCNTs.

The original paper utilising carbon nanotubes as electrodes was reported by Britto and co-workers[22] but largely neglected until Joesph Wang and co-workers demonstrated their use for the electroanalytical detection of NADH.[23] In this pioneering paper, Wang showed that carbon nanotube modified glassy carbon electrodes were "electro-catalytic" for the detection of NADH; a considerable reduction in the over-

potential compared to the underlying electrode was observed coupled with a large increase in the magnitude of the voltammetric signal and no surface fouling which usually plagued other carbon based electrodes.[23] Since this paper published by Wang, the use of carbon nanotubes in electroanalysis (and electrochemistry) continues to escalate as each year passes.[8,23-46] Another notable use of carbon nanotubes is their use in electrochemical biosensors. Due to their size CNTs can promote electron transfer reactions of proteins whereas other carbon based electrode substrates cannot since the redox centres of the protein are embedded in the glycoprotein shell and inaccessible to most electrodes.

Moreover, CNT modified electrodes, usually glassy electrode as a substrate, have demonstrated many advantages in electroanalysis over other carbon based electrodes which include low detection limits and high sensitivity due to their large electrochemical area, and low overpotentials resulting in increased specificity since the oxidation (or reduction) of interferents is precluded.[31,41,45] Due to their enhanced properties, carbon nanotube modified electrodes have been classed as electro-catalytic. However, until recently the exact origin of the 'electro-catalytic' properties of the carbon nanotubes had not been explained.

Recently, it has been shown that the edge plane like- sites / defects are the origin of the reactive sites for the electro-catalysis at MWCNTs modified electrodes since CNTs are effectively rolled up tubes of graphite with basal and edge plane sites. It has also been demonstrated that trapped metal impurities in carbon nanotubes are responsible for certain electro-catalysis.[47,48]

The aim of this chapter is to detail the recent investigations of carbon nanotube modified electrodes in electroanalysis as well as reporting on the fundamental advances in understanding the electrochemical reactivity of carbon nanotubes.

3.2.1 Carbon Nanotubes in Electrochemistry: Modifying the Nanotubes

Carbon nanotubes have been widely used in electrochemistry, none more so than electroanalysis, where carbon nanotube modified electrodes have been reported to have 'electro-catalytic' sensing properties. Based on their high chemical stability and excellent conductivity, CNTs have been used to modify the electrode surface since 1996. Moreover the CNTs can themselves be functionalised influencing their electrochemical performance. The methods to modify the surfaces of CNTs are divided into the following different areas: (1) Covalent functionalization including thermally activated chemistry, fluorination functionalization, and electrochemical activation; (2) modification via physical absorption on to the surface of CNTs and (3) modification of the CNTs with films such as surfactants. These modification strategies result in a unique response of the CNTs to the analyte of interest; the chemical and electrochemical modifications of CNTs are summarized with analytical examples encompassing various fields such as gas sensors and electrochemical biosensors.

3.2.1.1 Covalent Functionalization of CNTs and Their Applications

Due to the various applications of nanotubes in material and electronic devices the covalent chemical functionalization of CNTs has attracted much attention. The chemical modification of nanotubes can provide the fabrication of the composite nanostructures on their surface used in functional materials for biosensors and single electron transistors. With the covalent functionalization the surfaces of the carbon nanotubes can be tailored to support some specific recognition sites for analytes. In general, there are two different reactive sites on nanotubes, the open tube ends and sidewalls which are the "edge" and "basal plane-like" sites respectively; later on in this chapter we will look at this in detail. It is intuitive that the tube ends are more reactive

due to their five-member carbon rings and it has been reported that the nanotubes can be 'opened' by oxidizing caps with sulfuric acid or nitric acid, which transform the sp^2 into sp^3 hybridized carbon atoms and form different functional groups on the surface such as carbonyl and phenol groups.[42] In comparison, the chemical functionalization of the side walls of carbon nanotubes is not as easy and is usually achieved via chemical attachment via covalent bonds. For example, fluorine was covalently attached to the side-walls of SWNTs at temperatures ranging from 150 to 600 ^{0}C [49] with a limiting stoichiometry of C_2F achieved. These fluorinated nanotubes exhibit significant changes in their properties, especially improved solubility in organic solvents. Moreover a higher cell potential was observed when they were used as cathode materials in lithium batteries.[50] The chemical covalent functionalization of the open ends and the sidewalls of carbon nanotubes plays an important role in tailoring the properties of CNTs. The different kinds of functionalization approaches will be discussed in the following text, and we will highlight the electrochemical properties of the modified carbon nanotubes and especially demonstrate the mechanisms responsible for specific electro-catalysis.

3.2.1.2 CNTs oxidation and Subsequent Modifications

An inherent problem with studying carbon nanotubes is that of their purification. The main impurities are graphite sheets, metal catalysts, and amorphous carbon, which can be removed by oxidative treatment.[42] Carbon nanotubes can be 'chemically cut' into smaller fragments in a concentrated acid solution by sonication leaving the metal catalyst from their surfaces. Moreover, the resulting shorter carbon nanotubes can be separated into length distributions using chromatography.[51] These oxidizing procedures result in the opening of tube ends of the SWCNTs and form "hole-defect" sites on the sidewalls of SWCNTs, decorated with the oxygen functionalities such as carboxyl

groups as shown in Figure 3.6.[52,53] It is of no surprise that these oxidized carbon tubes could be electrochemically reduced. The corresponding 'diffusion coefficients' of the SWCNTs were measured in two different ionic liquids and these were found to be inversely proportional to the viscosity of the RTIL as expected.

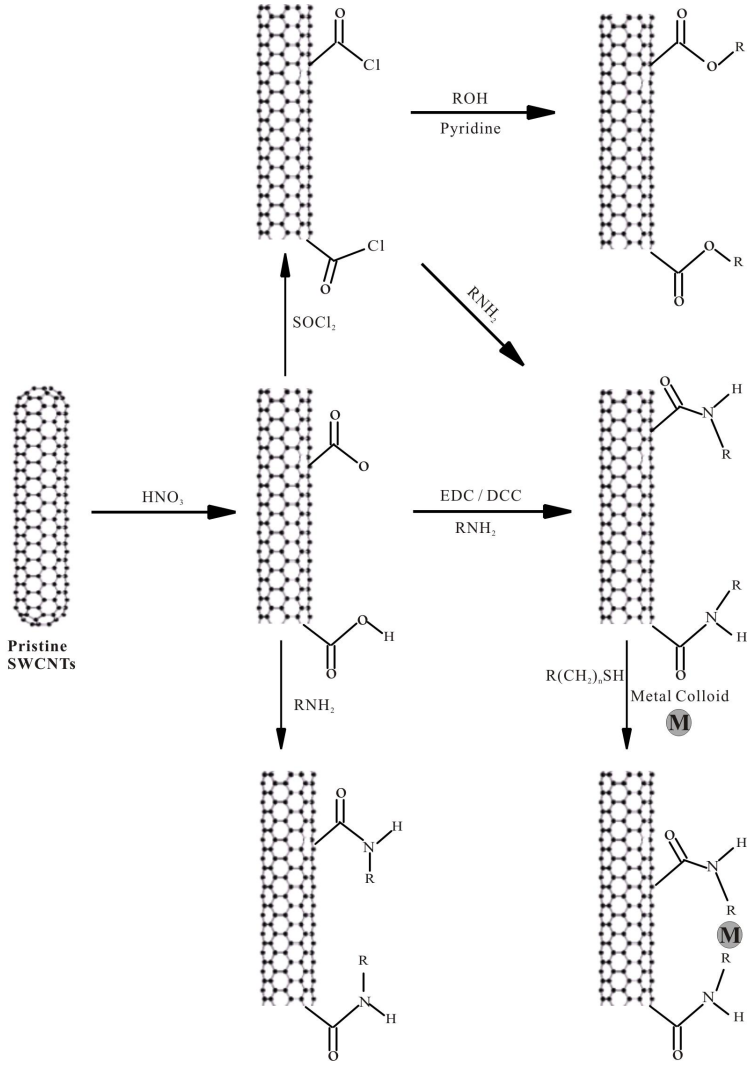


Figure 3.6 Schematic of common functionalization routes used to derivatize SWCNTs at ends and defect sites. Adapted from Ref [54]

The carboxyl functional groups on CNTs can further serve as useful sites for attachment of different kinds of chemical moieties onto the modified carbon nanotubes. Liu *et al* described aligned SWCNT arrays on gold surfaces using a wet chemical

approach.[55] Long SWCNT "ropes" were chemically cut into short lengths of open-ended and functionalizable tubes by concentrated acid oxidization. The produced carboxyl-terminated SWCNTs were further modified by reacting with cysteamine to form thiol-derivative SWCNTs, which could be self-assembled onto gold surface via Au-S chemical bonding as carbon nanotubes forests. This greater control over the distribution of carbon nanotubes on gold electrode indicates a new avenue for fabricating nanostructing array electrodes and performing nanonchemistry for various fields. Among the various reported applications of the chemically modified carbon tubes, the most are those where carbon nanotubes were used in electrochemical biosensors to improve the electrochemical reactivity of biomolecules, especially in some cases where the redox centre of proteins is contained deep within the glycoprotein shell such that the carbon nanotubes act as molecular wires to mediate the electrical communication between the working electrode and the proteins covalently attached to the functional carbon nanotubes, and hence give electrochemical signatures of protein activities.[56] Moreover, carbon tubes can also promote the rate of electron transfer for the direct redox reaction of proteins.[57] Azamian and co-workers successfully demonstrated various metalloproteins and enzymes could be physically absorbed onto the oxidized and carboxylated functionalized SWCNTs in aqueous solutions.[57] Figure 3.7 a shows an atomic force microscopy (AFM) image of a glucose oxidase (GOX)-modified SWCNT where GOX was strongly immobilized on the surfaces of SWCNTs. Note that its biocompatibility has been illustrated by electro-catalytic oxidation of glucose in aqueous solutions shown in Figure 3.7 b. With the functionalization groups introduced by thermally activated chemistry and surface immobilization of various biomolecules to carbon nanotubes, these can realise carbon nanotubes materials for use in highly sensitive nanoscale biosensors.

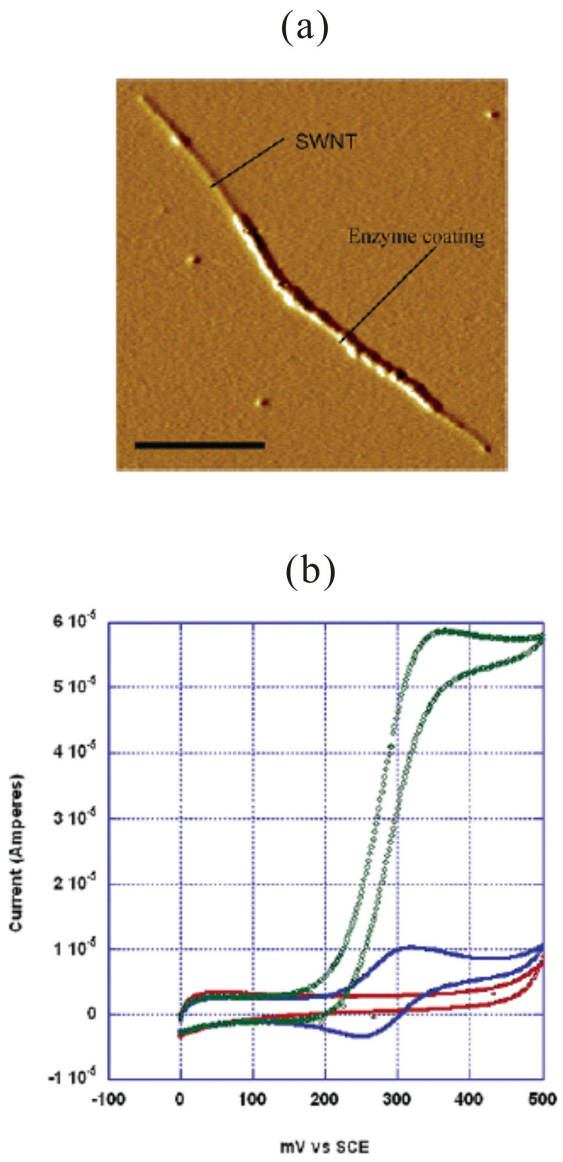


Figure 3.7 (a) AFM image of a glucose oxidase-modified SWNT. (b) Voltammetric response of a glucose oxidase-SWNT-modified GC electrode in the absence (red) and presence (blue) of 0.5 mM FMCA. The catalytic response (green) is observed on the addition of 50 mM glucose. Adapted from Ref [57].

3.2.1.3 Fluorinated Nanotubes and their Electrochemical Applications

The chemistry of carbon nanotubes is extensive and a wide range of their derivatives have been described.[51-53] More recently, fluorinated SWCNTs has attracted much attention not only because of their applications as cathode materials in lithium electrochemical cells,[50] but also they could offer new opportunities for further functionalization of the side wall of carbon nanotubes. Note that the fluorine on

sidewalls can be replaced chemically by reacting modified nanotubes with alkyl lithium or Grignard reagents since their C-F bonds are quite fragile with the eclipsing strain effect,[58] thus it can offer various functional groups on the nanotubes sidewall. Figure 3.8 summarizes a series of addition reactions to provide various functional groups onto the conjugated carbon network of carbon nanotubes. As for these fluorinated nanotubes, Peng *et al* found that the higher cell potentials were observed from them than those from carbon monofluoride in the lithium electrochemical cell, where the differences may come from the different shapes of carbon materials.[50] Further they suggested that carbon fluorine bond energies are dependent on the extent of sidewall fluorination. More recently, it was found that these fluorinated nanotubes could be easily recovered by sonication with hydrazine.[59]

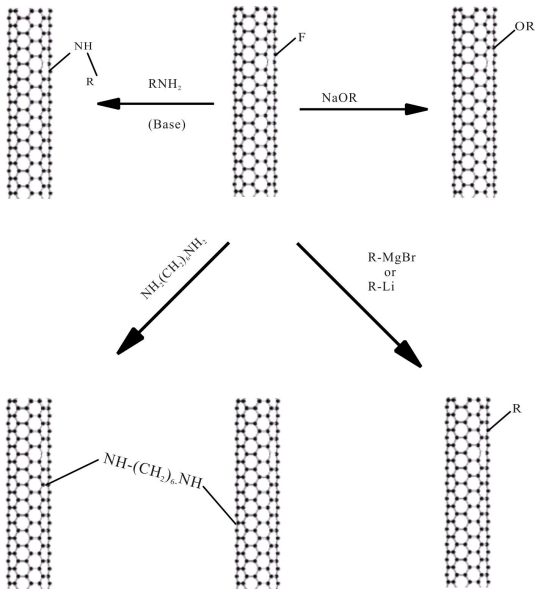


Figure 3.8 Functionalization of the sidewall in fluorinated nanotubes. Adapted from Ref [60]

3.2.1.4 Electrochemical Activation of CNTs and their Applications

Electrochemical pre-treatment, as one of the various techniques for the functionalization of carbon nanotubes with metals and related materials has been developed. This is a powerful technique for the deposition of many metals and / or the

surface modification of carbon nanotubes since it is rapid and facile thus allowing easily control of the nucleation and growth of metal nanoparticles. Such electrochemically deposited nanoparticles are often of very high purity, formed rapidly and have good adhesion to the carbon nanotube substrate.[61,62] We have electrochemically dispersed palladium nanoparticles of 1nm and less in diameter on 'bamboo' multi-walled CNTs and explored the CNT - palladium composites for the electrochemical oxidation of hydrazine.[62] Due to the size of the palladium nanoparticles a metastability occurs such that the CNT composites can be used in pH ranges that would otherwise be inaccessible since the voltammetric stripping of the palladium particles would occur. This approach allows electro-catalytic materials to perform in pH ranges which are normally unreachable. This palladium decorated bamboo MWCNTs can be used for the detection of hydrazine in an analytically useful concentration range, note that accidental hydrazine poisoning induces vomiting, severe irritation of the respiratory tract and long-term effects on the central nervous system.[63] Another advantage we need to point out is that this electrochemical pre-treatment could oxidize the nanotubes and introduce the required functional groups onto the sidewall of carbon tubes so that the surface properties of carbon nanotubes could be tailored via electrochemical modification since it allows for accurate control over the choice of suitable electrochemical conditions such as the deposition time and potentials. Day and co-workers successfully used SWCNT networks as templates to electrochemically deposit Ag and Pt nanoparticles.[64] The nucleation and growth processes of metal nanoparticles and nanowires grown on pristine SWCNT networks under electrochemical control were examined, and it was found that Ag growth was found to be rapid and progressive with an increasing nanoparticle density with time, whereas Pt deposition was characterized by lower nucleation densities and slower growth rates

with a tendency for larger particles to be produced over long times. Furthermore, they found that the density of nanoparticles could be influenced by the distance along the tube from the gold contact electrode, with a higher density being formed nearest the gold contact (Figure 3.9), which could be explained by the driving potential decreasing with distance along the nanotube axis.

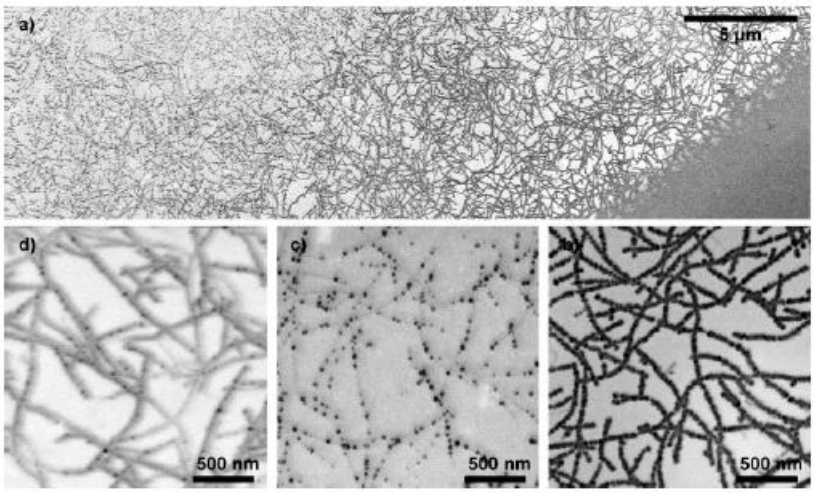


Figure 3.9 FE-SEM images showing (a) Pt deposited on SWNTs, using electrode device 1, from a solution containing 2 mM K_2PtCl_6 in 0.5 M perchloric acid. A deposition potential and time of - 0.4 V (versus Ag/AgCl) and 30 s were used. The SWNT network density was 6.8 µm SWNT µm $^{-2}$. In the bottom right of the image is the Au contact electrode which was also exposed to solution. (b)-(d) are higher resolution FE-SEM images: (b) close to, (c) ca. 15 µm from, and (d) further away (ca. 25 µm) from the contact electrode. Adapted from Ref [64]

Another electrochemical activation is via the reaction of organic radical species, which tend to form a film coated onto the sidewall of carbon nanotubes.[65] Electrochemistry is a well-suited tool for controlled modification of SWCNTs and layers of molecules could be formed around the SWCNTs using both oxidative and reductive coupling schemes.[66] Balasubramanian et al have shown that individual SWCNTs were electrochemically modified with 4-aminobenzylamine using the oxidative procedure and with 4-nitrobenzene diazonium tetrafluoroborate employing the reductive scheme shown in Figure 3.10.[67] It was found that SWCNTs remain

electronically unchanged which suggests that no bonds are broken with the oxidative modification and hence in this case the coated films (3 nm thickness) takes place via electropolymerization of the amine without the formation of covalent bonds between the resulting radicals and the SWCNTs. However, for reductive functionalisation of 4-nitrobenzene diazonium tetrafluoroborate, they found that the electrical resistance greatly increased indicating that the formed phenyl radicals had covalently modified the sidewalls of the nanotubes. Note that with this kind of covalent functionalization under an electrochemical regime, these nanotubes derivatives also demonstrated a significantly improved solubility in organic solvents in comparison with the unmodified carbon nanotubes, suggesting that this modification could tailor the physical properties of carbon tubes more suitable for different applications such as molecular electronics and field emission devices.

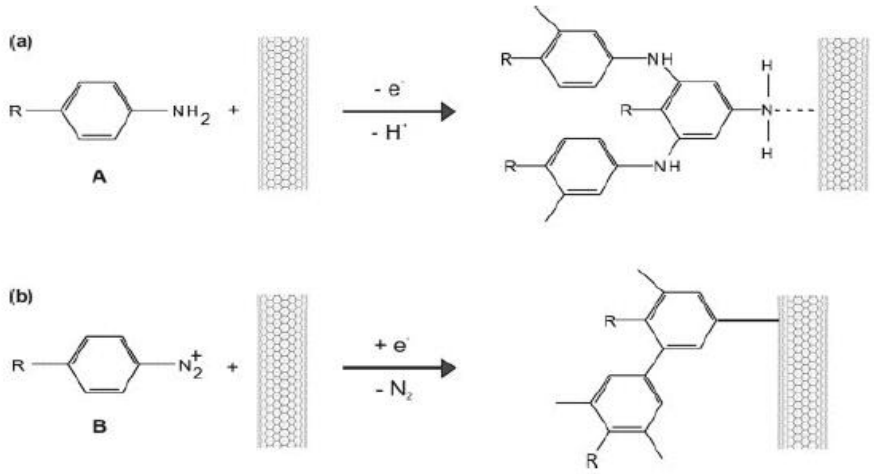


Figure 3.10 Reactions schemes for a) oxidative electrochemical modification with 4-aminobenzylamine (A) and b) reductive electrochemical modification with 4-nitrobenzene diazonium tetrafluoroborate (B). The broken line is part (a) indicates the formation of electropolymerized layers of A on the SWCNT without the creation of a chemical bond. In case of B, the experimental data give a strong indication of the formation of a chemical bond with the nanotube (bold line). Adapted from Ref [67].

3.2.2 The Applications of Un-functionalized CNTs in Electroanalysis

A common current whim amongst electro-analysts seeking new electro-catalytic surfaces is to modify a suitable electrode substrate (usually glassy carbon) with a film or layer of CNTs. In fact the number of papers reporting the use of carbon nanotubes as electrodes since Britto's first example in 1996 [22] increased slowly over a few years before exploding around 2002. Currently there are literally hundreds of papers involving the use of CNT modified electrodes in electroanalysis: Table 1 highlights a selection of different analytes that have been reported. It is clear that the carbon nanotube modified electrodes can be used to determine various kinds of analytes, which are very important in a biological context.

The claimed benefits of using these CNT modified electrodes include low detection limits, increased sensitivity, decreased overpotentials and resistance to surface fouling.[32] The method for making CNT modified electrodes was pioneered by Wang and co-workers.[23] This requires dispersing the desired CNTs into an organic solvent which is then pippetted onto a suitable electrode substrate (usually GC) which is allowed to volatize leaving a CNT 'film' or dispersion. It has been shown that Nafion allows the solubilisation of nanotubes in various liquid media while keeping the discriminative properties of the Nafion.[68] Another method was introduced by Moore et al, who explored the electro-reduction of ferricyanide and the oxidations of NADH, epinephrine and nore-epinprhine[69] using MWCNT modified basal plane pyrolytic graphite electrodes (BPPG) which were prepared via either abrasive or film modification. It involves gently rubbing a BPPG electrode on a fine quality filter paper containing the desired CNTs.

Table 1: Illustrative Systems Studied with CNT Modified Electrodes

Analyte	Support	Electrocatalytic w.r.t	LOD	Reference
NADH	GC	GC	0.1 mM	[23]
Hydrogen sulfide	GC	GC	0.3 μM	[70]
Morphine	GC	GC	0.2 μM	[71]
Brucine	GC	GC	0.2 μM	[72]
Amitrole	PE	[B]	0.57 μM	[73]
Cytochrome c	GC	GC	10 μM	[74]
Tinidazole	GC	GC/bare graphite	10 nM	[27]
Galactose	GC	GC	10 μM	[75]
Glucose	GC	GC	1 μM	[26]
Nitric oxide	GC	GC	80 nM	[29]
Cadmium(II)	[C]	GC	7.1 nM	[76]
Insulin	GC	GC	14 nM	[31]
Catechol	GC	GC	10 μM	[77]
Uric Acid	GC	GC	0.1 μM	[78]

Abbreviations: LOD: limit of detection; GC: glassy carbon electrode; PE: Paste electrode; [A]: Not specified, but is based on lowest addition; [B]: unknown; [C]: carbon nanotube array;

There are also a number of examples of electrochemical biosensors including the use of carbon nanotubes.[79,80] The most favourable method of preparation is that of the direct attachment of biomolecules to carbon nanotubes, where the direct electron transfers were observed. Wang et al have successfully used Nafion-dispersed carbon

nanotubes/ glucose oxidase (GOX) coated electrodes to determine glucose.[68] The resulting biosensors greatly benefit from the coupling of the efficient electro-catalytic action of CNT towards hydrogen peroxide and NADH. At the same time the CNT / Nafion association does not impair the electro-catalytic properties of CNT. Moreover, they developed an electrochemical DNA hybridization biosensor using carbon nanotubes dramatically amplifying the enzyme-based bioaffinity electrical sensing of proteins and DNA.[81] Here carbon nanotubes play a dual amplification role in both the recognition and transduction events, namely as carriers for numerous enzyme tags and for accumulating the product of the enzymatic reaction in the bioaffinity assays. It was found that the use of carbon nanotubes amplifiers (loaded with numerous ALP tags) has been combined with the pre-concentration feature of CNT transducers to yield a dramatic enhancement of the sensitivity. Many advantages for the modification of electrodes with carbon nanotubes have been shown above for electrochemical biosensing, and the use of carbon nanotubes molecular wires offer great promise for achieving efficient electron transfer from electrode surface to redox center of biomolecules.

3.2.3 Fundamental Understanding of the Electroactive Sites of Carbon Nanotubes

The establishment that carbon powder could produce analogous electro-catalytic properties to that of multi-walled carbon nanotubes[69] was the impetus of understanding the sites of electro-catalysis of multi-walled carbon nanotubes.

Moore and co-workers [69] explored the electro-reduction of ferricyanide and the oxidations of NADH, epinephrine and norepinephrine at multi-walled carbon nanotubes via both film and abrasive modification;[69] in the former case graphite powder or carbon nanotubes were dispersed in to an organic solvent, pipetted onto a

polished BPPG electrode, and allowed to volatilise leaving a carbon 'film' on the electrode surface while in the latter case abrasive attachment of CNTs onto BPPG electrodes is achieved via gently rubbing a polished BPPG electrode on a fine quality filter paper containing the nanotubes.

Excellent electro-catalysis was observed compared to the bare underlying electrode as reported in the literature. However, the key step was conducting a control experiment in which the MWCNTs were replaced with graphite powder. Similar catalytic behaviour was also seen at the graphite powder modified electrodes. The analogy was given that ' by taking graphite scrapped from your bar-b-que or chimney, you can easily mimic the electro-catalytic properties of carbon nanotubes!" [82]

The Fundamental understanding from the experiment discussed above allowed us to provide the first definitive evidence what the electro-catalytic properties of carbon nanotubes.[83] The electrochemical oxidation and reduction of epinephrine and ferricyanide respectively were chosen as electrochemical probes and were explored with at MWCNTs film modified BPPG electrode and compared directly with a bare BPPG electrode and an edge plane pyrolytic graphite electrode. Figure 3.11 details the voltammetric profiles recorded using the ferricyanide redox couple where clearly the edge plane pyrolytic graphite electrode and the MWCNTs film modified BPPG electrode exhibit clearly similar electrochemical responses. The similar peak-to-peak separations observed at the MWCNTs and edge plane pyrolytic graphite (EPPG) electrode demonstrates that there is little significant difference between the two indicating that the reactive sites, where heterogeneous charge transfer occurs, is due to edge plane like – sites / defects which occur at the open ends of the nanotubes or at defects along the tube axis.

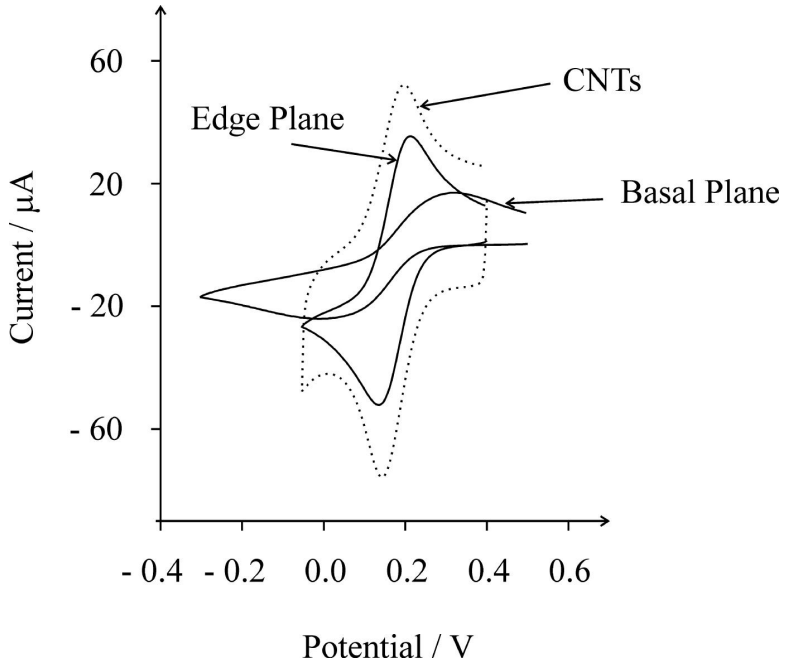


Figure 3.11 Cyclic voltammograms for the reduction of 1 mM ferricyanide at CNT film-modified BPPG electrodes compared with an EPPG electrode and a bare BPPG electrode showing *definitive evidence* that the electron transfer kinetic of the ferricyanide reduction are similar on EPPG and CNT modified electrodes. All scans recorded at 100 mVs^{-1}.

Further evidence for the role of edge plane sites in the electrochemistry of graphite surfaces was provided by two conclusive experiments using HOPG where the distance between the step site is unusually large and can be as much as 5 to 10 microns on carefully handled samples. The cyclic voltammetry response of simple, nominally outer sphere redox couples was shown to be inconsistent with that predicted for simple linear diffusion.[84,85] Rather the characteristic and unusual wave shapes were only consistent with a diffusional model in which the substrates effectively acted as an array of microband electrodes where the edge plane like – sites / steps act as electrochemically active microbands and the basal plane terraces as voltammetrically effectively inert material.[84,85]

The second experiment in defining the role of the edge plane sites as the site of electron transfer and the basal plane terraces as voltametrically inert was carried out using AFM in parallel with the voltammetry of modified HOPG surfaces. In particular

the cyclic voltammetric response of HOPG to various model redox couple was essentially unchanged when the basal plane terraces – but not the edge plane steps – were covered with a thick layer of MbO_2. This confirmed that the terraces were effectively voltammetrically inert and that measurable levels of electron transfer were confined to the edge plane steps defects.[84]

In fact this protocol was extended to MWCNTs where the edge plane like-sites/defects were coated with MbO_2 forming nanoplugs exclusively at the ends of the carbon nanotubes – again testimonial that the edge plane like- sites / defects are the origin of charge transfer at MWCNTs.[83]

3.2.4 The Role of Metal Oxide Impurities in Carbon Nanotubes

It was shown above that the origin of the heterogeneous charge transfer kinetics for carbon nanotubes is solely due to edge plane like – sites / defects. However, there were some cases in which the electrochemical response of the MWCNTs could not be explained by edge plane sites. Consider the electrochemical oxidation of hydrazine as shown in Figure 3.12. The response of the EPPG electrode does not match up with the response of the MWCNTs abrasively modified onto a BPPG electrode and electrochemical response of the MWCNTs must derive from other causes. A common feature in the field of carbon nanotubes is to acid wash the CNTs prior to use even though they are supplied with a 95 % or greater purity; the concept of acid washing was instigated by Wang and co-workers and has consequently been adapted by extensively. Typically, the CNTs are washed for 20 hrs in 2 M nitric acid, filtered, washed with copious amounts of water. After drying the CNTs are ready to use. Banks and co-workers[48] explored the effect of acid washing of ‘bamboo’ MWCNTs by comparing the EDAX of as-received, washed and super washed; washed is from acid washing for 20 hrs while “super” washed refers to an

acid washing of 30 hrs. EDAX on the CNTs revealed the presence of iron, copper and sulphur which was found to be unaffected by the acid washing technique. X-ray photoelectron Spectroscopy (XPS) was used to determine the oxidation state of the metal iron impurities which was found to correspond to Fe_2O_3. XPS data analysis of the unwashed MW-CNTs indicated that the sample was 98.9 atomic % carbon, 1.0 atomic % oxygen, 0.1 atomic % iron and trace (< 0.1 atomic %) copper and sulfur was observed. Thus it was inferred that the iron cannot be simply removed by washing and is likely trapped in graphite – like planes along the tube axis, or at the ends of the nanotubes, or contained within the carbon nanotubes.

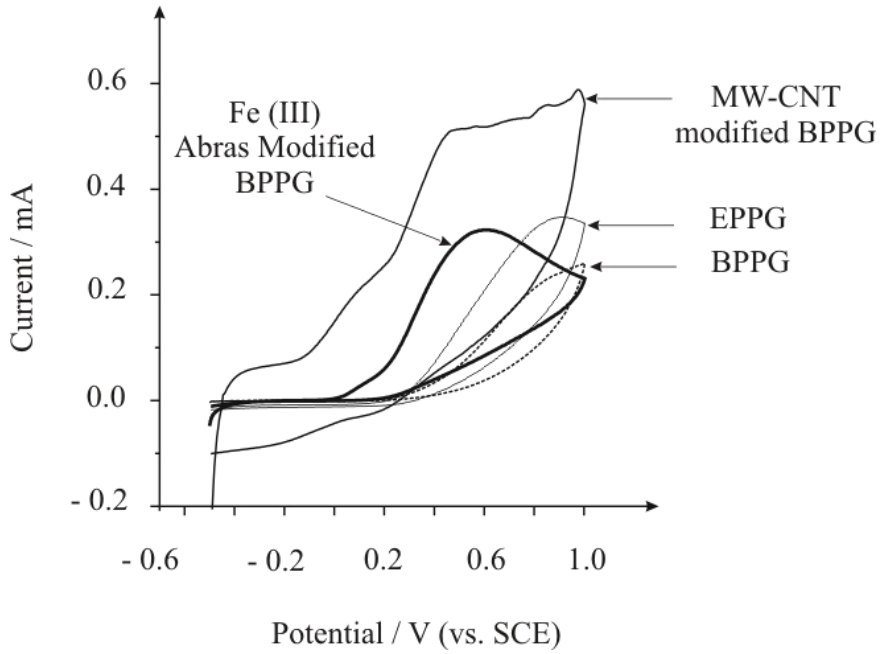


Figure 3.12 Cyclic voltammetric profiles resulting from the electrochemical oxidation of 6.5 mM hydrazine in a pH 7.2 phosphate buffer solution.

Returning to the voltammetric response of the MWCNTs, since iron is present an abrasively modified BPPG electrode of Fe(III) oxide was prepared and explored for the electrochemical oxidation of hydrazine which produces an identical response compared to the MWCNT modified electrode. Note that it is important that the peak potential is

identical to the MWCNTs and that the peak height simply reflects the amount, viz electrochemical area of the iron.

This fundamental understanding of the role of metallic impurities in carbon nanotubes has also been extended to the case of the electrochemical reduction of hydrogen peroxide, an important analyte in biosensing where again the iron impurities are the origin of the observed 'electro-catalytic' response.[86]

3.3 Edge Plane Pyrolytic Graphite Electrodes

Edge plane pyrolytic graphite electrodes, as mentioned above, are formed from cutting the surface of the HOPG perpendicular to the graphite layer. Due to the nature of the chemical bonding in graphite, these two planes, edge and basal, exhibit completely different electrochemical properties: the edge plane usually exhibits considerably faster electrode kinetics for the oxidation or reduction of redox species than in comparison with the basal plane. This means that in many instances an electrode consisting entirely of edge plane viz. an edge plane pyrolytic graphite electrode will show a nearly electrochemically reversible ("Nernstian") voltammogram while an electrode consisting mainly of basal plane can show electrochemically irreversible behavior for the same species depending highly on the amount of edge present. Davies et al have shown through numerical simulations and comparison with experiments, that the basal plane is effectively electrochemically inert; a BPPG electrode which has been adhesively prepared[2] has a percentage of edge plane defects between 1 – 10 % which are increased by abrasive modification.[86,87]

The question is, why is edge plane more reactive than basal plane? The answer can be found by considering the band theory of graphite as described by Wallace,[88] who derived this using the tight binding approximation. Graphite was found to be a semi-conductor with zero activation energy so that there are no free electrons at zero

temperature but they are created at higher temperatures by excitation to a band contiguous to the highest one normally filled. The electrical conductivity was extended as about 100 times as great parallel to as across crystal planes.

3.3.1 Utilising Edge Plane Pyrolytic Graphite Electrodes in Electroanalysis

Electrodes of both edge plane and basal plane have been widely used in electrochemistry and it is understood that the edge plane often shows faster electrode kinetics than the basal plane. Moreover, we now appreciate the 'electro-catalysis' of CNTs is due to edge plane like- sites / defects – This suggests the using of edge plane pyrolytic graphite electrode in electroanalysis; that is, an electrodes consisting entirely of edge plane. In this section we show key example of the use of EPPG electrodes in electroanalysis.

3.3.1.1 Thiol Dection: Replacing MWCNT Modified Electrodes in Routine Sensing

The first electroanalytical example of utilising the usually fast heterogeneous charge transfer kinetics of EPPG was explored in the quantification of the thiols, homocysteine, cysteine, N-acetylcysteine and glutathione.[89] Typically thiol detection is based either on indirect or direct electroanalytical methodologies. The indirect methods are based on monitoring an electroactive species or marker, such as N-N-diethyl-p-phenylenediamine or catechol which chemically reacts with the thiol under study resulting in a change in electroactive marker. Direct electrochemical techniques traditionally utilised a mercury electrode since the direct oxidation of thiols at bare solid electrodes results in poor voltammetric behaviours occurring at large overpotentials which results in the voltammetric signal occurring in the region of solvent decomposition.

Using an edge plane pyrolytic graphite electrode the direct oxidation of 80 μM homocysteine in pH 7 was explored with a large and easily quantifiable voltammetric peak

observed to occur at + 0.66 V (vs. SCE). Comparison of the edge plane pyrolytic graphite electrode with boron-doped diamond, basal plane pyrolytic graphite electrode and glassy carbon reveal no appreciable oxidation waves at the homocysteine concentration chosen to explore the voltammetric responses while a point of inflection was barely visible at a carbon nanotube modified basal plane pyrolytic graphite electrode. The quantification of homocysteine, cysteine, N-acetylcysteine and glutathione was explored at the edge plane pyrolytic graphite electrode where limit of detection (based on 3 sigma) was found to correspond to 2.1, 2.6, 1.7 and 1.7 micro-molar respectively over a large linear range; Figure 3.13 displays the response of addition of homocysteine into a pH 7 phopshate buffer recorded at an EPPG. The protocol was explored in a growth tissue medium, CMRL-1066, where the detection of cysteine in the tissue media was found to be in excellent agreement with the manufactures quoted value.[89]

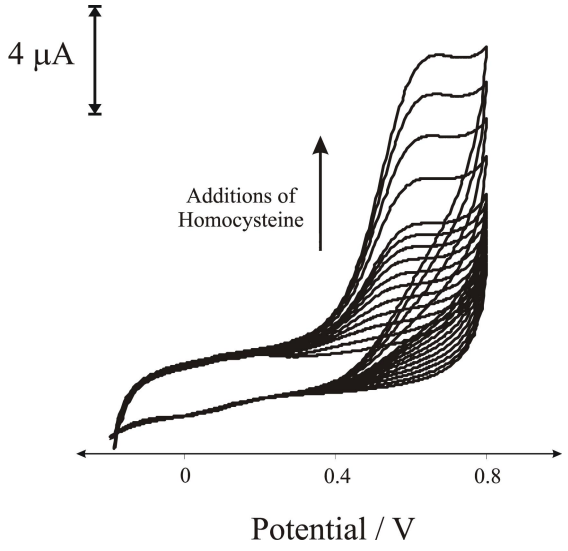


Figure 3.13 The response of addition of homocysteine into a pH 7 phopshate buffer recorded at an EPPG electrode.

3.3.1.2 NADH Detection

The use of edge plane pyrolytic graphite electrodes also allows one to understand the electroanalytical properties of carbon nanotubes modified electrodes, elucidating the origin of the observed electrochemical response. The electrochemical oxidation of nicotinamide

adenine dinucleotide (NADH) continues to receive considerable interest in the electrochemical community since around 300 dehydrogenases are known to be dependant on the coenzyme, NADH and its oxidised form and is therefore required in a whole diversity of dehydrogenese-based biosensors. However a major drawback is that the direct electrochemical oxidation occurs at large overpotentials (*ca.* > + 0.5 V) and also the oxidation product of NADH results in electrode fouling resulting in the gradual loss of sensitivity. The best direct electrochemical methodology has been reported using carbon nanotube modified electrodes,[23] where a large reduction in the over-potential coupled with low susceptibility to electrode fouling was observed.[23] This has since been followed up utilising a plethora of carbon nanotube permutations[90-95] with many more sensing methodologies for NADH oxidation employing carbon nanotubes are likely to be conceived. However, in these reports utilising carbon nanotubes, the observed improvement in the over-potential and low susceptibility to electrode fouling has never been explained in physico-chemical terms.

The electrochemical oxidation of NADH was explored at a multi-walled carbon nanotube abrasively modified basal plane pyrolytic graphite electrode and a 'film' modified multi-walled carbon nanotube basal plane pyrolytic graphite electrode;[96,97] Figure 3.14A and 3.14B shows the corresponding voltammetric profiles. In the case of the abrasively modified MWCNTs two oxidation waves are observed at *ca.* + 0.31 V and *ca.* + 0.48 V (both vs. SCE, 50 mV s^{-1}) in excellent agreement with the original 'state-of-the-art' carbon nanotube paper.[23] Figure 3.14 B depicts the voltammetric response of the MWCNT 'film' modified BPPG where a single oxidation wave is observed at + 0.30 V (vs. SCE, 50 mV s^{-1}). Note that the response is typical of carbon nanotube electrode modified via the method where 'thin layer behaviour is observed with the loss of the 'diffusional tail'. Figure 3.14C shows the response of the electrochemical oxidation of NADH at the EPPG

electrode which is observed to occur at *ca.* + 0.40 V (vs. SCE, 50 mVs^{-1}). The observed voltammetric response is due to the electrochemical oxidation of NADH:

$$NADH \rightarrow NAD^{+} + H^{+} + 2e^{-} \tag{3.1}$$

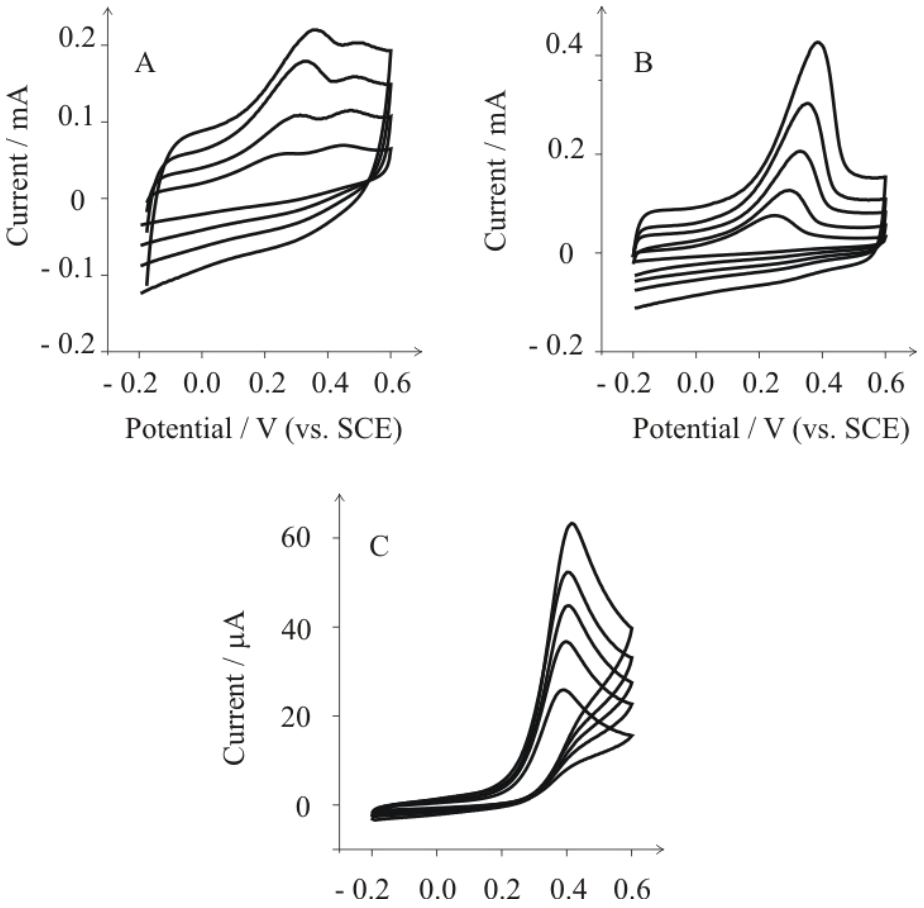


Figure 3.14 Cyclic voltammetric response of (A) abrasively modified MWCNT BPPG and (B) film modified MWCNTs on BPPG electrodes in a pH 7.4 phosphate buffer solution containing 1.2 mM NADH. All scans are 25, 50, 75, 100 and 150 mV s21. (D) shows the response of a EPPG electrode.

Tafel analysis of voltammograms recorded at the EPPG electrode corresponding to the oxidation of 1.2 mM NADH (at a scan rate of 100 mV s^{-1}) plotted as potential *vs.* $\log_{10}$(current) produced a value of 167 mV per decade. Using the following equation:

$$y = \frac{2.303RT}{\alpha n_a F} \tag{3.2}$$

where y (V) is the slope of potential vs. log_{10}(current), α is the transfer coefficient for the potential-determining heterogeneous electron transfer and n_a is the number of electrons transferred in the rate determining step, a value of 0.35 for $\alpha\ n_a$ was obtained suggesting that in the overall two electron oxidation of NADH, the first electron transfer is the rate determining step. This transfer coefficient is consistent with that observed by Moiroux and Elving,[98] who observed transfer coefficients of 0.37 at carbon electrodes and 0.43 at platinum electrodes for the electrochemical oxidation of NADH. This lower than expected value (usually 0.5) is perhaps not unexpected since the value results from a dissymmetry of the potential energy curves of the reactant and products in the context of Butler-Volmer kinetics suggesting that the irreversibility of the first electron transfer (rate determining step) is the likely cause of the observed large overpotential for the electrochemical oxidation of NADH. The mechanism of the oxidation of NADH is thought to be the following :[98]

$$NADH - e^- \longrightarrow NADH^{\bullet +} \tag{3.3}$$

$$NADH^{\bullet +} \xrightarrow{-H^+} NAD^{\bullet} \tag{3.4}$$

$$NAD^{\bullet} - e^- \longrightarrow NAD^+ \tag{3.5}$$

where *NADH* is irreversibly oxidised through loss of an electron to produce a cation radical $NADH^{\bullet +}$ equation (4), which then de-protonates to produce a neutral radical $NAD^{\bullet}$ equation (5). $NAD^{\bullet}$ is immediately oxidised to NAD^+ at the electrode surface at

the positive potential involved (typically 0.5 V) as described by equation (6). $NAD^{\bullet}$ can also exchange an electron with the cation radical in the bulk solution.[98]

Returning to the response of the EPPG electrode, the peak potential observed at the EPPG electrode (*ca.* + 0.40 V) is in excellent agreement with that of the abrasively modified MWCNTS (+ 0. 31 V) and the 'film' modified MWCNTs (see Figure 3.14) indicating that the origin of the electrochemical activity of MWCNTs resides in the edge plane like- sites/defects which occur at the open ends of the MWCNTs and along the tube axis where tubes 'terminate'.

In the case of Figure 3.14A, it is interesting to note that the second wave is not observed on the MWCNT film modified BPPG electrodes. This can be understood as follows. The response of a BPPG electrode, which consists of very little edge plane was explored for the electrochemical oxidation of NADH where an oxidation wave is observed at *ca.* + 0.81 V. The BPPG was then polished on a soft lapping pad with 0.1 micron sized alumina for 10 and 30 seconds. The polished BPPG electrode was then placed into the NADH solution with the voltammetric response found to occur at *ca.* + 0.41 and *ca.* + 0.46 V, respectively. The abrasive rubbing of the BPPG on the alumina introduces edge plane defects on the electrode surface resulting in a shift of the oxidation wave to less negative potentials coupled with a reduction in the background current, since the kinetics on the edge plane sites are considerably faster.

Therefore it can be inferred that the second wave observed only on the abrasive CNT modified BPPG electrode (see Figure 3.14A) is due to the nanotubes abrasively roughening the BPPG electrode which introduces edge plane sites; thus two waves are produced, the first from the high proportion of edge plane sites occurring on the carbon nanotubes and the second from electron transfer from the relatively smaller proportion of edge plane sites from the BPPG electrode surface.

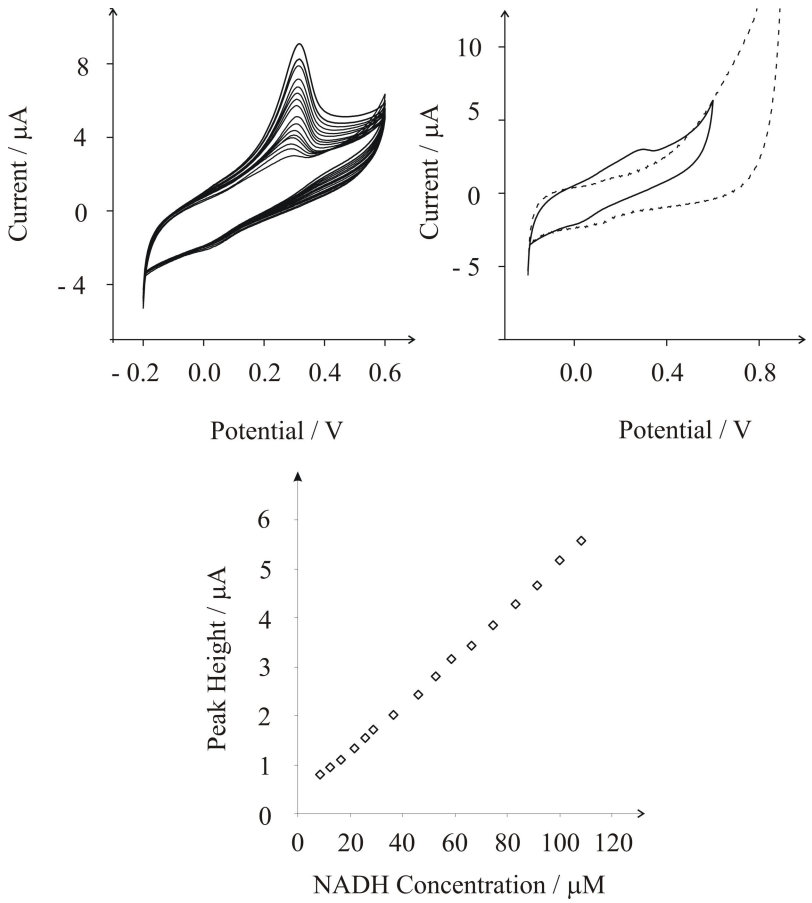


Figure 3.15 Voltammetric response observed at the edge plane pyrolytic graphite electrode from additions of 4.1 µM NADH to a pH 7.4 phosphate buffer solution from 8.2 µM to 108 µM (top left) with a typical calibration plot of peak height versus added NADH concentration from the voltammetric responses. Also show (top right) is the voltammetric response from the addition of 4.1 µM to the solution along with the corresponding blank (dashed line)

Exploration of the electrochemical response of the CNT modified electrodes with edge plane and basal plane electrodes allows a better understanding of the adsorption of NADH at CNTs and edge plane electrodes. It was inferred that adsorption occurs at edge plane sites and due to the high density of edge plane sites on CNTs and edge plane pyrolytic graphite electrodes meaning that they are unsusceptible to electrode passivation. This of course allows a better understanding of the requirement of electrochemical sensors which should ideally be graphite based having a large proportion of edge plane sites for the best detection limits.

Last the sensing applicability of edge plane pyrolytic graphite electrodes for NADH was explored. Using a pH 7.4 phosphate buffer solution additions of 4.1 μM NADH were made with the voltammetric response explored using a scan rate of 100 mV s^{-1}. The cyclic voltammograms are shown in Figure 3.15 along with a resulting calibration plot. Note also that the response of 8.1 μM NADH is also shown, where a large and quantifiable signal is observed which can be easily distinguished from the blank. Analysis of the voltammetric curves from additions of NADH were observed to linear from 8.3 μM to 108 μM with a plot of peak height (I_H) versus added NADH producing the following linear regression: I_H / A = 4.9 x 10^{-2} ([NADH] / M) + 3.6 x 10^{-7} A; R^2 = 0.98, *N = 16*). From the calibration plot, a limit of detection, based on a signal-to-noise ratio of 3 sigma was found to be 4.5 μM.

Next the amperometric response of the edge plane pyrolytic graphite electrode was explored. Figure 3.16 depicts the current – time response from additions of NADH to a pH 7.4 phosphate buffer solution under conditions where the potential was kept at + 0.4 V. As shown successive additions from 2.25 μM to 36 μM produced a well-defined response producing the following linear regression: I / A = 5.46 x 10^{-2} ([NADH] / M) + 8.34 x10^{-8} A; *N = 16*; R^2= 0.997. The plot of current versus NADH concentration is depicted in Figure 3.16 and from this graph a limit of detection (3 sigma) of 9.65 x 10^{-7} M was calculated. This experiment was repeated, but with smaller additions over the range 0.9 to 10.8 μM (I / A = 6.4 x 10^{-2} ([NADH] / M) – 3.1 x 10^{-8} A; *N = 12*; R^2= 0.997) and was found to produce a limit of detection of 3.3 x 10^{-7} M. The detection limits from cyclic voltammetry and amperometry are comparable to existing methods employing carbon nanotubes and nanotube polymer composites. Note that the detection limits achievable above are better than GC electrodes modified with transition metal complexes,

electroactive dyes, quinone functional mediators and poly(thionine) modified carbon electrodes.[96]

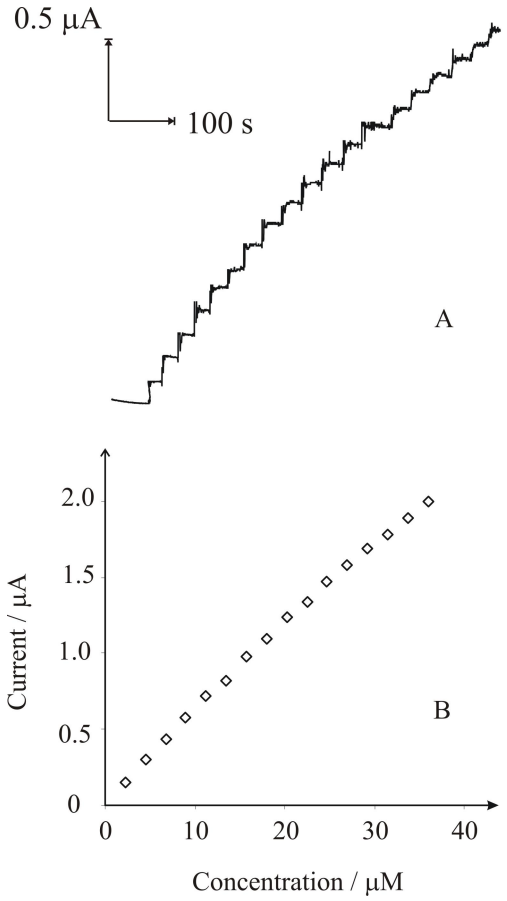


Figure 3.16 Amperometric response observed at the edge plane pyrolytic graphite electrode from 2.25 μM NADH additions to a pH 7.4 phosphate buffer solution at a rotating (13 Hz) edge plane pyrolytic graphite electrode. Operating potential, + 0.4 V (vs. SCE).

The edge plane pyrolytic graphite electrode has the advantage of simplicity for routine sensing of NADH over carbon nanotube modified electrodes and may be used as an alternative to the latter. For optimum dehydrogenase sensors, it is recommended that the carbon surface of the working electrode has a high density of edge plane sites by using either an EPPG electrode, a polished BPPG or a carbon nanotube modified electrode / composite.

Last the role of ascorbic acid (AA) on the electrochemical detection of NADH was explored; AA is one of the largest problems in the electrochemical determination of biological substances such as NADH since the latter are commonly oxidised at similar potentials. Figure 3.17 shows the cyclic voltammetric responses of equal concentrations of AA and NADH in a pH 7.4 phosphate buffer solution. The peak at +0.11 V (vs. SCE) is due to the electro-oxidation of ascorbic acid with the NADH signal at + 0.37 V (vs. SCE); this equates to a peak separation of 260 mV. Note that the peak separation of AA and NADH has been observed to be + 0.58 V for NADH and *ca*. +0.45 (pH 7.1) at boron-doped diamond electrodes, which equates to *ca.* 130 mV difference in peak positions, which was too small to give resolved voltammetric peaks with the presence of AA was observed as a shoulder on the NADH peak.[99] Note that this must be due to the oxidation of AA exhibiting a higher degree of electrochemical reversibility at the EPPG in comparison to BDD electrodes. Figure 3.17 indicates that EPPG electrodes can be used without any interference from ascorbic acid when used in conjugation with cyclic voltammetry.

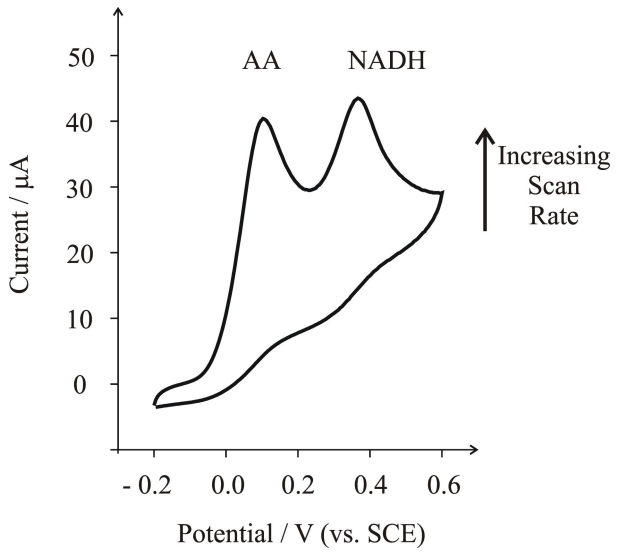


Figure 3.17 Voltammetric responses of an edge plane pyrolytic graphite electrode in a pH 7.4 phosphate buffer solution containing 500 μM ascorbic acid and NADH. Scans rate conducted at 100 mV s^{-1}.

3.3.1.3 Utilising Edge Plane Pyrolytic Graphite Electrodes: Other Examples

The gas sensing capabilities of edge plane electrodes has been explored in the electrochemical reduction of chlorine in nitric acid solutions. Figure 3.18 shows the response of the edge plane electrodes and in comparison to other commonly used carbon based electrode, the EPPG electrode exhibits the most electrochemically reversible signal. Thus one can infer from this that it is the edge plane sites that are responsible for the reduction in overpotential. Other examples of using EPPG electrode in electroanalysis are detailed in table 2.

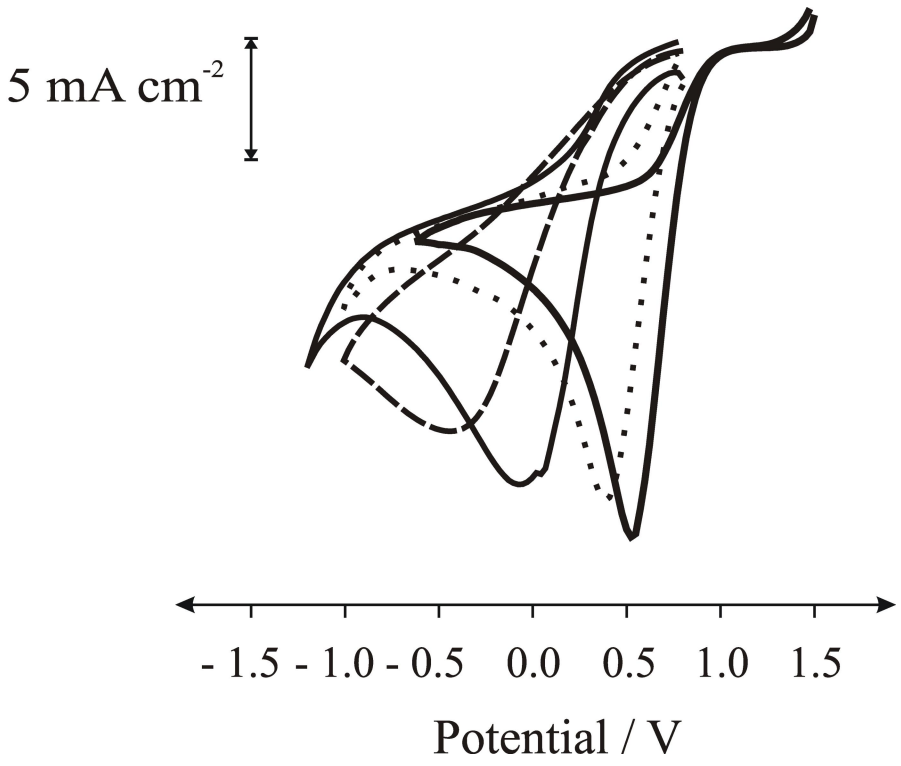


Figure 3.18 Cyclic voltammograms for reduction of chlorine in 0.1 M nitric acid solution using edge-plane pyrolytic graphite (blue), which is compared with a glassy carbon (orange), basal plane pyrolytic graphite (black) and boron-doped diamond (green) electrodes. All scans recorded at 100 mV s^{-1} vs. SCE.

Table 2: Illustrative Systems Studied with EPPG Electrode

Analyte	LOD	Reference
Manganese(II)	14 nM	100
Uric acid	30 nM	101
Ascorbic acid	80 nM	101
Bromide	1 μM	102
Cysteine	2.6 μM	103
Glutathione	2.7 μM	103
N-acetylcysteine	1.7 μM	103
Homocysteine	2.1 μM	103
NADH	5 μM	96

Abbreviations: LOD: limit of detection;

3.4 References

(1) Banks, C. E.; Davies, T. J.; Wildgoose, G. G.; Compton, R. G. *Chem. Commun.* **2004**, *7*, 829.

(2) McCreery, R. L. *in Electroanalytical Chemistry, ed. A. J. Bard, Marcel Dekker, New York,* **1990**, *17*, 221.

(3) Moore, A. W. *in Chemistry and Physics of Carbon, ed. P. L. Walker and P. A. Thrower, Marcel Dekker, New York,* **1973**, *11*, 69.

(4) Iijima, S. . *Nature* **1991**, *354*, 56.

(5) Zhu, H. W.; Xu, C. L.; Wu, D. H.; Wei, B. Q.; Vajtai, R.; Ajayan, P. M. *Science* **2002**, *296*, 884.

(6) Saito, R.; Dresselhaus, G.; Dresselhaus, M. S. *Physical Properties of Carbon Nanotubes: Theory and Applications, Imperial College Press, London* **1998**.

(7) Leonhardt, A.; Ritschel, M.; Bartsch, K.; Graff, A.; Taschner, C.; Fink, J. *Journal de Physique IV: Proceedings* **2001**, 11:Pr3=445.

(8) Wang, Y. Y.; Tang, G. Y.; Koeck, F. A. M.; Brown, B.; Garguilo, J. M.; Nemanich, R. J. *Diamond Relat Mater* **2004**, *13*, 1287.

(9) Ajayan, P. M.; Stephan, O.; Colliex, C.; Trauth, D. *Science* **1994**, *265*, 1212.

(10) Sato, K.; Noguchi, M.; Demachi, A.; Ok, N.; Endo, M. *Science* **1994**, *264*, 556.

(11) Baum, R. *Chem Eng News* **1997**, *75*, 29.

(12) Che, G.; Lakshmi, B. B.; Martin, C. R.; Fisher, E. R.; Ruoff, R. S. *Chem Mater* **1998**, *10*, 260.

(13) Britoo, P. J.; Santhanam, K. S. V.; Rubio, A.; Alonso, J. A.; Ajayan, P. M. *Adv Mater* **1999**, *11*, 154.

(14) Zhang, Y.; Ichihashi, T.; Landree, E.; Nihey, F.; Iijima, S. *Science* **1999**, *285*, 1719.

(15) Brabec, C. J.; Nsariciftc, I. S.; Hummelen, J. C. *Adv. Funct. Mater.* **2001**, *11*, 15.

(16) Schlapbach, L.; Zuttel, A. *Nature* **2001**, *414*, 353.

(17) Tammeveskia, K.; Kontturi, K.; Nichols, R. J.; Potter, R. J.; Schiffrin, D. J. *J Electroanal Chem* **2001**, *515*, 101.

(18) Baughman, R. H.; Zakhidov, A. A.; de Heer, W. A. *Science* **2002**, *297*, 787.

(19) Dimitrakopoulos, C. C.; Malefant, P. R. L. *Adv. Mater* **2002**, *14*, 99.

(20) Matsumoto, T.; Komatsu, T.; Arai, K.; Yamazaki, T.; Kijima, M.; Shimizu, H.; Takasawa, Y.; Nakamura, J. *Chem Commun.* **2004**, *7*, 840.

(21) Qu, J.; Shen, Y.; Qu, X.; Dong, S. *Chem Commun* **2004**, *1*, 34.

(22) Britto, P. J.; Santhanam, K. S. V.; Ajayan, P. M. *Bioelectrochem. Bioenerg.* **1996**, *41*, 121.

(23) Musameh, M.; Wang, J.; Merkoci, A.; Lin, Y. *Electrochem. Commun.* **2002**, 743.

(24) Zhang, G. Q.; Zhang, X., G.; Wang, Y. G. C. *Carbon.* **2004**, *178*, 42.

(25) Yuan, Z.; Wang, Y.; Zhang, J.; Lu, Y. *Huaxue Tongbao.* **2004**, *67*, 473.

(26) Yea, J. S.; Wen, Y.; Zhang, W. D.; Gan, L. M.; Xu, G. Q.; Sheu, F. S. *Electrochem. Commun.* **2004**, *6*, 66.

(27) Yang, C. *Anal. Sci.* **2004**, *20*, 821.

(28) Wu, K.; Fei, J. J.; Hu, S. S. *Anal Biochem.* **2003**, *318*, 100.

(29) Wu, F. H.; Zhao, G. C.; Wei, X. W. *Electrochem. Commun.* **2002**, *4*, 690.

(30) Wiles, P. G.; Abrahamson, J. *Carbon.* **1978**, *16*, 341.

(31) Wang, J.; Musameh, M. *Anal. Chim. Acta.* **2004**, *511*, 33.

(32) Wang, J. *Electroanalysis.* **2005**, *17*, 7.

(33) Sheu, F. S.; Ye, J. S. *Mater. Technol.* **2004**, *19*, 11.

(34) Sherigara, B. S.; Kutner, W. D.; Sorza, F. *Electrocatalysis.* **2003**, *15*, 753.

(35) Salimi, A.; Banks, C. E.; Compton, R. G. *Analyst.* **2004**, *129*, 225.

(36) Penn. S, G.; He, L.; Natan, M. J. *Curr Opin Chem Biol* **2003**, *7*, 609.

(37) Pedano, M. L.; Rivas, G. A. *Electrochem. Commun.* **2004**, *6*, 10.

(38) Malea, K. B.; Hrapovica, S.; Liua, Y.; Wang, D.; Luong, J. H. T. *Anal. Chim. Acta.* **2004**, *516*, 35.

(39) Li, N.; Wang, J.; Li, M. *Rev. Anal. Chem.* **2003**, *22*, 19.

(40) Lawrence, N. S.; Deo, R. P.; Wang, J. *Electroanalysis.* **2005**, *17*, 65.

(41) Lawrence, N. S.; Deo, R. P.; Wang, J. *Talanta.* **2004**, *63*, 443.

(42) Katz, E.; Willner, I. *ChemPhysChem.* **2004**, *5*, 1084.

(43) Hocevar, S. B.; Wang, J.; Deo, R. P.; Musameh, M.; Ogorevc, B. *Electroanalysis.* **2005**, *17*, 417.

(44) Frackowiak, E.; Jurewicz, K.; Delpeux, S.; Beguin, F. **2003**, *91*, 305.

(45) Deo, R. P.; Wang, J.; Block, I.; Mulchandani, A.; Joshi, K. A.; Trojanowicz, M.; Scholz, F.; Chen, W.; Lin, Y. *Anal. Chim. Acta.* **2005**, *530*, 185.

(46) Bianco, A.; Kostarelos, K.; Partidos, C. D.; Prato, M. *Chem. Commun* **2005**, *5*, 571.

(47) Banks, C. E.; Crossley, A.; Salter, C.; Wilkins, S. J.; Compton, R. G. *Angew. Chem.* **2006**, *118*, 2595.

(48) Banks, C. E.; Crossley, A.; Salter, C.; Wilkins, S. J.; Compton, R. G. *Angew. Chem.* **2006**, *45*, 2533.

(49) Mickelson, E. T.; Huffman, C. B.; Rinzler, A. G.; Smalley, R. E.; Hauge, R. H.; Margrave, J. L. *Chem. Phys. Lett.* **1998**, *296*, 188.

(50) Peng, H.; Gu, Z.; Yang, J.; Zimmerman, J. L.; Willis, P. A.; Bronikowski, M. J.; Smalley, R. E.; Hauge, R. H.; Margrave, J. L. *Nano. Lett.* **2001**, *1*, 625.

(51) Ajayan, P. M. *Chem. Rev.* **1999**, *99*, 1787.

(52) Deng, J. P.; Mou, C. Y.; Han, C. C. *Fullerene Science and Technology.* **1997**, *5*, 1033.

(53) Mawhinney, D. B.; Naumenko, V.; Kunznetsova, A.; Yates, J. T. *J. Am. Chem. Soc.* **2000**, *122*, 2383.

(54) Banerjee, S.; Benny, H., T.; Wong, S. S. *Adv. Mater.* **2005**, *17*, 17.

(55) Liu, Z.; Shen, Z.; Zhu, T.; Hou, S.; Ying, L.; Shi, Z.; Gu, Z. *Langmuir.* **2000**, *16*, 3569.

(56) Gooding, J. J.; Wibowo, R.; LIu, J. Q.; Yang, W. R.; Losic, D.; Orbons, S.; Mearns, F. J.; Shapter, J. G.; Hibbert, D. B. *J. Am. Chem. Soc.* **2003**, *125*, 9006.

(57) Azamian, B. R.; Davies, T. J.; Coleman, K. S.; bagshaw, C. B.; Green, M. L. H. *J. Am. Chem. Soc.* **2002**, *124*, 12664.

(58) Boul, P. J.; LIu, J.; Mickelson, E. T.; Huffman, C. B.; Ericson, L. M.; Chiang, I. W.; Smith, K. A.; Colbert, D. T.; Hauge, R. H.; Margrave, J. L.; Smaller, R. E. *Chem. Phys. Lett.* **1999**, *310*, 367.

(59) Mickelson, E. T.; Huffman, C. B.; Rinzler, A. G.; Smalley, R. E.; Hauge, R. H.; Margrave, J. L. *Chem. Phys. Lett.* **1998**, *296*, 188.

(60) Balasubramanian, K.; Burghard, M. *Small.* **2005**, *2*, 180.

(61) Wildgoose, G. G.; Jiang, L.; Jones, T. G. J.; Crossley, A.; Compton, R. G. *Small.* **2006**, *2*, 95.

(62) Ji, X.; Banks, C. E.; Holloway, A. F.; Jurkschat, K.; Thorogood, C. A.; Wildgoose, G. G.; Compton, R. G. *Electroanalysis.* **2006**, *18*, 2481.

(63) Garrod, S.; Bollard, M. E.; Nicholls, A. W.; Connor, S. C.; Connelly, J.; Nicholson, J. K.; Holmes, E. *Chem. Res. Toxi.* **2005**, *18*, 115.

(64) Day, T. M.; Unwin, R. P.; Wilson, N. R.; Wacpherson, J. V. *J. Am. Chem. Soc.* **2005**, *127*, 10639.

(65) Knez, M.; Sumser, M.; Bittner, A. M.; Wege, C.; Jeske, H.; Kooi, S.; Burghard, M.; Kern, K. *J. Electroanal. Chem.* **2002**, *522*, 70.

(66) Bahr, J. L.; Yang, J.; Kosynkin, D. V.; Bronikowski, M. J.; Smalley, R. E.; Tour, J. M. *J. Am. Chem. Soc.* **2001**, *123*, 6536.

(67) Balasubramanian, K.; Friedrich, M.; Jiang, C.; Fan, Y.; Mews, A.; Burghard, M.; Kern, K. *Adv. Mater.* **2003**, *15*, 1515.

(68) Wang, J.; Musameh, M.; Lin, Y. *J. Am. Chem. Soc.* **2003**, *125*, 5408.

(69) Moore, R. R.; Banks, C. E.; Compton, R. G. *Anal. Chem.* **2004**, *76*, 2677.

(70) Lawrence, N. S.; Deo, R. P.; Wang, J. *Anal. Chim. Acta.* **2004**, *517*, 131.

(71) Salimi, A.; Hallaj, R.; Khayatian, G.-R. *Electroanalysis* **2005**, *17*, 873.

(72) Wang, S. F.; Xu, Q. *Anal. Lett.* **2005**, *38*, 657.

(73) Chicharro, M. B., E.; Moreno, M.; Sanchez, A.; Zapardiel, A.; Rivas, G. *Electroanalysis* **2005**, *17*, 476.

(74) Wang, J.; Li, M.; Shi, Z.; Li, N.; Gu, Z. *Anal. Chem.* **2002**, *74*, 1993.

(75) Deo, R. P.; Wang, J. *Electrochem. Commun.* **2004**, *6*, 284.

(76) Liua, G.; Lin, Y.; Tub, Y.; Renb, Z. *Analyst.* **2005**, *130*, 1098.

(77) Xu, Z.; Chen, X.; Qu, X.; Dong, S. *Electroanalysis.* **2004**, *16*, 684.

(78) Ye, J. S.; Wen, Y.; Zhang, W. D.; Gan, L. M.; Xu, G. Q.; Sheu, F. S. *Electroanalysis.* **2003**, *15*, 1693.

(79) Dai, L.; He, P.; Li, S. *Nanotechnology.* **2003**, *14*, 1081.

(80) Wang, J. *Analyst.* **2005**, *130*, 421.

(81) Wang, J.; Liu, G.; Jan, M. R. *J. Am. Chem. Soc.* **2004**, *126*, 3010.

(82) Compton, R. G. *Royal Society of Chemistry Tilden Lecture.* **2006**.

(83) Banks, C. E.; Moore, R. R.; Davies, T. J.; Compton, R. G. *Chem. Commun.* **2005**, *16*, 1804.

(84) Davies, T. J.; Hyde, M. E.; Compton, R. G. *Angew. Chem.* **2005**, *117*, 5251.

(85) Davies, T. J.; Moore, R. R.; Banks, C. E.; Compton, R. G. *J. Electroanal. Chem.* **2004**, *574*, 123.

(86) Slijukic, B.; Banks, C. E.; Compton, R. G. *Nano. Lett.* **2006**, *6*, 1556.

(87) Dai, X.; Wildgoose, G. G.; compton, R. G. *Analyst.* **2006**, *131*, 901.

(88) Wallace, P. R. *Phys. Rev.* **1947**, *71*, 622.

(89) More, R. R.; Banks, C. E.; Compton, R. G. *Analyst.* **2004**, *129*, 755.

(90) Chen, J.; Bao, J.; Cai, C.; Lu, T. *Anal. Chim. Acta.* **2004**, *516*, 29.

(91) Valentini, F.; Orlanducci, S.; Terranova, M. L. A., A.; Palleschi, G. *Sensors and Actuators B.* **2004**, *1000*, 117.

(92) Valentini, F.; Salis, A.; Curulli, A.; Palleschi, G. *Anal. Chem.* **2004**, *76*, 3244.

(93) Antiochia, R.; Lavagnini, I.; Mago, F. *Anal. Bioanal. Chem.* **2005**, *381*, 1355.

(94) Liu, J.; Tian, S.; Knoll, W. *Langmuir.* **2005**, *21*, 5596.

(95) Rubianes, M. D.; Rivas, G. A. *Electroanalysis.* **2005**, *17*, 73.

(96) Banks, C. E.; Compton, R. G. *Analyst.* **2005**, *130*, 1232.

(97) Moore, R. R.; Banks, C. E.; Compton, R. G. *Anal. Chem.* **2004**, *76*, 2677.

(98) Moiroux, J.; Elving, P. J. *J. Am. Chem. Soc.* **1980**, *102*, 6533.

(99) Rao, T. N.; Yagi, I.; Miwa, T.; Tryk, D. A.; Fujishima, A. *Anal. Chem.* **1999**, *71*, 2506.

(100) Welch, C., M.; Banks, C. E.; Komorsky-Lovric, S.; Compton, R. G. *Croatica. Chemica. Acta.* **2006**, *79*, 27.

(101) Kachoosangi, R. T.; Banks, C. E.; Compton, R. G. *Electroanalysis.* **2006**, *18*, 741.

(102) Lowe, E. R.; Banks, C. E.; Compton, R. G. *Electroanalysis.* **2005**, *17*, 1627.

(103) Moore, R. R.; Banks, C. E.; Compton, R. G. *Analyst.* **2004**, *129*, 755.

CHAPTER 4

Oxygenated Species at Tube Ends Does Not Improve Electron Transfer Kinetics

In the previous chapter we have overviewed the role of carbon nanotubes in electro-analysis and seen how crucial edge plane pyrolytic graphite electrodes are, not only is sensing, but for understanding the fundamental properties of carbon nanotubes. In this chapter, the result of acid washing multi-walled carbon bamboo nanotubes is explored with voltammetry and X-ray Photoelectron Spectroscopy. It is found that the presence of oxygenated species formed as a result at the ends of the nanotubes does not measurably change the heterogeneous charge transfer kinetics. This work discussed in this chapter has been published as an article in *Electroanalysis*, **2006**, 18, 2137.

4.1 Introduction

Carbon nanotubes continue to receive remarkable attention in electrochemistry.[1-7] The modification of electrode substrates with multi-walled carbon nanotubes (MWCNTs) for use in analytical sensing is well documented to result in low detection limits, increased sensitivities, reduced overpotentials and resistance to surface fouling and therefore MWCNTs have been claimed as electro-catalysts.[1, 3, 4, 7, 8] Recently however these reported electrocatalytic properties of multi-walled carbon nanotubes

have been dispelled.[9, 10] We have demonstrated for most electroactive species, via the comparison of MWCNT modified electrodes with edge plane pyrolytic graphite electrodes that usually the electroactive sites of the MWCNTs are edge plane like- sites / defects which can occur at the ends of the nanotubes or along the nanotube where tube compartments terminate.[9, 11] Accordingly MWCNT modified electrodes are no more electrocatalytic than edge plane pyrolytic graphite electrodes except in a few cases where the observed response of the MWCNT modified electrodes could not be mirrored with edge plane pyrolytic graphite electrodes.[12] Specifically for the electrochemical oxidation of hydrazine and the electrochemical reduction of hydrogen peroxide we have shown that the electrocatalysis is due to metal impurities rather than edge plane like sites / defects.[12] These metal impurities remain from the carbon nanotube fabrication process which cannot be removed by acid washing and are trapped in-between graphite sheets. In summary, the electro-activity of multi-walled carbon nanotubes is a result of either edge plane like- sites / defects or metal impurities.[7, 9, 12] To determine the origins of the electro-activity we advocated that in all experiments using MWCNT modified electrodes a direct comparison with edge plane pyrolytic graphite electrodes should be performed.[10]

In correlating surface structure and electron transfer reactivity of carbon nanotubes the importance of oxygenated species needs to be considered. The oxygenated species of *single-walled* carbon nanotubes has been extensively explored. Gooding *et al*[13] have provided convincing evidence that the electron transfer kinetics of the ferricyanide / ferrocyanide redox couple is increased from oxygenating the nanotubes via acid treatment. However we are aware of only one study exploring the oxygenation of multi-walled carbon nanotubes. Luong *et al*[14] have explored the acid treatment of MWCNTS with ceric sulfate. After 2 hrs treatment they observed the presence of large

amounts of oxygen on the MWCNTs. However, this is an extreme pretreatment; the widely adopted literature procedure for the treatment of carbon nanotubes is to take the as-received nanotubes (typically ~ 95% purity) and 'wash' the nanotubes in 2 M nitric acid for ~ 20 hrs.[8, 15-17] Consequently in this chapter we explore the effects of washing MWCNTs in 2M nitric acid for 20 and 36 hrs on the electron transfer kinetics of the oxidation of potassium ferrocyanide and the reduction of hexaammineruthenium (III) chloride.

4.2 Experimental

4.2.1 Chemicals

Potassium hexacyanoferrate (II) trihydrate (Lancaster, 99%) was purchased at the highest grade available and used directly without further purification. Aqueous electrolyte solutions were prepared with KCl (99.5%) (Aldrich) using ultrapure water from a Vivendi UHQ grade water system (Vivendi, UK) with a resistivity of not less than 18.2 MΩ cm^{-1}. All the solutions were degassed with oxygen-free nitrogen (BOC Gases, Guildford, Surrey, UK). All experiments were carried out at a temperature of 295 ± 3 K.

4.2.2 Instrumentation

Electrochemical experiments were performed using a μ-Autolab type II potentiostat (Eco-Chemie, Utrecht, Netherlands) controlled by General Purpose Electrochemical Systems v.4.7 software. In the electrochemical experiments, Edge and basal plane pyrolytic graphite, (eppg, bppg, Le Carbone, Ltd. Sussex, U.K.) were used as working electrodes. In the former case discs of pyrolytic graphite were machined into a 4.9 mm diameter, which were orientated with the disc face parallel with the edge plane, or basal

plane as required. The counter electrode was a bright platinum wire, with a saturated calomel electrode completing the circuit. The eppg electrodes were polished on alumina lapping compounds (BDH) of decreasing sizes (5 - 0.1 μm) on soft lapping pads.

The basal plane pyrolytic graphite electrode was prepared by renewing the electrode surface with cellotape. This procedure involves polishing the bppg electrode surface on carborundum paper (P100 grade) and then pressing cellotape on the cleaned bppg surface which is removed along with attached graphite layers. This is then repeated several times. The electrode was then cleaned in water and acetone to remove any adhesive.

Bamboo multi-walled carbon nanotubes (> 95 % purity (10 - 20 nM diameter, 5-20 μm length) were obtained from NanoLab (Brighton, MA) and were used as received. The MWCNTs were cast onto the BPPG electrode surface. This involves first dispersing 2 mg of MWCNTs into 2 mL ethanol. The suspension is then placed into an ultrasonic bath for 1 minute after which 20 μL is pippetted onto the electrode surface. This is allowed to volatize at room temperature producing a random distribution of carbon nanotubes on the BPPG surface.

The MWCNTs were investigated using a JEOL 3000F Transmission Electron Microscopy (TEM) equipped with a Gatan imaging filter (GIF). In XPS the sample is irradiated with soft X-rays which causes core electrons to be ejected from the sample surface. A spectrum of the energies of these ejected electrons is produced. The electron energies of interest lie in the range 0 - 1500 eV. Because the escape depth of electrons at these energies is typically between 2 and 8 monolayers, XPS is surface specific. The binding energies (BE) of core electrons are dependent on the chemical state of the element. [BE = hν - KE. (The excitation energy (hν) in the case of Al Kα radiation is 1486.6 eV)] Thus it is possible to obtain elemental and chemical

information using this technique. The analyser energy can be selected to provide survey scans and detailed scans over the main peaks of interest. The area under the principal peak of each element in the spectrum, divided by an empirically derived sensitivity factor,[2] is proportional to the concentration of that element on the surface (approximately the top 10 nm). The sensitivity of the technique is about 0.1 atomic percent, depending on the element. All elements other than H and He can be detected.

Samples were pressed onto carbon conducting stubs ensuring a good coverage and hence no interference from the substrate. These were introduced into the instrument via a turbo molecular pumped entry lock. The entry lock was pumped for about 15 minutes to a pressure of 1 x 10^{-6} torr before the sample was introduced into the analysis chamber. XPS was performed in an ion pumped UHV chamber equipped with a VG nine channel CLAM4 electron energy analyser (base pressure 1 x 10^{-9} torr). 300 Watt Al X-ray excitation was used (the as received MWCNTs were examined with monochromated X-rays, the washed and super-washed samples were examined using unmonochromated X-rays). The CLAM 4 has variable slits for small area analysis. The largest slit (5mm) was used in this case with no apertures selected. The analyser was operated at constant pass energy of 100 eV for wide scans and 20 eV for detailed scans. Data was obtained using VGX900-W operating system. Peak areas were measured after background subtraction following methods of Shirley.[3]

4.3 Results and Discussion

4.3.1 TEM and XPS Analysis

The bamboo MWCNTs nanotubes (> 95 % purity) were purchased from NanoLab (Brighton, MA) which are 10 - 20 nM in diameter and 5-20 μm in length. First a sample of these MWCNTs where placed into a covered beaker containing 2 M nitric acid and stirred for 20 hours. This was then filtered and washed with copious amounts

of distilled water, after which they were allowed to dry overnight at room temperature. Another sample of MWCNTs were taken and subjected to a similar procedure but with the time in the acid extended to 36 hours. Figure 4.1 shows TEM images of the bamboo MWCNTs where the unique structure of the nanotubes can be clearly observed. Note that the nanotubes are periodically closed (bamboo modification) along the length of the nanotube, which consists of approximately 4 graphite layers (see insert of Figure 1) dividing the nanotubes into compartments giving the nanotube its 'bamboo' name.

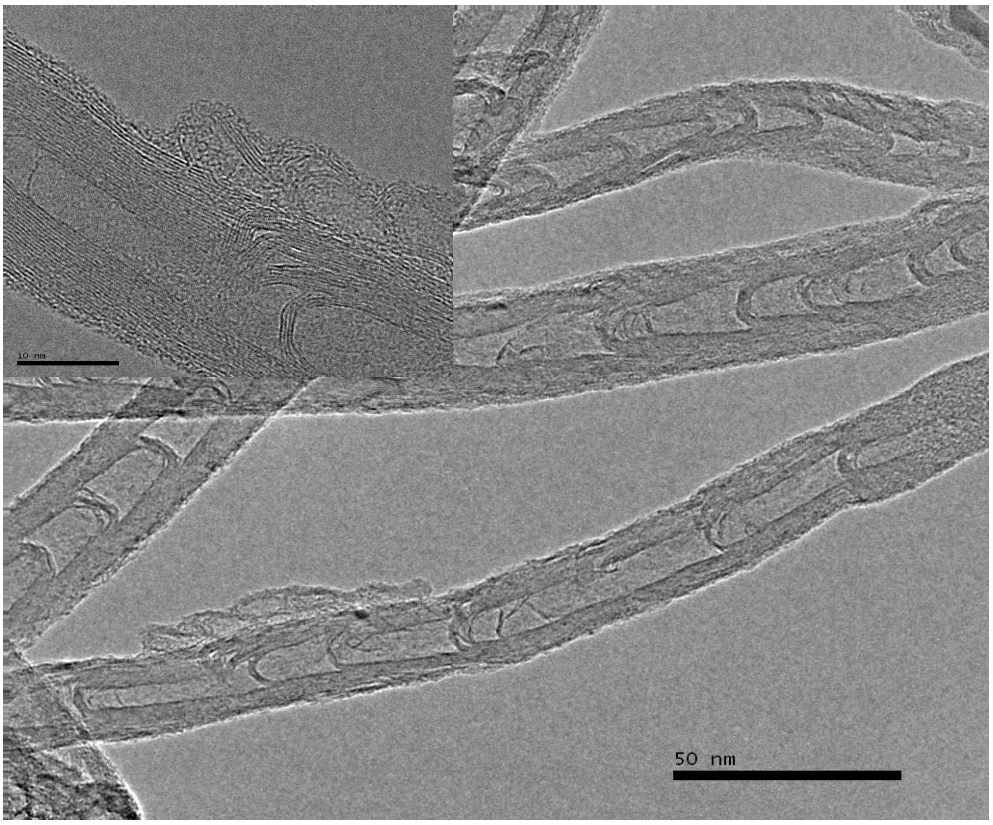


Figure 4.1 TEM micrographs of bamboo MWCNTs and with magnification (insert)

X-ray Photoelectron Spectroscopy (XPS) was conducted on the washed and super-washed MWCNTs and compared with the as-received MWCNTs; wide XPS scans are shown in Figure 4.2. No oxygen is observed on the as-received MWCNTs. Analysis of the XPS data of the washed MWCNTs indicates that a few atomic percent of oxygen was detected on the washed MWCNTs (~ 2.6 atomic % oxygen), which remains

unchanged for the super-washed MWCNTs. The largest part of the shoulder at 286.4 eV corresponds to C-O but is difficult to convolute from the contributions of C = O. The detailed scans show a slight increase in intensity on the high kinetic energy side of the main C 1s peak that can be attributed to chemical oxidation. Note that there may possibly be rather more C=O on the super-washed sample.

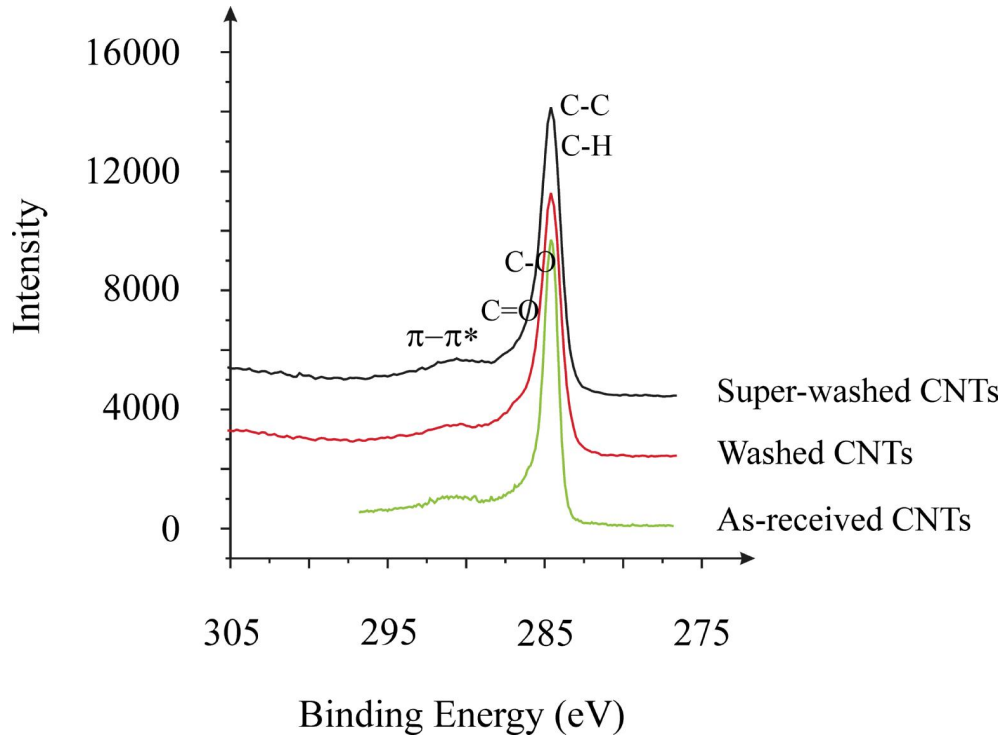


Figure 4.2 XPS spectra of as-received, washed and super-washed MWCNTs

The MWCNTs consist of periodically closed concentric graphite tube (see Figure 4.1) where the area of one tube A_{tube} of distance d, is $A_{tube} = 2\pi rd$. At the end of this tubular section edge plane like- sites / defects occur where each graphite tube terminates. This typically consists of 4 graphite layers, where the spacing between each layer is ~ 3.4 Å [19] (see Figure 4.1). The area of this 'edge' section, A_{edge} is given by: $A_{edge} = 2\pi r$ x (4 x 3.4Å). Thus the area of one edge region (A_{edge}) divided by the area of tube region (A_{tube}) is: A_{edge} / A_{tube} ~ 4 x 3.4 Å / d. Thus d (distance of one graphite

compartment) is found to be ~ 536 Å. Given that from TEM images (Figure 4.1) that each tube is approximately 250 Å, it can be estimated that a significant fraction ~ 0.5 (± 0.4) of the edge plane like- sites / defects are covered with oxygenated species.

4.3.2 Voltammetric Characterisation of Various CNTs

The voltammetric profiles of the as-received, washed and super-washed MWCNTs were explored using the electrochemical oxidation of potassium ferrocyanide and the electro-reduction of hexaammineruthenium (III) chloride. Figure 4.3 shows the voltammetric responses obtained using the hexaammineruthenium (III) chloride (Figure 4.3A) and potassium ferrocyanide (Figure 4.3B) redox probes. Analysis of the peak-to-peak separation (ΔEp) using the potassium ferrocyanide redox probe reveals an ΔEp of 69 mV for the as-received, (unwashed) MWCNTs which is in good agreement with previous reports.[18] The Δ Ep for the washed and super-washed MWCNTs remain unchanged with Δ Ep found to be 69 mV and 68 respectively. Similarly the peak-to-peak separations obtained using the hexaammineruthenium (III) chloride redox probe reveal an ΔEp of 68 mV for the as-received MWCNTs with the peak-to-peak separation only marginally increasing to 73 mV for the washed MWCNTs and 79 mV for the super-washed MWCNTs.

Clearly there is no significant change in the peak-to-peak separations from washing or super-washing the bamboo MWCNTs indicating no enhancement in the heterogeneous charge transfer kinetics of the MWCNTs. However, for certain electro-active species these oxygenated groups may be essential to allow, for example, the chemical functionalization of the MWCNTs. Note that the as-received MWCNTs (unwashed) already indicate fast heterogeneous charge transfer kinetics; undoubtedly

the presence of oxygenated species does not improve heterogeneous charge transfer kinetics of the MWCNTs.

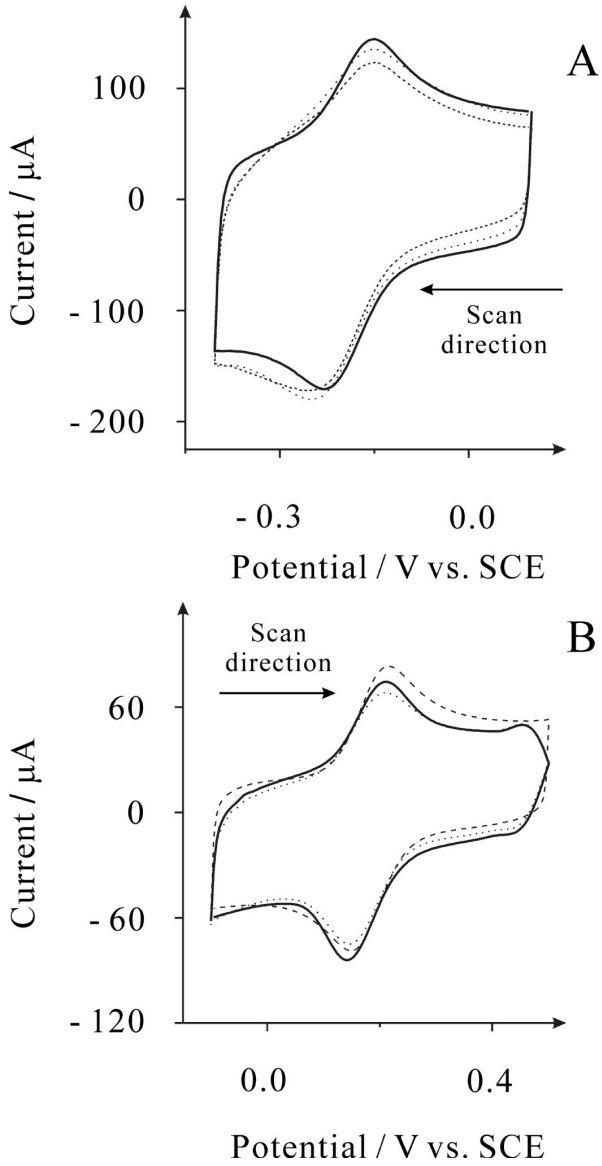


Figure 4.3 Comparison of bamboo multi-walled carbon nanotubes as received (solid line), washed (dotted line) and super-washed (dashed line) explored with the $Ru(NH_3)_6^{3+}$ (A) and $Fe(CN)_6^{4-}$ (B) and redox couples.

Next the electrochemical response of an edge plane pyrolytic graphite electrode using the ferrocyanide probe was sought. A peak-to-peak separation of 75 mV was observed (at 100 mVs^{-1}) while an iron(II) oxide and iron(III) oxide abrasively modified basal plane pyrolytic graphite electrode revealed ΔEp of 160 and 112 respectively (at

100 mVs^{-1}). It is evident that the electrochemical response of the as-received bamboo MWCNTs is due to the edge plane like- sites / defects that occur at the ends and along the tube axis rather than metal impurities.

Gooding *et al*[13] explored the 'cutting' of single-walled carbon nanotubes and observed that as the oxygenated species increased, as evidenced via XPS, the heterogeneous charge transfer kinetics increased. However, due to the nature of the experiment two variables were changing; the SWCNTs were sonicated in an acid mixture, which results in the cutting or shortening of the SWCNTs (as evidence by TEM) and also the chemical oxidation of carbon to oxygenated species. Thus it is difficult to unambiguously attribute the origin of the improvement of the electrode kinetics to either edge plane like- sites / defects or oxygenated species. We surmise here that the observed increase in the electrode kinetics, as observed by Gooding *et al*[13] may be due to 'cutting' of the SWCNTs into nanotubes of shorter length thus introducing a higher density of edge plane like sites / defects. This is supported up by reports that in a comparison of single-walled CNTs with bamboo-multi-walled CNTs, the latter exhibit faster electron transfer kinetics over the former due to a higher density of edge like defects / sites.[18] This is also consistent with that seen at basal plane pyrolytic graphite electrodes where the introduction of edge plane like- sites / defects on the electrode surface significantly increase the electrode kinetics.[19, 20]

4.4 Conclusion

We have explored acid washing bamboo multi-walled carbon nanotubes, a common practice in the literature, with voltammetry and XPS. While it is found that the acid washing results in a few atomic percent of oxygen on the MWCNTs no improvement in the electrode kinetics is observed indicating that for multi-walled carbon nanotubes the

origin of the heterogeneous charge transfer is likely due to the high density per unit area of edge plane like- sites / defects which occur at the ends and along the nanotubes axis where tube compartments terminate.

4.5 References:

[1] A. Merkoci, *Microchimica Acta* **2006**, *152*, 157.

[2] M. Valcarcel, B. M. Simonet, S. Cardenas, B. Suarez, *Anal. Bioanal. Chem.* **2005**, *382*, 1783.

[3] J. J. Gooding, *Electrochimica Acta* **2005**, *50*, 3049.

[4] A. Merkoci, M. Pumera, X. Llopis, B. Perez, M. del Valle, S. Alegret, *TrAC, Trends in Analytical Chemistry* **2005**, *24*, 826.

[5] Y. Lin, W. Yantasee, J. Wang, *Frontiers in Bioscience* **2005**, *10*, 492.

[6] S. E. Kooi, U. Schlecht, M. Burghard, K. Kern, *Angewandte Chemie Int Ed* **2002**, *41*, 1353.

[7] C. E. Banks, R. G. Compton, *Analyst* **2006**, *131*, 15.

[8] J. Wang, M. Musameh, Y. Lin, *J. A. Chem. Soc.* **2003**, *125*, 2408.

[9] C. E. Banks, R. R. Moore, T. J. Davies, R. G. Compton, *Chem. Commun* **2004**, *16*, 1804.

[10] R. R. Moore, C. E. Banks, R. G. Compton, *Anal. Chem.* **2004**, *76*, 2677.

[11] C. E. Banks, R. G. Compton, *Analyst* **2005**, *130*, 1232.

[12] C. E. Banks, A. Crossley, C. Salter, S. J. Wilkins, R. G. Compton, *Angewandte Chemie In Press*.

[13] A. Chou, T. Boecking, N. K. Singh, J. J. Gooding, *Chem. Commun* **2005**, *7*, 842.

[14] J. H. T. Luong, S. Hrapovic, Y. Liu, D.-Q. Yang, E. Sacher, D. Wang, C. T. Kingston, G. D. Enright, *J. Phys. Chem. B* **2005**, *109*, 1400.

[15] J. Wang, M. Musameh, *Anal. Chem.* **2003**, *75*, 2075.

[16] M. Musameh, N. S. Lawrence, J. Wang, *Electrochem. Commun.* **2005**, *7*, 14.

[17] M. Musameh, J. Wang, A. Merkoci, Y. Lin, *Electrochem. Commun.* **2002**, *4*, 743.

[18] L. Y. Heng, A. Chou, J. Yu, Y. Chen, J. J. Gooding, *Electrochem. Commun.* **2005**, *7*, 1457.

[19] C. E. Banks, R. G. Compton, *Analyst* **2006**, *131*, 15.

[20] E. R. Lowe, C. E. Banks, R. G. Compton, *Anal. Bioanal. Chem.* **2005**, *382*, 1169.

CHAPTER 5

Multi-walled Carbon Nanotubes Resist Intercalation Whereas Pyrolytic Graphite Can Exfoliate in Propylene Carbonate

In this chapter, a generic approach is presented allowing the sensing of electroactive species at carbon based electrode in otherwise potentially intercalating media. Graphite electrodes are known to suffer intercalation leading to exfoliation in propylene carbonate solution containing tetra-n-butylammonium perchlorate as supporting electrolyte. In this chapter we report contrasting behaviour at bamboo multi walled carbon nanotubes, where intercalation / exfoliation does not occur, so allowing useful electroanalytical measurements to be made. This work discussed in this chapter has been published as an article in *Electroanalysis,* **2006**, 18, 2141.

5.1 Introduction

Carbon has been widely used in electrochemical systems for a long time. In many aspects, it is an ideal electrode material owing to its attractive features, including the good corrosion resistance, high electrical conductivity, low cost and a wide anodic potential window in aqueous solutions.[1-4] According to the degree of graphitization, it is morphologically diverse, existing in a various forms from carbon black to glassy carbon, carbon fibres and pyrolytic graphite.[1, 5] Typically for carbon electrodes, there

are two graphite planes: the basal plane, which is an exposed hexagonal surface that is parallel to the graphite layer with an interlayer spacing of 3.35 Å and the edge plane, which is the surface perpendicular to the graphite layer; a schematic representation is shown in Figure 5.1. Surface defects occur in the form of steps exposing the edges of the graphite layers as a basal plane will typically containing mostly basal terraces separated by a few edge plane steps. Due to the nature of the chemical bonding in graphite, these two planes, edge and basal, exhibit completely different electrochemical properties:[4, 6, 7] the edge plane usually exhibits considerably faster electrode kinetics for the oxidation or reduction of redox species in comparison with the basal plane. This means that in many instances an electrode consisting entirely of edge plane *viz*. an edge plane pyrolytic graphite electrode will show a nearly electrochemically reversible ("Nernstian") voltammogram while an electrode consisting mainly of basal plane can show electrochemically irreversible behavior for the same species but depending highly on the number of edge steps present.[4, 7, 8]

Another fascinating form of carbon, are carbon nanotubes (CNTs). CNTs are concentric graphitic cylinders which may be closed at either end due to the presence of five-membered rings.[9] CNTs are assigned into two distinctive classes: single walled (SWCNTs) and multi-wall carbon nanotubes (MWCNTs). The former consist of a single graphite sheet rolled flawlessly producing a tube diameter of ca. 1-2 nm while the latter comprise several such concentric tubes fitted one inside the other.[9]

Carbon nanotubes have been widely used in electrochemistry, none more so than electroanalysis, where carbon nanotube modified electrodes (see Figure 5.1C) have been reported to have superior 'electrocatalytic' sensing properties. When considering the electrochemical performance of CNTs, it has been suggested that the edge plane - like sites / defects which occur at the ends and along the tube axis are often responsible

for the electrocatalysis of CNTs.[6, 10] However, very recently, our group observed that the catalysis of CNTs can arise not only from the edge plane like sites / defects but also from the presence of metal (iron) oxide impurities in the CNTs can act as nano-particulate centers for redox activity electrically 'wired' via the CNTs;[11] see Figure 5.1C for a representation.

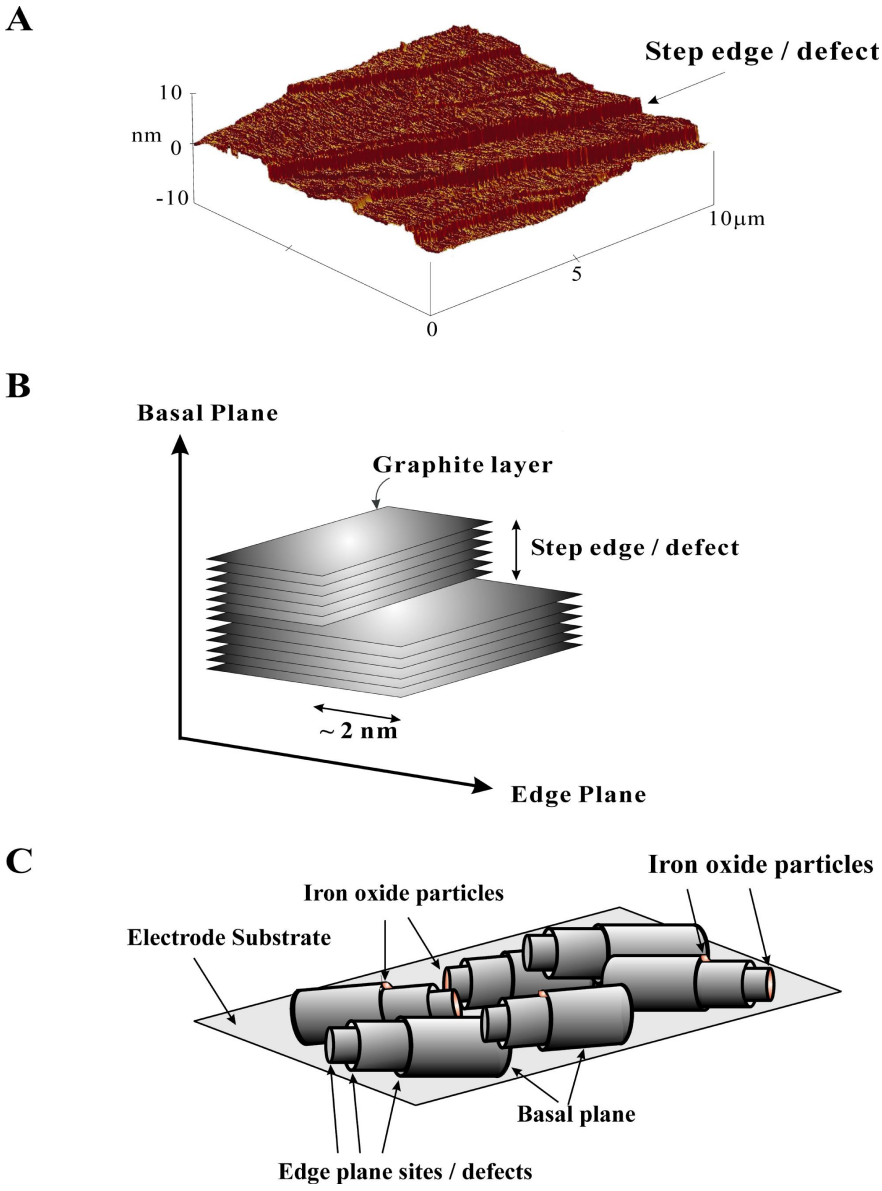


Figure 5.1 (A) Atomic Force Microscopy image of the surface of a highly order pyrolytic graphite electrode, where the step edges / defects can be clearly observed. (B) A schematic representation is shown for a 6 graphite layer highly order pyrolytic graphite surface depicting how the edge pane and basal plane electrodes are constructed from the highly ordered pyrolytic graphite.(C) shows a dispersion of multi-walled carbon nanotubes on an electrode surface detailing the two electroactive sites, edge plane -like defects and iron oxide nanoparticles.

Despite the many and varied attractive features of carbon electrodes they can have limited use in non-aqueous solutions due to intercalation processes; for example in electroanalysis intercalation can effectively passivate the surface of many different graphite based electrodes so precluding any useful measurements. In this chapter we explore this phenomenon with pyrolytic graphite electrodes using the example of the electrochemical oxidation of ammonia in propylene carbonate solvent containing tetra-butylammonium perchlorate as supporting electrolyte. We demonstrate that intercalation processes dominate and prevent the determination of the electrochemical oxidation of ammonia at basal plane pyrolytic graphite electrode. Nevertheless this can be circumvented by using multi-walled carbon nanotube modified electrodes where the unique *rigid* structural morphology prevents propylene carbonate and supporting electrolyte intercalation so allowing quantitative electroanalysis.

5.2 Experimental Section

5.2.1 Chemicals

Propylene carbonate (Aldrich, 99.7%) and tetra-n-butylammonium perchlorate (TBAP, Fluka) were purchased at the highest grade available and used directly without further purification. Pure ammonia and nitrogen gas (BOC, Guildford, Surrey, UK) were used for electrochemical experiments as described below. All the solutions were vigorously degassed with oxygen-free nitrogen (BOC Gases, Guildford, Surrey, UK) until oxygen was not electrochemically detectable. All experiments were carried out at a temperature of 295 ± 3 K.

5.2.2 Instrumentation

Electrochemical experiments were performed using a μ-Autolab type II potentiostat (Eco-Chemie, Utrecht, Netherlands) controlled by General Purpose

Electrochemical Systems v.4.7 software. For all electrochemical experiments carried out in the electrolyte, the working electrodes used were glassy carbon (GC), a basal plane pyrolytic graphite electrode (BPPG, Le Carbone, Ltd. Sussex, U.K. For BPPG electrode, discs of pyrolytic graphite were machined into a 4.9 mm diameter. The counter electrode was a bright platinum wire with a large surface area, with a silver wire quasi-reference electrode completing the circuit.

The GC was polished using diamond lapping compounds (Kemet, UK). The BPPG electrode was prepared by first polishing the BPPG electrode surface on carborundum paper and then pressing cellotape on the cleaned BBPG surface before removing along with general attached graphite layers. Before use the electrode was then cleaned in acetone to remove any adhesive.

Bamboo Multi-walled carbon nanotubes (> 95 % purity, 10 - 20 nM diameter, 5-20 μm length) were obtained from NanoLab (Brighton, MA, USA) and were used as received. The MWCNTs were cast onto the desired electrode surface by first dispersing 2 mg of MWCNTs into 2 mL ethanol. The suspension is then placed into an ultrasonic bath for 1 minute after which 20 μL is pippetted onto the electrode surface. This is allowed to volatize at room temperature producing a preseumed random distribution of carbon nanotubes on the GC surface.

The electrochemical cell used was a septum sealed three-necked flask which was always held under a nitrogen atmosphere ensuring a fixed amount of ammonia was maintained throughout the experiments. In experiments where ammonia was utilised, the gas was directly introduced from a cylinder containing volume percentages (10 vol %, BOC Gases, Guildford, Surrey, UK) by bubbling the ammonia directly into the solution (nitrogen comprises the remaining part of all the gas mixtures).

AFM measurements were performed in a Digital Instruments MultiMode SPM operating in contact mode. A scanner (type 'J') with *x* and *y* limits of 125 μm and a *z* limit of 6 μm and standard silicon nitride tip (type 'NP') (supplied by Digital Instruments) with a force constant of approximately 0.32 NM^{-1} were used. Scans were collected at a scan rate of 1 Hz. Optical images were obtained using a microscope based on a SONY XC-999P CCD camera.

High resolution ttransmission electron microscopy was performed with a JEOL 4000EX operating at 400kV, samples were dispersed in ethanol and loaded onto copper grids coated with Formvar. X-ray diffraction was performed using a Philips PANalytical X'pert pro diffractometer with $Cu_{K\alpha}$ radiation, ë=1.5406 nm, 40 kV, 40 mA.

5.3 Results and Discussion

5.3.1 Voltammetric Response of Ammonia in Propylene Carbonate

The electrochemical oxidation of ammonia was investigated by bubbling 10 % ammonia gas into 25 mL propylene carbonate containing 0.1 M TBAP for a period of 45 seconds. Glassy carbon (GC) and basal plane pyrolytic graphite (BPPG) electrodes were in turn used with the voltammetric responses explored via cyclic voltammetry. The observed cyclic voltammograms are depicted in Figure 5.2, where a large oxidation wave with a peak potential at *ca.* + 1.6 V (vs. Ag wire) is seen at the glassy carbon electrode. The electrochemical oxidation of ammonia likely proceeds via the following[12]electrochemical step:

$$4NH_3(g) - 3e^- \rightleftarrows 3NH_4^+ + 1/2N_2(g) \qquad (5.1)$$

On the reverse (reductive seen) a CE process takes place:

C: $$NH_4^+ \rightleftarrows NH_3(g) + H^+ \qquad (5.2)$$

in which a proton formed via dissociation of NH_4^+ is electrochemically reduced to produce hydrogen; at the glassy carbon electrode this is seen at *ca.* – 0.65 V (vs. Ag wire):

$$E \qquad H^+ + e^- \rightleftharpoons 1/2\ H_2(g) \qquad (5.3)$$

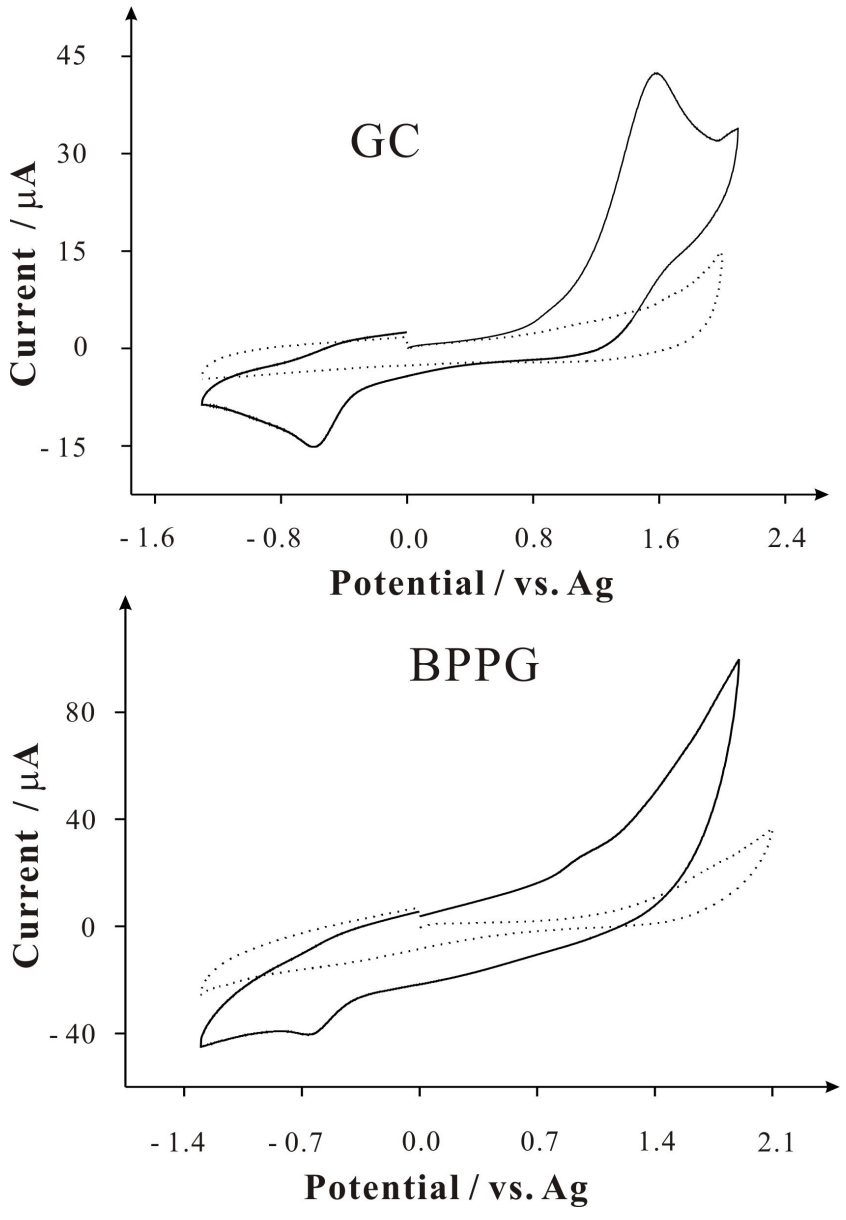


Figure 5.2 Cyclic voltammograms recorded in a propylene carbonate solution containing 0.1 M TBAP which has been bubbled with 10% vol ammonia for 45 seconds obtained at a range of electrodes: glassy carbon electrode (GC), basal plane pyrolytic graphite electrode (BPPG). The dashed line is the response of the electrode in the absence of ammonia. The scan rate in all cases was 100 mV s^{-1}.

Next the electrochemical oxidation of ammonia at the BPPG electrode was explored. The voltammetric response, as depicted in Figure 5.2, recorded at electrode show no oxidation wave corresponding to the electrochemical oxidation of ammonia. Moreover, comparison of the accessible potential windows[13] in propylene carbonate reveals that GC has a window of 5.9 V while BPPG has a potential window of just 3.7 V. The anodic limit in propylene carbonate extends up to *ca.* + 2.7 V for GC before the onset of solvent breakdown, while the BPPG electrode has an anodic limit of *ca.* + 1.9 V (vs. Ag wire). It may be inferred that, given the lower anodic limit of the BPPG electrode compared with that of the GC electrodes, that the oxidation of ammonia may occur in the region of solvent decomposition making it appear voltametrically 'invisible'.

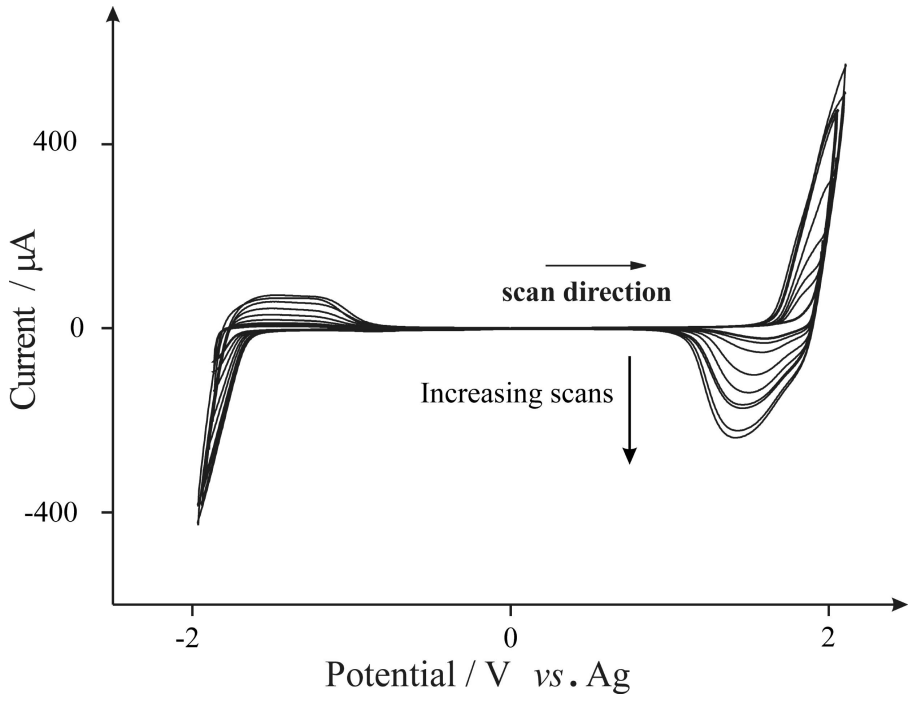


Figure 5.3 Successive cyclic voltammograms recorded at a basal plane pyrolytic graphite electrode in propylene carbonate containing 0.1 M TBAP. Scans were recorded at 100 mVs^{-1}.

It is known that propylene carbonate can intercalate graphite when driven by appropriate applied potentials resulting in exfoliation of the graphite layers and destruction of the graphite structure,[14-16] so precluding useful voltammetry. In particular considering TBAP as supporting electrolyte,[17, 18] the TBA^+ and ClO_4^- ions are reported to co-intercalate into graphite layers with the solvent. Due to the insertion of a large cation TBA^+ into the graphite layer the expanded space is thought to further facilitate the insertion of PC. It has also been reported that ammonia co-intercalates graphite with alkali or alkaline earth metals.[19] Figure 5.3 shows consecutive voltammetric scans recorded at a basal plane pyrolytic graphite electrode in propylene carbonate containing 0.1 M TBAP. In the process of scanning, the potential window is reduced as a result of potential driven intercalation.

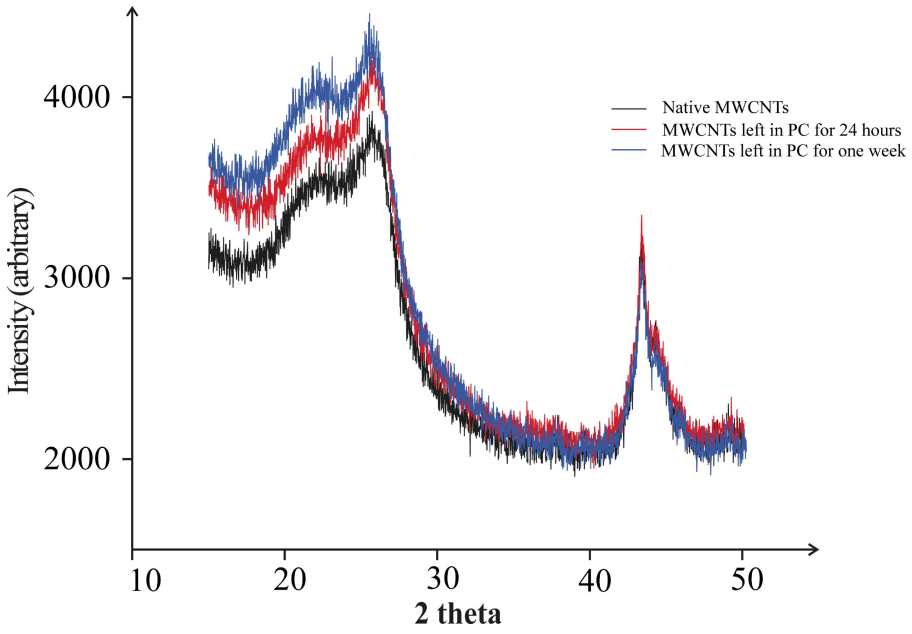


Figure 5.4 XRD patterns of bamboo MWCNTs before and after exposure to propylene carbonate

In the experiments reported above it is likely that propylene carbonate intercalates into the graphite planes at potentials near the limits of the potential sweeps and exfoliates graphite layers, irreversibly damaging the electrode which may account for

the absence of any voltammetry corresponding to ammonia in propylene carbonate observed at the basal plane pyrolytic graphite electrode (see Figure 5.2 and Figure 5.3) under the accessible potential window. That is the reduced potential window is due to the intercalation and this prevents electro-analytical measurements of ammonia. Next, the same experiments as above we repeated on a MWCNT modified GC electrode. MWCNTs were immobilised onto a glassy carbon electrode[20] and placed into 25 mL propylene carbonate containing 0.1 M TBAP. After repeated cycles under the accessible potential window (between + 2.2 V and – 2.5 V vs. Ag), the voltammetric responses were stable, and even after a few hours cycling, the cyclic voltammograms were unchanged without showing any irreversible change due to intercalation of propylene carbonate into the carbon nanotubes. The upper time limit for the cycling experiments was constrained by the physical loss of MWCNTs from the GC electrode surface. Note that before use the MWCNTs were characterized by XRD and TEM as shown in Figure 5.4 and 5.5, respectively. The interlayer spacing of 3.35 Å was unchanged even after exposure to propylene carbonate and TBAP for periods up to one week.

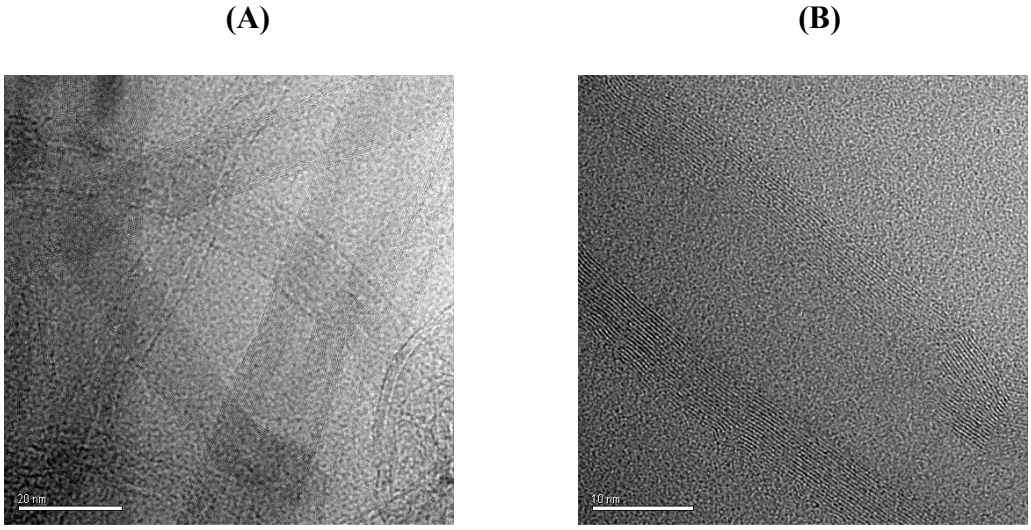


Figure 5.5 TEM images of MWCNTs before (A) and after (B) exposure to propylene carbonate for 7 days.

5.3.2 Electrochemical Behavior of MWCNTs in Propylene Carbonate

Next we turned to conducting ammonia detection experiments with bamboo multi-walled carbon nanotubes. MWCNTs were placed into 25 mL propylene carbonate containing 0.1 M TBAP. 10% ammonia gas was bubbled through the latter for 45 seconds. As observed in Figure 5.6A a voltammetric peak is observed at *ca.* + 1.15 V (vs. Ag wire). Samples of the MWCNTs were then left in the propylene carbonate solution for 24 hours and 7 days. After various time periods of exposure of the nanotubes to propylene carbonate had elapsed, the MWCNTs were washed with ethanol and filtered under vacuum. The MWCNTs samples were then dispersed [20] onto the glassy carbon. Figure 5.6B and 5.6C depict the response in the propylene carbonate solution containing ammonia: Indistinguishable voltammetric responses are observed after leaving the MWCNTs in propylene carbonate for 24 hours (Figure 5.6B) and 7 days (Figure 5.6C) respectively compared to the initial response of the MWCNTs.

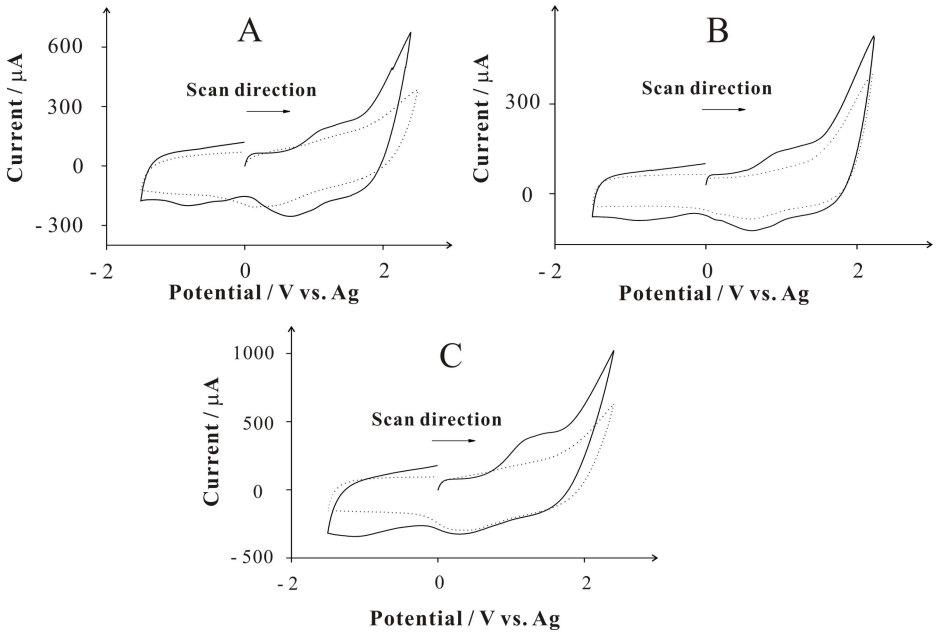


Figure 5.6 Cyclic voltammetric responses of multi-walled carbon nanotube modified GC electrodes in a propylene carbonate (PC) solution containing 0.1 M TBAP which has been bubbled with 10% vol ammonia for 45 seconds. (A) MWCNT in PC for 30 minutes, (B) MWCNT after being left in PC for 24 hours, and (C) MWCNT after being left in PC for one week. The dashed line is response of the electrodes in the absence of ammonia. The scan rate was 100 mV s^{-1}.

Given the contrasting behaviour seen at the basal plane pyrolytic graphite electrode (Figure 5.2) with that of the multi-walled carbon nanotubes (Figure 5.6), it is almost certain that propylene carbonate molecule intercalates into the graphite layers at the pyrolytic graphite electrodes resulting in exfoliation and irreversibly damage to the electrode structure. A schematic representation of this process is shown in Figure 5.7 (A) for the initial stages of intercalation of propylene carbonate between the graphite layers. However, due to the unique and relatively rigid structure of the MWCNTs the propylene carbonate solvent molecules may not penetrate in-between the graphite layers since the rigid structure caused by the concentric carbon rolls prevents exfoliation of the carbon layers and the voltammetric responses corresponding to the oxidation of ammonia are observed on the MWCNTs modified glassy carbon electrodes unperturbed by any competing intercalation or exfoliation. A schematic representation of the electrochemical process is shown in Figure 5.7(B).

5.4. Conclusions

In summary multi-walled carbon nanotube based surfaces are a promising modified electrode material which can be used in media which may otherwise intercalate with graphite media for sensing via electrochemistry. By exploring the electrochemical oxidation of ammonia in propylene carbonate solutions, it has been shown that the basal plane pyrolytic graphite electrode can become intercalated with propylene carbonate and TBAP, and the surface of the pyrolytic graphite electrode becomes unsuitable for electroanalysis. However, for the multi walled carbon tubes, excellent and quantitative voltammetric responses corresponding to the oxidation of ammonia are observed, confirming that the propylene carbonate molecule cannot penetrate between the concentric tubes and hence there is no intercalation within the carbon nanotubes.

Therefore the multi walled carbon nanotubes provide new avenues in otherwise intercalating media for sensing of electroactive species.

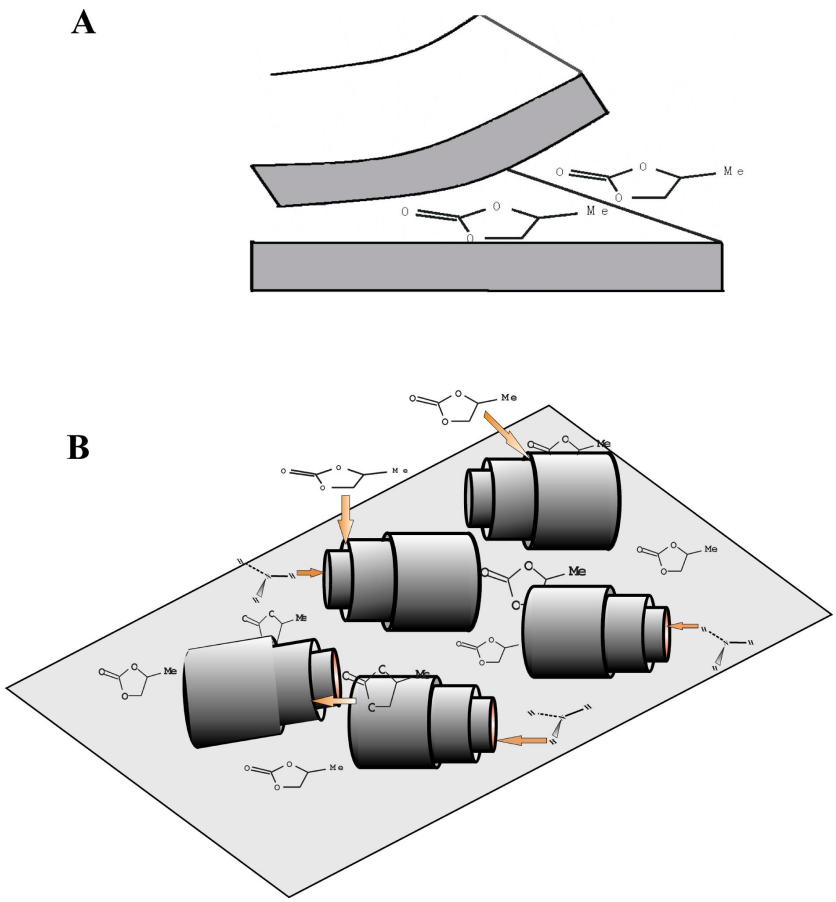


Figure 5.7 A schematic representation is shown for the intercalation of propylene carbonate (PC) with pyrolytic graphite (A) leading to the graphite layer becoming exfoliated. Note that also TBA^+ and ClO_4^- co-intercalates into the graphite layers. (B) illustrates the suggested route for the electron transfer reaction between multi walled carbon nanotubes (MWCNTs) and propylene carbonate. It is impossible for the PC molecules penetrate between the carbon layers because of the rigid concentric tube structure, hence there is no intercalation observed on MWCNTs with PC, rather electron transfer occurs at the edge plane like defects.

5.5 References:

[1] M.A.T. Gilmartin, J.P. Hart, *Analyst* **1995**, *120*, 1029.

[2] E. Frackowiak, F. Beguin, *Carbon* **2001**, *39*, 937.

[3] N.L. Pocard, D.C. Alsmeyer, R.L. McCreery, T.X. Neenan, M.R. Callstrom, *J. Mat. Chem.* **1992**, *2*, 771.

[4] C.E. Banks, T.J. Davies, G.G. Wildgooses, R.G. Compton, *Chem. Commun.* **2004**, *7*, 829-841.

[5] R. L. McCreery, *Electroanalytical Chemistry*, Marcel Dekker, New York, 1990

[6] C.E. Banks, R.R. Moore, T.J. Davies, R.G. Compton, *Chem. Commun.* **2005**, *16*, 1804-1805.

[7] T.J. Davies, M.E. Hyde, R.G. Compton, *Angewandte Chemie* **2005**, *117*, 5251-5256.

[8] T.J. Davies, R.R. Moore, C.E. Banks, R.G. Compton, *J. Electroanal. Chem.* **2004**, *574*, 123.

[9] C.N.R. Rao, B.C. Satishkumar, A. Govindaraj, M. Nath, *ChemPhysChem* **2001**, *2*, 78.

[10] R.R. Moore, C.E. Banks, R.G. Compton, *Anal. Chem.* **2004**, *76*, 2677-2682.

[11] C.E. Banks, A. Crossley, C. Salter, S.J. Wilkins, R.G. Compton, *Angewandte Chemie* **2005**, 45, 2533.

[12] M.C. Buzzeo, D. Giovanelli, N.S. Lawrence, C. Hardacre, K.R. Seddon, R.G. Compton, *Electroanalysis* **2004**, *16*, 888.

[13] *The accessible potential windows where explored in a propylene carbonate solution containing 0.1 M TBAP where the potential window is defined as the range of potentials between which the current is less than +/-1.6 mA cm^{-2} in the anodic and cathodic directions.*

[14] M. Herstedt, A.M. Andersson, H. Rensmo, H. Siegbahn, K. Edstrom, *Electrochimica Acta* **2004**, *49*, 4939.

[15] Y. Hu, W. Kong, Z. Wang, H. Li, X. Huang, L. Chen, *Electrochem. Sol. St. Lett* **2004**, *7*, A442.

[16] C. Wang, H. Nakamura, H. Komatsu, M. Yoshio, H. Yoshitake, *J. Power Sources* **74**, *74*, 142.

[17] G.-C. Chung, H.-J. Kim, S.-I. Yu, S.-H. Jun, J.-W. Choi, M.-H. Kim, *J. Electrochem. Soc.* **2000**, *147*, 4391.

[18] R. Santhanam, M. Noel, *J. Power Sources* **1995**, *56*, 101.

[19] N. Akuzawa, S. Kawahara, H. Sakuno, T. Amemiya, and Y. Takahashi, Carbon **1988,** *26,* 104.

[20] *2 mg of MWCNTs are dispersed into 2 mL ethanol. The suspension is then placed into an ultrasonic bath for 1 minute after which 20 µL is pippetted onto the electrode surface. This is allowed to volatize at room temperature producing a random distribution of carbon nanotubes on the GC surface.*

CHAPTER 6

'Oxygenated' Edge Plane Sites Slow the Electron Transfer Kinetics of the Ferrocyanide / Ferricyanide Redox Couple at Graphite Electrodes

The electron transfer kinetics of ferrocyanide, potassium hexachloro-iridate (III), hexaammineruthenium (III) chloride, and *N,N,N',N'*-tetramethyl-p-phenylenediamine (TMPD) have been examined at basal plane and edge plane pyrolytic graphite electrodes which have been allowed to aerial oxidise in air for various periods of time. Via voltammetric and XPS analysis that oxygenated species formed at edge plane sites / defects decrease the electron transfer kinetics of ferrocyanide but that the rates for potassium hexachloro-iridate (III), hexaammineruthenium (III) chloride and TMPD are insensitive to the oxygenated species, and the possible reasons for this contrasting behaviour are discussed. This work discussed in this chapter has been published as an article in *ChemPhysChem,* **2006**, 7, 1337.

6.1 Introduction

The correlation of surface structure and electron transfer reactivity of carbon electrodes is the subject of many investigations.[1-6] Three different classes of behaviour have been reported.[3] The first are redox systems which are very sensitive to surface cleanliness where the observed electron transfer rates strongly depend on the surface history. The second, some redox systems are sensitive to the presence of surface oxides

which catalyse electron transfer or modify the surface charge. Third, the microstructure of the carbon has large effect with the basal plane of highly ordered pyrolytic graphite exhibiting much slower electron transfer rates than glassy carbon.[3] Indeed, it has recently been demonstrated that the basal plane of highly ordered pyrolytic graphite is effectively inert[7] and does not contribute to charge transfer.

In considering surface oxides it has been reported that oxide sites on oxidised glassy carbon or highly ordered pyrolytic graphite electrodes catalyse electron transfer for $Eu_{aq}^{+2/+3}$, $Fe_{aq}^{+2/+3}$ and $V_{aq}^{+2/+3}$.[2, 8] For example the heterogeneous rate constant for $Eu_{aq}^{+2/+3}$ was increased by a factor of 500 after a glassy carbon electrode was oxidised electrochemically.[2, 8] Furthermore the effect of 2,6-anthraquinone disulfonate (AQDS) adsorption was explored for $Fe(CN)_6^{-4/-3}$ where the heterogeneous rate constant was found to decrease by factors of 10 – 25 when the glassy carbon electrodes were covered with a monolayer of AQDS. However the absorption had minor effects on the heterogeneous rate constants of $Ru(NH_3)_6^{+3/+2}$ and $IrCl_6^{-2/-3}$; it was therefore concluded for $Fe(CN)_6^{-4/-3}$ that it either undergoes an inner-sphere route or some other factors dependant on surface chemistry operate.[2] However subsequent reports for $Fe(CN)_6^{-4/-3}$ suggested that the heterogeneous rate constant does not appear to depends on surface oxides except for a fairly small factor (2-3).[9] It has also been noted that potassium hexachloro-iridate (III), hexaammineruthenium (III) chloride are examples of outer-sphere electron transfer reactions, where the rates of these are insensitive to surface chemistry.[3]

In this chapter we explore the effects on the electron transfer kinetics of ferrocyanide, potassium hexachloro-iridate (III), hexaammineruthenium (III) chloride, and *N,N,N',N'*-tetramethyl-p-phenylenediamine (TMPD) from leaving freshly prepared basal plane and edge plane pyrolytic graphite electrodes in air for various periods of

time. It is found via voltammetric and XPS analysis that oxygenated species decrease the electron transfer kinetics of ferrocyanide but the rates for potassium hexachloro-iridate (III), hexaammineruthenium (III) chloride, and TMPD are insensitive to the presence or absence of oxygenated species. The behaviour of the ferrocyanide / ferricyanide redox couple is discussed in the light of a very recent report[10] that oxygenation of the tube ends of carbon single walled nanotube *speeds up* the electron transfer kinetics of the ferro- cyanide / ferri- cyanide couple.

6.2 Experimental

6.2.1 Chemicals

Potassium hexacyanoferrate (II) trihydrate (Lancaster, 99%), potassium hexachloro-iridate (III) (Aldrich, 99%), *N,N,N',N'*-tetramethyl-p-phenylenediamine (Aldrich, 98%), Tetra n-butylammonium perchlorate (Fluka, 99+%), acetonitrile (Fisher, HPLC grade) and hexaammineruthenium(III) chloride (Sigma-Aldrich, 98+%) were purchased at the highest grade available and used directly without further purification. Aqueous electrolyte solutions were prepared with KCl (99.5%) (Aldrich) using ultrapure water from an Vivendi UHQ grade water system (Vivendi, UK) with a resistivity of not less than 18.2 MΩ cm^{-1}. All the solutions were degassed with oxygen-free nitrogen (BOC Gases, Guildford, Surrey, UK). All experiments were carried out at a temperature of 295 ± 3 K.

6.2.2 Instrumentation

Electrochemical experiments were performed using a μ-Autolab type II potentiostat (Eco-Chemie, Utrecht, Netherlands) controlled by General Purpose Electrochemical Systems v.4.7 software. For all electrochemical experiments, the

working electrodes used were a basal plane pyrolytic graphite electrode (BPPG, 4.9 mm diameter, Le Carbone, Ltd. Sussex, U.K), an edge plane pyrolytic graphite electrode (EPPG, 4.9 mm diameter, Le Carbone, Ltd. Sussex, U.K), and a highly oriented pyrolytic graphite slab (HOPG, 4.9 mm diameter, SPI supplies). For BPPG and EPPG electrodes, discs of pyrolytic graphite were machined into a 4.9 mm diameter, with the disc face parallel with the edge plane, or basal plane as required. The counter electrode was a platinum wire, with a saturated calomel reference electrode (Radiometer, Copenhagen, Denmark) completing the circuit.

The EPPG electrode was polished on alumina lapping compound of decreasing sizes (0.1 – 5 μm) on soft lapping pads. The BPPG electrode surface was renewed using cellotape.[11] This procedure involves polishing the BPPG electrode surface on carborundum paper and then pressing cellotape on the cleaned BBPG surface before removing along with general attached graphite layers. After repeating several times, the electrode was then cleaned in acetone to remove any adhesive.

Bamboo multi-walled carbon nanotubes (> 95 % purity (10 - 20 nM diameter, 5-20 μm length) were obtained from NanoLab (Brighton, MA) and were used as received. The MWCNTs were cast onto the desired electrode surface.. This involves first dispersing 2 mg of MWCNTs into 2 mL ethanol. The suspension is then placed into an ultrasonic bath for 1 minute after which 20 μL is pippetted onto the electrode surface. This is allowed to volatize at room temperature producing a random distribution of carbon nanotubes on the BPPG surface. Conversely for the iron (II) oxide and iron (III) oxide film modified electrodes the same procedure was employed.

X-Ray photoelectron spectroscopy (XPS) of the highly ordered graphite pyrolytic electrodes was performed on a VG Clam 4 MCD analyzer system at the OCMS Begbroke Science Park, University of Oxford, UK using X-ray radiation from the Al

Ka band (hn 5 1486.7 eV). All XPS experiments were recorded using an analyzer energy of 100 eV with a takeoff angle of 90u. The base pressure in the analysis chamber was maintained at not more than 2.0 x 10^{-9} mbar. The HOPG slab was renewed by pressing cellotape on the slab surface to remove general attached graphite layers. This step was repeated several times until a shiny and smooth electrode surface was observed. The carbon sample studied was mounted on to a stub using double sided adhesive tape and then placed in the ultrahigh vacuum analysis chamber of the spectrometer. To prevent the sample from becoming positively charged when irradiated due to emission of photoelectrons, the sample surface was bombarded with an electron beam (10 eV) from a ''flood gun'' within the spectrometer's analysis chamber. The Microcal Origin 6.0 was used to analyze the resulting spectra. Assignment of spectral peaks was determined using the UKSAF24 and NIST25 databases.

AFM measurements were performed in a Digital Instruments MultiMode SPM operating in contact mode. A scanner (type 'J') with *x* and *y* limits of 125 μm and a *z* limit of 6 μm and standard silicon nitride tip (type 'NP') (supplied by Digital Instruments) with a force constant of approximately 0.32 NM^{-1} were used. Scans were collected at a scan rate of 1 Hz. Optical images were obtained using a microscope based on a SONY XC-999P CCD camera.

6.3 Results and Discussion

6.3.1 Electrochemical Behaviour of Pyrolytic Graphite Electrodes

It is well known that a variety of bulk carbon structures exist and that variations in the structure substantially influence the electrochemical behaviour of carbon electrodes. Typically for carbon electrodes, there are two graphite planes: basal plane, which is an exposed hexagonal surface that is parallel to the graphite layer and edge plane, which is

where the surface is cut parallel to the graphite layer as shown in Figure 6.1. These exhibit contrasting electrochemical properties due to the nature of chemical bonding in the graphite layer. As previously reported,[12, 13] the edge plane typically shows faster electron transfer kinetics than the basal plane for a range of redox couples. Therefore for some redox couples an electrode consisting entirely of edge plane *viz*. an edge plane pyrolytic graphite electrode can show a nearly reversible voltammogram while an electrode consisting mainly of basal plane can show electrochemically irreversible behaviour with the kinetics often depending on the amount of edge plane defects present in many instances.[12, 14]

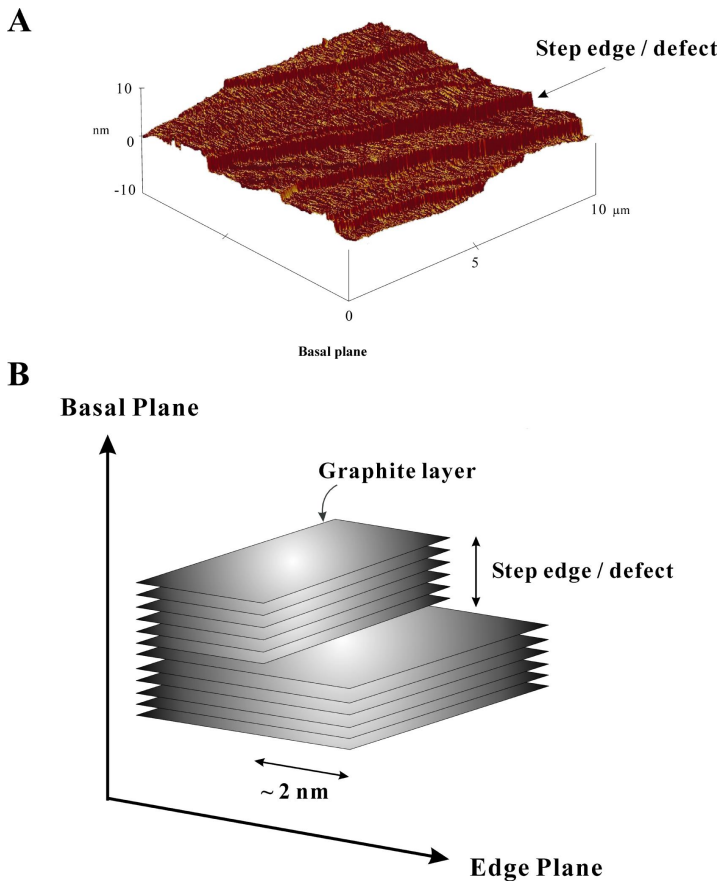


Figure 6.1 An AFM image (A) of HOPG showing multiple edge plane steps and a schematic diagram (B) of a 6 layer step edge.

Figure 6.2 shows the cyclic voltammetric responses obtained at edge (solid line) and basal (dashed line) plane pyrolytic graphite electrodes in a solution of 1 mM ferrocyanide in 0.1 M KCl which exhibit noticeable differences. The edge plane pyrolytic graphite electrode exhibits a peak-to-peak potential separation (ΔE_p) of 75 mV while the basal plane electrode exhibits a peak-to-peak separation of 230 mV. The basal plane electrode is prepared by polishing the surface on carborundum paper and then pressing cellotape on to the BBPG which removes general attached graphite layers.[11] This preparation method, which is described in more detail in the experimental section, produces a low coverage of edge plane sites / defects on the HOPG surface. Depending on the preparation of the basal plane electrode, the peak-to-peak separation at the basal plane electrode can be up to 500 mV depending on the percentage coverage of edge plane sites on the electrode surface.[7, 12, 14] Conversely edge plane sites / defects can be introduced by roughening of the electrode surface, simply induced by polishing the basal plane electrode with alumina on a soft lapping pad.[15]

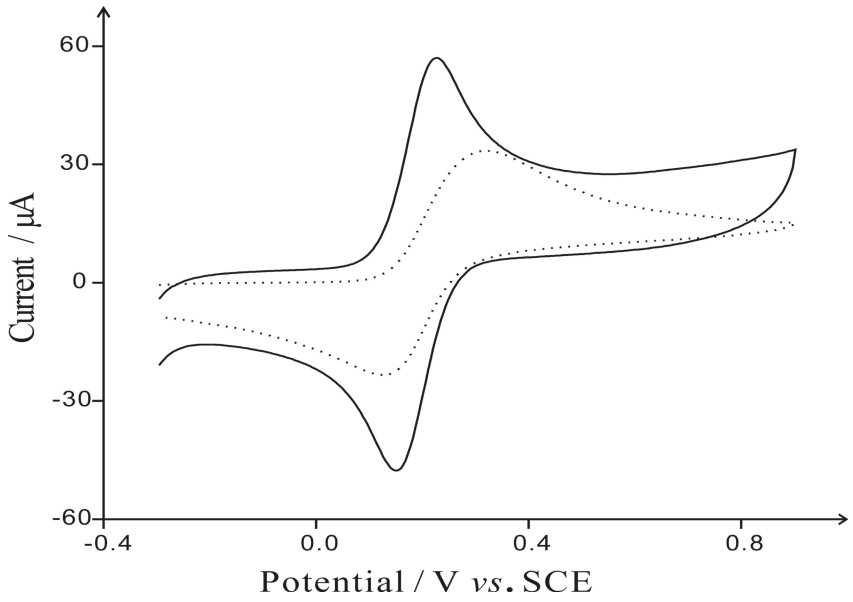


Figure 6.2 Contrast between edge plane and basal plane pyrolytic graphite electrodes in a 1mM ferrocyanide / 0.1 M KCl solution.

6.3.2 The Influences of Exposure time of Oxygen to Electrochemical Behaviour of Pyrolytic Graphite Electrodes

Given the overall goal of relating surface characteristics to electrochemical performance, there are many variables which determine carbon surface reactivity, especially the formation of surface oxides such as carbonyl, quinones etc[1] on the surfaces of the carbon electrodes which are chemically irreversibly formed. In order to obtain a better understanding of the role of surface oxides/functional groups on the electrode kinetics, the effect of leaving a freshly prepared BPPG electrode in air was explored using the ferrocyanide / ferricyanide redox couple in the aqueous solutions.

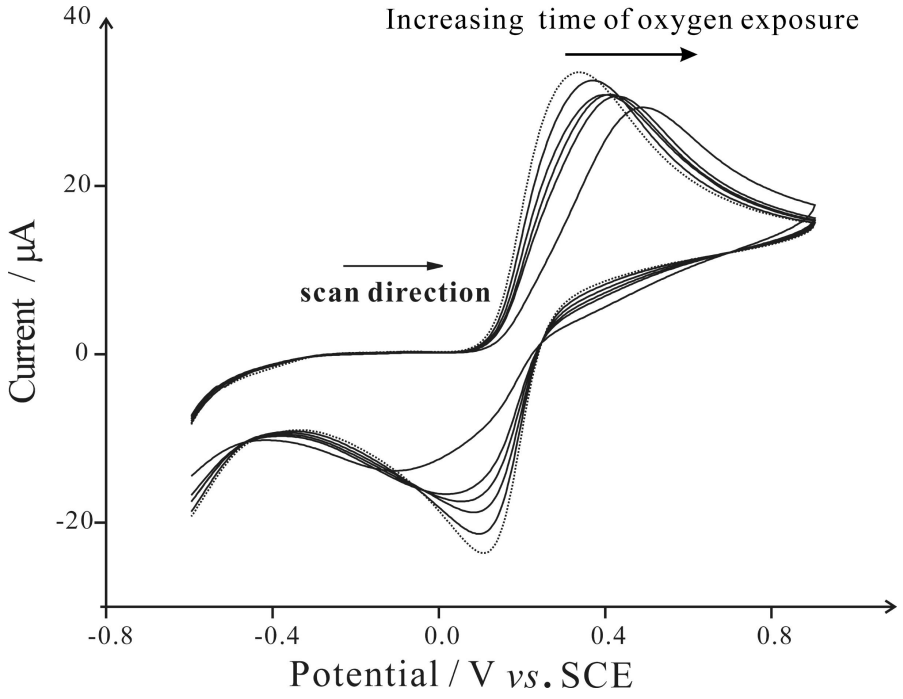


Figure 6.3 The result of leaving the basal plane pyrolytic graphite electrode in air for 0, 10, 30, 60 and 120 minutes (left to right). Cyclic voltammograms were recorded at 100 mVs^{-1} in 1 mM ferrocyanide / 0.1 M KCl solution. The initial response is represented as the dotted line. Note the peak-to-peak separation increases with increasing time of exposure to oxygen.

A freshly prepared BPPG electrode was placed directly into a solution of 1 mM ferrocyanide in 0.1 M KCl with the cyclic voltammetric response recorded at a scan rate of 100 mV s^{-1}. Next a freshly prepared BPPG electrode was left in air for 5 minutes,

after which the cyclic voltammogram was recorded in the ferrocyanide solution. This procedure was repeated with the freshly prepared BPPG electrode being (separately) left in air for 10, 30, 60 and 120 minutes. After each time period the cyclic voltammetric response was recorded Note that at the start of each time period the electrode was freshly prepared with carborundum paper (see above). All the voltammograms recorded above are depicted in Figure 6.3. One can immediately see that leaving the electrode surface in air for increasing periods of time has resulted in the peak-to-peak separation to increase indicating a decrease in heterogeneous electron transfer rate. Table 1 summarises the values analysed from the peak-to-peak separation (ΔE_p) for each CV at each time period the electrode is exposed to air, which is observed to increase from 227 to 596 mV from leaving the electrode in air for 5 and 120 minutes respectively. It can be inferred that there are some changes occurring on the surface of BPPG electrode, which may be explained by surface functional groups on the edge plane sites / defects on the graphite surface, which has been formed by exposure to oxygen in air.

Next we investigated the influence of leaving a freshly prepared EPPG in air. Similar to that performed using the BPPG electrode, the EPPG electrode was polished with alumina and was left in air for 1, 3, 6, 12 and 24 hours. Figure 6.4 shows the cyclic voltammograms recorded in a 1 mM ferrocyanide in 0.1 M KCl. Comparison of the effect of aerial oxidation on the edge plane (Figure 6.4) and the basal plane (Figure 6.3) reveals that the peak to peak separation decreases to a lesser extent at the edge plane. This probably simply reflects the effect of the much larger spacing between the edge plane sites / defects on the basal surface as compared to the pure edge plane electrodes which amplifies the effects of a reduced electrochemical rate constant at the edge plane ends in the voltammetry.[7, 13]

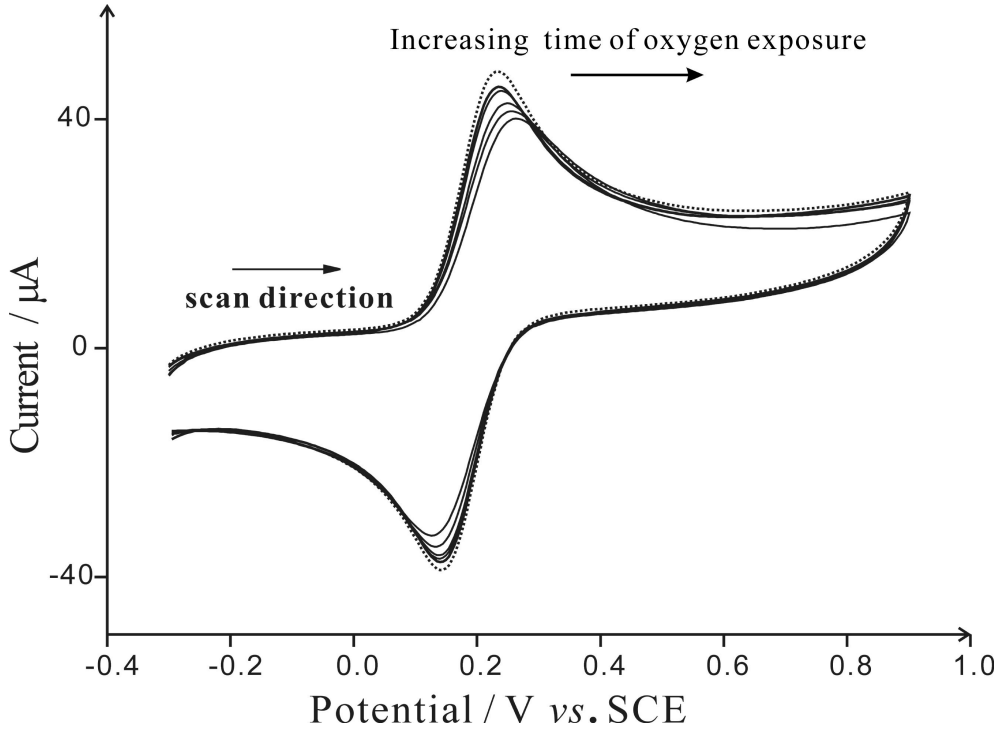


Figure 6.4 The effect of leaving an edge plane pyrolytic graphite electrode in air for 0, 1, 3, 6, 12 and 24 hours (left to right). Cyclic voltammograms were recorded at 100 mVs^{-1} in 1 mM $[Fe(CN)_6]^{3-}$ in 0.1M KCl. The initial response is represented as the dotted line.

Table 1: The result of leaving basal and edge plane pyrolytic graphite electrodes in air for various periods of time on the peak-to-peak (ΔE_p) separation of the ferrocyanide/ferricyanide redox couple in 0.1 M KCl.

Time (min)	0	5	10	30	60	120
Basal Plane /ΔE_p (mv)	227	269	317	360	407	596
Edge Plane /ΔE_p (mv)	89	95	99	109	118	137
MWCNTS[1,2]	66	-	-	-	66	66

1; 1mM $Fe(CN)_6^{3-/4}$ in 0.05 M KCl and 0.05 M NaH_2SO_4 pH =7

2; Supported on glassy carbon

In order to get a better understanding of the phenomenon observed on the BPPG electrode, the following subsequent experiment was performed. Figure 6.5 details cyclic voltammograms showing (scan rate 100 mV s^{-1}) for a solution of 1 mM ferrocyanide in 0.1 M KCl obtained at two "freshly prepared" BPPG electrodes. The first BPPG electrode was prepared as described above ; the second was that a newly prepared BPPG electrode was placed in 0.1 M KCl solution and cycled from - 0.5 to + 0.5 V and back again for 20 times; this has been reported to induce surface functionalities on the electrode surface and 'improve' the electrochemical response.[1] As shown in Figure 6.5, the peak-to-peak separation increases indicating the slowing of the electron transfer rate at the BPPG electrode in the KCl solution as compared with the normal BPPG electrode that has not been electrochemically pre-treated. At the first glance, it is somewhat surprising that the heterogeneous charge transfer rate constant decreases due to the increasing of the surface functional groups, since they have been reported to be involved in electron-transfer activation.[16] However, in aqueous solutions for example, if surface carboxylate were involved these might be deprotonated and repel the anionic $Fe(CN)_6^{4-/3-}$, leading to a decreased concentration of $Fe(CN)_6^{4-/3-}$ near the electrode surface and a decreased apparent electron transfer rate. Equally phenol groups or possibly carbonyl groups might be implicated. Moreover, for this often studied redox system $Fe(CN)_6^{4-/3-}$, it has been suggested that it is an outer-sphere charge transfer route in aqueous solutions.[17] To the contrary, McCreery and co-workers[2] have reported that this couple is very sensitive to surface structures, which greatly influences the observed electron transfer rates. By the of use adsorption effects of AQDS on rate constant for $Fe(CN)_6^{3-/4-}$, it was found that the decrease of rate constant is much larger than the decease in rate constant observed for the other outer-sphere route couples.

Therefore they suggested that the electron transfer process for $Fe(CN)_6^{3-/4-}$ is an inner-sphere route which, of course, can be dependent on the surface functional groups.[2]

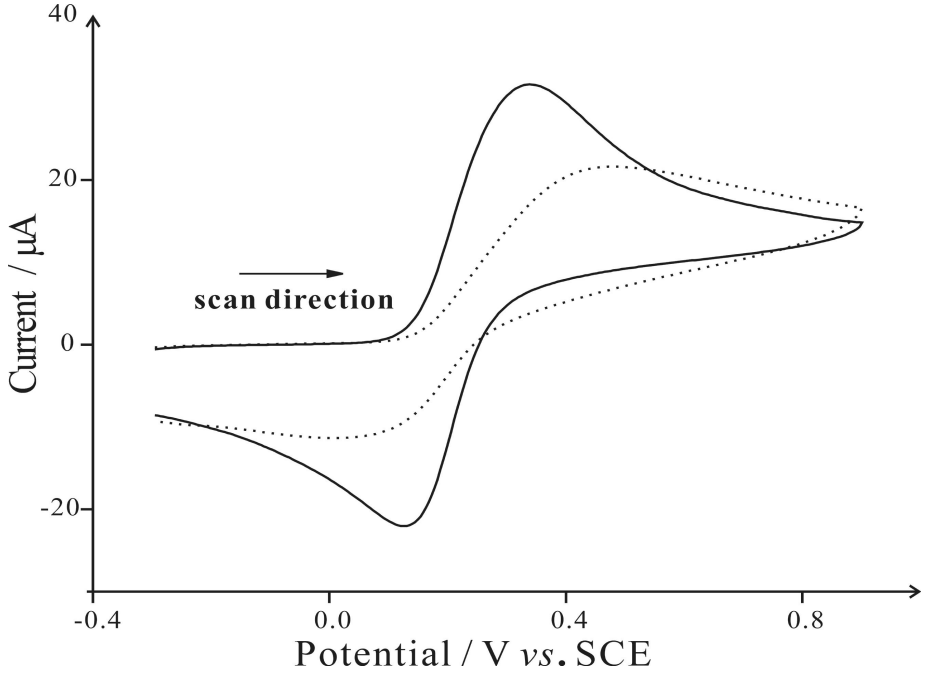


Figure 6.5 The result of cycling a basal plane pyrolytic graphite electrode in 0.1 M KCl from - 0.5 to + 0.5 V and back again for 20 cycles (dotted line) compared with the response before cycling (solid line). Cyclic voltammograms were recorded at 100 mVs^{-1} in 1 mM ferrocyanide / 0.1 M KCl solution.

Next surface oxides on a freshly prepared highly order pyrolytic graphite electrode was characterized with XPS. The XPS spectrum is shown in Figure 6.6 which compares the HOPG electrode before (A) and after (B) being left in air for 10 minutes. Clearly two peaks are observed with kinetic energies of 1202 eV and 953 eV respectively corresponding to carbon and oxygen atoms.[18, 19] Note the type of oxygen functionalities was unable to be de-convoluted: it may be due to O-O, C-O and C=O. However the XPS data provides evidence that oxygenated species are indirectly responsible for the decrease in the heterogeneous charge transfer for ferro/ferri cyanide redox couple, which arises because the oxygenated moieties must 'block' the edge plane sites (see below).

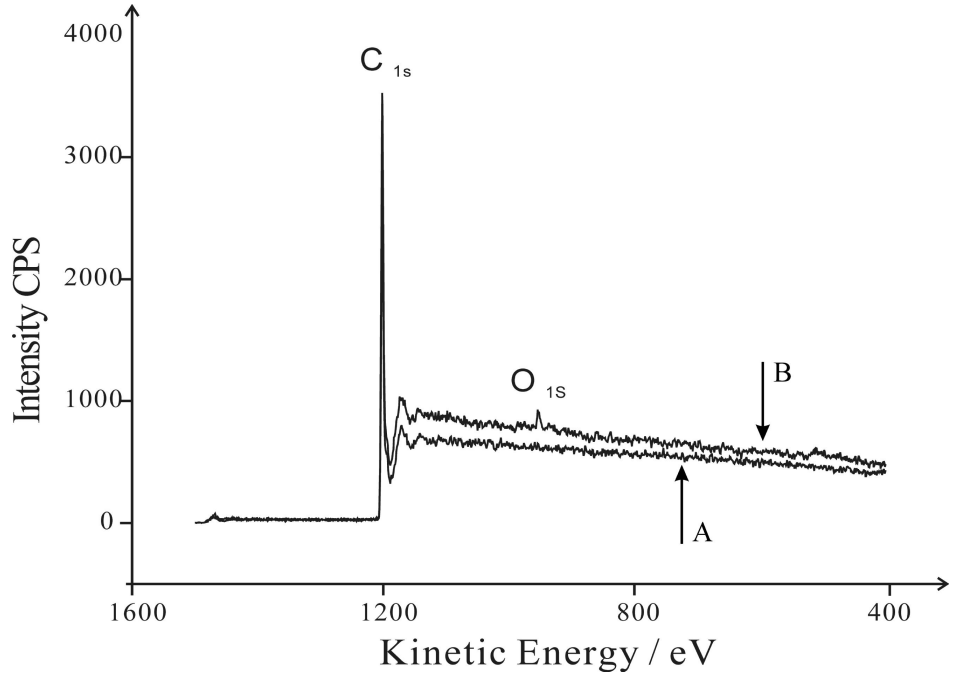


Figure 6.6 XPS spectra for a HOPG electrode before (A) and after (B) being left in air for 10 minutes.

In order to further explore the above proposals, we took a freshly prepared BPPG electrode and left it in MeCN for 30 and 60 minutes (separately) and subsequently explored the voltammetry of aqueous 1 mM ferrocyanide in 0.1 M KCl and compared it with the response of a freshly prepared BPPG electrode that had not been exposed to air or MeCN. Figure 6.7 shows the resulting cyclic voltammograms. It is interesting to note that leaving the electrode in MeCN for both 30 and 60 minutes has had no measurable effect on the heterogeneous charge transfer rate for the $Fe(CN)_6^{4-/3-}$ couple on the BPPG electrode, suggesting that the surface of BPPG electrode has been not modified by the MeCN solvent and that oxygen moieties are not present on the electrode surface. This also confirms that the freshly prepared BPPG electrodes are influenced by the oxygen in the air, producing oxygenated surface functionalities / oxides, but that emersion in a solvent 'protects' the surface from oxidation.

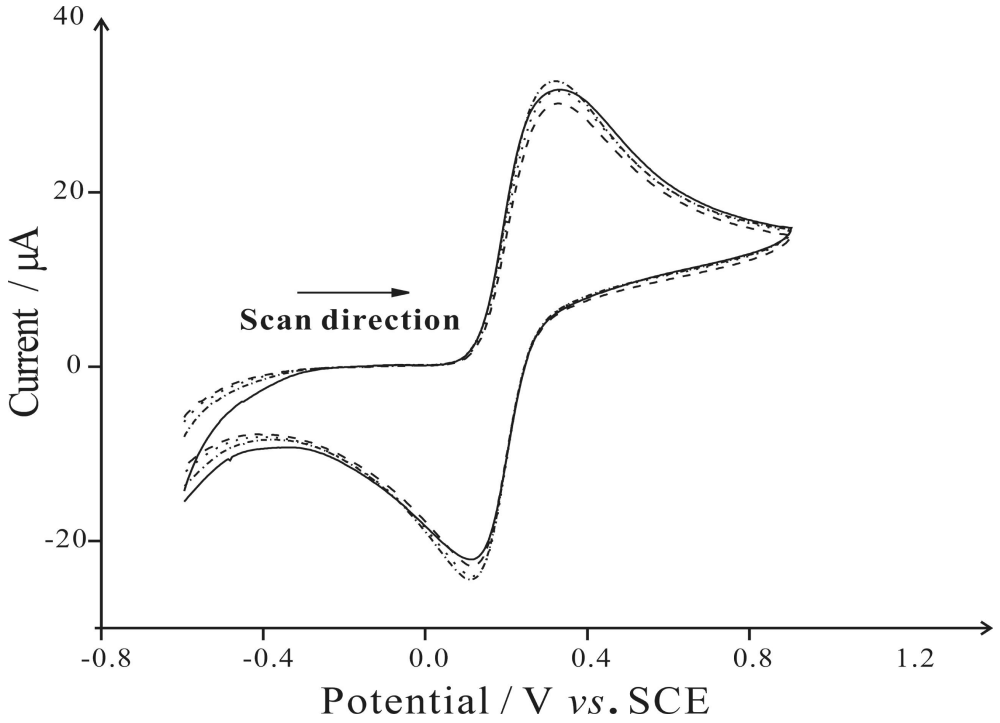


Figure 6.7 The result of leaving a basal plane pyrolytic graphite electrode in MeCN for 0, 30 (dashed) and 60 (dash-dot) minutes. The cyclic voltammograms were recorded at 100 mVs^{-1} in 1 mM ferrocyanide / 0.1 M KCl solution.

Next three outer-sphere redox species, potassium hexachloro-iridate (III), hexaammineruthenium(III) chloride, and *N,N,N',N'*-tetramethyl-p-phenylenediamine (TMPD) were used to examine the possible influence of aerial oxidation on the basal plane graphite surfaces. Figure 6.8 illustrates the cyclic voltammograms at a scan rate of 100 mV s^{-1} at different BPPG electrodes as prepared in the same way as Figure 6.2 in: A, 1 mM $K_3[Ir(Cl)_6]$ in aqueous 0.1 M KCl, B: 1 mM $Ru(NH_3)_6Cl_3$ in aqueous 0.1 M KCl, C: 1 mM TMPD in aqueous 0.1 M KCl. It is interesting to note that there is no observed change in the electron transfer rate for these couples when oxygenated surface functional groups are present. However, McCreery[2] has reported that these $[Ru(NH_3)_6]^{3-}$, TMPD, $[Ir(Cl)_6]^{3-}$ redox couples occur via outer-sphere routes, which suggests, as observed, that the electron transfer reaction for these redox systems are not

sensitive to the electrode surface.[2] On the other hand, compared with these couples, it is reasonable to assume that the electron transfer rate observed for the $Fe(CN)_6^{3-/4-}$ couple could be influenced by the specific surface sites, which agrees with "inner-sphere route" proposed by McCreery.[2]

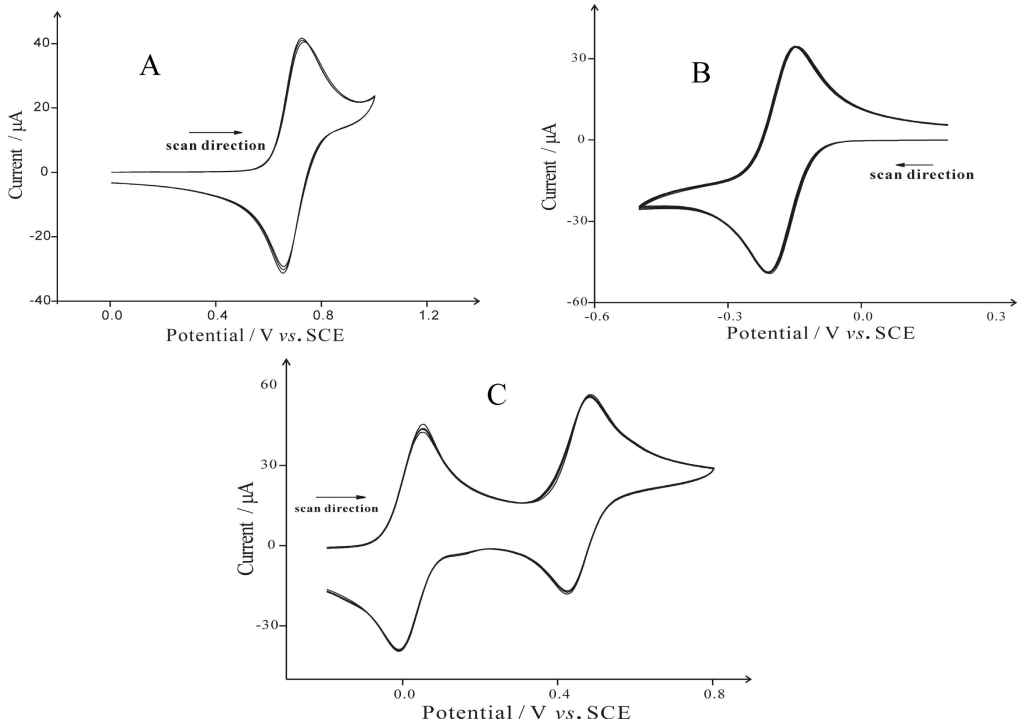


Figure 6.8 The effect of leaving a basal plane pyrolytic graphite electrode in the air various amounts of time then explored using the following redox systems: A, 1mM $[Ir(Cl)_6]^{3-}$ of 0.1 KCl for 0, 30 and 60 minutes. B, 1mM $[Ru(NH_3)_6]^{3-}$ of 0.1 KCl for 0, 30 and 60 minutes and C, 1mM TMPD of 0.1 KCl for 0, 5, 10, 30, 60 and 120 minutes.

6.3.3 Electrochemical Behaviour of CNTs

Very recently Gooding et al[10] have elegantly demonstrated with the ferri- / ferro-cyanide redox couple that increasing the amount of oxygenated species at the ends of single-walled carbon nanotubes by oxidising with nitric acid, speeds up the electron transfer kinetics.[10] Since carbon nanotubes are effectively rolled up tubes of graphite with basal and edge plane sites[12, 14] there appears contrasting behaviour with the experiments reported above.

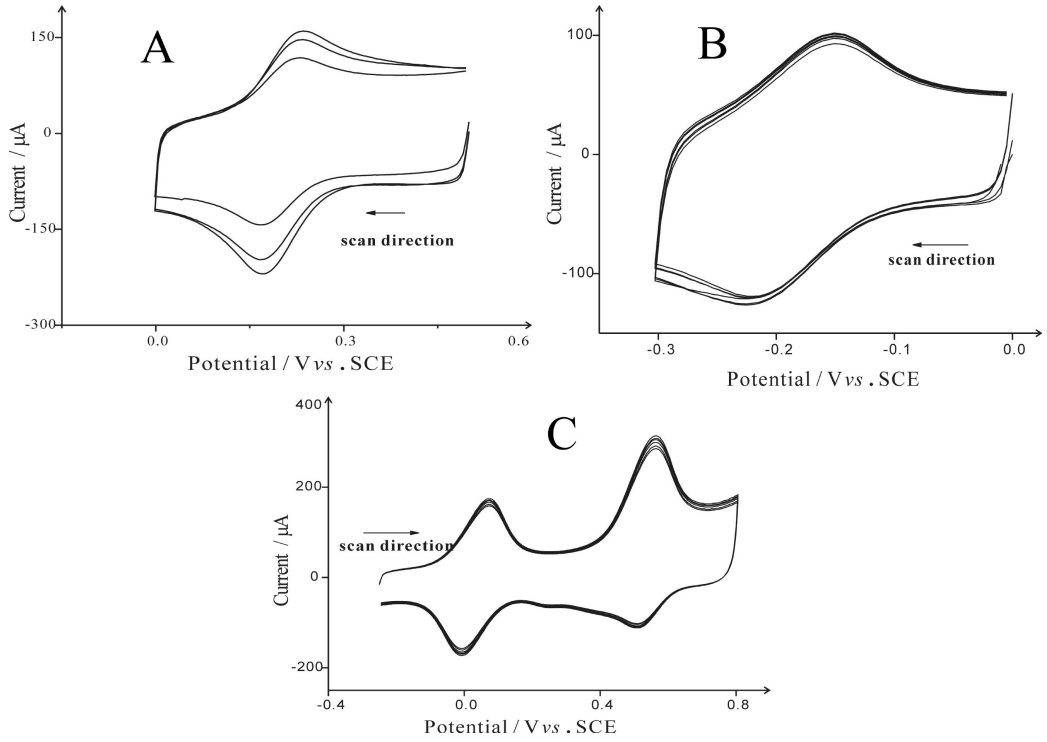


Figure 6.9 The effect of aerial oxidation on MWCNT 'film' modified basal plane pyrolytic graphite electrode in (A) 1 mM ferricyanide / 0.05 M KCl and 0.05 M NaH_2SO_4 pH = 7 after 0, 12 and 24 hrs. B is using 1mM $[Ru(NH_3)_6]^{3-}$ / 0.1 KCl and (C) 1mM TMPD / 0.1 KCl for 0, 1, 3, 6, 12 and 24 hrs. The cyclic voltammograms were recorded at 100 mVs^{-1}.

We therefore turn to considering the effect of aerial oxidation of 'bamboo' multi-walled carbon nanotube modified basal plane pyrolytic graphite electrodes using TMPD, hexaammineruthenium (III) chloride and the ferricyanide redox systems**.** Note that the basal plane pyrolytic graphite electrode was allowed to aerial oxidise for 12 hours prior with the modification with MWCNTs. Also note that the MWCNTs as used had been exposed to air for a very long time (> weeks) so that the ends of the tube are likely fully oxygenated. Figure 6.9 shows the voltammetric response on the electrode transfer kinetics for A: ferricyanide, B: hexaammineruthenium (III) and C: TMPD. Inspection of the peak-to-peak separations (see Table 2) reveals fast heterogeneous charge transfer kinetics in all cases including that of the ferrocyanide/ferrocyanide couple.

Table 2: Comparison of the effect of the aerial oxidation of basal plane pyrolytic graphite and multi-walled carbon nanotube modified electrodes for various redox systems.

Redox System	Basal Plane[1]	Edge Plane	MWCNTs
$[Ru(NH_3)_6]^{3-}$	68 mV	71 mV	66 mV
TMPD	62 mV	66 mV	78 mV
	62 mV	66 mV	53 mV
$[Ir(Cl)_6]^{3-}$	78 mV	83 mV	-
$[Fe(CN)_6]^{3-/4-}$	596 mV	99 mV[2]	66 mV

1. After maximum aerial oxidation (120 mins)
2. After 3 hrs aerial oxidation

TMPD: *N,N,N',N'*-tetramethyl-p-phenylenediamine

It is established that for most cases of MWCNTs electrocatalysis arises due to the electron transfer at the tube ends. On the other hand in a few cases, notably the oxidation of hydrazine[20] the catalysis arises due to the presence of metal (iron) oxide impurities in the CNTs which act as nano-particulate centers for redox activity electrically 'wired' via the CNTs. To verify that this was not the case for the MWCNT catalyzed electron transfer kinetic in respect of the $Fe(CN)_6^{3-/4-}$ couple the response of an iron (II) oxide and an iron (III) oxide 'film' modified basal plane pyrolytic graphite electrode was explored. Figure 6.10A shows the comparison of the bare basal plane (dashed line) and an iron (II) oxide 'film' modified basal plane electrode (solid line) while Figure 6.10B compares an iron (III) oxide 'film' modified basal plane electrode with a bare basal plane pyrolytic graphite electrode (dotted) The peak-to-peak separation has increased from 278 mV (bare basal) to 160 mV at the iron (II) oxide modified electrode while using iron (III) oxide the peak-to-peak separation has decreased from 256mV (bare basal) to 112 mV, indicating in both cases that the iron oxide partly catalyses the heterogeneous kinetics of $Fe(CN)_6^{3-/4-}$. Furthermore it is

interesting to note that SWCNTs used by Gooding *et al*[10] were fabricated with an iron catalyst. We presume that this occurs at the ends of the MWCNTs that have fully reacted with oxygen since they have been exposed to air for a considerable period. It appears that fast kinetic are seen for oxygenated MWCNTs as well as SWCNTs.

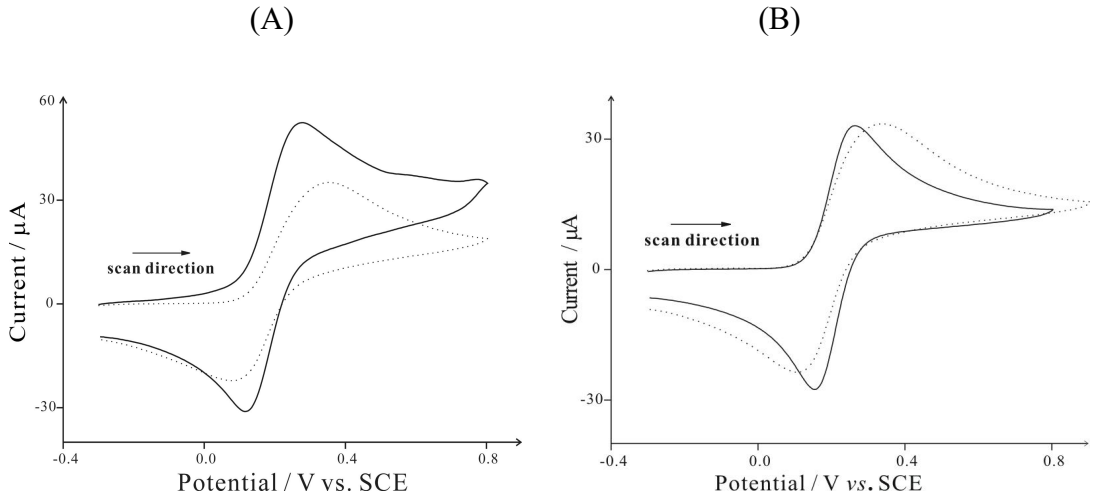


Figure 6.10 The cyclic voltammetric response of 1 mM ferrocyanide in 0.1M KCl at a bare basal plane pyrolytic graphite electrode (dashed line) for an (A) iron (II) oxide 'film' modified basal plane pyrolytic graphite electrode. B shows the response of an iron (III) oxide 'film' modified basal plane pyrolytic graphite electrode compared to a bare basal plane pyrolytic graphite electrode (dashed line) Both scans recorded at 100 mVs^{-1}

Cleary there is contrasting behaviour between highly ordered pyrolytic graphite and single walled carbon nanotubes[10] where in the later, the oxygenated functionalities (carboxylic acid moieties) speed up the heterogeneous charge transfer kinetics. Similarly the MW-CNTs even after long term exposure to air show rapid electrochemical charge transfer in respect of the ferri- / ferro- cyanide couple. We propose therefore that the structural differences between the graphite and the CNTs may change the nature of the functional groups formed by reaction of oxygen with edge plane and edge plane- like sites. In particular Gooding has provided[10] convincing evidence that carboxylated groups are formed at single walled carbon nanotubes.

Similar groups likely exist at the ends of MW-CNTs. In the case of graphite however, there is the possibility of linking between the sheets. For example peroxide formation might occur as shown in Figure11.

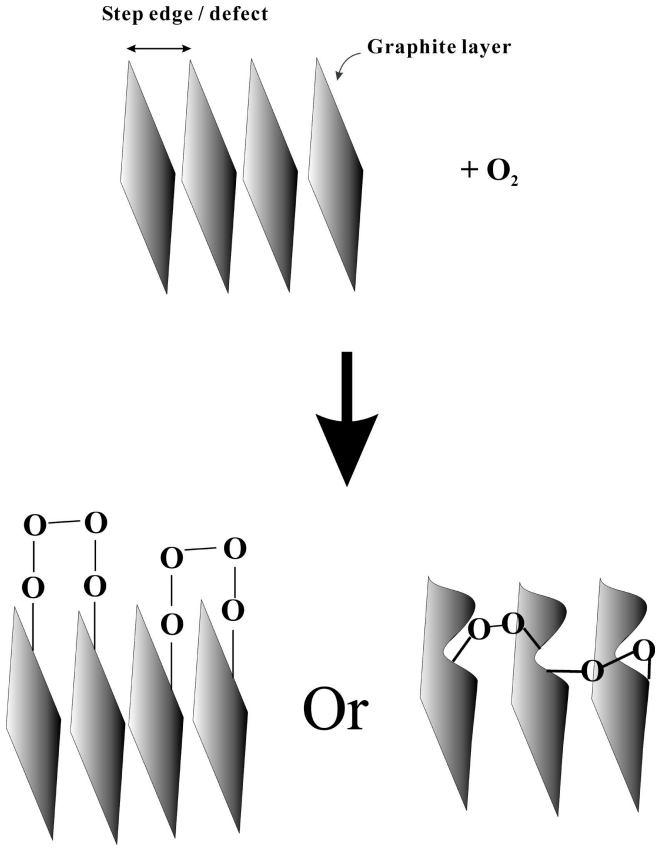


Figure 6.11 Schematic representation of the possible arrangement of oxygenated species at graphite planes of highly order pyrolytic graphite

Given that the intra-planar distance between the graphite sheets in pyrolytic graphite is 3.35 Å[12] and that typically the carbon – oxygen single bond length is 1.43 Å and that the oxygen – oxygen single bond length is 1.48 Å curvature of the graphite sheets is probably required if this happens. The contrasting behavior seen at multi-walled and single walled carbon nanotubes compared to pyrolytic graphite can be, in-part, explained in these terms. Multi-walled carbon nanotubes consist of a central tube of nanometric diameter surrounded by graphitic layers separated by ~ 3.4 Å,[21] Given

the rigid structure of carbon nanotubes it is unlikely that any curvature of the graphite planes at the carbon nanotubes can occur as in pyrolytic graphite and thus the carbon ends do not become capped in the same way as we surmise may happen in pyrolytic graphite. Peroxide formation as shown in Figure 11 is entirely speculative but might be a plausible first step leading subsequently to phenol and/or carbonyl groups. Formation of carboxylate groups is unlikely to be quick or easy.

6.4 Conclusions

The effect of aerial oxidation has been explored at basal plane and edge plane pyrolytic graphite electrodes with the effect on heterogeneous charge transfer explored with several common redox probes. Aerial oxidation is found to influence the charge transfer of the 'inner sphere' ferro/ferri cyanide redox couple while it has little effect on the 'outer sphere' redox systems, namely potassium hexachloro-iridate (III), hexaammineruthenium (III) chloride, and TMPD. Complimentary XPS analysis confirms that oxygenated carbon species are formed on the graphite surface. The aerial oxidation of bamboo multi-walled carbon nanotubes are also explored in light of recent reports that the presence of oxygenated carbon species increase the charge transfer of the ferri/ferro cyanide redox couple at single-walled carbon nanotubes.[10]

Contrasting behaviour is seen between highly ordered pyrolytic graphite and single walled carbon nanotubes[10] where in the later, the oxygenated functionalities (carboxylic acid moieties) speed up the heterogeneous charge transfer kinetics. We propose that that there is the possibility of peroxide or other linkages forming between graphite sheets in pyrolytic graphite which result in the carbon ends becoming capped and unable to participate in electron transfer. However, for multi-walled carbon nanotubes, given that the interlayer spacing is ~ 3.4 Å it is highly unlikely that any curvature of the

graphite planes at the carbon nanotubes can occur due to the more rigid structure. Thus the carbon ends do not become capped in the same way as we surmise may happen in pyrolytic graphite.

6.5 References

(1) R. L. McCreery, *Electroanalytical Chemistry*, Marcel Dekker, New York, 1990

(2) K.K. Cline, M.T. McDermott, R.L. McCreery, *J. Phys. Chem.* **1994**, *98*, 5314-5319.

(3) P. Chen, M.A. Fryling, R.L. McCreery, *Anal. Chem.* **1995**, *67*, 3115.

(4) N. Sinkaset, A.M. Nishimura, J.A. Pihl, W.C. Trogler, *J. Phys. Chem. A* **1999**, *103*, 10461.

(5) Q. Chen, G.M. Swain, *Langmuir* **1998**, *14*, 7017.

(6) P.L. Runnels, J.D. Joseph, M.J. Logman, R.M. Wightman, *Anal. Chem.* **1999**, *71*, 2782.

(7) T.J. Davies, R.R. Moore, C.E. Banks, R.G. Compton, *J. Electroanal. Chem.* **2004**, *574*, 123.

(8) C.A. McDermott, K.R. Kneten, R.L. McCreery, *J. Electrochem. Soc.* **1993**, *140*, 2593.

(9) S. Ranganathan, T.-C. Kuo, R.L. McCreery, *Anal. Chem.* **1999**, *71*, 3574.

(10) A. Chou, T. Bocking, N.K. Singh, J.J. Gooding, *Chem. Commun.* **2005**, 842.

(11) R.R. Moore, C.E. Banks, R.G. Compton, *Anal. Chem.* **2004**, *76*, 2677-2682.

(12) C.E. Banks, T.J. Davies, G.G. Wildgooses, R.G. Compton, *Chem. Commun.* **2004**, *7*, 829-841.

(13) T.J. Davies, M.E. Hyde, R.G. Compton, *Angewandte Chemie* **2005**, *117*, 5251-5256.

(14) C.E. Banks, R.R. Moore, T.J. Davies, R.G. Compton, *Chem. Commun.* **2005**, *16*, 1804-1805.

(15) E.R. Lowe, C.E. Banks, R.G. Compton, *Anal. Bioanal. Chem.* **2005**, *382*, 1169.

(16) R. Bowling, R.T. Packard, R.L. McCreery, *Langmuir* **1989**, *5*, 683-688.

(17) J.C. Curtis, T.J. Meyer, *Inorg. Chem.* **1982**, *21*, 1562-1571.

(18) Http://srdata.nist.gov/xps/,

(19) Http://www.uksaf.org/,

(20) C.E. Banks, A. Crossley, C. Salter, S.J. Wilkins, R.G. Compton, *Angewandte Chemie In Press*

(21) C.N.R. Rao, B.C. Satishkumar, A. Govindaraj, M. Nath, *ChemPhysChem* **2001**, *2*, 78.

CHAPTER 7

Edge Plane Sites on Highly Ordered Pyrolytic Graphite as Templates for Making Palladium Nanowires via Electrochemical Decoration

In this chapter, an approach for the fabrication of metal nanowires is presented. Palladium wires with diameters less than 50 nm were produced by electrochemical decoration of step edge sites on the surface of highly ordered pyrolytic graphite via the following three steps. A merit of this approach is that it allowed metal nanowires to be fabricated without the simultaneous formation of nanoparticles on the basal plane terraces in contrast to other studies of this type. The mesoscopic palladium wires are shown to be useful for the electrochemical sensing of hydrazine. This work discussed in this chapter has been published as an article in *J. Phys. Chem. B*, **2006**, 110, 22306.

7.1 Introduction

Nano-sized materials have become the focus of intensive research due to their fascinating electronic, mechanical and chemical properties. Recognition of their wide potential applications in areas ranging from semiconductors, molecular computing, sensors, nanoelectronics and energy storage have rapidly promoted research in these areas.[1,2] Mesoscopic materials such as nanoparticles, nanowires and nanotubes are generally defined as nanostructures with one-dimension between 1 nm and 100 nm.[3-6]

They have a high surface-to-volume ratio and offer novel electron transfer properties.[1,7-10]

So as to implement nano materials in real world applications, it is desirable to develop new techniques to produce nanowires and nanoparticles particularly with more controllable and uniform sizes. Hitherto, as regards nanowires, several fabrication approaches including template synthesis, electrochemical deposition, laser assisted catalytic growth, solution-phase reactions have been developed.[11-17] All have various merits but in this report we concern ourselves with electrochemical deposition. This is a powerful technique for the deposition of many metals since it is rapid and facile allowing easily control of the nucleation and growth of metal nanoparticles and nanowires.[18] It can provide an attractive route for producing metal nanowires in the pores of suitable templates imparting size control.[19,20] Thurn-Albrecht *et al.* have obtained vertical arrays of cobalt nanowires by direct current electrodeposition using arrays of nanopores as templates.[21] Additionally, note that varying the electrochemical potential can switch the balance of the rates of atom deposition and dissolution so careful control of the electrochemical parameters are required in order to create nanowires rather than nanoparticles.[22,23] Penner and coworkers[23] have used *direct* electrodeposition to grow palladium mesowire arrays with diameters ranging from 50 to 300 nm on highly ordered pyrolytic graphite (HOPG) surfaces and successfully applied them for hydrogen analysis. In their subsequent studies, they found that the size-selective electro-deposition of metal nanoparticles and nanowires could be obtained using step edge decoration on HOPG. However, it was impossible to prepare narrower noble metal nanowires without producing nanoparticles on the basal plane sites.[24]

7.2 Experimental

7.2.1 Chemicals

Palladium (II) chloride (Aldrich, 99%), sodium sulphate (Aldrich, 99%), hydrazine (Aldrich, 99%) and sulfuric acid (BDH, 98%) were purchased at the highest grade available and used directly without further purification. Aqueous electrolyte solutions were prepared with KCl (99.5%) (Aldrich) using ultrapure water from an Vivendi UHQ grade water system (Vivendi, UK) with a resistivity of not less than 18.2 MΩ cm^{-1}. All the solutions were degassed with oxygen-free nitrogen (BOC Gases, Guildford, Surrey, UK). All experiments were carried out at a temperature of 295 ± 3 K.

7.2.2 Instrumentation

Electrochemical experiments were performed using a μ-Autolab type II potentiostat (Eco-Chemie, Utrecht, Netherlands) controlled by General Purpose Electrochemical Systems v.4.7 software. For all electrochemical experiments, the working electrode used was a highly oriented pyrolytic graphite slab (HOPG, 4.9 mm diameter, SPI supplies). The HOPG electrode was fabricated by attaching the HOPG slab to a mild steel plate using a sliver epoxy with PTFE sheath, which improve the reproducibility of electrochemical experiments. The counter electrode was a platinum wire, with a saturated calomel reference electrode (Radiometer, Copenhagen, Denmark) completing the circuit.

The basal plane HOPG electrode was prepared by first disassembling the electrode housing and taking the HOPG slab out. The slab was renewed by pressing cellotape on the slab surface to get rid of general attached graphite layers. This was repeated several times until a shiny and smooth electrode surface was observed and the electrode was then placed back in the housing for further experiments.

AFM measurements were performed in a Digital Instruments MultiMode SPM operating in contact mode. A scanner (type 'J') with *x* and *y* limits of 125 μm and a *z* limit of 6 μm and standard silicon nitride tip (type 'NP') (supplied by Digital Instruments) with a force constant of approximately 0.32 NM^{-1} were used. Scans were collected at a scan rate of 1 Hz. Optical images were obtained using a microscope based on a SONY XC-999P CCD camera.

STM tips were prepared by electrochemical etching of tungsten wire (0.25 mm, Agar Scientific) in 2 M NaOH and coated with apiezon wax or mechanically from 0.25 mm diameter Pt : Ir (80 : 20) wire. Since molecular-scale STM resolution is highly tip-dependent, only those tips which gave well defined, stable images were used. STM experiments were carried out with a Molecular Imaging Pico STM (Model MS300) with a "D" or "A" scanner in conjunction with a Nanoscope IIIa controller (Digital Instruments). Imaging was carried out at room temperature in air. Images presented here were subject to a first-order flattening program.

7.3 Results and Discussion

7.3.1 Fabrication of Palladium Wires Produced by Electrochemical Decoration

In this chapter we have electrochemically *exclusively* deposited palladium nanowires on the step edge sites on the highly ordered pyrolytic graphite surface without nanoparticle formation and explored these mesoscopic palladium wires for the electrochemical oxidation of hydrazine. By a three-step procedure designed to activate the step edges, palladium nanowire growth was accomplished in the following way. First an electrochemical activation step was used to oxidize the edge plane sites and defects on highly ordered pyrolytic graphite surfaces. Second, a potential cycling step was applied to form palladium oxide (s) and/or complexes of Pd on the step edges.

Third Pd nanowires were formed by electro-reduction. An increased height of step edge sites was observed following electrochemical oxidation (step 1). This is likely due to surface functional groups such as quinoid, carbonyl and carboxyl being introduced.[25] The diameters of the continuous Pd nanowires produced on these activated graphite sites, as estimated from atomic force microscopy (AFM) images, ranged from 41 to 50 nm with a high degree of uniformity along the step edges. This approach could allow various metal nanowires to be fabricated without the simultaneous formation of nanoparticles on the basal plane terraces.

The strategy of decorating HOPG with palladium wires is adapted from the methodology initially reported by Guo and Li[26] for single-walled carbon nanotubes. This involves the following three steps:

i) Electrochemical oxidation activation of the edge plane sites and defects on HOPG via potential cycling from + 1.8 V to – 0.4 V (all vs. SCE) at 200 mV s^{-1} for 10 cycles in 0.5 M Na_2SO_4. This step probably introduces oxygen containing functional groups on the surface of the HOPG (see below).

ii) The electrode is transferred into a 1 mM $PdCl_2$ solution in 0.1M H_2SO_4 with potential cycling from + 0.4 to + 1.5 V for 5 cycles at 200 mV s^{-1}. This is thought to produce palladium oxide (s) and/or complexes of Pd on the step edge and defect sites of HOPG at various oxygen containing functional groups.

iii) Formation of Pd wires is brought along by transferring the modified electrode into 0.1 M H_2SO_4 and potential cycling from + 1.1 V to – 0.5 V at a scan rate of 300 mVs^{-1} for 5 scans.

7.3.2. Investigation of Decoration with Atomic Force Microscopy

Figure 7.1 shows schematically the growth of Pd nanowires using the three-step electrochemical decoration sequence as described above.

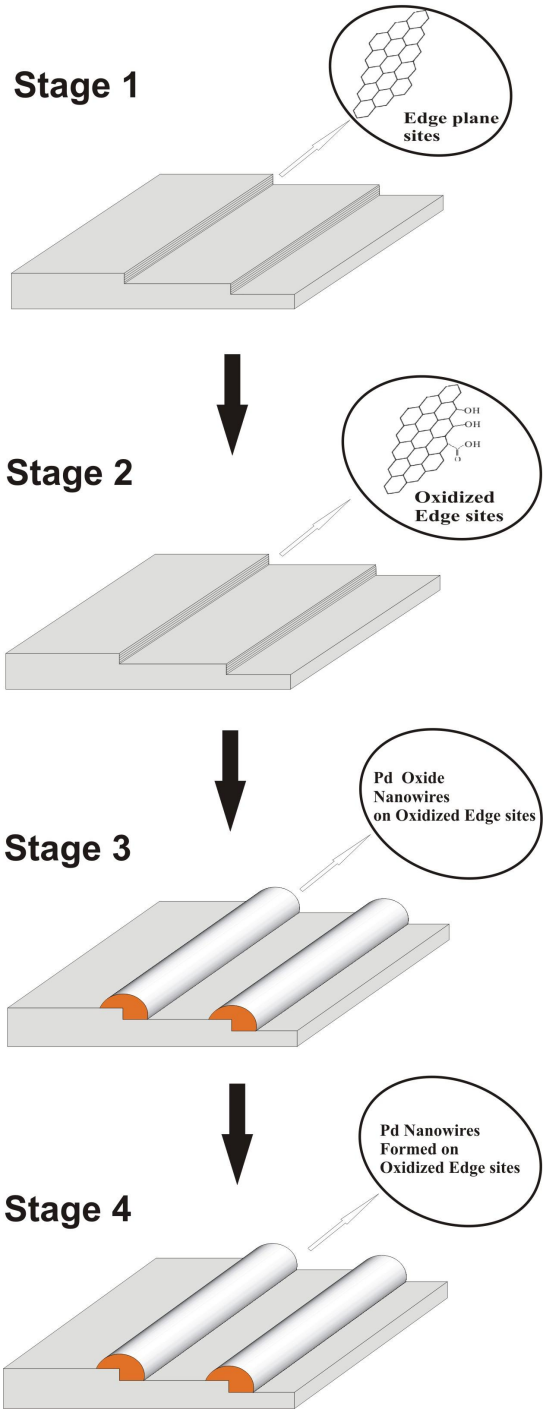


Figure 7.1 Schematic diagram of three electrochemical decoration steps to produce padllium nanowires

The Pd mesoscopic wires were investigated using a Digital Instruments MultiMode SPM operating in contact mode. An overview AFM image is presented in Figure 7.2a, showing that these wires are exclusively formed along the step edge sites on HOPG and ranged from 41 to 52 nm in diameter. In the following high resolution of AFM micrographs (Figure7.2b-d), it can be clearly seen that Pd wires formed exclusively on the step edges whilst no Pd nanoparticles or wires were found on the basal plane sites.

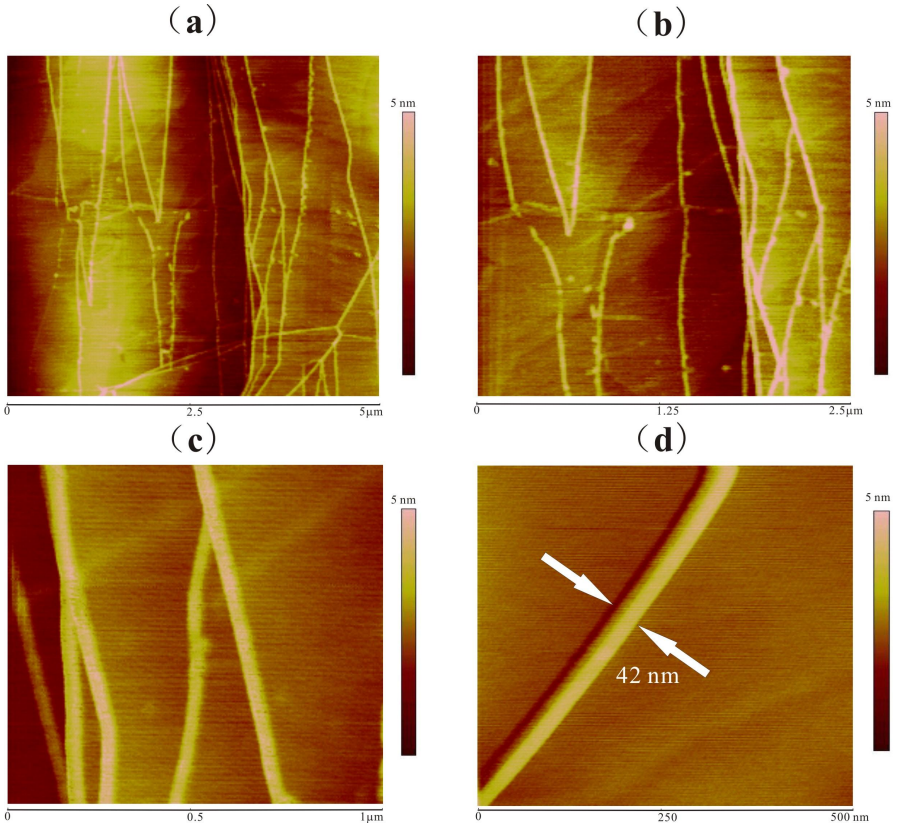


Figure 7.2 AFM micrographs of Pd nanowires grown along the edge plane on the graphite surfaces. (a-d) in different ranges

Figure 7.3 shows a three dimensional AFM micrograph of one Pd nanowire. Penner and his coworkers have demonstrated that direct metal electrodeposition at large overpotentials results in instantaneous nucleation and these non-selective metal nuclei are formed at the basal plane and edge plane sites on the graphite surfaces.[27,28] In previous works, Metal nanowire growth was always accompanied with the formation of

particles on the graphite surface using the electrodeposition method. It was found that the formation of metal particles could be reduced but not eliminated by the application of a nucleation pulse, which promoted nanowire formation on edge plane sites.[24] In our experiments, no Pd nanoparticles were observed on the basal plane. The electrochemical oxidation of the edge plane sites is necessary for the ready growth of nanowires at the edge sites.[29]

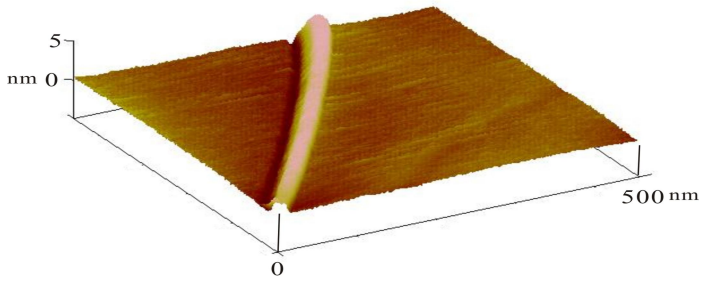


Figure 7.3 A three-dimensional AFM image of one Pd mesoscopic wire on the graphite surface.

For electrochemistry, the edge plane on the graphite typically shows faster electron transfer kinetics than the basal plane for a range of redox couples, shown by Figure 7.4 detailing the voltammetric profiles recorded using the ferricyanide redox couple where the edge plane and basal plane pyrolytic graphite electrodes exhibit significant differences of electrochemical responses.[30] According to previous work,[26,29] the first step, the electrochemical decoration of the graphite surface, is likely to produce oxygen containing functional groups such as carbonyls and hydroxyls at the step and defect sites, where the affinity at the edge plane sites of Pd atoms could be increased and subsequently facilitate nucleation processes. Thus the nucleation of Pd likely occurs selectively at step edges present on the HOPG surface.

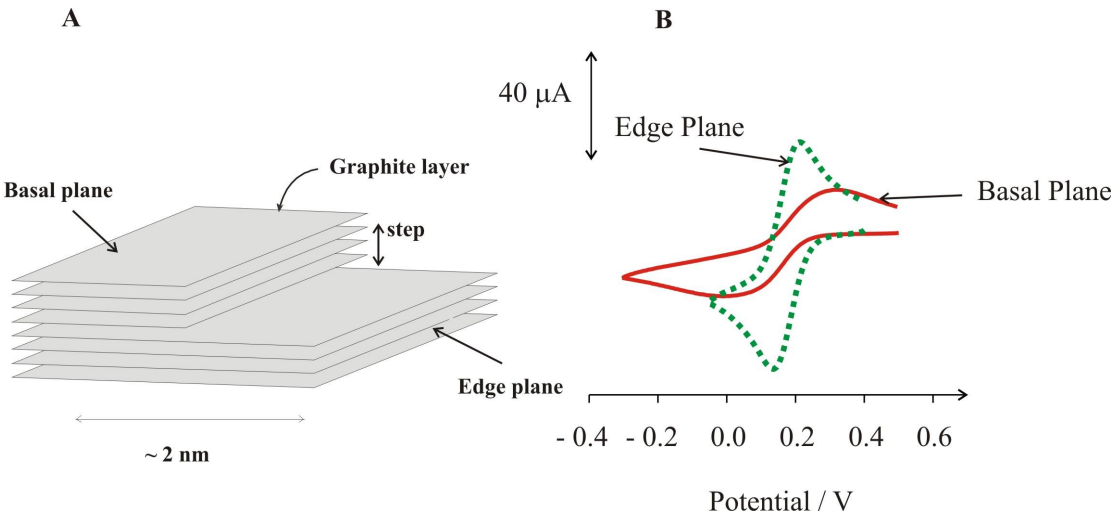


Figure 7.4 A schematic diagram (a) of a six-layer step edge and Cyclic voltammograms (b) obtained from bppg and eppg electrodes (4.9 mm diameter) for the reduction of 1 mM ferricyanide (in 0.1M KCl). All are recorded at a scan rate of 100 mV s^{-1}.

7.3.3 Investigation of Decoration with Scanning Tunneling Microscopy

Next, we provide direct evidence of the oxidation of edge-plane-like defect sites by observing this exit-situ process using scanning tunneling microscopy (STM). Topographical STM images of the surface before and after the electrochemical modification procedure (step 1) are presented (see Figure 7.5). It can be clearly seen from these images that the step edge is no longer rectangular and on the contrary becomes more circular. The increase of step edge height was achieved with corresponding cross section analysis using scanning probe image processor version 4.3.2 (Image Metrology). A line scan analysis of step height on HOPG surface before any experiment has an order of ca. 3.33 Å (see Figure 7.6a), in good agreement with the reported value of the interplanar distance between the graphite sheets in pyrolytic graphite, 3.35 Å.[30] However, after electrochemical oxidation activation step in 0.5 M Na_2SO_4 the step height has increased to 5.15 Å, shown from a line scan analysis across the step (in supporting information Figure 7.6).

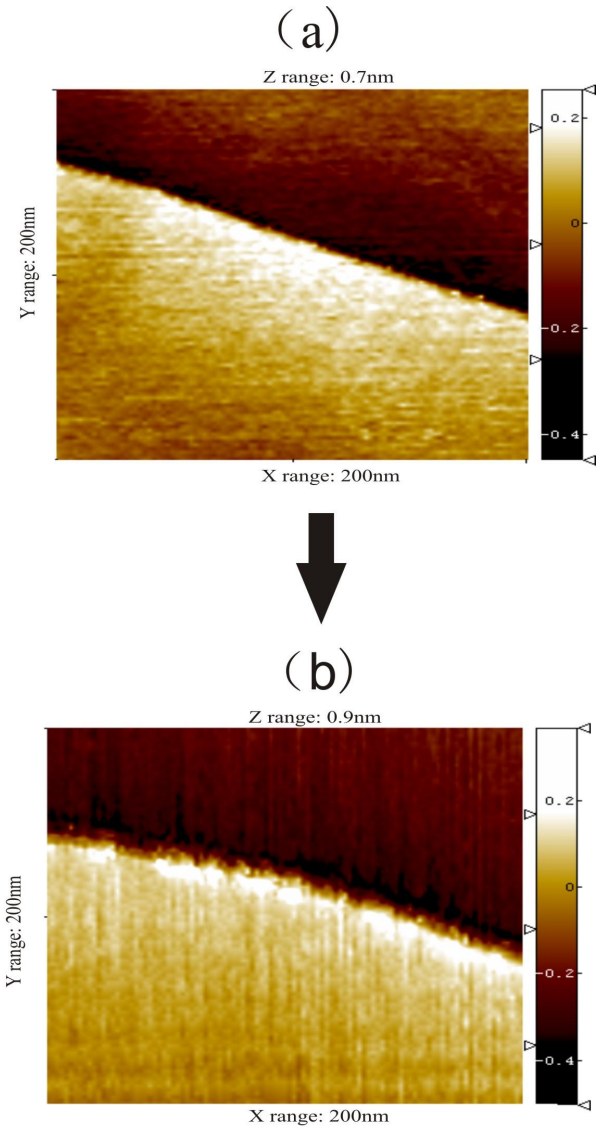


Figure 7.5 Topographical STM images of changes of graphite surfaces before (a) and after (b) the electrochemical decoration procedure

The distance between the graphite layers has lifted by ca 1.8 Å, resulting in a "round"-like shape at the edge. Note that the width of this edge, measured over step defects also increases. Since analysis of the step height and width both showed an obvious increase this suggests that functional groups corresponding to quinoid, carbonyl and/or carboxyl groups resulting from the electrochemical oxidation are introduced. These likely modify graphitic surfaces by changing the surface structures of

these edge-plane-like defect sites and thus increase the nucleation density of metal along the step edge.

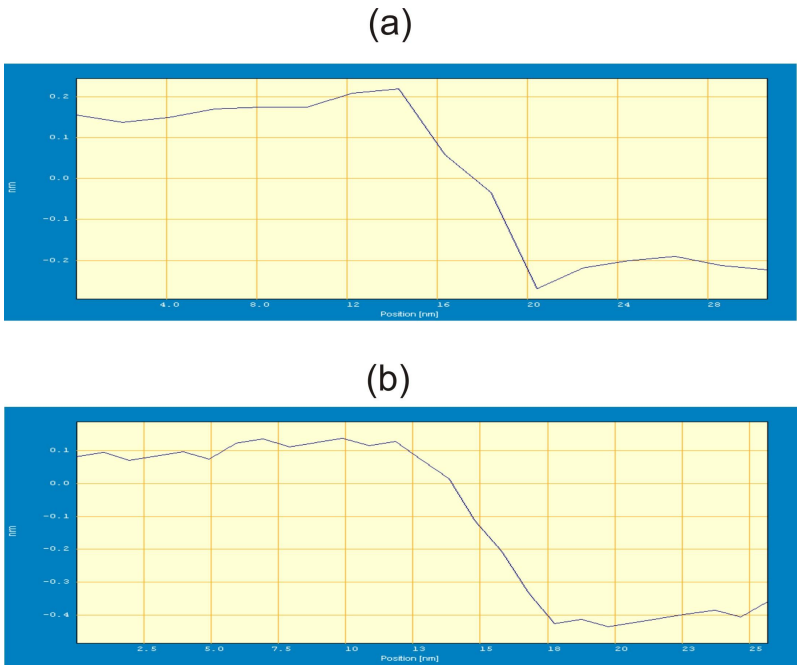


Figure 7.6 A line scan analysis of the AFM image of a step defect on a HOPG crystal taken before (a) and after (b) the electrochemical decoration

Then the influence of Pd concentration for producing nanowires using the electrochemical decoration was briefly explored. The concentration of $PdCl_2$ in the second step was changed to 0.1 mM, ten time less in comparison with that of original solution (1 mM). We continue to employ the other experimental conditions as above mentioned. Figure 7.7 details the AFM image of Pd 'nanowires' grown along the decorated step edge on the graphite surfaces. It is interesting to note that after the decreased concentration of Pd the nanowires produced from higher concentration have been replaced by almost continuous lines of nanoparticles. It is reasonable to assume that the number of metal nuclei along step edges decreases with the dilution of Pd(II) solution, leading to the formation of the "beaded nanowires".

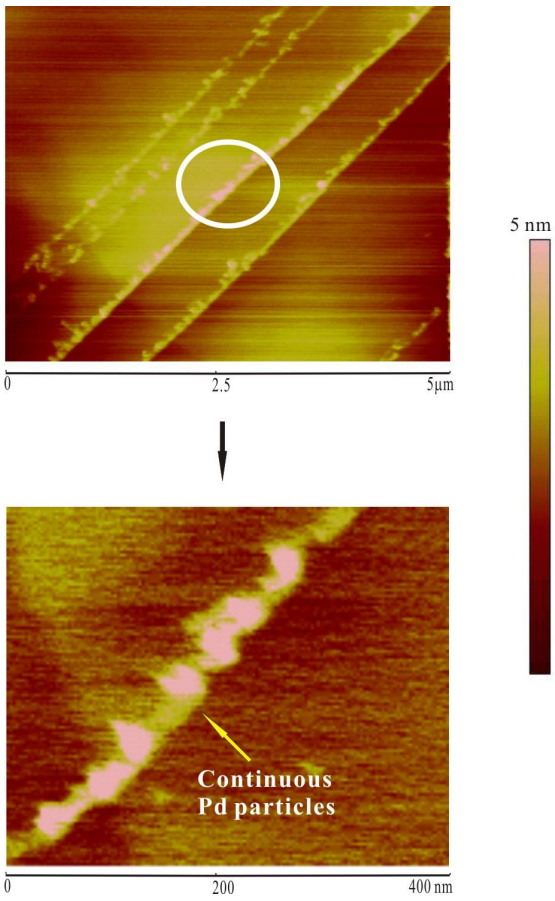


Figure 7.7 AFM micrographs of Pd nanoparticles grown along step edges.

7.3.4 Voltammetric Responses of Hydrazine on Pd Nanowires

The electroanalytical use of the palladium nanowires for hydrazine sensing was next investigated. Figure 7.8 shows the linear sweep voltammetric response obtained at a Pd nanowire modified HOPG electrode in a solution of 1 mM hydrazine in 0.1 M phosphate buffer (pH 7). The overlaid line is the response obtained from the bare HOPG electrode. A large characteristic voltammetric profile is observed at *ca*. + 0.04 V (vs. SCE) which is in good agreement with literature reports[31], showing the possible analytical uses. The electrochemical oxidation of hydrazine at metallic surfaces can be described by the following [31]

$$N_2H_5^+ - 4e^- \rightarrow N_2 + 5H^+ \qquad (1)$$

Note that hydrazine oxidation potential on Pd nanowires in comparison with that obtained at a Pd macro-electrode is shifted more positive,[31] indicating that the electrochemical process on Pd wires is shifted electrochemically more irreversible, resulting from the nanowires, which will have a faster mass transport regime than a Pd macroelectrode.[32]

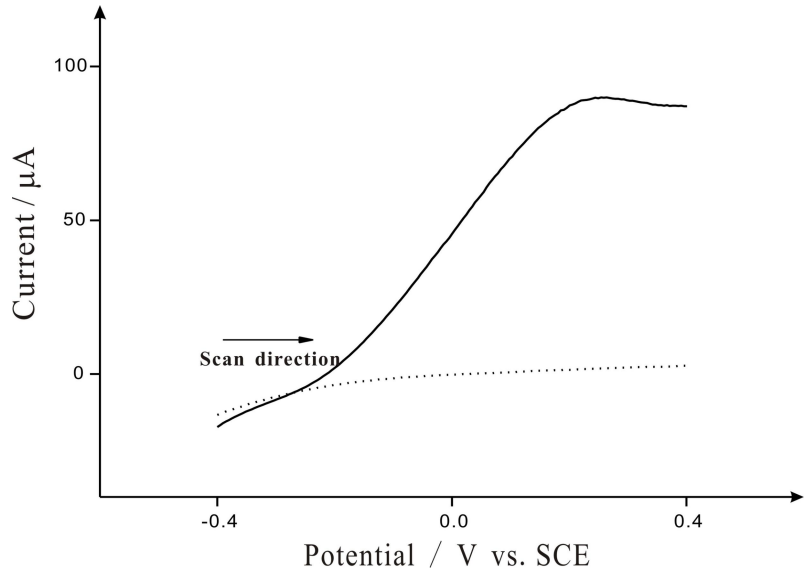


Figure 7.8 Linear sweep voltammograms of 1 mM hydrazine recorded at a palladium nanowires modified HOPG electrode in a pH 7 buffer solution at a scan rate of 100 mV s^{-1}. The overlaid voltammogram corresponds to the response of bare HOPG electrode.

7.4 Conclusion

In summary, we here described a method for preparing arrays of metal nanowires. Pd nanowires were obtained by selectively using a three-step electrochemical decoration procedure of the step edges on highly ordered pyrolytic graphite surfaces. The merit of this method is that it allowed the fabrication of nanowires without the simultaneous formation of nanoparticles on the basal plane terraces. Finally, the electrochemical oxidation of hydrazine was explored on these mesoscopic palladium wires showing the analytical potential of nano-wire arrays.

7.5 References

(1) Ramirez, J. P.; Vigeland, B. *Angew, Chem. Int. Ed.* **2005**, *44*, 1112.

(2) Pease, R. F. *in "Nanostructures and Mesoscopic Systems," Academic, New York* **1992**.

(3) Pan, Z. W.; Dai, Z. R.; Wang, Z. L. *Science.* **2001**, *291*, 1947.

(4) Patzke, G. R.; Krumeich, F.; Nesper, R. *Angew, Chem. Int. Ed.* **2002**, *41*, 2446.

(5) Cushing, B. L.; Kolesnichenko, V. L.; O'Connor, C. J. *Chem. Rev.* **2004**, *104*, 3893.

(6) Fang, X. S.; Ye, C. H.; Zhang, L. D.; Xie, T. *Adv. Matter.* **2005**, *17*, 1661.

(7) Tremel, W. *Angew, Chem. Int. Ed.* **1999**, *38*, 2175.

(8) Wu, Y.; Yan, H.; Huang, M.; Messer, B.; Song, J. H.; Yang, P. *Chem. Eur. J.* **2002**, *8*, 1260.

(9) Janata, J.; Josowicz, M. *Nature. Mater.* **2003**, *2*, 19.

(10) Xia, Y.; Yang, P.; Sun, Y.; Wu, y.; Mayers, B.; Gates, B.; Yin, Y.; Kim, F.; Yan, H. *Adv. Matter.* **2003**, *15*, 353.

(11) Martin, C. R. *Science.* **1994**, *266*, 1961.

(12) Liu, Z. P.; Yang, Y.; Liang, J. B.; Hu, Z. K.; Li, S.; Peng, S. *J. Phys. Chem. B.* **2000**, *107*, 12658.

(13) Zhang, Z. B.; Sun, X. Z.; Dresselhaus, M. S.; Ying, J.; Heremans, J. *Phys. Rev. B.* **2000**, *61*, 4850.

(14) Cui, Y.; Lieber, C. *Science.* **2001**, *291*, 851.

(15) Molares, M. T.; Buschmann, V.; Dobrev, D.; Neumann, R.; Scholz, R.; Schuchert, I. U. *Adv. Matter.* **2001**, *13*, 62.

(16) Monson, C. F.; Wolley, A. T. *Nano. Lett.* **2003**, *15*, 303.

(17) Chang, Y.; Lye, L. M.; Zeng, C. H. *Langmuir.* **2005**, *21*, 3746.

(18) Welch, C. M.; Compton, R. G. *Anal. Biochem.* **2006**, *384*, 601.

(19) Almawlawi, D.; Liu, C. Z.; Moskovits, M. *J. Phys. Chem. B.* **1994**, *9*, 1014.

(20) Sun, L.; Searson, P. C.; Chien, C. L. *Appl. Phys. Lett.* **1999**, *74*, 2803.

(21) Thurn-Albrecht, T.; Schotter, J.; Kastle, G. A.; Emley, N.; Shibauchi, T.; Krusin-Elbaum, L.; Guarini, K.; Black, C. T.; Tuominen, M. T.; Russell, P. *Science.* **2000**, *290*, 2126.

(22) Schmickler, W. *Interfacial Electrochemistry, Oxford University Press, New York, NY.* **1996**.

(23) Favier, F.; Walter, E.; Zach, M. P.; Benter, T.; Penner, R. M. *Science.* **2001**, *293*, 2227.

(24) Penner, R. M. *J. Phys. Chem. B.* **2002**, *106*, 3339.

(25) Bjelica, L., J.; Jovanovic, L. S. *Electochim. Acta.* **1992**, *37*, 371.

(26) Guo, D. L.; Li, H., L. *J. Coll. Int. Sci.* **2005**, *286*, 274.

(27) Nyffenegger, R. M.; Craft, B.; Shaaban, M.; Gorer, S.; Penner, R. M. *ChemPhysChem.* **1998**, *10*, 1120.

(28) Zoval, J. V.; Lee, J.; Gorer, S.; Penner, R. M. *J. Phys. Chem. B.* **1998**, *102*, 1166.

(29) Walter, E.; Murray, B. J.; Favier, F.; Kaltenpoth, G.; Grunze, M.; Penner, R. M. *J. Phys. Chem. B.* **2002**, *106*, 11407.

(30) Banks, C. E.; Davies, T. J.; Wildgoose, G. G.; Compton, R. G. *Chem. Commun.* **2004**, *7*, 829.

(31) Batchelor-McAuley, C.; Banks, C. E.; Simm, A. O.; Jones, T. G. J.; Compton, R. G. *Analyst.* **2006**, *131*, 106.

(32) Davies, T. J.; Banks, C. E.; Compton, R. G. *J. Solid. State. Electrochem.* **2005**, *9*, 797.

CHAPTER 8

"Instantaneous" Growth of Cobalt Nanoparticles on Boron-doped Diamond Electrodes

In situ Atomic Force Microscopy (AFM) is used to study in situ the growth of cobalt nuclei on a boron doped diamond electrode under potentiostatic control. The rate of growth of the nuclei at the electrode surface is monitored using AFM as a function of time at different deposition potentials. The nucleation of cobalt nuclei is found to be apparently "instantaneous" and the growth of the nuclei is shown to be kinetically rather than diffusionally controlled over periods of tens and hundreds of seconds. At very short times (<10 seconds) the kinetics of nucleation are apparent. This work discussed in this chapter has been published as an article in *ChemPhysChem*, **2006**, 7, 704.

8.1 Introduction

The electro-deposition of metals is an area of intense interest due to its significant technological importance in respect of electroplating and electrowinning of metals. Fundamental studies interpret the deposition process in terms of nucleation followed by growth and the scientific area generally relies on the use of current transient analysis, with for example the current generated by an applied potential being examined, for

determining nucleation rates, saturation nucleus densities and steady-state growth rates. Such an approach in the hands of experts can yield considerable insights but nevertheless is inherently strongly model dependent and as such any conclusions can rarely be unambiguous.

We recently showed[1] that in-situ atomic force microscopy (AFM) can be used to *directly* study the growth of individual nuclei and the rates at which they appear as a function of time and applied potential allowing the assumptions of the various models employed in the analysis of potentiostatic current transients to be tested in an independent manner. A limitation of this method is the requirement for very flat electrode surfaces to be examined and this restriction had previously largely limited the application of AFM in the area of metal deposition to the study of under potential deposition of adatoms on the surfaces of single crystals. However we were able to show that samples of polycrystalline boron doped diamond could be prepared with the necessary degree of flatness and were suitable substrates for in situ studies of bulk metal deposition.

Our initial studies focussed on the growth of lead nuclei on boron doped diamond electrodes[1]. So called progressive nucleation was observed with the number of active nuclei increasing with time. Such a concept arises as a limit from the commonly made but not uncriticised[2,3] assumption that the number of nuclei as a function of time is given by an equation of the type

$$N(t) = N(\infty)[1 - \exp(-At)] \qquad (8.1)$$

where $N(\infty)$ is the total number of active sites and A is a constant activation rate of sites[4-8]. Depending on the magnitude of A the limits of progressive and instantaneous nucleation arise with the latter corresponding to a large enough value of A so that the

number of nuclei on the surface “immediately” attains the value of N(4) following the a application of a potential of suitable magnitude. However equation (1) has been ferociously criticised by Fletcher [2,3] as being inherently unphysical since it neglects non-steady state effects caused by rapid changes in driving force. In particular Fletcher[9] asserts that there is sufficient experimental evidence derived from the deconvolution of current transients to conclude that “instantaneous nucleation does not exist.” In particular he stresses that the nucleation rate does not switch on and off at the same moment as the electrode potential switches on and off but that rather the nucleation rate always lags behind changes in the overpotential since a finite time must elapse during which non steady state nucleation rates prevail.

In this chapter we use in situ atomic force microscopy to monitor in real time the nucleation and growth of cobalt nanoparticles on a boron doped diamond electrode surface. It will be seen that at first sight the process appears to have the characteristics of >instantaneous= nucleation in that the number of nuclei on the surface is constant throughout the experiment. However a closer inspection shows that at very short times (less than ca 10 seconds) the non steady state behaviour inferred indirectly by Fletcher in a limited number of other systems[9-12] is apparent: It is observed that nucleation rates control the cobalt deposition as endorsed both by AFM and current transient data. Nevertheless the value of the concept of “instantaneous nucleation” is seen to be an important limiting form of behaviour; beyond the initial few seconds the number of nuclei remains absolutely fixed so that the nucleation is indeed, when viewed from later times, effectively instantaneous.

8.2 Experimental

8.2.1 Chemicals

All reagents were of analytical grade and used without further purification. The reagents used were: boric acid (Aldrich, A.C.S Reagent, 99.5+%), magnesium sulphate (Aldrich, 99%) and cobalt(II) nitrate hexahydrate (Aldrich, A.C.S Reagent, 98+%). All solutions were prepared using water with a resistivity of not less than 18.2 MΩcm at 25 ^{o}C prepared using a Synergy water purification system (Millipore, UK). Solutions were degassed in oxygen free N_2 prior to all experiments.

8.2.2 Instrumentation

The working electrode was made of boron doped diamond. The prepolished BDD film (5 x 5 x 0.535 mm, resistance approximately 0.4 Ω), grown on graphite by chemical vapour deposition, was supplied by Element Six (Berkshire, UK). It was pressed into a PTFE mounting, and an electrical connection made to a metal stub on the rear of the mounting using silver loaded epoxy resin (RS). BDD was chosen as an electrode surface to be used in this study due to its extremely flat surface (having a height variation of only 5 nm over 5 x 5 μm areas). This property is extremely useful in distinguishing nuclei from the electrode surface. While glassy carbon has previously been used in voltammetric studies of cobalt nucleation[13] it is unsuitable for such a study using AFM due to its irregular and poorly reproducible surface.[1]

Experiments were performed in a Digital Instruments AFM fluid cell. The volume of the cell was kept to the minimum amount required to cover the working electrode surface and ensure contact between the 3 electrodes in the system, this was usually around 0.5 mL. The cell was placed on top of the working electrode which sat face up

on the AFM scanner head. The gap between the cell and the working electrode surface was sealed using a small rubber o-ring leaving around a 3mm diameter area of the working electrode surface exposed to the solution. The solution was added into the cell inlet using a small syringe, the counter electrode a platinum wire was coiled inside the input syringe. A small reservoir was placed at the cell outlet in which the saturated calomel reference electrode (SCE, Radiometer, Copenhagen, Denmark) was placed.

The microscope used was a Digital Instruments (Santa Babara, CA) Multimode SPM, operating in Contact Mode with a "J" scanner, having a lateral range of 125 x 125 μm and a vertical range of 5 μm. Standard silicon nitride probes having a force constant of approximately 0.58 nm^{-1} were used. Tapping mode is used in preference to contact mode for in situ electro deposition studies despite the better lateral resolution of contact mode imaging. As the force exerted between the tip and sample is greater using contact mode than using tapping mode, contact mode is found to "sweep" the surface clear of deposits[14]. As we have previously shown[1], tapping mode properly applied need not cause the same problem.

High-resolution scanning electron microscopy (SEM) imaging was performed using a Jeol JSM 6500F FEGSEM (Field effect gun). Energy dispersive X-ray detection (EDX) was used to obtain information about the composition of the sample. All samples were carbon coated prior to SEM analysis.

8.3 Results and Discussion

8.3.1 Voltammetric Response of Cobalt(II) at a BDD Electrode

In order to investigate the mechanism of the electrodeposition of metallic cobalt, first we examined the voltammetric response of cobalt(II) at a boron doped diamond electrode. Figure 8.1 shows the cyclic voltammogram (CV) obtained at a 3 mm

diameter BDD for a solution of 10 mM $[Co(H_2O_3)_6](NO_3)_2$ in 0.1 M $MgSO_4$ with 0.1M H_3BO_3 (pH = 5.48). It can be clearly seen that a sharply increasing cathodic current was observed at ca. -1.1V (vs. SCE), corresponding to the reduction of aqueous Co^{2+} to metallic Co at the electrode surface. An oxidation wave is also visible on the reverse scan at –0.3 V corresponding to the dissolution of solid metallic cobalt back into the solution.

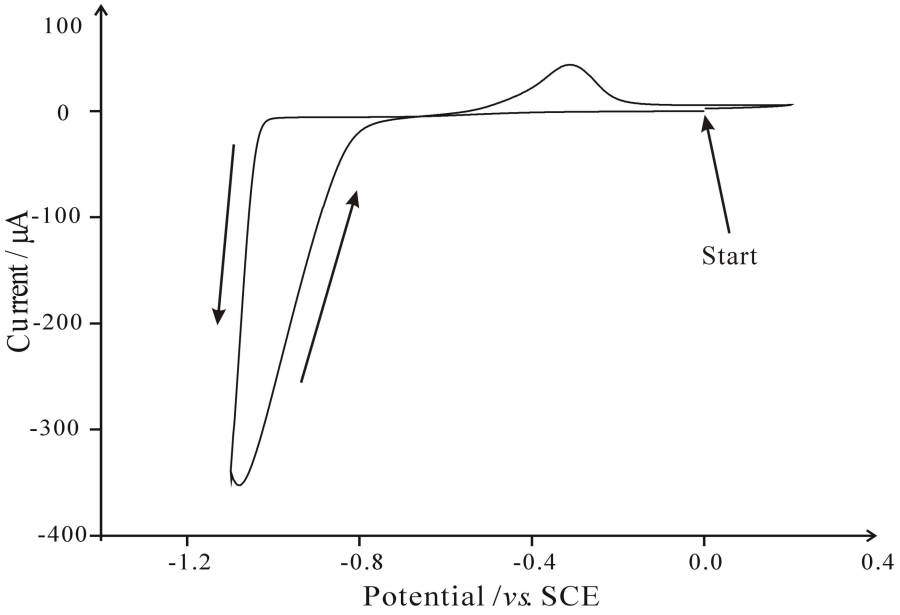


Figure 8.1 A cyclic voltammogram of a solution of 10 mM $[Co(H_2O_3)_6](NO_3)_2$ in 0.1 M $MgSO_4$ with 0.1M H_3BO_3 performed at 100 mV/s.

EDX analysis was then performed (Figure 8.2) on the electrode surface after deposition to confirm the depositing species was elemental cobalt. Figure 8.2 shows the presence of a large quantity of carbon, as would be expected at a carbon electrode surface. Large cobalt peaks can be seen confirming the presence of cobalt at the electrode surface, no other significant peaks were observed.

Using information gained from the cyclic voltammetric experiments different potentials were applied to clean BDD surfaces for one minute and the current recorded as a function of time in order to examine the nucleation of cobalt at the BDD surface.

Three potentials were chosen for analysis, these were –1.05 V, -1.1 V and –1.15 V. Figure 8.3 shows the current/time transients recorded at each of these potentials. It can be seen that initially the current rises from zero and then achieved a steady state after about 10s. The value of the steady state current is seen to increase with increasing potential applied.

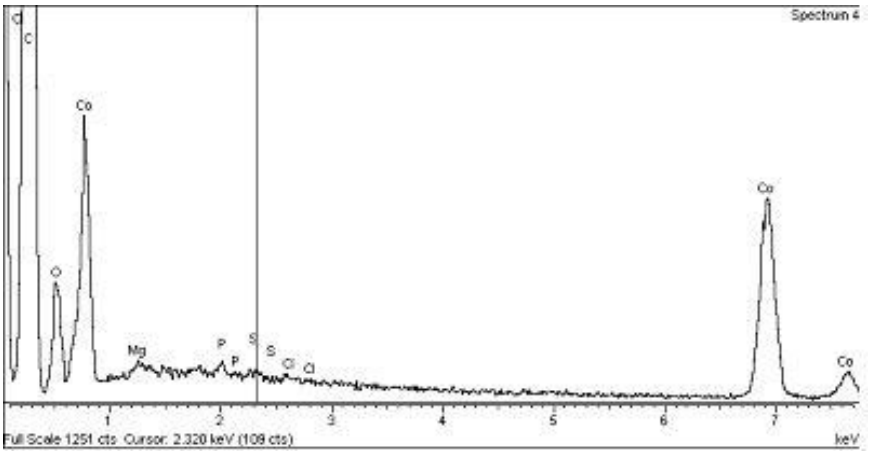


Figure 8.2 An EDX scan taken after 60s of cobalt deposition at a potential of –1.1V.

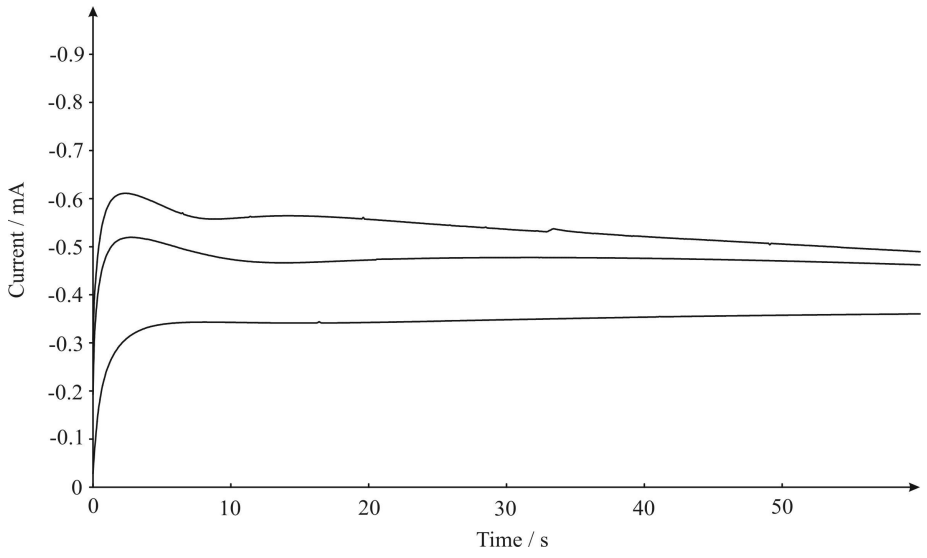


Figure 8.3 Potential transients performed at –1.05 V, - 1.1V and –1.15V (vs. SCE) respectively, in a 10 mM $[Co(H_2O_3)_6](NO_3)_2$ in 0.1 M $MgSO_4$ with 0.1M H_3BO_3 solution.

8.3.2 In situ AFM

Experiments in which a potential was applied to the electrode while the surface was being imaged were then performed using an in-situ AFM cell. The procedure used was the same for each experiment; the cell was assembled over the AFM scanner head and the solution injected into the cell with the potentiostat disconnected. The scanner was engaged over the electrode surface using a scan size of 5 μm x 5 μm at a scan rate of 1 Hz (using a resolution of 256 lines per scan). An image of the bare electrode surface was then recorded before starting electrochemical experiments. The potentiostat was then connected and the potential was applied for a set period of time (2 or 10 seconds) between each AFM scan. During the period the potential was applied the slow scan axis was disabled, pausing the movement of the AFM tip in the y axis. After the applied potential was switched off the slow scan axis was re-enabled and an image was recorded. In each case rather than one single application of a potential to the electrode, the total duration was split into short intervals where the potential was applied and then the surface imaged. This was continued until the cumulative time reached either 60 seconds or 10 seconds depending on the experiment.

Figure 8.4 shows the 3 dimensional AFM images recorded using a potential of –1.15 V applied for 10s in between each image, as an example of the quality of the data typically recorded. The first image shows the bare surface of BDD in solution before any potential has been applied it demonstrates the high degree of flatness and local uniformity found at a BDD surface, no imperfections of the surface are visible. The next images were taken after each subsequent 10 seconds of potential had been applied, the final image shows the surface after a total of 60 seconds of deposition. The growth of cobalt nuclei on the BDD surface can clearly be seen over this timescale. It can be seen in Figure 8.4 that all the nuclei grown during the experiment appeared during the

1st application of the potential at –1.15 V, no new nuclei are seen to form during any subsequent application of potential. That is to say the nucleation appears "instantaneous".

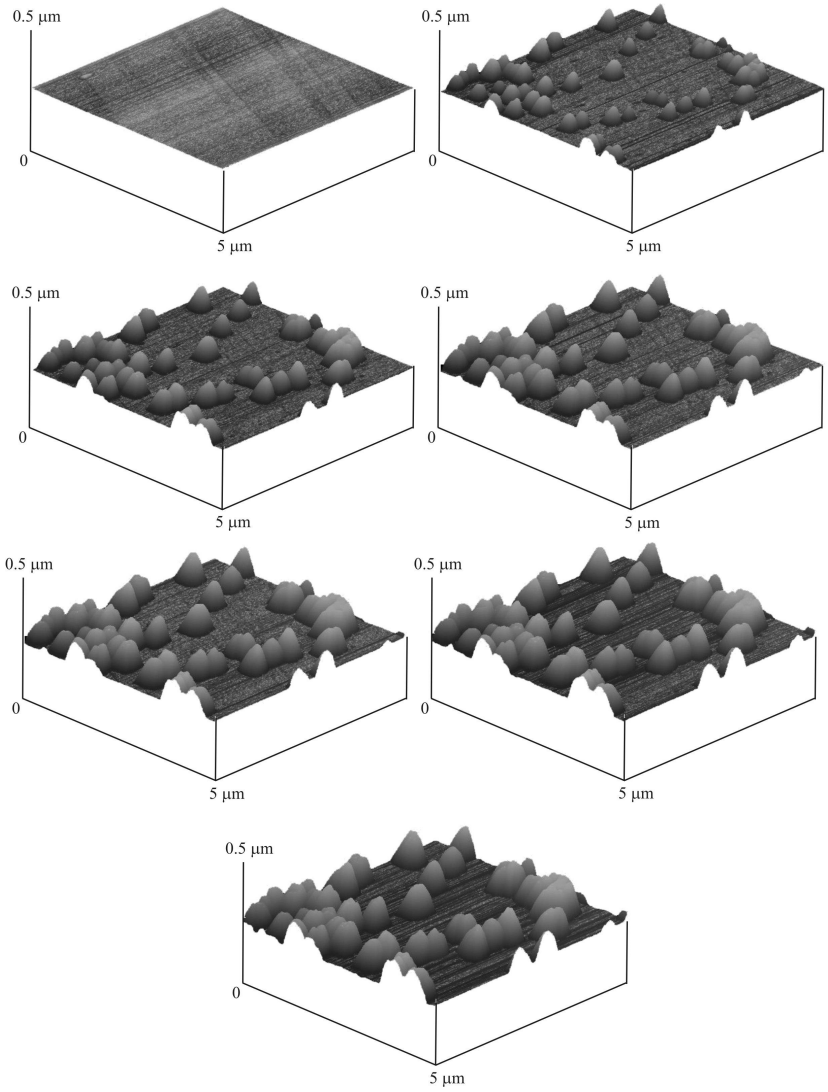


Figure 8.4 In-situ tapping mode AFM images, of cobalt nuclei grown on a BDD surface from a 10mM Co(II) solution, the images show the surface after the –1.15 V potential has been applied for 10 second periods up to a total of 60 seconds.

The experiments were repeated at each potential selected and the images recorded in the same way. At each potential used particles of cobalt were seen to nucleate "instantaneously" and remain constant in number throughout the experiment, no new

particles of cobalt were seen to nucleate at any point after the initial application of potential. The size of the particles as expected was seen to increase with time but also with the increasing potentials used, Figure 8.5. The Figure shows the final images taken at each potential after 60 seconds of deposition.

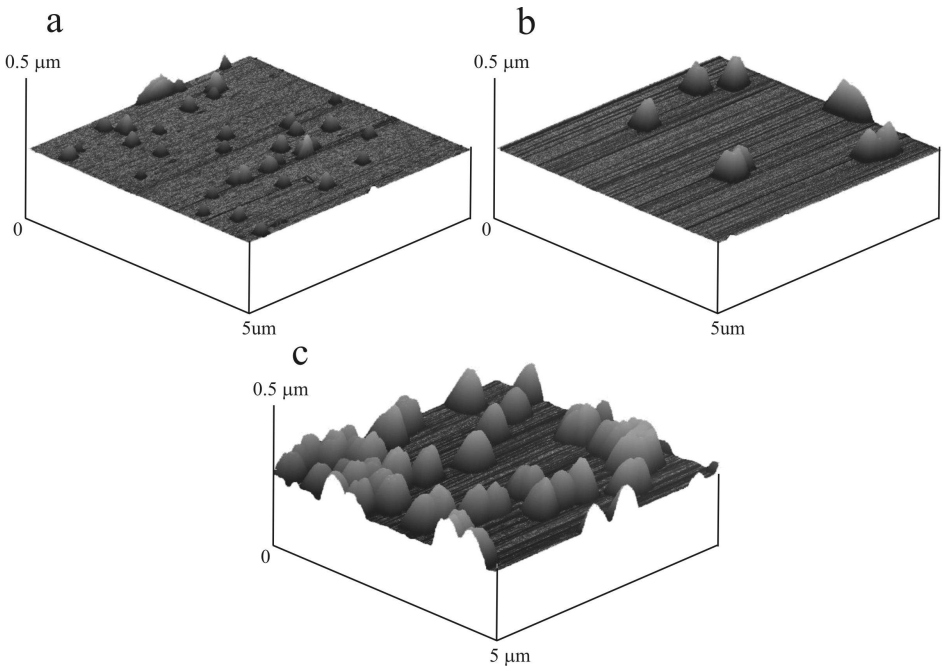


Figure 8.5 In-situ tapping mode AFM images, of cobalt grown on a BDD surface from a 10mM Co(II) solution, images are shown taken at 60s after applying a potential of (a) –1.05 V, (b) –1.1V and (c) –1.15V.

It is difficult to assign any significance in the numbers of nuclei seen at different potentials used in the AFM images as different areas of the BDD surface are found to have different densities of nuclei. This can clearly be seen in the SEM images shown in Figure 8.6. The Figure shows images taken of the surface after 1 minute of deposition at –1.1V from a 10mM Co(II) solution. The images show clusters of nuclei that appear to highlight different areas of the BDD surface, it is possible that these zones represent different surface morphologies with different nucleation properties.

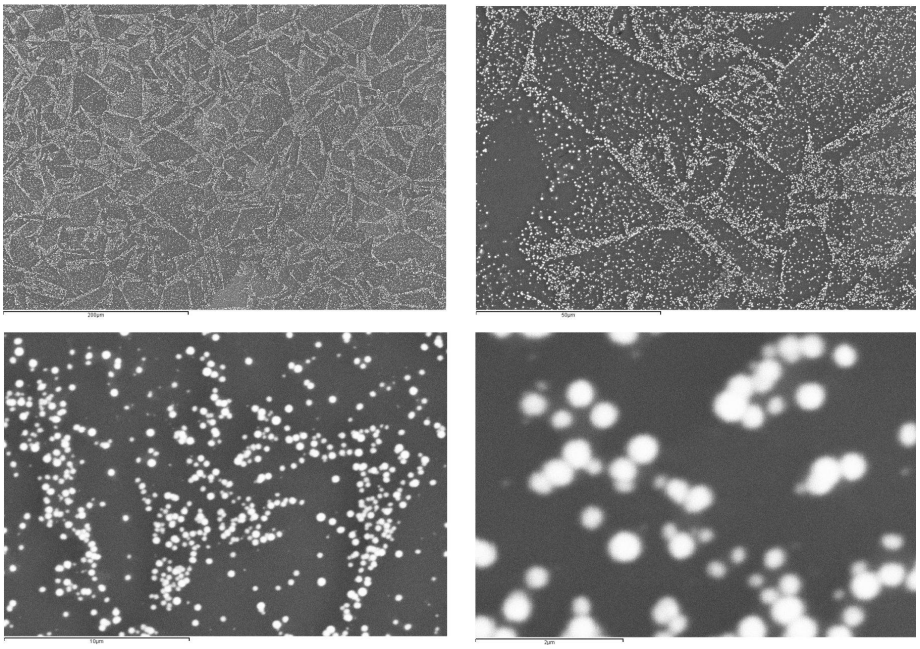


Figure 8.6 SEM images of Co deposited on a BDD electrode at –1.1V for 60s from a 10mM Co(II) solution. Magnifications are (a) 250x, (b) 1000x, (c) 5000x and (d) 20,000x.

The experiments were then repeated at the potentials of –1.1 V and -1.15 V over a total time period of 10 seconds in 2 second intervals while the volume of the particles was monitored again as a function of time, as with the experiments where six applications of a 10 second potential were used all the nuclei formed were found to appear during the 1st application of a potential.

8.3.3 Growth Rate of Individual Nuclei

The Digital Instruments Nanoscope software was used to analyse the AFM data obtained. The software allows a baseline to be set within the image, which was placed at the electrode surface; the high degree of flatness of the BDD electrode allowed this to be positioned accurately. The software was then able to measure the base area of each particle individually at the baseline and the height profile of the particle surface protruding above this point. This allowed the volumes of the particles to be monitored as a function of time for each potential used, the results of which can then be plotted.

As a comparison the theoretical diffusion controlled growth rate for a single hemispherical nucleus was calculated in each case. This was calculated from the established equations for hemispherical diffusion;[15]

$$\left(\frac{\partial V}{\partial t}\right) = \frac{2\pi r D c M}{\rho} \tag{8.2}$$

which integrates to give;

$$V = \frac{4}{3}.2^{1/2}.\pi\left(\frac{M}{\rho} Dct\right)^{3/2} \tag{8.3}$$

where V is the volume of the nucleus, c is the solution concentration, D is the diffusion coefficient of the depositing species, t is the time after the potential was applied, M is the molar mass of the depositing species and ρ is the density of the depositing species. However the calculated values exceeded the volumes measured using AFM by over 2 orders of magnitude, table 1.

Table 1 showing the range of volumes of nuclei found at each potential used after 60s (in μm^3) compared with the value for an individual nuclei under diffusional control.

Potential Applied	**Volume of Nuclei after 60s (μm^3)**
-1.05 V	0.001 - 0.01
-1.1 V	0.02 - 0.08
-1.15 V	0.01 - 0.1
Theoretical Diffusionally controlled Value	1.5

Even after accounting that the calculated value is based on one independent nucleus and some of the AFM images showed that some of the nuclei were close together. Such that they were not diffusionally independent and would be diffusionally "feeding" off each other over longer timescales. It demonstrates that the nucleation and growth of cobalt particles on the BDD surface is not diffusionally controlled, rather the growth must be determined by the electrode kinetics, consistent with the potential dependence of the steady state currents shown in Figure 8.3.

Theoretical volumes of the particles grown in each case were calculated using the density of nuclei obtained from AFM experiments together with the current found at steady state when the potential was applied, using values taken from Figure 8.3. The volumes of the particles were estimated using the following argument:

If the current flowing per nucleus is given by;

$$\frac{I}{N}$$

where N is the number of nuclei on the electrode surface as estimated from AFM measurements and I is the steady state current taken from the experimental transients, then;

$$\frac{dQ}{dt} = \frac{I}{N} \quad \therefore Q = \frac{It}{N} \tag{8.4}$$

where Q is the charge and t is the time after the potential is applied, then;

$$V = \frac{M}{\rho} = \frac{MW \times moles}{\rho} \text{ and } Moles = \frac{It}{NF}$$

where ρ is the density of cobalt, MW is the molecular weight of cobalt and F is the Faraday constant therefore the volume of a nuclei at time t is given by:

$$V = \frac{MW}{\rho} \cdot \frac{It}{NF} \tag{8.5}$$

The values calculated assume steady state behaviour throughout duration of each potential application and so neglect the non steady state contributions to the current at the start of the potential appliance. However the latter are of short duration, see Figure 8.3. The calculation can therefore be used to provide "ball park" estimates as to the particle size at a given time.

Figure 8.7 shows the volume each cobalt particle growing on the surface plotted as a function of time for the in-situ experiments. It was found that when comparing with the volumes found for the experiments conducted over a 60 s timescale the calculated values were found to have better than order of magnitude agreement. The experiments conducted at the lower timescale of 10 seconds showed good agreement with the theoretical values as can be seen in Figure 8.7. It is noted that in Figure 8.7c where the growth of nuclei using a potential of –1.15 V over a timsescale of 10s is shown the growth of each particle on the surface is seen to be linear intersecting the axis at almost exactly one second. This suggests that immediately after the potential is applied there is a "lag" before the onset of instantaneous nucleation, where non steady state nucleation rates apply.

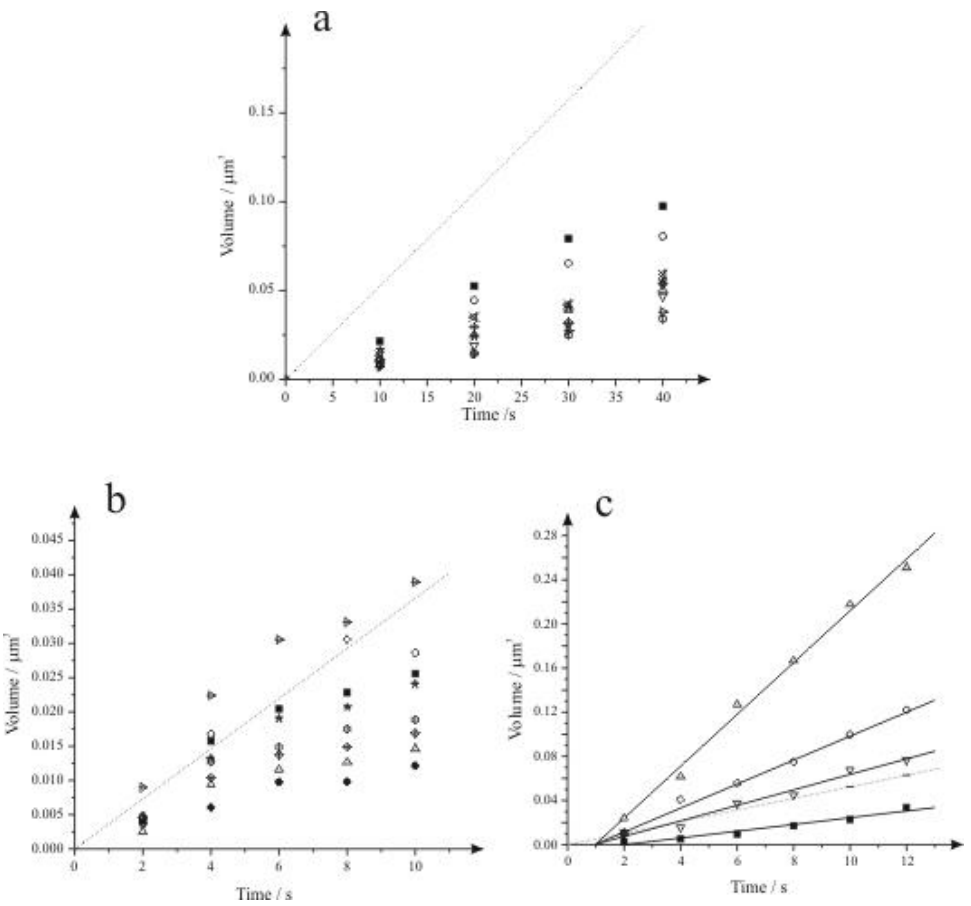


Figure 8.7 Cobalt particle growth rates at potentials of (a) –1.15 V over 40s , (b) –1.1 V over 10s and (c) –1.15V over 12s. The dotted line in each case represents the calculated value.

The difference between those particles that were found to approximate well to theoretical values and those that are smaller than predicted can be explained by looking at their location on the electrode surface. A clear example of this is given in Figure 8.8. As the growth rate of diffusionally independent isolated nuclei is greater than the growth rate of a small cluster of nuclei as these particles are diffusionally feeding off each other before eventually merging to form a single particle. Figure 8.8 shows that the isolated nuclei in the top half of the image have a much greater growth rate than the three nuclei in the bottom left hand corner of the image which are growing at a slower rate due to their overlapping diffusion layers.

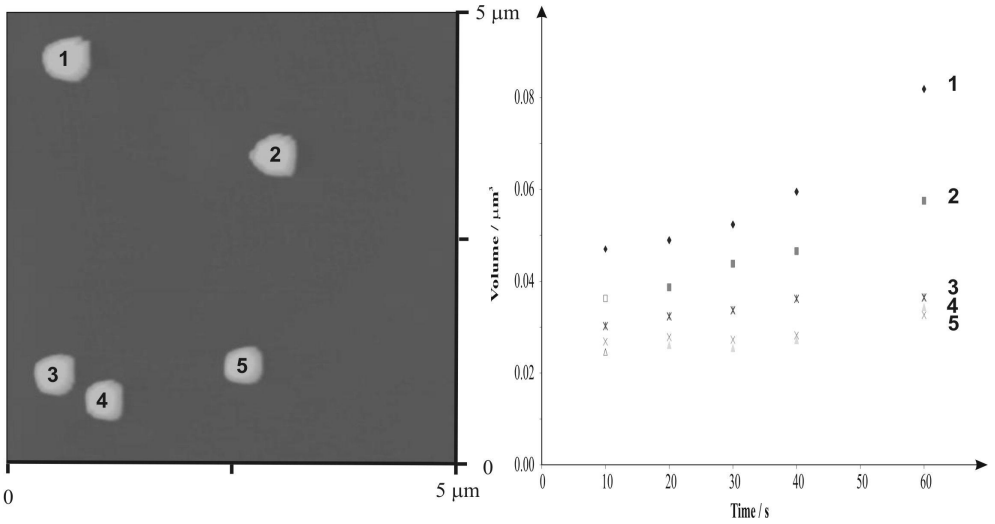


Figure 8.8 An example of an AFM image used for particle analysis, the image shows the surface after two 10 second applications of a potential of –1.1 V. Each individual particle is numbered and shown with the corresponding growth rate data for the duration of the experiment.

8.4 Conclusion

The nucleation and growth of cobalt at a boron doped diamond electrode has been successfully studied using in-situ atomic force microscopy. The nucleation is found to be effectively "instantaneous process" and the growth is found to occur under kinetic control. At the higher deposition potentials studied there appears to be a ca. 1-2 second lag after the potential is applied where transient nucleation rates operate.

8.5 References

(1) Hyde, M. E.; Jacobs, R.; Compton, R. G., *J. Phys. Chem. B,* **2002**, *106*, 11075.

(2) Fletcher, S., *J. Electroanal. Chem.,* **2002**, *530*, 105.

(3) Fletcher, S., *J. Electroanal. Chem.,* **2002**, *530*, 119.

(4) Abyaneh, M. Y., *J. Electroanal. Chem.,* **2002**, *530*, 82.

(5) Abyaneh, M. Y.; Fleischmann, M., *J. Electroanal. Chem.,* **2002**, *530*, 89.

(6) Abyaneh, M. Y., *J. Electroanal. Chem.,* **2002**, *530*, 96.

(7) Abyaneh, M. Y.; Fleischmann, M., *J. Electroanal. Chem.,* **2002**, *530*, 108.

(8) Abyaneh, M. Y.; Fleischmann, M., *J. Electroanal. Chem.,* **2002**, *530*, 123.

(9) Deutscher, R. L.; Fletcher, S., *J. Chem. Soc. Faraday Trans.,* **1998**, *94*, 3527.

(10) Fletcher, S., *J. Chem. Soc. Faraday Trans.,* **1983**, *79*, 467.

(11) Deutscher, R. L.; Fletcher, S., *J. Electroanal. Chem.,* **1988**, *17*, 239.

(12) Deutscher, R. L.; Fletcher, S., *J. Electroanal. Chem.,* **1990**, *1*, 277.

(13) Fletcher, S.; Halliday, C. S.; Gates, D.; Westcott, M.; Lwin, T.; Nelson, G., *J. Electroanal. Chem.,* **1983**, *159*, 267.

(14) Ziegler, J. C.; Wielgosz, R. I.; Kolb, D. M., *Electrochim. Acta,* **1999**, *45*, 827.

(15) Hills, G. J.; Schiffrin, D. J.; Thompson, J., *J. Electrochim. Acta,* **1974**, *19*, 657.

CHAPTER 9

The Electrochemical Reduction of Aqueous Hexamminecobalt(III)

This chapter reports the electrochemical reduction of aqueous hexamminecobalt(III) studied using cyclic voltammetry. The current-voltage response using a range of scan rates covering seven orders of magnitude. At lower scan rates, it is clear that the voltammetry is diffusion-controlled, but as the scan rate is increased, the system undergoes a transition to a regime that is governed by adsorption. This work discussed in this chapter has been published as an article in *J. Electroanal. Chem.*, **2005**, 581, 249.

9.1 Introduction

Transition metal complex ions, such as hexamminecobalt(III), constitute a topic of abiding interest for the examination of heterogeneous electron transfer reactions. The electroreduction of $[Co(NH_3)_6]^{3+}$ has been investigated extensively over the years on a wide variety of electrode surfaces.[1-19] Laitinen *et al* [2-4] have studied the polarographic reduction of hexamminecobalt(III) in various supporting electrolytes. They showed that the first step in the reduction process is an irreversible one-electron transfer to form hexamminecobalt(II). They also reported that the half-wave potential and the diffusion

limited current were dependent on the nature of the electrolyte employed. In 1986, Hamelin *et al*[13] discussed the one-electron reduction of $[Co(NH_3)_6]^{3+}$ in an acidified aqueous solution containing 0.1 M $NaClO_4$ electrolyte at Au(111), Au(100), and Au(110) electrodes. Compared with mercury and silver electrodes, the measured heterogeneous rate constants were greater on the single-crystal gold surfaces, increasing in the order Au(110)<Au(100)<Au(111). As a conclusion, the authors speculated that the kinetics of outer-sphere processes can be sensitive to the nature of the electrode material to an extent which lies beyond that considered by conventional double-layer effects. More recently, Fawcett *et al*[16,17] studied double layer effects at single-crystal gold electrodes for the reduction of hexamminecobalt(III) in aqueous solution and found that the electrokinetics depends only on the potentials of zero charge for the different crystallographic orientations. They[16,17] suggest that the reduction of $[Co(NH_3)_6]^{3+}$ is a model outer-sphere reaction in the sense that "the role of the metal is that expected for an adiabatic outer-sphere electron-transfer process".

The above research demonstrates that the reduction of $[Co(NH_3)_6]^{3+}$ in aqueous solution is a slow diffusion-controlled one electron transfer. However, it has been suggested that $[Co(NH_3)_6]^{2+}$ can hydrolyse in aqueous solution with rapid loss of the first three ammonia ligands, followed by slower loss of the remaining three obtained from ref :[20]

$$[Co(NH_3)_6]^{2+} \rightleftharpoons [Co(NH_3)_3]^{2+} + 3NH_3 \qquad k > 10^6\ s^{-1}$$

$$[Co(NH_3)_3]^{2+} \rightleftharpoons [Co(NH_3)_2]^{2+} + NH_3 \qquad k \approx 6 \times 10^4\ s^{-1}$$

$$[Co(NH_3)_2]^{2+} \rightleftharpoons [Co(NH_3)]^{2+} + NH_3 \qquad k \approx 1 \times 10^4\ s^{-1}$$

$$[Co(NH_3)]^{2+} \rightleftharpoons [Co]^{2+} + NH_3 \qquad k \approx 1.5 \times 10^3\ s^{-1}$$

Dissociation in this manner is thermodynamically favourable when the concentration of ammonia in the solution is low. Figures 9.1 and 9.2 show the thermodynamic dependence of the favoured cobalt species on ammonia concentration in aqueous solution. These distributions were calculated using complex stability constants given in table 1,[21,22] together with these equations:

$$Co^{m+} + n[NH_3] \rightleftharpoons [Co(NH_3)_n]^{m+} \quad (9.1)$$

$$C^0_{Co} = [Co]^{m+} + \sum_{n=1}^{6} [Co(NH_3)_n]^{m+} \quad (9.2)$$

where C^0_{Co} is the total concentration of cobalt, $[NH_3]$ is the concentration is of free ammonia in the solution (the solubility of ammonia is 89.9 g L^{-1} in water at 273K), and $\sum_{n=1}^{6} n\,[Co(NH_3)_n]^{m+}$ is the concentration of cobalt bound in complexes (m = 2, 3, n = 1-6). It is evident that the existence of ammine compounds is independent of cobalt concentration and depends exclusively upon the concentration of free ammonia. Figure 9.1 shows that the main composition of cobalt (II) in solution is $[Co(NH_3)_5]^{2+}$ and $[Co(NH_3)_6]^{2+}$ at high concentrations of ammonia. The favoured Co(II) species in solution becomes increasingly hydrolysed with decreasing concentration of ammonia. Finally, $[Co(H_2O)_6]^{2+}$ becomes the dominating species in solution in the absence of any free ammonia. Thus, when kinetically inert $[Co(NH_3)_6]^{3+}$ is electrochemically reduced, even in the presence of 1M ammonia, the kinetically labile $[Co(NH_3)_6]^{2+}$ that is formed will rapidly hydrolyse and lose all of the ammonia ligands.

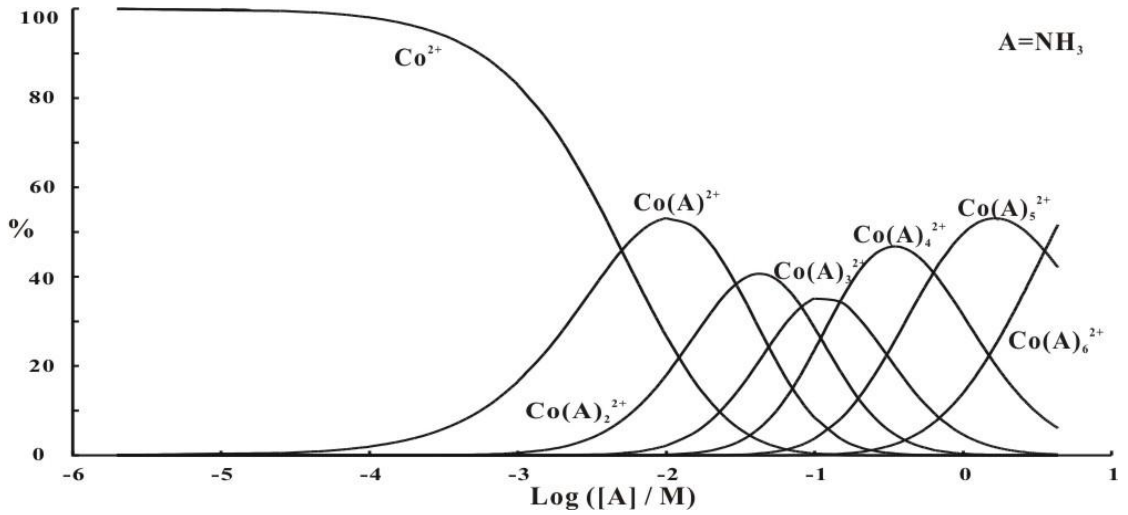


Figure 9.1 Species of hexamminecobalt(II) that exist in solution with varying concentrations of free ammonia (Mol dm^{-3}).

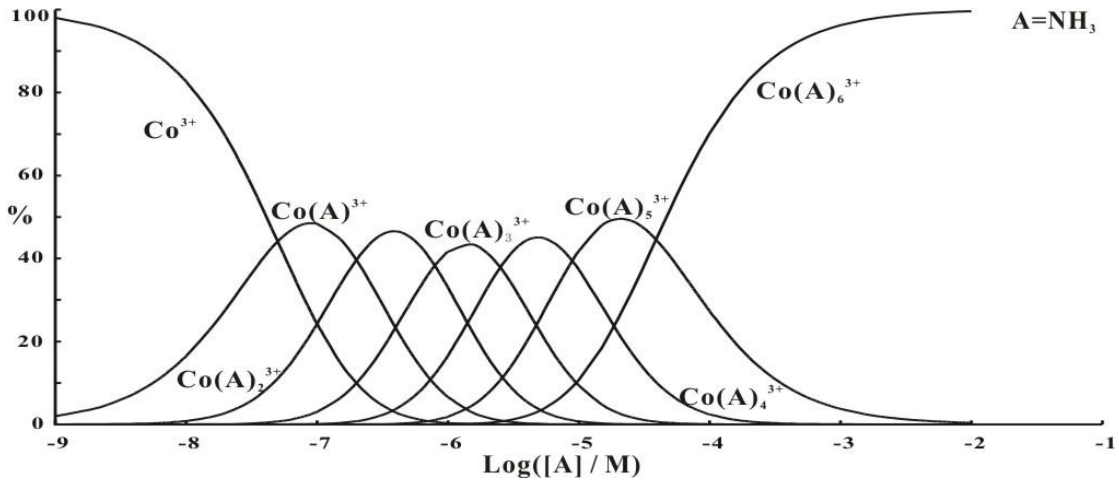


Figure 9.2 Species of hexamminecobalt(III) that exist in solution with varying concentrations of free ammonia (Mol dm^{-3}).

In addition, Kolthoff *et al*[23] proposed that under similar conditions, the following hydrolysis mechanism takes place. As a result of the fast hydrolysis reaction in the absence of any free ammonia, it is impossible to see the oxidation of $[Co(NH_3)_6]^{2+}$ on the reverse sweep at conventional scan rates. However, assuming that the process remains diffusion-controlled, it may be possible to invoke fast scan cyclic voltammetry to outrun the homogeneous processes.

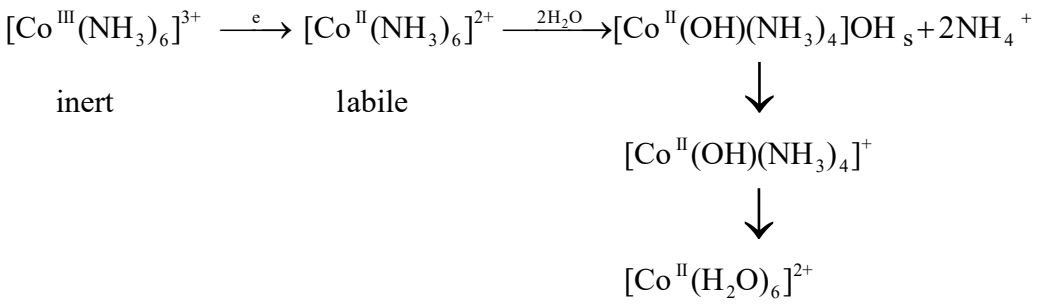


Table 1 Equilibrium constants for Co^{II} and Co^{III} systems at 298 k

Reaction	Equilibrium constant
$Co^{2+} + NH_3 \rightleftharpoons [Co(NH_3)]^{2+}$	Log K_1 = 2.30
$[Co(NH_3)]^{2+} + NH_3 \rightleftharpoons [Co(NH_3)_2]^{2+}$	Log K_2 = 1.53
$[Co(NH_3)_2]^{2+} + NH_3 \rightleftharpoons [Co(NH_3)_3]^{2+}$	Log K_3 = 1.09
$[Co(NH_3)_3]^{2+} + NH_3 \rightleftharpoons [Co(NH_3)_4]^{2+}$	Log K_4 = 0.83
$[Co(NH_3)_4]^{2+} + NH_3 \rightleftharpoons [Co(NH_3)_5]^{2+}$	Log K_5 = 0.20
$[Co(NH_3)_5]^{2+} + NH_3 \rightleftharpoons [Co(NH_3)_6]^{2+}$	Log K_6 = -0.55
$Co^{3+} + NH_3 \rightleftharpoons [Co(NH_3)]^{3+}$	Log K_1 = 7.30
$[Co(NH_3)]^{3+} + NH_3 \rightleftharpoons [Co(NH_3)_2]^{3+}$	Log K_2 = 6.70
$[Co(NH_3)_2]^{3+} + NH_3 \rightleftharpoons [Co(NH_3)_3]^{3+}$	Log K_3 = 6.10
$[Co(NH_3)_3]^{3+} + NH_3 \rightleftharpoons [Co(NH_3)_4]^{3+}$	Log K_4 = 5.60
$[Co(NH_3)_4]^{3+} + NH_3 \rightleftharpoons [Co(NH_3)_5]^{3+}$	Log K_5= 5.05
$[Co(NH_3)_5]^{3+} + NH_3 \rightleftharpoons [Co(NH_3)_6]^{3+}$	Log K_6= 4.41

On the other hand, if any of the species involved undergo adsorption onto the electrode, it may be the case that at the fast scan, the currents resulting from adsorption dominate those arising from mass transport, giving a linear dependence between the peak current and the scan rate. It is our intention in this chapter to study the reduction wave of hexamminecobalt(III) over a very wide range of scan rates using gold electrodes. If the response is typical of adsorption at the faster scan rates, then we intend to apply a previously developed mathematic model to examine the transition from diffusion control to surface control.

9.2. Numerical Simulation

9.2.1 Model

Electrosorption processes have been modelled analytically or numerically by numerous authors.[24-34] The model below has been extensively studied in a previous publication.[34] Therefore the authors only present here what is necessary for an understanding of the system at hand. Full details can be found in ref.[34]

We consider a general mechanism for the electrosorption process given in Figure 9.3, in which A_{ads} and B_{ads} are the adsorbed forms of the reacting species, A_{surf} and B_{surf} the unadsorbed forms near the surface of the electrode and A_{bulk} and B_{bulk} the forms in the bulk solution.

The surface coverages for A and B are denoted respectively as θ_A and θ_B, the concentrations in the solution $[A]$ and $[B]$, $[A]_{bulk}$ and $[B]_{bulk}$ being their values away from the electrode. k_f and k_b are the electrochemical rate constants (in s^{-1}), k_{a1}, k_{a2} are the adsorption rate constants (in cm s^{-1}) and k_{d1},k_{d2} are the desorption rate constants (in mol cm^{-2} s^{-1}).

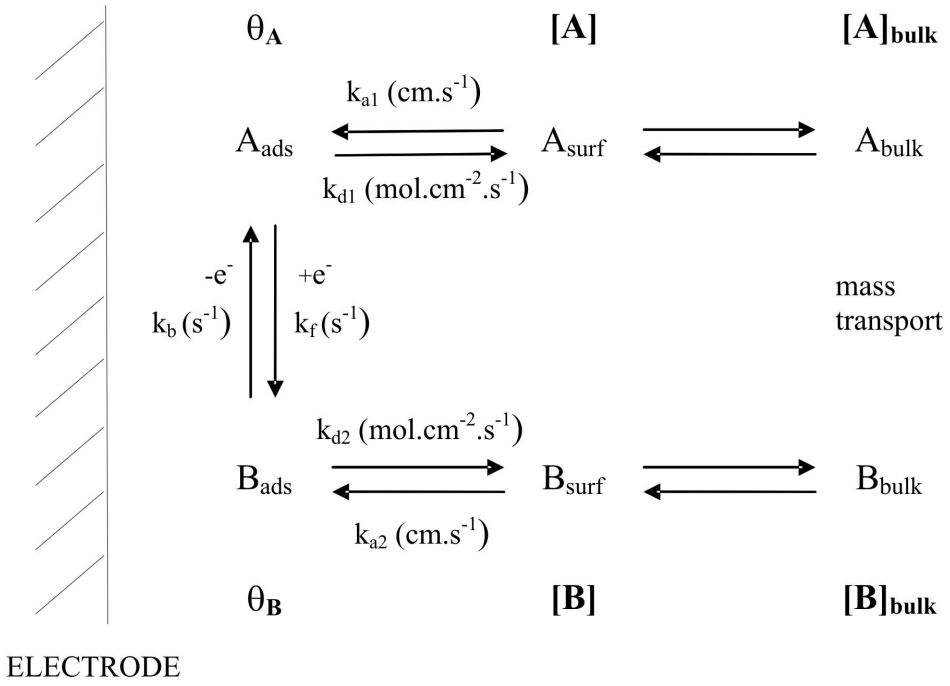


Figure 9.3 Mechanism for electrosorption.

We assume that the adsorption kinetics are independent of the electrode potential and ignore the interactions between the adsorbed molecules (Langmuirian adsorption). The time-dependent equations describing the mass transport and adsorption of all the species to a microdisk electrode of radius r_d written in the cylindrical coordinates are

$$\frac{\partial [A]}{\partial t} = D_A \, \Delta_{r,z} [A] \tag{9.3}$$

$$\frac{\partial [B]}{\partial t} = D_B \, \Delta_{r,z} [B] \tag{9.4}$$

$$\Gamma \frac{\partial \theta_A}{\partial t} = k_{a1} (1 - \theta_A - \theta_B) [A]_{z=0} - k_{d1} \theta_A - k_f \, \Gamma \, \theta_A + k_b \, \Gamma \, \theta_B \tag{9.5}$$

$$\Gamma \frac{\partial \theta_B}{\partial t} = k_{a2} (1 - \theta_A - \theta_B) [B]_{z=0} - k_{d2} \theta_B + k_f \, \Gamma \, \theta_A - k_b \, \Gamma \, \theta_B \tag{9.6}$$

where D_A and D_B are the diffusion coefficients of species A and B;

$\Delta_{r,z} = \left(\partial^2 / \partial r^2\right) + \left(1/r\right)\left(\partial / \partial r\right) + \left(\partial^2 / \partial z^2\right)$ is the Laplacian in the cylindrical coordinates, in which r represents the radial coordinate and z the coordinate normal to the surface of the disk and Γ represents the monolayer saturation coverage (mol cm^{-2}) (the two species A and B are assumed to adsorb 'competitively', that is, they can occupy the same adsorption sites).

The forward and backward rate constants are defined as

$$k_f = k_0 \exp\left(-\frac{\alpha F}{RT}\left(E - E^0\right)\right) \tag{9.7}$$

$$k_b = k_0 \exp\left(\frac{(1-\alpha) F}{RT}\left(E - E^0\right)\right) \tag{9.8}$$

where k_0 is the standard rate constant for the A_{ads}/B_{ads} couple, α is the transfer coefficient and E^0 is the standard potential.

Before the electrochemical experiment is started, only the species A is present in the solution, therefore the initial conditions (t = 0) for the concentrations of the species taking part in the reaction mechanism (Figure 9.3) are

$[A] = [A]_{\text{bulk}}$ for $0 \le r < \infty$ and $0 \le z < \infty$ (9.9)

$[B] = 0$ for $0 \le r < \infty$ and $0 \le z < \infty$ (9.10)

The initial condition for adsorption is determined by experimental conditions. Two main limiting cases can be examined depending on the time taken between the start of the experiment and immersion of the electrode into the solution. If the electrode is left long enough in the medium, then the surface coverage can be assumed to be equal to its equilibrium value:

$$\theta_A = \frac{K[A]_{bulk}}{1+K[A]_{bulk}} = \theta_{Aeq} \qquad \text{for} \qquad 0 \le r \le r_d \qquad \text{and} \qquad z = 0 \tag{9.11}$$

with K equal to the ratio k_{a1}/k_{d1}.

But if the experiment starts instantly after the electrode is immersed in the solution, then the system is very far from equilibrium and the surface coverage may be close to zero:

$$\theta_A = 0 \qquad \text{for} \qquad 0 \le r \le r_d \qquad \text{and} \qquad z = 0 \tag{9.12}$$

The boundary conditions completing the mathematical model are given in Table 2.

Table 2 Boundary conditions

Equations	Boundary region	
$[A] = [A]_{\text{bulk}}$	$0 \le r < \infty$	$z \to \infty$
$[B] = 0$	$0 \le r < \infty$	$z \to \infty$
$\left.\frac{\partial [A]}{\partial r}\right\|_{r=0} = 0$	r=0	$0 \le z < \infty$
$\left.\frac{\partial [B]}{\partial r}\right\|_{r=0} = 0$	r=0	$0 \le z < \infty$
$D_A \left.\frac{\partial [A]}{\partial z}\right\|_{z=0} = k_{a1}(1-\theta_A-\theta_B)[A]_{z=0} - k_{d1}\theta_B$	$0 \le r \le r_d$	$z = 0$
$D_B \left.\frac{\partial [B]}{\partial z}\right\|_{z=0} = k_{a2}(1-\theta_A-\theta_B)[B]_{Z=0} - k_{d2}\theta_B$	$0 \le r \le r_d$	$z = 0$
$\left.\frac{\partial [A]}{\partial z}\right\|_{z=0} = 0$	$r > r_d$	$z = 0$
$\left.\frac{\partial B}{\partial z}\right\|_{z=0} = 0$	$r > r_d$	$z = 0$

The current flowing at the electrode surface is due to the contribution of two different processes, the first one being the reduction of A_{ads} to give B_{ads} and the second being the desorption of B_{ads} leading to additional flow of charge at the electrode. The mathematical expression used to calculate the current is given by:

$$i = 2\pi F\left[\Gamma\int_0^{r_d}\frac{\partial\theta_B}{\partial t}r\,dr + k_{d2}\int_0^{r_d}\theta_B\,r\,dr\right] \tag{9.13}$$

Since the coverage of a microelectrode is not only a function of time but also a function of the position at the electrode surface due to the non-uniform accessibility of the latter, the interpretation of the results can be simplified by introducing an average coverage defined for a microdisk as:

$$\overline{\theta}_i = \frac{2}{r_d^2}\int_0^{r_d}\theta_i\,r\,dr \tag{9.14}$$

9.3. Experimental

9.3.1 Chemicals

Hexamminecobalt(III) chloride (Sigma, 99.999%), tetra-*n*-butylammonium perchlorate (TBAP, Fluka, >99%), ferrocene (Cp_2Fe, Aldrich, 98%) and acetonitrile (MeCN, Fisher Scientific, >99.99) were purchased at the highest grade available and used directly without further purification. Aqueous buffer electrolyte solutions were prepared with Na_2SO_4 (99%), Na_2HPO_4 (99%) and H_3PO_4 (AnalaR grade) (all Aldrich) using ultrapure water from an Elgastat UHQ grade water system (Elga, UK) with a resistivity of not less than 18 MΩ cm^{-1}. All the solutions were degassed with oxygen-free nitrogen (BOC Gases, Surrey, UK) for at least 30 min prior to experimentation and a nitrogen atmosphere was maintained throughout. All experiments were carried out at a temperature of 295 ± 3 K.

9.3.2 Instrumentation

The 'fast scan' potentiostat used was built in-house and is capable of attaining scan rates of up to ~2 H 10^6 V s^{-1} and was used with minimum filtering. This potentiostat is similar to that described and utilised by Amatore *et al*[35,36] and can achieve ohmic drop compensation by means of an internal positive feedback circuit. The potential was applied with a TTi TG1304 programmable function generator (Thurlby Thandar Instruments Ltd, Huntingdon, Cambs., UK) and the current was recorded with a Tektronix TDS 3032 oscilloscope (300 MHz band-pass, 2.5 GS s^{-1}) with the ohmic drop compensation set to 100%. Electrochemical experiments at scan rates below 900 V s^{-1} were performed using a μ-Autolab type II potentiostat (Eco-Chemie, Utrecht, Netherlands) controlled by General Purpose Electrochemical Systems v.4.7 software.

For experiments at a macrodisk, a 1mm diameter gold electrode was used, together with a platinum wire counter electrode, and a saturated calomel reference electrode (Radiometer, Copenhagen, Denmark). The working electrode was polished using 1.0 μm alumina-water slurry (Buehler, Illinois, USA) on a soft polishing pad (Kermet, Kent, UK) prior to every measurement. For experiments at a microdisk, a 12.9 μm diameter gold electrode was fabricated by sealing a gold microwire into a sodaglass capillary.[37] The gold microelectrode was polished for 15 min before experiments using 1.0 μm alumina-water slurry, followed by 0.3 μm alumina-water slurry (Buehler) on soft polishing pads (Microcloth, Buehler). The microelectrode diameter was calibrated electrochemically by examining the steady state current of 2.0 mM ferrocene in acetonitrile with 0.1 M TBAP, using a literature diffusion coefficient of 2.30×10^5 cm^2 s^{-1}.[38,39] A silver wire quasi-reference electrode was used, together with a platinum wire counter electrode.

9.4. Results and Discussion

9.4.1 Cyclic Voltammetry at Macro and Micro Gold Electrodes

Figure 9.4 shows cyclic voltammograms at various scan rates obtained at a 1 mm diameter gold electrode for a solution of 5.0 mM $[Co(NH_3)_6]Cl_3$ in 0.1 M Na_2SO_4 with 0.1M phosphate buffer (pH = 7.00). The plot of the reduction peak current against the square root of scan rate (20～1000 mVs^{-1}) shows an excellent linear direct relationship, which suggests that the reduction of $[Co(NH_3)_6]^{3+}$ is a diffusion-controlled electron transfer process rather than surface-controlled at these scan rates.

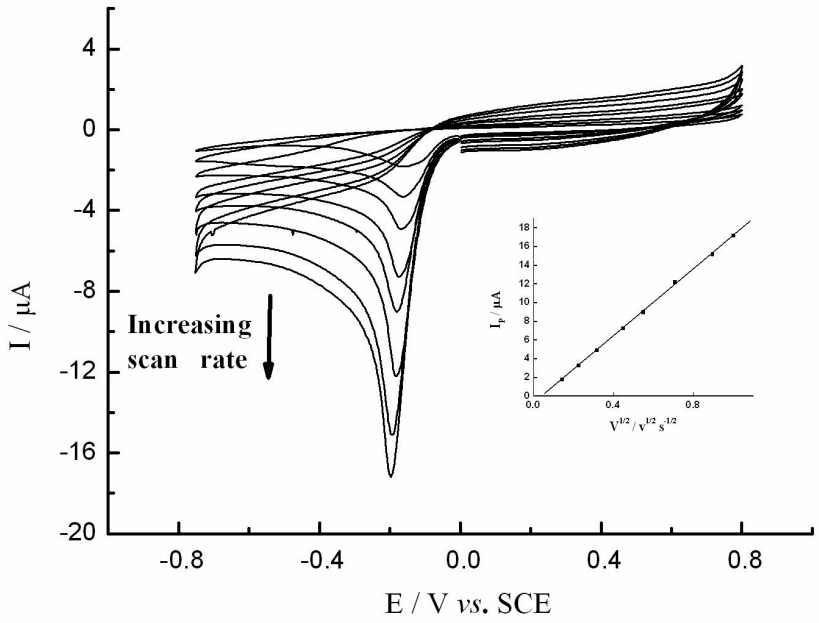


Figure 9.4 Cyclic voltammograms obtained at a 1 mm gold electrode for 5.0 mM $[Co(NH_3)_6]Cl_3$ in 0.1 M Na_2SO_4 with 0.1 M phosphate buffer (pH=7.00) with scan rates 20, 50, 100, 200,300, 500, 800, 1000 mVs^{-1}. Inset: The plot of the reduction peak current against the square root of scan rate.

In order to obtain a better understanding of the electrochemical process, we performed a Tafel analysis on a selected voltammogram (scan rate of 100 mV s^{-1}), assuming that the electron transfer process is electrochemically irreversible. The plot of

potential vs. log(current) is shown in Figure 9.5. The gradient of 116 mV suggests that the assumption of irreversibility is justified.[40] Eqn. (9.15) gives the gradient (*b*) as

$$b = \frac{2.303RT}{\alpha F}. \tag{9.15}$$

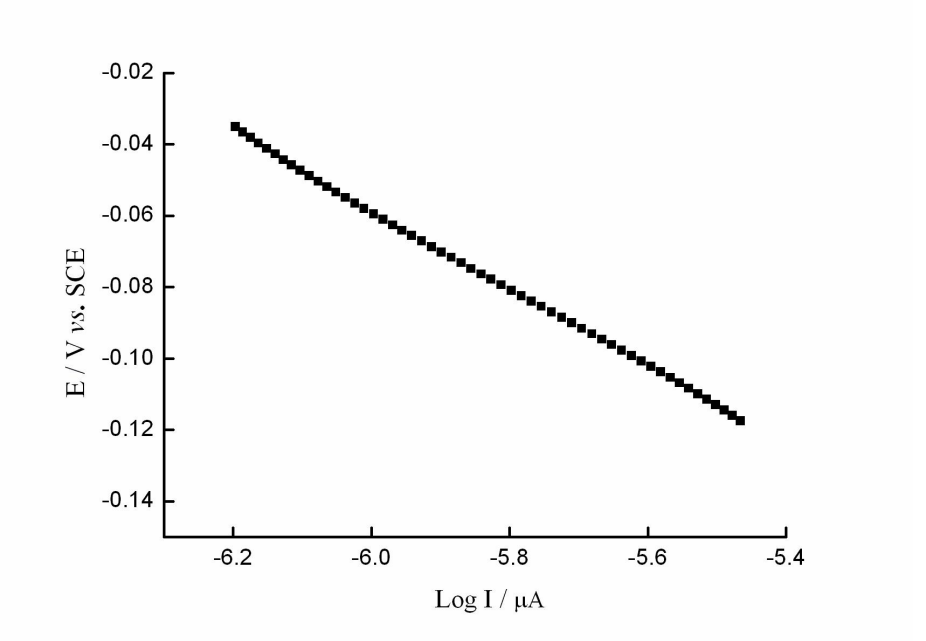


Figure 9.5 Tafel analysis of cyclic voltammogram obtained at a 1 mm gold electrode for 5.0 mM $[Co(NH_3)_6]Cl_3$ in 0.1 M Na_2SO_4 with 0.1 M phosphate buffer (pH = 7.00) at 100 mVs^{-1}.

A value of 0.51 for the charge transfer coefficient (α) was calculated which is indicative of a simple electron transfer reaction with a symmetrical energy barrier. The diffusion-controlled electrochemically irreversible peak current is given by eqn. (9.16)

$$I_P = (2.99\times10^5)(\alpha n')^{1/2} A C_0 D^{1/2} v^{1/2} \tag{9.16}$$

where *A* is the electrode area (cm^2), C_0 is the bulk concentration (mol cm^{-3}), *D* is the diffusion coefficient ($cm^2\ s^{-1}$) and *v* is the scan rate ($V\ s^{-1}$). The value for *D* obtained from eqn. (15) is $5.6 \pm 0.3 \times10^{-6}$ $cm^2\ s^{-1}$, which is close to the value reported by Hromadova *et al.*[16] Figure 9.6 shows the steady state voltammogram for 2.0 mM $[Co(NH_3)_6]Cl_3$, measured using the gold microelectrode at a scan rate of 10 mV s^{-1}. The limiting current was analyzed according to eqn. 9.17.

$$I_{\lim} = 4FDC_0 r \tag{9.17}$$

where r is the radius of electrode. This gave $D = 5.3 \pm 0.2 \times 10^{-6}$ cm^2 s^{-1}, which agrees well with the value determined at a macrodisk assuming irreversibility.

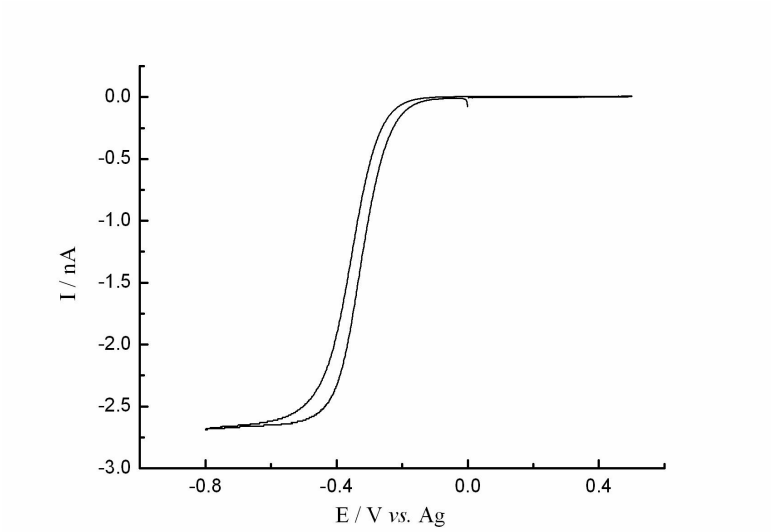


Figure 9.6 Cyclic voltammetric reponse (10 mVs^{-1}) obtained at a 12.9 μm diameter gold micro-disk electrode for 2.0 mM $[Co(NH_3)_6]Cl_3$ in 0.1 M Na_2SO_4 with 0.1 M phosphate buffer (pH = 7.00).

9.4.2 Fast Scan Cyclic Voltammetry

A solution of 2.0 mM $[Co(NH_3)_6]Cl_3$ containing 0.1 M Na_2SO_4 and 0.1 M phosphate buffer (pH =7.00) was selected to investigate the scan rate dependence of the peak current response using a 12.9 μm diameter gold electrode. The voltammograms at scan rates from 4.8 to 140 kV s^{-1} were obtained using the fast scan potentiostat described previously, and are shown as the inset Figure 9.7(b). They show a single reduction wave, which is consistent with observations at the gold macroelectrode. The reduction peak potential shifts to more negative values with increasing scan rate, suggesting sluggish kinetics for the electrochemical step. There is no oxidation wave appearing in this potential range, suggesting that the hydrolysis reaction of $Co(NH_3)_6^{2+}$ is very rapid, and still occurs even when scan rates as fast as 140 kV s^{-1} are employed.

Voltammograms at scan rates below 900 Vs^{-1} were obtained using an Autolab potentiostat and these are shown as inset Figure 9.7(a). Figure 9.7 shows the reductive peak currents for all these voltammograms plotted against scan rate in log-log form. The peak currents were measured relative to a linear background current that was extrapolated from the pre-wave currents in the voltammetry. It is clear that the gradient of the plot undergoes a transition from 0.5 at low scan rates to 1 at higher scan rates. This suggests that the reaction is indeed dominated by diffusion control at low scan rates, but that increasing the scan rate results in a shift to voltammetry that is governed by adsorption effects at fast scan rates. Using the model we have developed, we are now in a position to simulate the experimentally observed trend and directly compare theory and experiment.

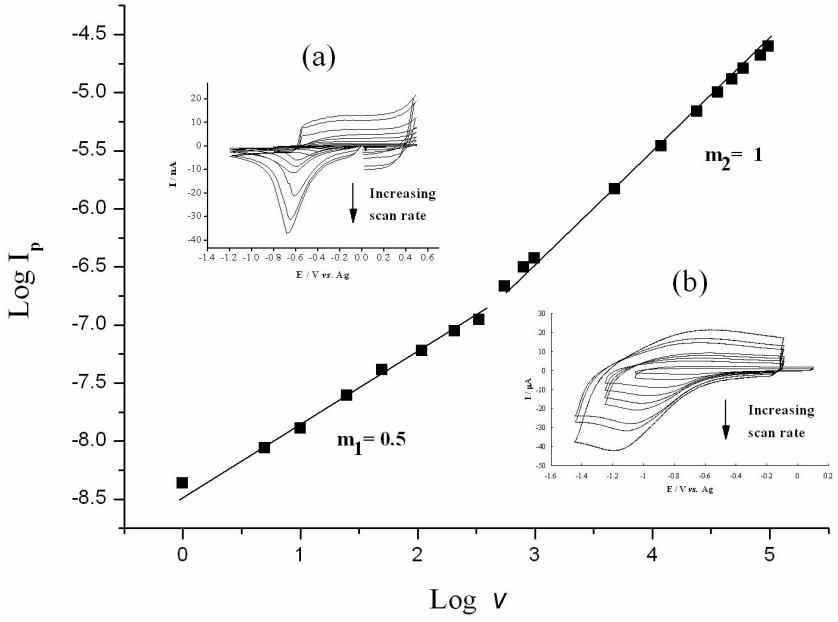


Figure 9.7 Log I_p *vs.* Log v for a solution of 2.0 mM $[Co(NH_3)_6]Cl_3$ in 0.1 M Na_2SO_4 with 0.1 M phosphate buffer (pH = 7.00). Inset 5(a): Cyclic voltammograms obtained at 12.9 μm diameter gold micro-disk electrode with scan rates 1, 5, 10, 50,100, 193, 335, 504, 889 V s^{-1} using a μ-Autolab type II potentiostat and 5(b) with scan rates 4.8, 12, 24, 36, 48, 60, 84, 98, 140 kV s^{-1} using 'fast scan' potentiostat.

9.4.3 Theoretical Results

First, we discuss the theoretical effect of increasing the scan rate on the current-voltage response of adsorbing systems at a microdisk electrode. We will then compare the results obtained with those predicted by the theory for a simple E mechanism at a microdisk electrode.[40-42]

In both cases (adsorbing and non-adsorbing systems), two main phenomena contribute to the overall response of the system: the mass transport in the bulk of the solution and the surface process.

When dealing with a simple E mechanism at a microelectrode, one usually assumes that the diffusion coefficient of the reduced species is at least equal to the that of the oxidised species. This assumption allows one to avoid the situation where the system is limited by the mass transport of the reduced species. The same kind of problem can arise if there is a strong accumulation of the reduced species on the electrode surface. In the case of an electrosorption mechanism, the same situation can arise if there is a strong accumulation of the reduced species on the electrode surface. For simplicity and clarity reasons, we will not consider this situation here and we will assume in the following discussion that the reduced species cannot completely cover the surface ($\theta_B < 1$).

We will denote the characteristic numbers for the mass transport and surface process by χ_T and χ_S respectively.

In both cases considered, the characteristic number for the mass transport is defined by:

$$\chi_T = \frac{D_A}{\delta} \tag{9.18}$$

where δ is the diffusion layer thickness ($\delta = c\sqrt{D_A t}$ where c is a constant $\sqrt{2} < c < 6$).[40,41] Surface processes, however, have a characteristic number dependent on the system under consideration. In the case of a non-adsorbing system we have:

$$\chi_S = k_0 \tag{9.19}$$

and in the case of an electrosorption process, χ_S becomes:

$$\chi_S = K\Gamma k_0 \tag{9.20}$$

It is obvious that these different numbers have the same units (cm s^{-1}) and therefore they can be directly compared with one another. As they represent the relative speed of each process, it is straightforward to determine which one is the rate-limiting process. The ratio χ_T / χ_S is given by ζ and three different situations can arise. If $\zeta < 1$, this corresponds to the case where the mass transport is slower than the surface process. The system is therefore limited by the amount of oxidised species reaching the electrode surface. It should be noted that if $\zeta << 1$, then diffusion is convergent (diffusion to a point) and a steady state is reached.[38-40]

In the case where $\zeta = 1$, the system is "balanced"; the speed at which the electroactive species reaches the electrode surface is the same as the speed at which the oxidised species is reduced.

The final possible situation is where $\zeta > 1$, in which case the surface process is slower than the mass transport and is therefore the rate limiting step.

These results are more easily seen on a log-log plot of the variation of the peak current value as a function of scan rate. It has been shown in ref[37] that given certain limiting conditions (very fast adsorption/desorption) the mathematical model presented

in the theory section gives the same results as the one obtained for a simple E reaction at a microdisk. Using this property we were able to generate the log-log plot for a non-adsorbing system in which the oxidized and reduced species are not adsorbed at the electrode surface. The results are shown in Figure 9.8 (the simulation parameters are given in the Figure legend).

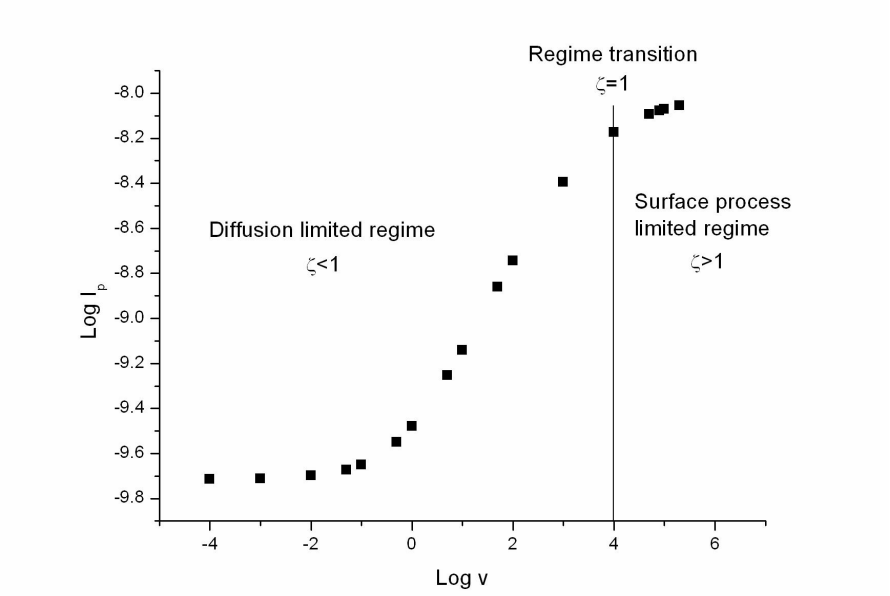


Figure 9.8 Simulation of Log I_p *vs.* Log v for a simple E process at a microdisk electrode. The simulation parameters are as follow: $[A]_{bulk} = 1\times10^{-6}$ M, $r = 1\times10^{-3}$ cm, $\alpha = 0.5$, $D = 1\times10^{-6}$ cm^2 s^{-1}, $k_0 = 0.1$ cm s^{-1}.

The different regimes described previously are clearly noticeable and in good agreement with the theory (according to equations 9.18 and 9.19, the regime transition should occur for $v \geq 20000$ V s^{-1}. Figure 9.7 presents the experimental results obtained for the reduction of hexamminecobalt(III) in aqueous solution. Once again the different controlling regimes are easy to identify. In order to use our simulation program, it is necessary to know the values of some parameters. The diffusion coefficient, D_A, as well as the transfer coefficient, α, has been calculated using experimental results (see

section 9.4.1). Their respective values are $5.3 \pm 0.2 \times 10^{-6}$ cm^2 s^{-1} and 0.51. The value of the maximum monolayer coverage, Γ , can also be determined from the following relationship using experimental results obtained in the surface controlled regime:

$$\Gamma = \frac{1}{nFA_{elec}} \int_t i\, dt \tag{9.21}$$

The value of Γ has been found to be equal to 2×10^{-9} mol cm^{-2}. From Figure 9.7 we can see that the transition between the diffusion-controlled and the surface process controlled regimes occurs for a scan rate approximately equal to 300 V s^{-1}. Using this value we can calculate an approximate diffusion layer thickness, δ , (using a value of $\sqrt{2}$ for c as it is more realistic from a physical point of view) and hence an approximate value for χ_T using equation 14 ($\chi_T \approx 6 \times 10^{-3}$ cm s^{-1}). At the transition point we have $\zeta = 1$; therefore using the known values of Γ and χ_T we can estimate the value of the product Kk_0. The value obtained is 3×10^6 cm^3 mol^{-1} s^{-1}.

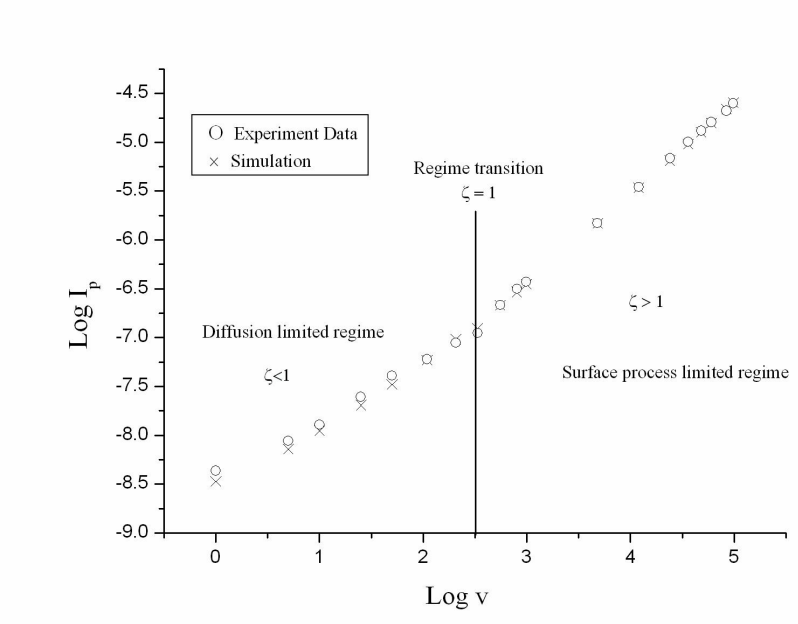


Figure 9.9 Comparison between experimental and theoretical results. The parameters used for the simulation are as follow: $[A]_{bulk} = 2 \times 10^{-6}$ M, $r = 6.45 \times 10^{-4}$ cm, $\alpha = 0.51$, $D = 5.3 \pm 2 \times 10^{-6}$ cm^{2}s^{-1}, $Kk_0 = 3 \times 10^6$ cm^3 mol^{-1} s^{-1}, $\Gamma = 2 \times 10^{-9}$mol cm^{-2}, θ_A (t = 0) = 0.1, E_{start} = 0 V and E_{stop} = -0.8 V (μ-Autolab type II potentiostat), E_{start} = 0 V and E_{stop} = -1.45 V ('fast scan' potentiostat).

At this point we know enough parameters to run the simulation program described in the theory section and to compare the theoretical data with the experimental results. It should be noted that the initial coverage θ_A (t = 0) is difficult to calculate using Equation 4 as we only know the value of the product Kk_0, so its value is optimized to give the best results. The comparison of experimental data with theoretical results is shown in Figure 9.9; it can be seen that the results are in very good agreement thus validating our previous discussion.

9.5 Conclusions

The electrochemical reduction of aqueous hexamminecobalt(III) at gold macro- and micro-electrodes has been investigated. Our results have confirmed that the electrochemical reduction is an irreversible diffusion-controlled process when scan rates of less than ~300 Vs^{-1} are employed. However, it has been found that when faster scan rates are used, the voltammetry becomes characteristic of an adsorbed process. The peak currents measured from the microdisk voltammetry have been simulated using a previously developed mathematical model of adsorption. Excellent agreement has been found between the experimental and theoretical results. Most importantly, this study demonstrates the importance of examining an electrochemical reaction over a wide timescale, as an inference of mechanism from data obtained solely at long timescales may represent an over-simplification. In particular, the 'model' outer-sphere assumption[16,17] may need revisiting.

9.6 References

(1) Willis, J. B.; Friend, J. A.; Mellor, D. P. *J. Am. Chem. Soc.* **1945**, *67*, 1680.

(2) Laitinen, H. A.; Bailar, J. C.; Holtzclaw, H. F.; Quagliano, J. V. *J. Am. Chem. Soc.* **1948**, *70*, 2999.

(3) Laitinen, H. A.; Frank, A. J.; Kivalo, P. *J. Am. Chem. Soc.* **1953**, *75*, 2865.

(4) Laitinen, H. A.; Kivalo, P. *J. Am. Chem. Soc.* **1953**, *75*, 2198.

(5) Masek, J. *J. Electroanal. Chem.* **1959**, *60*, 416.

(6) Kolthoff, I. M.; Khalafalla, S. E. *Inorg. Chem.* **1963**, *2*, 133.

(7) Satterberg, T. L.; Weaver, M. J. *J. Phys. Chem.* **1978**, *82*, 1784.

(8) Barr, S. W.; Guyer, K. L.; Weaver, M. J. *J. Electroanal. Chem.* **1980**, *111*, 41.

(9) Ogura, K.; Fukushima, Y. *Electrochim. Acta.* **1980**, *26*, 93.

(10) Sahami, S.; Weaver, M. J. *J. Electroanal. Chem.* **1981**, *124*, 35.

(11) Yamada, A.; Yoshikuni, T.; Kato, Y.; Tanaka, N. *Anal. Chim. Acta.* **1981**, *133*, 421.

(12) Farquharson, S.; Milner, D.; Tadayyoni, M. A.; Weaver, M. J. *J. Electroanal. Chem.* **1984**, *178*, 143.

(13) Hamelin, A.; Weaver, M. J. *J. Electroanal. Chem.* **1986**, *209*, 109.

(14) Fawcett, W. R.; Fedurco, M.; Kovacova, Z. *J. Electrochem. Soc.* **1994**, *141*, L30.

(15) Wandlowski, T.; Levie, R. D. *J. Electroanal. Chem.* **1995**, *380*, 201.

(16) Hromadova, M.; Fawcett, W. R. *J. Phys. Chem. A.* **2000**, *104*, 4356.

(17) Fawcett, W. R.; Hromadova, M.; Tsirlina, G. A.; Nazmutdinov, R. R. *J. Electroanal. Chem.* **2001**, *498*, 93.

(18) Irena, J.; Algirdas, V.; Asta, G.; Eugenijus, N. *Chemija.* **2002**, *13*, 12.

(19) Jager, R.; Hark, E.; Moller, P.; Nerut, J.; Lust, K.; Lust, E. *J. Electroanal. Chem.* **2004**, *566*, 217.

(20) Simic, M.; Lilie, J. *J. Am. Chem. Soc.* **1974**, *96*, 291.

(21) Bjerrum, J. *Metal Amine Complex Formation*; P. Haase and Son: Copenhagen, 1941.

(22) Yatsimirskii, K. B.; Volchenskova, I. I. *Theoretical and Experimental Chemistry* **1968**, *4*, 808.

(23) Kolthoff, I. M.; Khalafalla, S. E. *Rev. Polarogr.* **1963**, *11*, 11.

(24) Delahay, P.; Trachtenberg, I. *J. Am. Chem. Soc.* **1957**, *79*, 2355.

(25) Delahay, P.; Fike, C. T. *J. Am. Chem. Soc.* **1958**, *80*, 2628.

(26) Laviron, E. *J. Electroanal. Chem.* **1972**, *35*, 333.

(27) Laviron, E. *J. Electroanal. Chem.* **1973**, *43*, 415.

(28) Laviron, E. *J. Electroanal. Chem.* **1981**, *124*, 19.

(29) Laviron, E. *J. Electroanal. Chem.* **1982**, *140*, 247.

(30) Fanelli, N.; Záliš, S.; Pospíšil, L. *J. Electroanal. Chem.* **1990**, *288*, 263.

(31) Laviron, E. *J. Electroanal. Chem.* **1995**, *382*, 111.

(32) Laviron, E.; Roullier, L. *J. Electroanal. Chem.* **1998**, *443*, 195.

(33) Climent, V.; Coles, B. A.; Compton, R. G. *J. Phys. Chem. B.* **2002**, *106*, 5988.

(34) Chevallier, F. G.; Klymenko, O. V.; Jiang, L.; Jones, T. G.; Compton, R. G. *J. Electroanal. Chem.* **2004**, *574*, 217.

(35) Amatore, C.; Maisonhaute, E.; Simmonneau, G. *Electrochem. Commun.* **2000**, *2*, 81.

(36) Amatore, C.; Maisonhaute, E.; Simmonneau, G. *J. Electroanal. Chem.* **2000**, *486*, 141.

(37) Clegg, A. D.; Rees, N. V.; Klymenko, O. V.; Coles, B. A.; Compton, R. G. *J. Am. Chem. Soc.* **2004**, *126*, 6185.

(38) Sharp, P. *Electrochim. Acta.* **1983**, *28*, 301.

(39) Jacob, S. R.; Qi, H.; Coles, B. A.; Compton, R. G. *J. Phys. Chem. B.* **1999**, *103*, 2963.

(40) Bard, A. J.; Faulkner, L. F. *Electrochemical Methods: Fundamentals and Applications*, 2nd edition ed.; John Wiley: New York, 2001.

(41) Aoki, K.; Tokuda, K. *J. Electroanal. Chem.* **1987**, *237*, 163.

(42) Aoki, K. *Electroanalysis* **1993**, *5*, 627.

CHAPTER 10

The Electrochemical Oxidation of Ammonia at Boron-Doped Diamond Electrodes

Boron-doped diamond electrodes are shown in this chapter to exhibit well-defined analytically useful voltammetric signals for the electrochemical oxidisation of ammonia in aqueous solutions in comparison to commonly used electrode substrates. Proof-of-concept is shown for the construction of a miniature amperometric ammonia gas sensor utilising conductive boron-doped diamond particles supported on a PTFE gas-porous, hydrophobic support. This work discussed in this chapter has been published as an article in *Analyst*, **2005**, 130, 1345.

10.1 Introduction

The sensing of ammonia is of wide importance due to its high toxicity and numerous applications where the gas is used or generated, which includes environmental protection, clinical diagnosis, industrial processes, food processing and power plants.[1-5] Ammonia detection is also important for the diagnosis of diseases such as renal inadequacy and diabetes.[2-5] Another important arena for ammonia

determination is in water samples where it indicates organic material decomposition which can be harmful to human health,[6] whilst higher ammonia levels are of analytical interest in industrial operations such as refrigeration or fertilizer manufacture. It is evident that there is a whole diversity of applications that require ammonia monitoring.

Sensors for ammonia are typically based on the gas diffusion cell approach where ammonia gas diffuses through a gas permeable hydrophobic membrane into an electrolyte recipient solution where ammonia is detected by electrochemical, potentiometric or colorimetric methodologies.[7] In these approaches, interferents are removed providing selectivity in complex media.[7] In these sensor designs, electrochemical strategies are advantageous due to their minimization, low cost, rapid response and their inherent high sensitivity and selectivity. Amperometric electrochemical techniques commonly utilize metal electrodes such as gold, silver, platinum and copper.[4, 5]

In this chapter we report the first example of the electrochemical oxidation of ammonia at boron-doped diamond electrodes. The voltammetric response is directly compared with other commercially available electrode substrates, namely glassy carbon, edge plane and basal plane pyrolytic graphite and highly ordered pyrolytic graphite electrodes. Boron-doped diamond is shown to provide an analytically useful signal, suggesting that boron-doped diamond electrodes are a near optimal choice as electrode substrates in amperometric electrochemical ammonia sensors. We also show proof-of-concept of by constructing a miniature gas sensor for the amperometric detection of ammonia utilising conductive boron-doped diamond particles supported on a PTFE gas-porous hydrophobic support.

10.2 Experimental

10.2.1 Chemicals

All chemicals used were of analytical grade and used as received without any further purification. Ammonia was obtained from BOC Gases (Guildford, Surrey, UK). Extreme care is need when handling this gas. Solutions were prepared with deionised water of resistivity not less than 18.2 M Ohm cm (Vivendi water systems, UK). In all experiments the solution was purged first with oxygen-free nitrogen gas to remove any oxygen present (BOC Gases, Guildford, Surrey, UK) for at least 30 minutes. Ammonia was introduced into the solution directly from a cylinder containing 0.1 % ammonia (1000 ppm) by saturating the solution for various periods of time.

10.2.1 Instrumentation

Voltammetric measurements were carried out using a μ-Autolab II potentiostat (ECO-Chemie, The Netherlands) with a three electrode configuration. The working electrode used were boron-doped diamond, (BDD, 3 mm diameter, Windsor Scientific Ltd) glassy carbon, (GC, 3 mm diameter BAS Technicol, USA) and edge and basal plane pyrolytic graphite electrodes, (EPPG, BPPG, Le Carbone, Ltd. Sussex, U.K.) Discs of pyrolytic graphite were machined into a 4.9 mm diameter, which was oriented with the disc face parallel with the edge plane, or basal plane as required. The counter electrode was a bright platinum wire, with a saturated calomel electrode completing the circuit. The GC and BDD electrode was polished using diamond pastes of decreasing sizes (Kemet, UK) while the edge plane pyrolytic graphite electrode was polished on alumina lapping compounds (BDH) of decreasing sizes (0.1 - 5 μm) on soft lapping pads. The basal plane pyrolytic graphite electrode was prepared by renewing the electrode surface with cellotape. This procedure involves polishing the BPPG electrode

surface on carborundum paper and then pressing cellotape on the cleaned BPPG surface before removing along with general attached graphite layers. This is then repeated several times. The electrode was then cleaned in acetone to remove any adhesive. The highly ordered pyrolytic graphite electrode (HOPG) was constructed in house and is described in detail in ref.[8]

10.3 Results and Discussion

10.3.1 Electrochemical oxidation of NH_3

Initial examination was made of the cyclic voltammetric responses of boron-doped diamond (BDD), glassy carbon (GC), edge plane and basal plane pyrolytic graphite (EPPG, BPPG) electrodes in a 0.1 M potassium chloride solution through which 0.1 % ammonia was bubbled for 4 minutes. The observed responses are shown in Figure 10.1 where it can be clearly seen that boron-doped diamond electrode exhibits the most analytically most useful oxidation wave at *ca.* + 1.1 V (vs. SCE). Note that the voltammograms are also shown in the absence of ammonia (dashed lines, Figure 10.1) confirming that the wave corresponds to the electrochemical oxidation of ammonia. The GC and BPPG electrodes exhibit a voltammetric wave corresponding to the electrochemical oxidation of ammonia that is ill-defined with large background currents which will inevitably limit their analytical efficiency. Note that in comparison to the BPPG and GC electrodes, a low background current is observed at the BDD electrode for the oxidation of ammonia, which has made BDD electrodes attractive for use in the field of electroanalysis, facilitating low detection limits and high sensitivities.[9]

It is interesting to note that the edge plane electrode did not exhibit an oxidation wave, which is in contrast to that seen at the basal plane electrode. At first sight this is somewhat surprising since the published research by our group[10] has demonstrated that edge plane sites typically exhibit faster heterogeneous charge transfer than basal plane sites and thus a greater number of edge plane sites should show improved electrochemical reversibility, that is, the peak should shift to less positive potentials as the number of edge plane sites are increased.

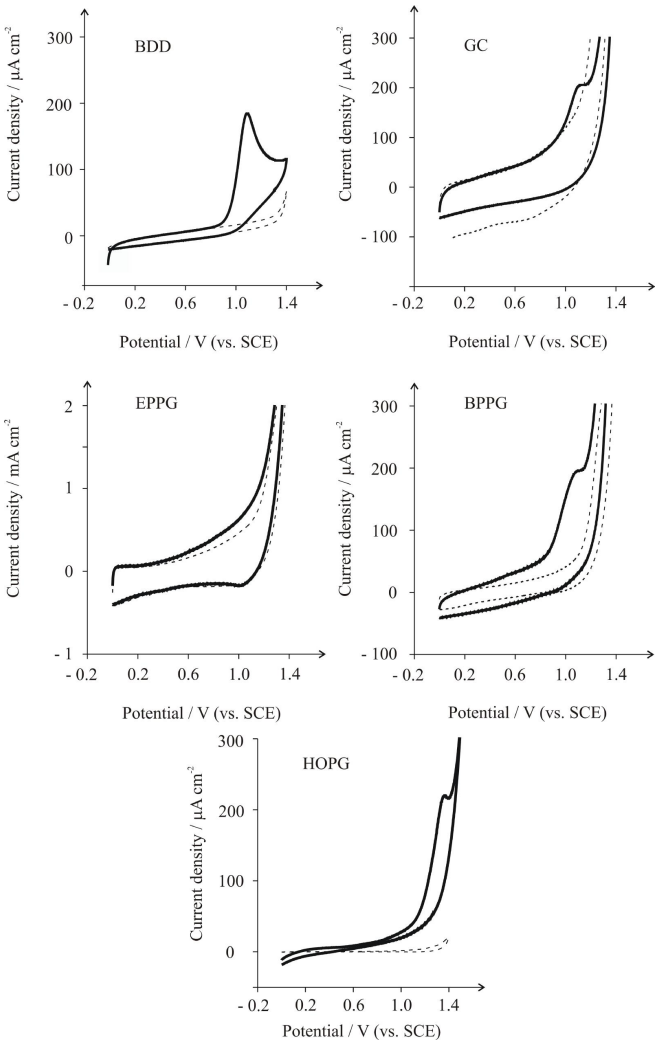


Figure 10.1 Cyclic voltammetric response of boron-doped diamond (BDD), glassy carbon (GC), edge plane pyrolytic graphite (EPPG), basal plane pyrolytic graphite (BPPG) and (HOPG) electrodes in a 0.1 M KCl aqueous solution which has had 0.1 % ammonia bubbled through it for 4 minutes. The dashed line is the response of the electrode in the absence of ammonia. The scan rate in all cases were 100 mVs^{-1}.

The way the BPPG is prepared results in a low proportion of edge plane sites (and consequently a large number of basal plane sites); there are even less edge plane sites at the HOPG electrode. To further explore this, the electrochemical oxidation of ammonia at a HOPG electrode was examined. As shown in Figure 10.1 an oxidation wave is observed at *ca.* + 1.36 V (vs. SCE). Comparison of the edge plane, basal plane and highly ordered pyrolytic graphite electrodes reveals that initially, as the proportion of edge plane sites are increased the voltammetric response shifts to less negative potentials, as evidenced by the oxidation peak of ammonia at + 1.36 on HOPG shifting to + 1.1 V at the BPPG. However, when a large proportion of edge plane sites are introduced, (when the EPPG electrode is used) a large current density is observed in comparison to the other electrode substrates but with no visible oxidation peaks observable. We note that it is well known that ammonia intercalates graphite together with alkali or alkaline earth metals.[11, 12] Furthermore research in this group has shown that lithium cations can partially intercalate at edge plane defect sites in between plane layers.[13] Such an intercalation process following or preceding intercalation might explain the large currents seen in Figure 10.1 at relatively low potentials which appears Faradaic rather than capacitative and the absence of any waves corresponding to the oxidation of ammonia. It is clear that pyrolytic graphite electrodes with a high proportion of edge planes, and carbon nanotubes where the edge plane sites are at the open ends and along the tube axis, are probably less suitable for use in electrochemical ammonia sensors.

Figure 10.2 illustrates the voltammetric response of the BDD electrode in a 0.1 M KCL solution with 0.1 % ammonia gas bubbled through the solution for periods of four minutes up to 30 minutes. A linear response of peak height versus bubbling time is shown in the insert of Figure 10.2. The observed high solubility of ammonia in aqueous

solution is well known where ammonia acts as a base, acquiring hydrogen ions from water to yield ammonium and hydroxide ions. To ensure that the response in Figure 10.1 and Figure 10.2 arises purely from the electrochemical oxidation of ammonia and not oxidation of hydroxide ions, hydroxide solutions were prepared over the range 1 mM to 1 M with the voltammetric response explored. The voltammogram was swept from 0 V up to 1.4 V which is just before the onset of solvent decomposition, but no voltammetric waves were observed.

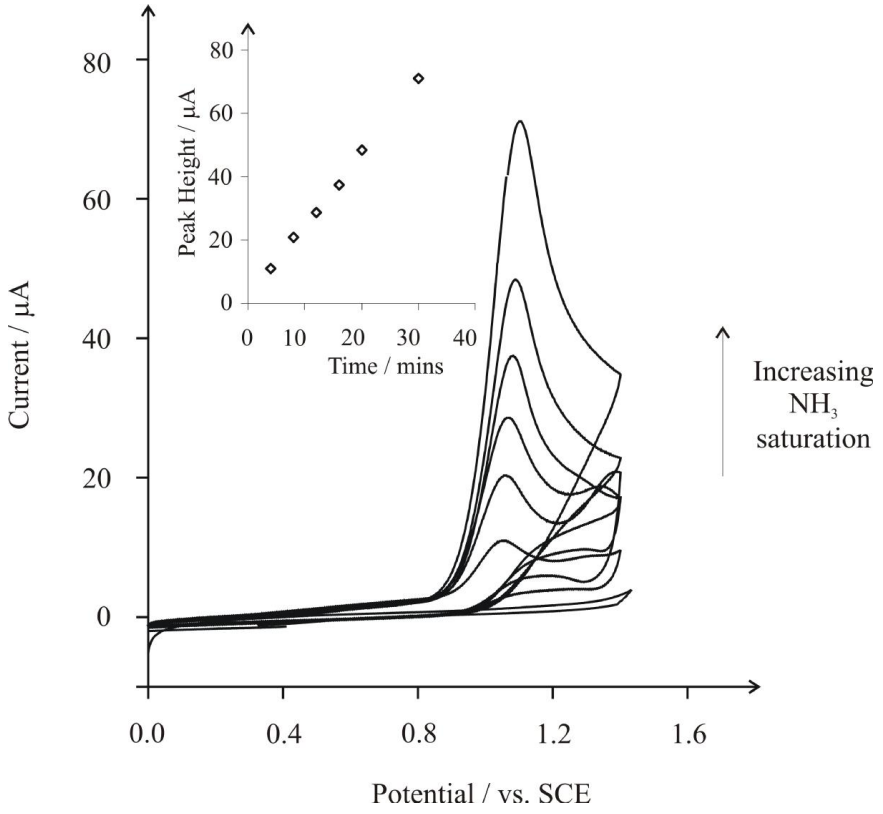


Figure 10.2 Cyclic voltammetric responses from exposing a solution of 0.1 M KCl aqueous solution to 0.1 % ammonia for 4, 8, 12, 16, 20 and 30 minutes using a (3mm diameter) boron-doped diamond electrode. Solution volume was 25 mL. Scans were run at 100 mV s^{-1}.

Next a 0.1 M KCl solution was saturated with 0.1 % ammonia for 30 minutes with the response of increasing the scan rate explored. The observed voltammetric response is depicted in Figure 10.3, where a plot of peak height (I_H) versus square root of scan rate shows a linear response (I_H / A = 2.03 x 10^{-4} $V^{1/2}s^{-1/2}$) indicating that the

voltammetric response arises from diffusion rather than adsorption. Tafel analysis of voltammograms, plotted as potential vs. log current produced a value of 142 mV per decade (at a scan rate of 100 mVs^{-1}) suggesting an electrochemically irreversible process. The oxidation of ammonia in 0.1 M sodium hydroxide (pH 13), 0.1 M borate buffer (pH 10) and 0.1 M ammonium chloride (pH 4.5) were explored and found to produce identical responses as that shown in Figure 10.1. The mechanism of the electrochemical oxidation of ammonia is likely to be:

$$4NH_3(g) - 3e^- \rightarrow 3NH_4^+ + 1/2N_2(g) \qquad (10.1)$$

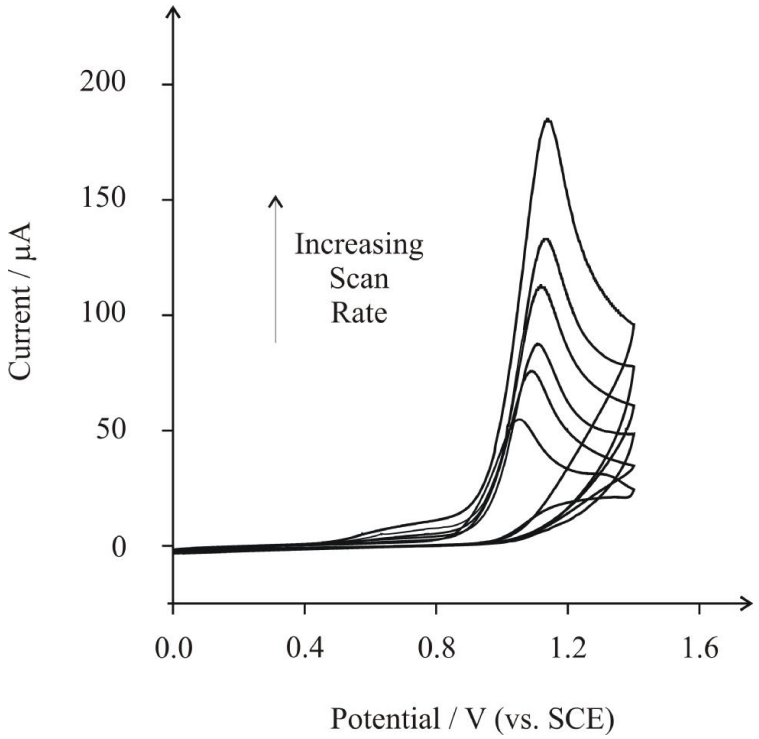


Figure 10.3 Response of increasing the scan rate at a boron-doped diamond electrode (3 mm diameter) in a 0.1 M KCl solution which has had 0.1 % ammonia bubbled through it for 30 minutes. The scan rates are (from bottom to top) 50, 100, 200, 300, 500, 800 mV s^{-1}.

10.3.2 A Miniature Amperometric Sensor

Next we turn to showing proof-of-concept of using a boron-doped diamond in to a miniature amperometric electrochemical sensor, which is based on the gas diffusion cell approach. An electrode substrate was first constructed by adding Fluon® (tetrafluoroethylene co-polymer) into water - surfactant solution containing boron-doped diamond particles (Element Six, The Netherlands). This is then 'baked' in an oven at > 300^{o}C to initiate polymerisation which binds the BDD particles onto a gas-porous matrix. This is then machine pressed onto a gas-porous, hydrophobic support which comprises Gore^{TM} PTFE (*ca.* 2.5 cm diameter). This was then incorporated into the electrochemical cell as shown in Figure 10.4 which has a three-electrode arrangement with a graphite counter electrode and silver wire acting as a quasi-reference electrode. Each of the electrodes are separated by wetting filters with the overall size of sensor being approximately 3 cm in diameter and 1.5 cm in height with 0.1 M KCl as the supporting electrolyte. This basic and universal configuration is similar to commercially available ammonia sensors. Shown in Figure 10.6A is an SEM image of the edge of the BDD electrode which highlights how the electrode is constructed, where it can be observed that BDD conductive particles are immobilised onto the PTFE gas-porous hydrophobic support. Further SEM images of the electrode surface are presented in Figure 10.5, where the BDD particles range in size from *ca.* 1 micron up to *ca.* 5 microns.

The electrochemical sensor was connected to a potentiostat and operated amperometrically with the working electrode held at a potential of + 1.08 V (vs. Ag wire). After *ca.* 66 seconds 0.1 % ammonia gas was flowed over the top of the electrochemical sensor at the gas permeable membrane (see Figure 10.4) for *ca.* 5 seconds. The response is shown in Figure 10.6B, where a rapid jump in current is

observed due to the ammonia diffusing to the electrode and being rapidly oxidised as described via equation 10.1.

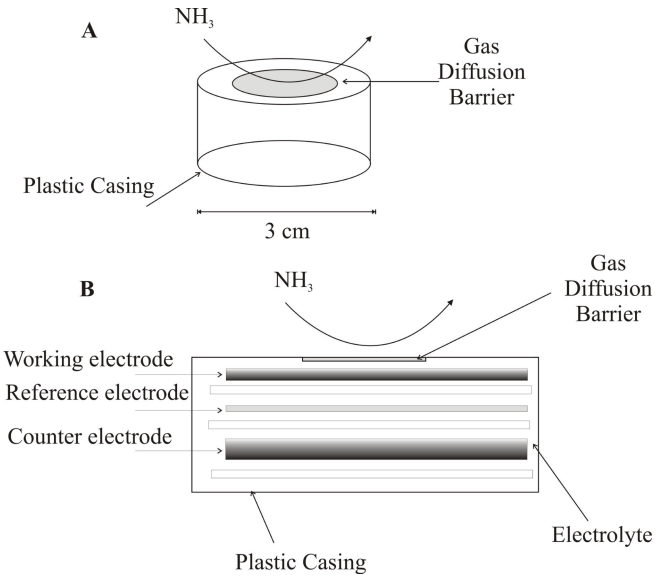


Figure 10.4 Schematic representation of an electrochemical gas sensor (A) incorporating a gas diffusion membrane which is approximately 3 cm by 1.5 cm. The sensor is based on a three-electrode arrangement (B) with BDD as the working electrode with a graphite counter and a silver wire as the reference electrode. The supporting electrolyte was 0.1 M KCl.

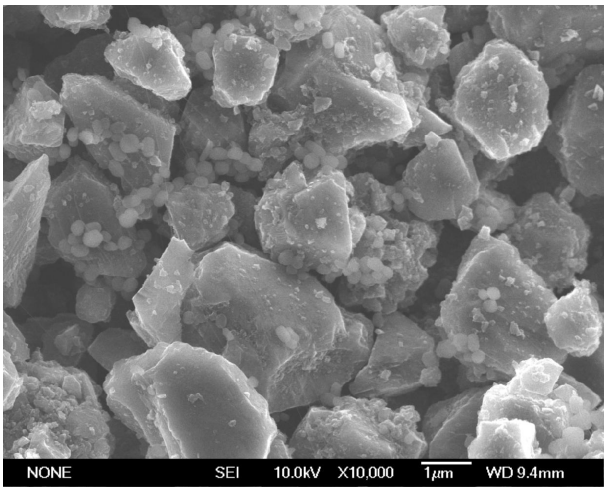


Figure 10.5 SEM images of the BDD conductive particles which make up the BDD working electrode. The particles are conductive BDD particles which are in the range of *ca.* 1 micron up to *ca.* 5 microns in size.

The ammonia gas was then stopped at *ca.* 71 seconds after which the current was observed to slowly decrease as ammonia is continuously electrochemically oxidised or diffuses out of the sensor. Nitrogen gas was introduced (at *ca.* 82 seconds) to help

accelerate the current back to a stable baseline, which reaches the same current magnitude as before the 0.1 % ammonia was introduced. At *ca* 102 seconds 0.1 % ammonia gas was again introduced above the gas permeable membrane for *ca.* 5 seconds which has again results in a large current increase. The current is again observed to decrease as the ammonia is electrochemically oxidised at the BDD surface or diffuses from the device and reaches back to the current level that was observed before the ammonia was introduced, which indicates that the sensor can be used repetitively times. The observed sharp rises in current when ammonia is introduced above the gas permeable membrane might be used to trigger an alarm to indicate the escape of ammonia gas, for example in industry settings.

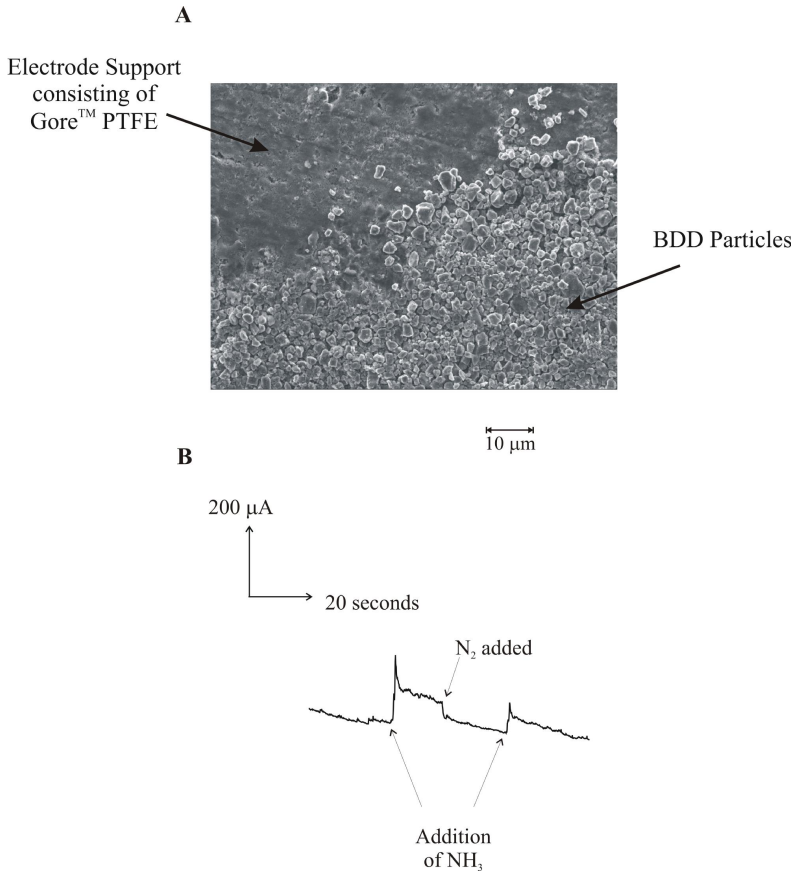


Figure 10.6 SEM image of the BDD working electrode (A). The image is of the edge of the working electrode which highlights the BDD conductive particles immobilised onto the PTFE gas-porous hydrophobic support. (Further SEM images of the electrode surface are presented in Figure 10.5) The amperometric response of the cell which utilising the BDD conductive particles is shown in (B).

10.4 Conclusion

The direct oxidation of ammonia at boron-doped diamond electrode provides the basis for the sensitive, direct detection of ammonia using Clark cell type gas sensors in conjugation with aqueous electrolyte. We have reported the first ever example of using boron-doped diamond (BDD) electrodes for the oxidation of ammonia. It is demonstrated that BDD produces the best voltammetric response in comparison to the other electrode substrates suggesting that BDD is routinely used in commercial electrochemical sensors for the detection of highly toxic ammonia. Proof-of-concept is also shown for an amperometric sensor which is constructed (based on commercial gas sensing methodologies) where the working electrode consists of conductive boron-doped diamond particles supported on a PTFE gas-porous hydrophobic support.

10.5 References:

(1) Timmer, B.; Olthuis, W.; van den Berg, A. *Sensors and Actuators B*. **2005**, *107*, 666.

(2) Vidotti, M.; Dall, L. H.; Cordoba de Torresi, S. I.; Bergamaski, K.; Nart, F. C. *Anal. Chim. Acta*. **2003**, *489*, 207.

(3) Lopez de Mishima, B. A.; Lescano, D.; Molina Holgado, T.; Mishima, H. T. *Electrochimica Acta*. **1998,** *43*, 395.

(4) de Vooys, A. C. A.; Koper, M. T. M.; van Santen, R. A.; van Veen, J. A. R. *J. Electroanal. Chem*. **2001**, *506*, 127.

(5) Giovanelli, D.; Buzzeo, M. C.; Lawrence, N. S.; Hardacre, C.; Seddon, K. R.; Compton, R. G. *Talanta* **2004**, *62*, 904.

(6) Burgess, R. M.; Perron, M. M.; Cantwell, M. G.; Ho, K. T.; Serbst, J. R.; Pelletier, M. C. *Archives of Environmental Contamination and Toxicology* **2004**, *47*, 440.

(7) Lahdesmaki, I.; Kubiak, W. W.; Lewenstam, A.; Ivaska, A. *Talanta* **2000**, *52*, 269.

(8) Bowler, R.; Davies, T. J.; Hyde, M. E.; Compton, R. G. *Anal. Chem.* **2005**, *77*, 1916.

(9) Compton, R. G.; Foord, J. S.; Marken, F. *Electroanalysis* **2003**, *15*, 1349.

(10) Banks, C. E.; Davies, T. J.; Wildgoose, G. G.; Compton, R. G. *Chem. Commun.* **2005**, *7*, 829.

(11) Qian, X. W.; Solin, S. A. *Solid Stat Commun.* **1987**, *62*, 117.

(12) Akuzawa, N.; Kawahara, S.; Sakuno, H.; Amemiya, T.; Takahashi, Y. *Carbon* **1988**, *26*, 104.

(13) Wildgoose, G. G.; Wilkins, S. J.; Williams, G. R.; France, R. R.; Carnahan, D. L.; Jiang, L.; Jones, T. G. J.; Compton, R. G. *ChemPhysChem* **2005**, *6*, 352.

CHAPTER 11

Electrode Kinetic Studies of Hydroquinone and Benzoquinone in Propylene Carbonate

The oxidation of hydroquinone and reduction of benzoquinone have been studied by cyclic voltammetry at glassy carbon electrodes in propylene carbonate. Simulation was used to model the cyclic voltammetric responses of macroelectrodes to give electrode kinetic information for the electrochemical oxidation of hydroquinone and reduction of benzoquinone. Next, the reaction between ammonia and hydroquinone was investigated. It is shown that ammonia reversibly removes one proton from the hydroquinone molecules, resulting in a new wave observed at *ca.* + 0.15 V (vs. Ag wire). Finally by measuring the peak current of new wave as function of ammonia concentration its analytical utility for ammonia sensing was examined in the range from 10 and 100 ppm. This work discussed in this chapter has been published as an article in *J. Phys. Chem. C*, **2007**, 111, 1496.

11.1 Introduction

The electrochemical behaviour of quinones has previously been studied in a number of traditional aprotic solvents including acetonitrile.[1-12] In such media, the oxidation of hydroquinone (QH_2) at platinum electrodes is an electrochemically irreversible two-

electron process[4,5] whereas in water[11,13,14] the electrode kinetics are fast. A single irreversible two-electron reduction wave was observed on the reverse sweep following the oxidation of hydroquinone. In 1969, Eggins has also shown the influence of the hydroxyl base on the voltammetric response of hydroquinone in acetonitrile. The redox potential after adding an excess of tetra-n-butylammonium hydroxide to an acetonitrile (MeCN) solution containing hydroquinone almost shifted negatively to 1 V (vs. *SCE*) to much the same potential as that of benzoquinone,[5] suggesting that a chemical-electrochemical (CE) step took place:

$$QH_2 + 2OH^- \rightleftharpoons Q^{2-} + 2H_2O \tag{11.1}$$

$$Q^{2-} \overset{-e}{\rightleftharpoons} Q^{-\cdot} \overset{-e}{\rightleftharpoons} Q \tag{11.2}$$

in which the hydroquinone dianion formed via dissociation of hydroquinone is electrochemically oxidized to benzoquinone in two separate one-electron transfer steps. It is clear that the redox potential of the hydroquinone can be changed by adding the base to remove protons, making the oxidative process easier. Developing this idea, Giovanelli *et al* examined whether the acid-base equilibria between ammonia and hydroquinone in *N,N*-dimethylformamide could be used for ammonia sensing.[15] It was shown that in the presence of ammonia a new wave at a less positive potential appeared, and it was attributed to ammonia removing one proton from the hydroquinone. Furthermore they successfully illustrated the analytical ability of this system for ammonia sensing assessed by measuring the peak current of the pre-wave as function of ammonia concentration in *N,N*-dimethylformamide.

In this chapter, we have investigated the electrochemical oxidation of hydroquinone and reduction of benzoquinone in propylene carbonate (PC) at glassy carbon electrodes. We discuss chronoamperometric experiments which gave diffusion coefficients of these two species, reflecting the higher viscosity of propylene carbonate (2.51 mPa s at 298 K) compared to the inert familiar aprotic solvent (MeCN, 0.34 mPa s at 298 K),[16] resulting in slower mass transport and lower diffusion coefficients. By using simulation, the cyclic voltammetric responses for both hydroquinone and benzoquinone have been modelled successfully, employing the mechanisms shown in more details in the text below. Excellent agreement is found between experimental and theoretical results.

Next the reaction between ammonia and hydroquinone has been explored and a new oxidation wave was formed at *ca.* + 0.15 V (vs. Ag wire). It was found that the oxidation peak current of the new voltammetric response was linearly dependent on the concentration of ammonia, exhibiting its analytical utility for ammonia sensing, especially noting that the sensing of ammonia is of wide importance due to its high toxicity and numerous applications where the gas is used or generated, which includes environmental protection, clinical diagnosis, industrial processes, food processing and power plants.[17-20] Moreover, the solvent used here, propylene carbonate has some properties desirable for an ammonia gas sensor, most notably low volatility in comparison with acetonitrile or *N,N*-dimethylformamide.[21] The most common design for commercial gas sensors is based on the gas diffusion cell approach where the gas under investigation diffuses through a gas permeable hydrophobic membrane into an electrolyte recipient solution where ammonia is detected either by amperometric ('Clark Cell'), potentiometric or colorimetric methodologies.[20] In these approaches, possible interferents may be removed via employing the use of a membrane which provides selectivity in complex media.[20] Generally the electrolyte employed in the

sensors is water based. The appreciable vapour pressure of water, 17.5 mm Hg (at 290 K), inevitably means that the sensor will dry out over time so limiting the lifetime at typical operating temperatures and restricting the sensor reliability.[22] Note the vapour pressure of propylene carbonate is 0.03 mm Hg (at 290 K).[22] Therefore by using propylene carbonate based electrolytes the sensor lifetime maybe greatly extended as the tendency for the sensor to 'dry-out' is significantly reduced.

11.2. Experimental

11.2.1. Chemicals

Propylene carbonate (Aldrich, 99.7%), tetra-n-butylammonium perchlorate (TBAP, Fluka), hydroquinone (Aldrich, 99%), and benzoquinone (Aldrich, 98%) were purchased at the highest grade available and used directly without further purification. Pure ammonia and nitrogen gas (BOC, Guildford, Surrey, UK) were used for electrochemical experiments as described below. All the solutions were vigorously degassed with oxygen-free nitrogen (BOC Gases, Guildford, Surrey, UK) until oxygen was not electrochemically detectable. All experiments were carried out at a temperature of 295 ± 3 K.

11.2.2 Instrumentation

Electrochemical experiments were performed using a μ-Autolab type II potentiostat (Eco-Chemie, Utrecht, Netherlands) controlled by General Purpose Electrochemical Systems v.4.7 software. For electrochemical experiments carried out at macrodisk in the electrolyte, the working electrode used was glassy carbon (GC), together with a platinum wire counter electrode, and a silver wire reference electrode. The GC was polished using diamond-lapping compounds (Kemet, UK). The

electrochemical cell used was a septum sealed three-necked flask which was always held under a nitrogen atmosphere. In experiments where ammonia was utilised, the gas was directly introduced from a cylinder containing volume percentages (0.001 vol %, 0.005 vol %, 0.01 vol % 0.1 vol % and 10 vol %, BOC Gases, Guildford, Surrey, UK) by bubbling the ammonia directly into the solution for various periods of time (nitrogen comprises the remaining part of all the gas mixtures).

For experiments at the microdisk, two 25 μm diameter gold and platinum electrodes were used. The microelectrodes were polished using 1.0 μm alumina-water slurry (Buehler) on soft polishing pads (Microcloth, Buehler). The microelectrode diameter was calibrated electrochemically by examining the steady state current of 2.0 mM ferrocene in acetonitrile with 0.1 M TBAP, using a literature diffusion coefficient of 2.30×10^{-5} cm^2 s^{-1}.[23,24] A silver wire reference electrode was used, together with a platinum wire counter electrode.

In situ electrochemical ESR experiments were carried out using a gold tube flow cell, the construction and characterization of which has been described previously.[25] A gold gauze counter electrode was positioned downstream from the gold working electrode and a silver wire reference was placed up stream. As a result of the highly resistive nature of the cell design, it was necessary to attach a 0.1 μF capacitor between the reference and counter electrodes in order to ensure electrochemical stability under steady-state potentiostat control. Fluid motion was maintained using a gravity flow system employing glass capillaries to achieve slower flow rates. The volume flow rates achieved were in the range of 0.1×10^{-3} to 100×10^{-3} cm^3 s^{-1}. The tube electrode surface was cleaned between experiments with 3 micron diamond spray (Kemet) using a tungsten rod to polish. The electrode length was calibrated at 1.7 mm using a diffusion

coefficient of ferrocene in supported acetonitrile.[23, 24] The tube diameter was measured at 1 mm using callipers.

ESR spectra were obtained using a JEOL JES-FA100 X-band spectrometer with a cylindrical (TE011) cavity resonator.[26] The cell was positioned in this cavity such that x_{gap}, the distance between the upstream edge of the electrode and the end of the sensitive region of the cavity, measured 2 mm. Cavity tuning was achieved using the JEOL spectrometer software (A-SYSTEM v.1.100, FA-MANAGER v.1.01). To account for variations in cavity Q, signal intensities were measured relative to a standard marker consisting of solid MgO dispersed with Mn^{2+}, inserted into the cavity at the time of measurement. In all of the experiments, a microwave power of 1 mW was used and regular tests were carried out to check that increasing the microwave power increased the ESR signal. Doing so ensured that the system was not power saturated such that the doubly integrated ESR signal intensity gave a direct measure of the number of electrogenerated spins in the cavity.[26]

11.3 Results and Discussion

11.3.1 Electrochemical Study of Hydroquinone

11.3.1.1 Cyclic Voltammetry of Hydroquinone in PC

The electrochemical oxidation of hydroquinone (QH_2) was first investigated by recording the cyclic voltammetry of 0.5mM hydroquinone in a propylene carbonate (PC) solution supported with 0.1 M TBAP using a 3 mm diameter glassy carbon (GC) electrode. The voltammetric response is shown in Figure 11.1 where a single oxidation wave at *ca.* + 1.0 V (vs. Ag wire) and a corresponding reductive wave at *ca.* + 0.3 V (vs. Ag wire) is observed. The inset Figure shows the plot of the oxidative and reductive peak currents against the square root of scan rate (50～1000 mVs^{-1}).

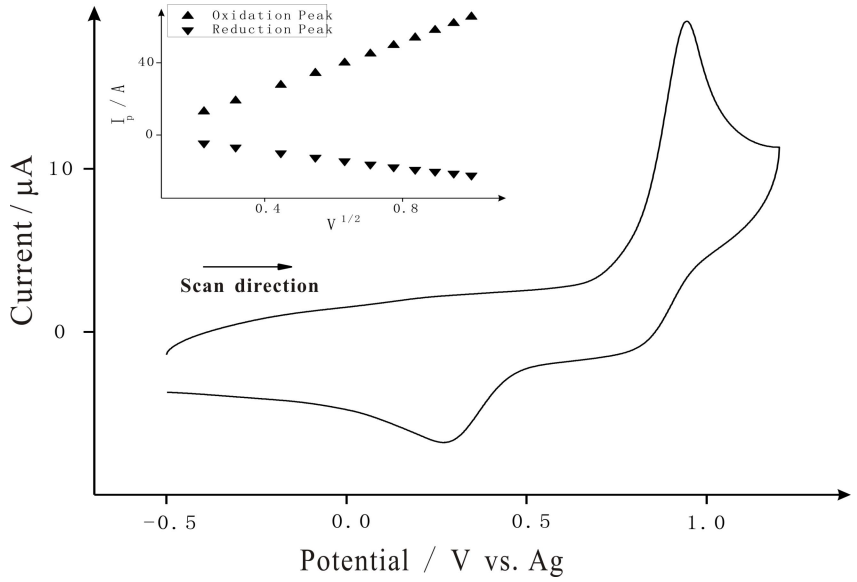


Figure 11.1 Cyclic voltammetric responses of 0.5 mM hydroquinone in 0.1M TBAP with propylene carbonate (PC) as the solvent using a (3 mm diameter) glassy carbon electrode (GC). Scans were run at 100 mV s^{-1}. Inset: The plot of the oxidation peak current and the reduction current for hydroquinone against the square root of scan rates (50, 100, 200,300, 500, 600, 700, 800, 900, 1000 mV s^{-1})**.**

Excellent linear relationships are observed suggesting that the electrochemical processes involved solution based processes rather than surface-controlled at these scan rates. The electrochemical oxidation of hydroquinone most likely proceeds via the following electrochemical step:[27-31]

$$QH_2 \overset{-2e}{\rightleftharpoons} QH_2^{2+} \tag{11.3}$$

where QH_2^{2+} is doubly protonated p-benzoquinone. The stability of this di-cation in the aprotic solvent, PC, was proved by continuous cyclic voltammetric scans shown in Figure 11.2. It was found that no new waves either oxidation or reduction appear on the second or subsequent scans, demonstrating that the oxidation product of hydroquinone can combine with protons in PC in the experiment time scale. Moreover, the number of

electron transfer has been shown to be two by chronoamperometric experiment as explained below.

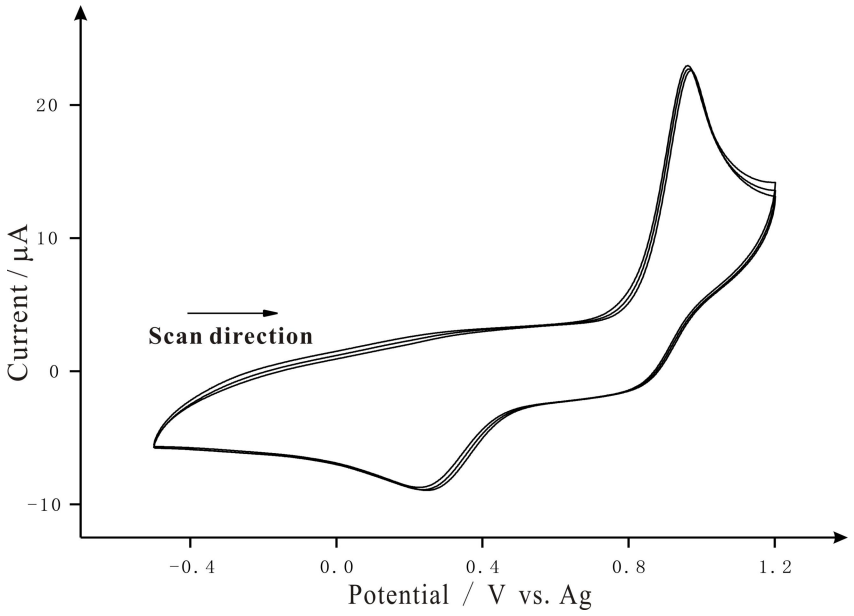


Figure 11.2 Cyclic voltammetric response (100 mVs^{-1}) obtained at GC electrode for 1.0 mM hydroquinone in PC with 0.1M TBAP.

Next the voltammetry at a calibrated platinum microelectrode was recorded in an PC solution containing 5.0 mM hydroquinone supported with 0.1M TBAP at a scan rate of 10 mV s^{-1}. The 'steady-state' voltammetric response is depicted in Figure 11.3, and the inset shows the chronoamperometric response. The chronoamperometric transients was attained by stepping a potential from a region of no current flow to a potential of a +1.4 (vs. Ag wire) where the two-electron oxidation of hydroquinone occurs at a diffusion controlled rate, and the current response monitored as a function of time. The recorded transients were fitted using nonlinear curve fitting function available in ORIGIN 6.0 (Microcal Software Inc.) with the following equations (4-6),[32] as previously employed by Compton and co-workers.[33, 34]

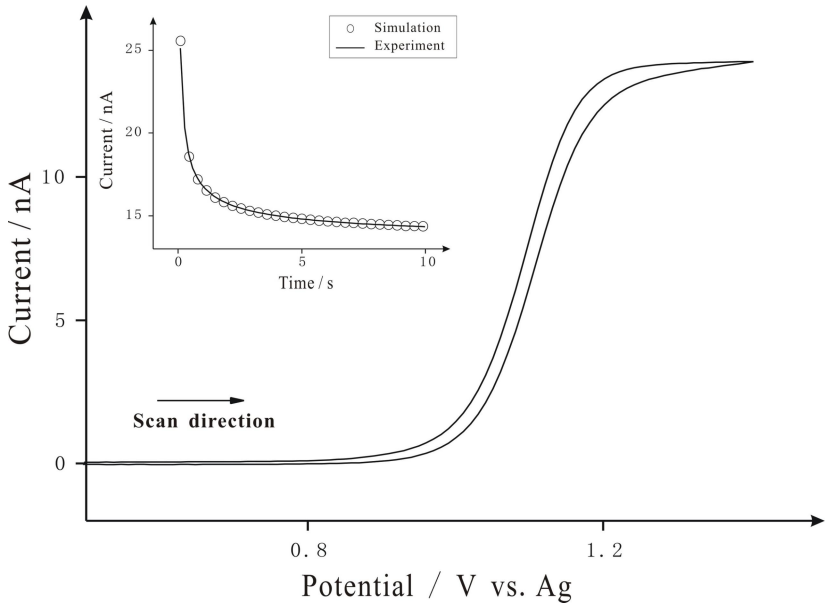


Figure 11.3 Steady state voltammogram of 5.0 mM hydroquinone (10 mVs^{-1}) in PC with 0.1M TBAP obtained at a 25 μm platinum microdisk. The inset Figure is the experimental (–) and fitted theoretical (○) chronoamperometric transient following a potential step from 0 V to +1.4 V.

$$I = -4nFDcr_d f(\tau) \tag{11.4}$$

$$f(\tau) = 0.7854 + 0.8863\tau^{-1/2} + 0.2146e^{-0.7823\tau^{-1/2}} \tag{11.5}$$

$$\tau = \frac{4Dt}{r_d^2} \tag{11.6}$$

where n represents the number of electrons transferred, F is the Faraday constant, D is the diffusion coefficient, c is the concentration, r_d is the radius of the micro disk electrode and t is the time. At this point with the fixed value of the radius of electrode it is possible to obtain the value for diffusion coefficient, D, of the species and the result of the concentration multiplied with the number of electrons, nC transferred by fitting the experiment data over an appropriate time period. Thus via the chronoamperometry, it was confirmed that the electrochemical oxidation of hydroquinone is a two-electron process. Moreover, the diffusion coefficient of hydroquinone in propylene carbonate via transient fitting was found to be $2.7 \pm 0.3 \times 10^{-6}$ cm^2 s^{-1}. This compares with a value

of D, 3.16 ± 0.15 $\times 10^{-5}$ cm^2 s^{-1}, determinated in the case of acetonitrile.[28, 35] It illustrates that the diffusion coefficient in PC is approximately one order of magnitude less. Note that the viscosity of the solvents are different: Hector has reported that the viscosity of propylene carbonate (2.51 mPa s) is one order of magnitude larger than that of acetonitrile (0.34 mPa s) at 298 K.[16] As a result, it is not unreasonable to find that diffusion of electroactive species in propylene carbonate solvent is slowed by a similar factor.

11.3.1.2 Simulating the Oxidation of Hydroquinone

The commercial voltammetric simulation package DIGISIM® (version 3.0, BAS Technicol, USA) was used to model the cyclic voltammograms over a range of scan rates (50-800 mVs^{-1}) for 0.5mM hydroquinone. In DigiSim, all heterogeneous electron transfer reactions must be of the following form:

$$A = B + ne \quad (\mathrm{n} \geq 1) \tag{11.7}$$

When n>1, Marcusian kinetics is disabled in the software and by default Butler-Volmer kinetics are operative as follows:

$$Io = nFk_s \{[B]\exp[-\alpha(nF/RT)(E - E_o)] - [A]\exp[\beta(nF/RT)(E - E_o)]\} \tag{11.8}$$

where $\alpha + \beta = 1$ ensures consistency with the Nernst equation. For the oxidation of hydroquinone, the chronoamperometric experiment above has confirmed that the electron transfer number, n, in the electrochemical process is 2. If the reaction scheme is considered as two separate steps:

$$R \underset{}{\overset{k_1}{\rightleftharpoons}} Y + e \tag{11.9}$$

$$Y \underset{}{\overset{k_2}{\rightleftharpoons}} O + e \tag{11.10}$$

Suppose Butler-Volmer kinetics apply to each of the steps (11.9 and 11.10) and that these have individual transfer coefficients β and $\beta_{2.}$ If the first step (11.9) is rate determining, then the rate is proportional to

$$[R]_{surface} \exp\left(\frac{\beta_1 F}{RT}(E - E_f^{'o}(R/Y))\right) \tag{11.11}$$

On the other hand, if the rate determining step is (11.10), then a pre-equilibrium exist between R and Y such that:

$$\frac{[Y]_{surface}}{[R]_{surface}} = \exp\left(\frac{F}{RT}(E - E_f^{'o}(R/Y))\right) \tag{11.12}$$

So that the rate is proportional to:

$$[Y]_{surface} \exp\left(+\frac{\beta_2 F}{RT}(E - E_f^{'o}(Y/O))\right) \tag{11.13}$$

or

$$[R]_{surface} \exp\left(\frac{(1+\beta_2)FE}{RT} - \frac{F}{RT}E_f^{'o}(R/Y) - \frac{\beta_2}{RT}E_f^{'o}(Y/O)\right) \tag{11.14}$$

If the same transition state occurs in the reverse reaction as in the forward reaction, then the rate of the back reaction will be proportional to

$$[O]_{surface} \exp\left(\frac{-\alpha_2 F}{RT}(E - E_f^{'o}(Y/O))\right) \tag{11.15}$$

when $\left(E^{'o}(Y/O)\right)$ and $\left(E_f^{'o}(R/Y)\right)$ are the corresponding formal potentials of the Y/O and R/Y couples, respectively.

Comparsion with equation (11.8), it shows that

$$1+\beta_2 = n\beta \tag{11.16}$$

$$\alpha_2 = n\alpha \tag{11.17}$$

$$\beta n E_o = E_f^o\left(R/Y\right)+\beta_2 E_o\left(Y/O\right) \tag{11.18}$$

$$\alpha n E_o = \alpha_2 E_{\mathrm{f}}^{\mathrm{o}}\left(Y/O\right) \tag{11.19}$$

So that

$$2E_o = E_f^o\left(R/Y\right)+E_f^o\left(Y/O\right) \tag{11.20}$$

as expected. If the first process (11.9) is the rate determining step, the charge transfer coefficients for the first step, β_1, is likely to be approximately equal to 0.5. On the other hand, $1+\beta_2$ is likely to be approximately equal to 1.5 if the rate determining step is the second step, (11.10).

In order to optimize the fit between the experimental and simulated voltamograms the rate constant (k_s) was optimized along with all the other parameters (see table 1) except the known diffusion coefficient of QH_2. This gave a value of k_s, 2.8×10^{-7} cm s^{-1}, $\alpha n = 0.5$ and $\beta n = 1.5$, which indicate the electrochemical oxidation of hydroquinone in propylene carbonate is a slow two-electron transfer process with the second oxidation step rate determining. The best fit was achieved between the experimental and simulated voltammograms at various scan rates (50, 100, 200, 300 mV s^{-1}). Furthermore the redox peak currents and potentials of experimental and simulated voltammograms over a range of scan rates (50-800 mV s^{-1}) were compared each other

and recorded. The results above confirm that all parameters shown in table 1 from theoretical simulation are reasonable. On the other hand it is obvious that the value of the diffusion coefficient (*D*) of hydroquinone obtained from simulation is in excellent agreement with the value from chronoamperometric experiment. The shifting peak potential also confirms the quasi-irreversibility of the electrode kinetics.

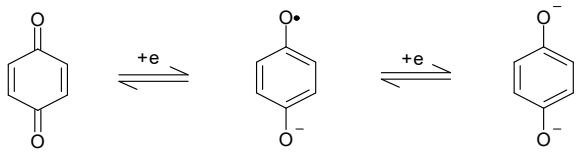
Table 1 Parameters fixed in digital simulation of hydroquinone

Parameters	Propylene carbonate (solvent)
E_0 (V)	0.765
αn	0. 5
βn	1.5
k_s (cm s^{-1})	2.8×10^{-7}
D (Q H_2)(m^2s^{-1})	3.0×10^{-10}
D (QH_2^{2+})(m^2s^{-1})	2.2×10^{-10}

11.3.2 Electrochemical Study of Benzoquinone

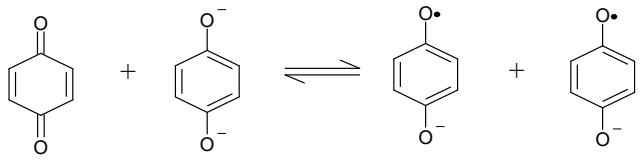
11.3.2.1 Cyclic Voltammetric Responses and Electrochemical ESR Behavior of Benzoquinone in PC

Figure 11.4 shows cyclic voltammetric response of 1mM benzoquinone obtained at a GC electrode in a propylene carbonate solution containing 0.1 M TBAP. It is clear that apart from the slower rate of diffusion in propylene carbonate, the voltammetric wave closely is similar to that behaviour observed from the acetonitrile. The mechanism of the electrochemical process is outlined below,[10]



where there are two species capable of undergoing a heterogeneous electron transfer in the potential window of interest; *viz* the benzoquinone substrate itself and the radical

anion $BQ^{-\cdot}$. Obviously the first reduction wave (a) is attributed to the BQ and with the more negative potentials a further one-electron reduction of the $BQ^{-\cdot}$ becomes favorable leading to a second reductive wave (b). Note that when reversing the second reductive wave there is no apparent oxidation wave observed in Figure 11.4. Russell and Janicke suggested that it might be due to the following fast conproportionation between the BQ and the resulting dianion within the diffusing layer:[36]



Additionally, the resulting dianion is strongly influenced by the supporting electrolyte owing to the ion pairing and the formation of insoluble products on the electrode surface.[36]

$$BQ^{2-} + TBA^{+} \rightleftharpoons \left[BQTBA\right]^{-} \tag{11.21}$$

The voltammetric response of BQ reported above is similar to the previous studies on this system in other aprotic solvents.

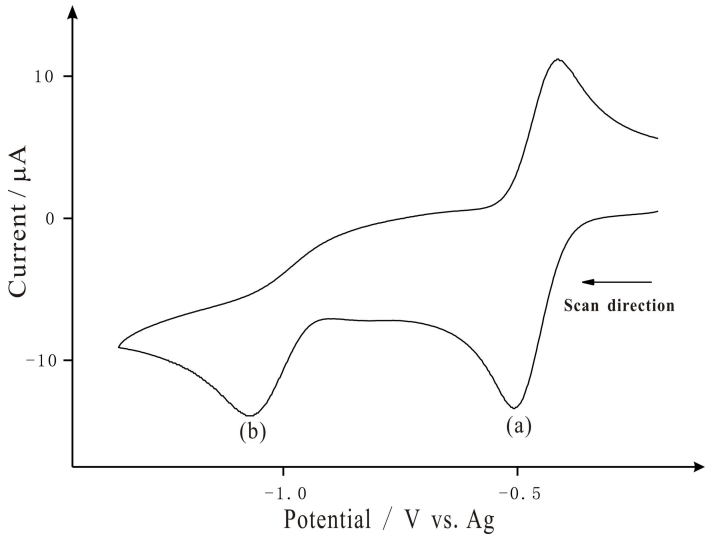


Figure 11.4 Cyclic voltammetric response (100 mVs^{-1}) obtained at a GC electrode for 1.0 mM Benzoquinone in PC with 0.1M TBAP.

Steady state voltammogram of 5.0 mM benzoquinone in PC containing 0.1M TBAP obtained at a 25 μm gold micro electrode at a scan rate of 10 mV s^{-1} was shown in Figure 11.5. The inset Figure in it was a chronoamperometric response at a step potential of -0.6 (vs. Ag wire), giving the diffusion coefficient of benzoquinone in propylene carbonate, 4.2 ± 0.2 $\times 10^{-6}$ cm^2 s^{-1} by using the same analysis method as mentioned above, which is one order of magnitude less than that obtained from acetonitrile, 2.4 ± 0.3 $\times 10^{-5}$ cm^2 s^{-1},[37, 38] and it also confirmed that n = 1 in the first reduction step of BQ. The observed difference in diffusion coefficients is due to the higher viscosity of the propylene carbonate as discussed above.

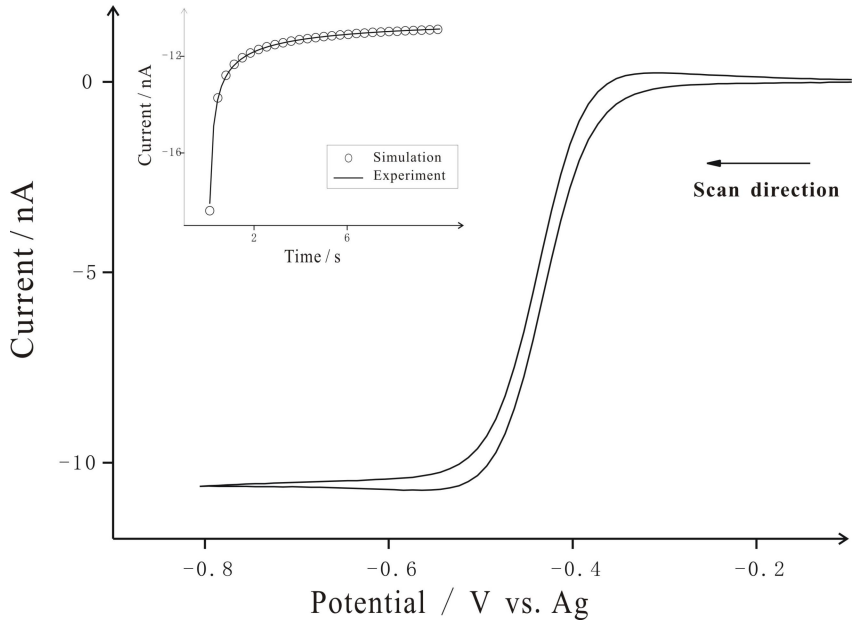


Figure 11.5 (a) Comparisons of the oxidation peak current and the reduction current of 0.5mM hydroquinone in 0.1M TBAP with PC between experimental results and simulation data at various scan rates. (b, c) Comparisons of the redox peak potentials between experimental results and simulation data at various scan rates.

Next electrochemical Electron Spin Resonance (ESR) using a tubular flow cell (in which species electrolyzed at a gold tube working electrode are transported into an ESR

cavity resonator) was performed to investigate this conproportionation process. Electrolysis of 2 mM solutions of BQ at a potential of -0.6 V (vs. Ag wire) gave single line ESR spectrum shown in Figure 11.6. The inset Figure is the normalised voltammogram of 2mM BQ obtained at the gold tube working electrode, where it indicated two step potentials, -0.6 V and -1.4 V (vs. Ag wire), for the electrochemical ESR experiment.

Furthermore, the limiting currents (i_{lim}) and signal intensities (S) were measured at various flow rates (V_f), giving the plots of i_{lim} against V_f. Note that the i_{lim} obtained at -1.4 V were doubled that obtained from -0.6 V for all the flow rates, confirming that the electrochemical reduction of benzoquinone took place in two separate one-electron transfer steps. In terms of the signal intensity reflecting the concentration of benzoquinone radical anion, it will increase when the recorded potential goes more negative than 0 V, then followed by a decrease after the potential is more negative than -0.6 V where the radical anion has been consumed to form the dianion provided there is no conproportionation taking place. In order to investigate this process, then the plot of $\log(S/i_{lim})$ against $\log(V_f)$ at two separated potentials for all flow rates were recorded in both cases, giving a slope close to -2/3. As Wain *et al* suggested before,[25] this indicates that the benzoquinone radical anion is stable on the experimental time scale. Moreover, it is interesting to note that these two lines are almost overlayed against each other, revealing that the signal intensities were nearly doubled at -1.4V in comparison with the values obtained at -0.6 V. The above data suggests that benzoquinone reacts effectively quantitatively with benzoquinone dianion to form the radical anion with a conproportionation process as shown above.

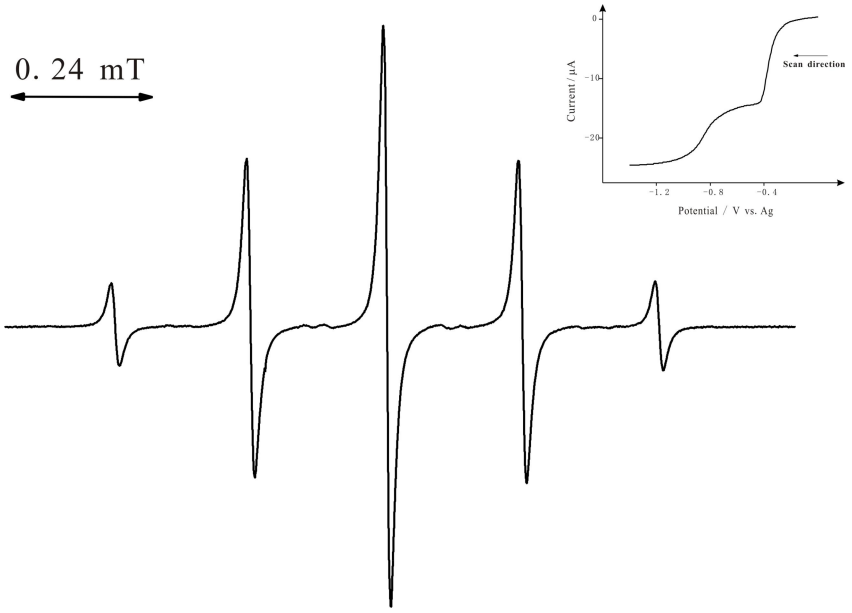


Figure 11.6 ESR spectra for 2mM benzoquinone in PC with 0.1M TBAP observed during in situ electrolysis using a modulation width of 0.24 mT. The inset Figure is steady state voltammetric response ($10mVs^{-1}$) obtained from a gold tube working electrode.

11.3.2.2. Simulating the Reduction of Benzoquinone

We consider the simulation of the electrochemical process of BQ. It is helpful to fix some of parameters beforehand through their independent determination. In the accessible potential window, the kinetics of the heterogeneous electron transfer process of the first reduction of BQ can be obtained using the DigiSim simulation. Then the cyclic voltammetric responses were recorded in a solution of 1.0 mM Benzoquinone at various scan rates. In 1965, Nicolson reported that the behaviour of the peak-to-peak separation ($\triangle E_p$) with the increasing scan rate could be utilized to give the kinetic parameters when assuming one-electron transfer and that the direction of the potential sweep is reversed at least 90 mV beyond the anodic peak presuming that this step involves the one electron transfer. The mathematical expression of this Nicholson method is defined as:[39]

$$\psi = \frac{(RT)^{\frac{1}{2}}(\frac{D_O}{D_R})^{\frac{\alpha}{2}}k_o}{(\pi D_O FV)^{\frac{1}{2}}} \quad (11.22)$$

where R is the gas constant, F is the Faraday constant, T is the room temperature, D is the diffusion coefficient, α is the charge transfer coefficient, V is the scan rate, the subscripts O and R are corresponding to the species undergoing the oxidation and reduction, respectively. The heterogeneous rate constant could be obtained from the relationship between ψ and the $\triangle E_p$ at various scan rates. Furthermore, in comparison with Nicholson method, Evans and Compton calculated the $\triangle E_p$ from the equation above associated with the scan rate referring to each ψ for a given k^o by using the DigiSim simulation.[33]

Table 2

ψ	$\triangle E_p$ (mV) Nicholson	$\triangle E_p$ (mV) DIGISIM®
20	61	59
7	63	61
6	64	62
5	65	63
4	66	64
3	68	66
2	72	70
1	84	82
0.75	92	90
0.50	105	105
0.35	121	122
0.25	141	142
0.10	212	217

The comparable results are shown in table 2, in which these two calculations are matching with each other well. Next the values of ψ for the first reduction of BQ at

each scan rate was obtained according to this table. A plot of ψ against the $V^{-1/2}$ was shown in Figure 11.7. Equation (11.22) shows this plot will be a straight line through the origin and give a gradient corresponding to the k^o. Accordingly, using the diffusion coefficient for BQ from chronoamperometric experiment above, the value of k^o, 7.2 $\times 10^{-3}$ cm s^{-1}, was obtained with the assumption of $\alpha = 0.5$. We found that the ratio of $D_{(BQ.-)}/ D_{(BQ)}$ is equal to 0.48. Usually in solvents such as N,N-dimethylformamide and acetonitrile the ratio of the diffusion coefficients of a radical ion to its parent is close to unity[40],[38] although in viscous ionic liquids it has been found to be significantly less than unity. The ratio seen for BQ and $BQ^{\cdot -}$ in PC possibly reflects the greater viscosity of the latter solvent.

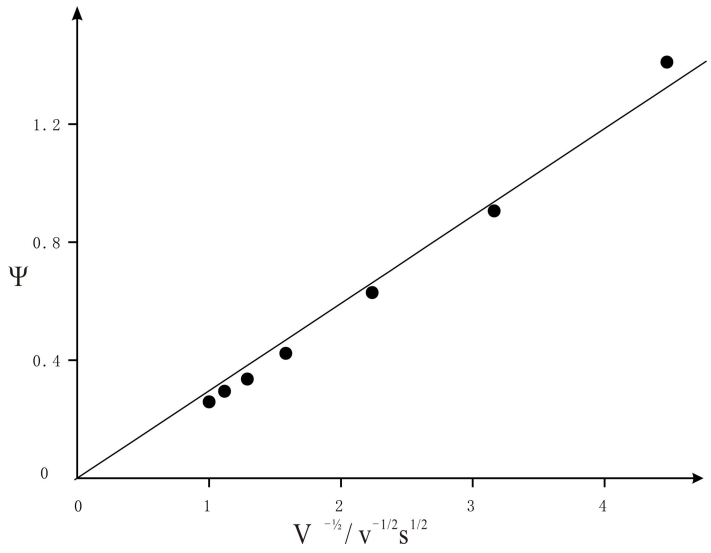


Figure 11.7 Nicholson plot of ψ versus the square root of various scan rates for the 1.0 mM Benzoquinone in propylene carbonate with 0.1M TBAP.

The value of the heterogeneous rate constant is two orders of magnitude less than that obtained in MeCN. Similar behavior has been also observed for the TMPD in propylene carbonate compared with that from MeCN, which could be due to a noticeable effect of solvent reorientation dynamics on the charge transfer process.[16] In

order to further verify our calculated k^o, the DIGISIM® was used to model the cyclic voltammograms over a range of scan rates (50-1000 mVs^{-1}) for 1mM benzoquinone with the following mechanism:

$$BQ + e = BQ^{\cdot -} \tag{11.23}$$

The results are summarized in Table 3. A value of k^o, 6.0 $\times 10^{-3}$ cm s^{-1}, was found to give the excellent fit observed between the experimental (solid line) and simulated (dotted line) voltammograms at various scan rates (50, 200, 600, 1000 mV s^{-1}) shown in Figure 11.8. This agrees well with the value determined from the Nicholson calculation. In addition, the value of diffusion coefficient of BQ radical anion, 2.0 $\times 10^{-6}$ cm^2 s^{-1}, was obtained from the simulation.

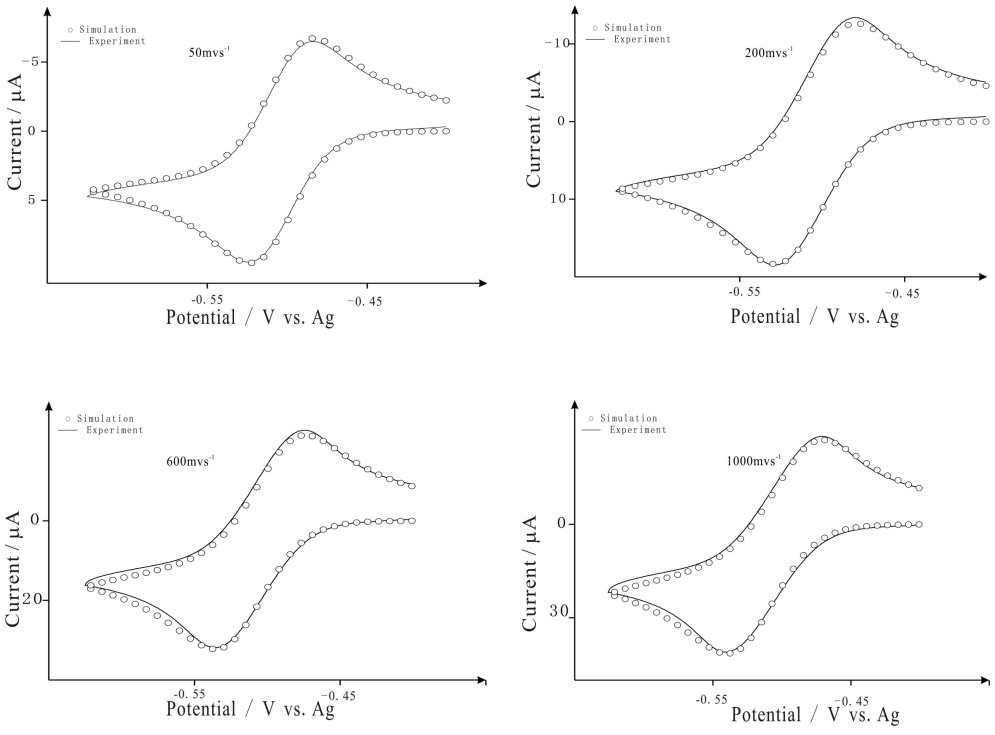


Figure 11.8 Comparison between experimental (—) and simulated (○) cyclic voltamograms at various scan rates for a solution of 1 mM benzoquinone in 0.1 M TBAP with PC obtained at GC. The simulation parameters are as follow: $[BQ]_{bulk}$ = 1×10^{-3} M, r = 3×10^{-3} m, α = 0.5, β = 0.5 $D_{(BQ)}$= 4.2×10^{-10} m^2 s^{-1}, $D_{(BQ^{\cdot -})}$= 2.0×10^{-10} m^2 s^{-1}, n = 1, E_0 (V) = -0.455 V, k_0 = 6.0×10^{-3} cm s^{-1}.

Table 3 Parameters fixed in digital simulation of the first reduction step of BQ

Parameters	Propylene carbonate (solvent)
E_0 (V)	-0.455
n	1
α	0. 5
β	0.5
k_0 (cm s^{-1})	6.0×10^{-3}
D (BQ)(m^2s^{-1})	4.2×10^{-10}
D ($BQ^{\cdot-}$)(m^2s^{-1})	2.0×10^{-10}

Now we are in a position to simulate the electrochemical reduction of benzoquinone in the whole range with the help of the accurate parameters obtained from the calculations and simulation above. The entered mechanisms are as follows:

$$BQ + e = BQ^{\cdot-} \quad (11.24)$$

$$BQ^{\cdot-} + e = BQ^{2-} \quad (11.25)$$

$$BQ + BQ^{2-} = 2BQ^{\cdot-} \quad (11.26)$$

$$BQ^{2-} + TBA^{+} \rightleftharpoons [BQTBA]^{-} \quad (11.27)$$

$K_{eq,1}$ and $K_{eq,1}$ are the equilibrium constants for those two chemical steps (11.25) and (11.26), respectively. The variation of the parameters for the homogeneous and heterogeneous steps were optimized in order to get a good fit between theory and experiment but using those that could be attained by independent measurements. First of all, the diffusion coefficient of benzoquinone was obtained directly from the experiment determination, then the simulation gives diffusion coefficient of benzoquinone radical anion as described above. Hence that of benzoquinone dianion is still uncertain. In the light of these two known values, the difference indicates that the diffusion coefficient of a species with a negative charge has its diffusion coefficient reduced up to a half of its initial value. Accordingly an initial assumption was made that the value of diffusion coefficient for the benzoquinone dianion is 50% of that of

the radical anion when optimized a value of 1.2 was found to for the diffusion coefficient of BQ^{2-}. Referring to that conproportionation step, the height of the oxidation peak (corresponding to the second reduction of benzoquinone) is much smaller than expected in the absence of conproportionation and hence a forward rate constant of the homogeneous step, $C + A = 2B$, needs to be set sufficiently high. Moreover, voltametrically it is possible to make the oxidation 'disappear' with the various values of the rate constant of ion pairing step. Note that if both the A/B and B/C steps are electrochemically reversible then the voltammetry is 'blind' to the conproportionation. Although the two couples appear quasi-reversible in PC it was found that the ion pairing step was essential to simulate the observed ion of the oxidation of C in the voltammetry.

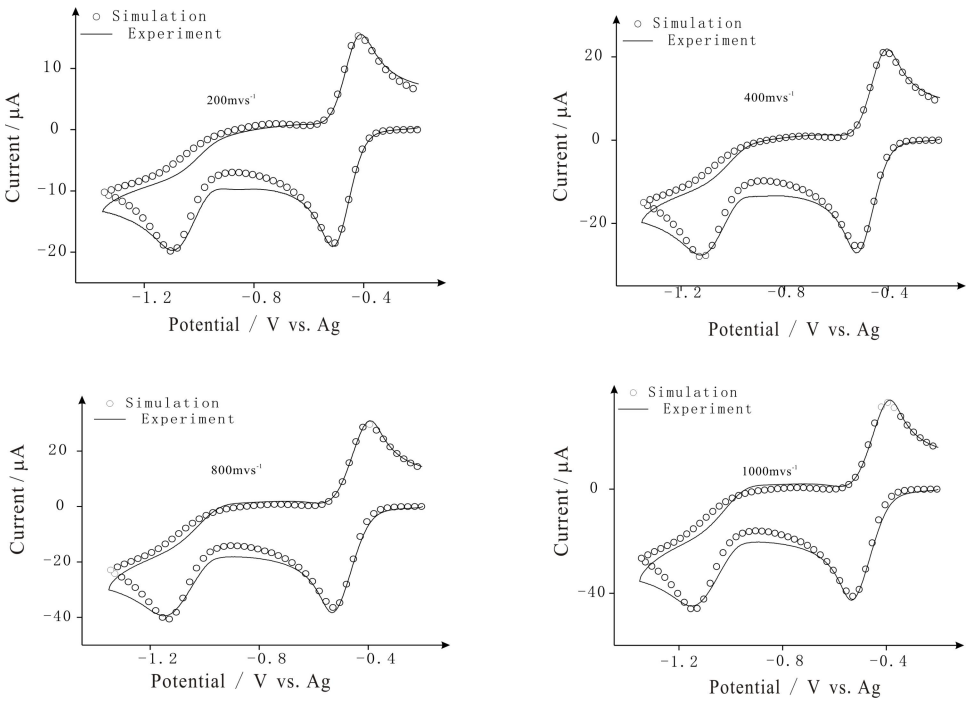


Figure 11.9 Comparison of experimental (—) and fitted theoretical (○) cyclic voltammograms for the reduction of benzoquinone in PC under the conditions (as shown in table 4).

Finally, taking all the factors into account good fits were achieved between simulated and experimental voltammograms at various scan rates (shown in Figure 11.9). The results are summarized in table 4. This gave the value of equilibrium constant of conproportionation step, 7.2×10^{7}, which is determined by the thermodynamic calculation using the difference between the two formal electrode potentials (E_1 - E_2 = 0.465 V). As was expected, the peak potentials difference in MeCN is 0.635 V [36], corresponding to the value of $K_{eq,1}$, 2.25×10^{10}. More significantly, in terms of the ion pairing step, $K_{eq,2}$ was adjusted so as to optimize the fit between simulated and experimental voltammetric waves. A value of 40 M^{-1} was found to give the best agreement for $K_{eq,2}$ in PC. This agrees well with the value, 48 M^{-1}, obtained from the MeCN solvent indicating the change from ordinary solvent to propylene carbonate does not influence the equilibrium constant.[36]

Table 4 Parameters fixed in digital simulation of two reduction steps of BQ

Parameters	Propylene carbonate (solvent)
E_{01} (V)	-0.455
E_{01} (V)	-0.920
α_1	0.5
α_2	0.5
k_{01} (cm s^{-1})	6.0×10^{-3}
k_{02} (cm s^{-1})	2.1×10^{-4}
Keq,1	7.2×10^{7}
Keq,2 (dm^3mol^{-1})	40
k_1 ($dm^3mol^{-1}s^{-1}$)	1.1×10^{6}
k_2 ($dm^3mol^{-1}s^{-1}$)	200
D (BQ)(m^2s^{-1})	4.2×10^{-10}
D ($BQ^{\cdot-}$)(m^2s^{-1})	2.0×10^{-10}
D (BQ^{2-})(m^2s^{-1})	1.2×10^{-10}
D (TBA-BP^{-})(m^2s^{-1})	4.0×10^{-10}
D (TBA^{+})(m^2s^{-1})	Kinetically insignificant

11.3.3 Kinetic Analysis of Hydroquinone in the Presence of Ammonia in PC

Ammonia gas (10%) was bubbled into the votlammetric cell containing 0.5mM hydroquinone in PC solution with 0.1 M TBAP for 60s, the consequent voltammetric response was overlaid as dashed line in Figure 11.10. In comparison with the oxidation of hydroquinone (shown as solid line), it was clear that after bubbling the ammonia the oxidation wave (shown as dashed line) was shifting to less positive potential (+ 0.3 V vs. Ag wire).

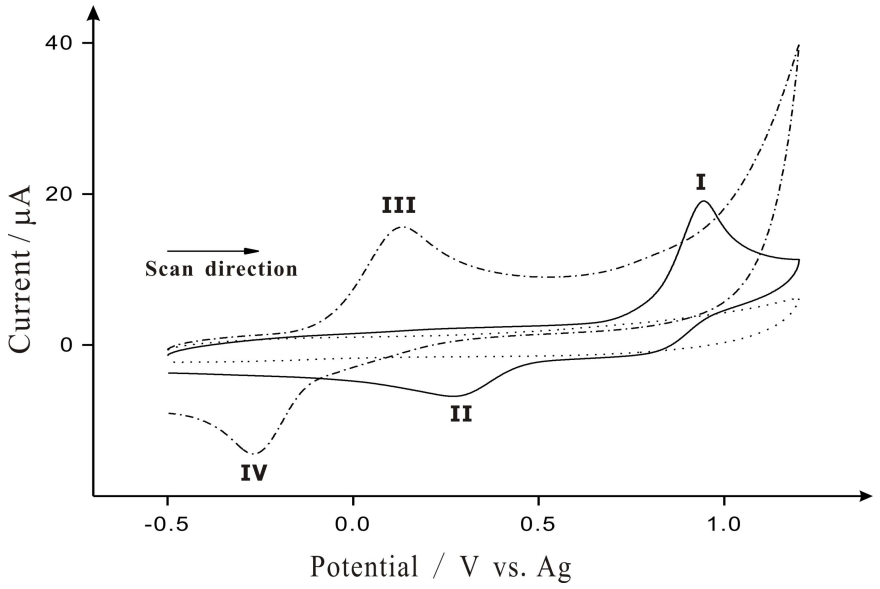


Figure 11.10 Cyclic voltammetric responses of 1 mM hydroquinone with bubbling 10% vol ammonia for 60 seconds (dashed line) and without ammonia (solid line) in PC with 1M TBAP at GC.

Note that Eggins has shown that the observed redox potential of the hydroquinone shifted by approximately -1V, and this peak exhibited the same redox potential as that of benzoquinone, by adding tetra-n-butylammonium hydroxide as a strong base into hydroquinone in acetonitrile.[4,5,35] It is believed that the hydroquinone dianion was formed as a result of removing two protons from hydroquinone. Hence, in this case, on adding of ammonia to hydroquinone in PC, it is not surprising to see the similar behaviour. However, the new redox potential is not the same as that of benzoquinone,

suggesting that in this homogeneous step the hydroquinone only lost one proton. The possible mechanism of electrochemical process of hydroquinone with ammonia was described as follow:

$$QH_2 + NH_3 \rightleftharpoons QH^- + NH_4^+ \quad (11.28)$$

$$QH^- \overset{-2e}{\rightleftharpoons} QH^+ \quad (11.29)$$

In order to support our proposed mechanism, the voltammetric response of benzoquione (BQ) and hydroquinone (QH_2) in the presence of ammonia on a GC electrode in PC was studied, as shown in Figure 11.11.

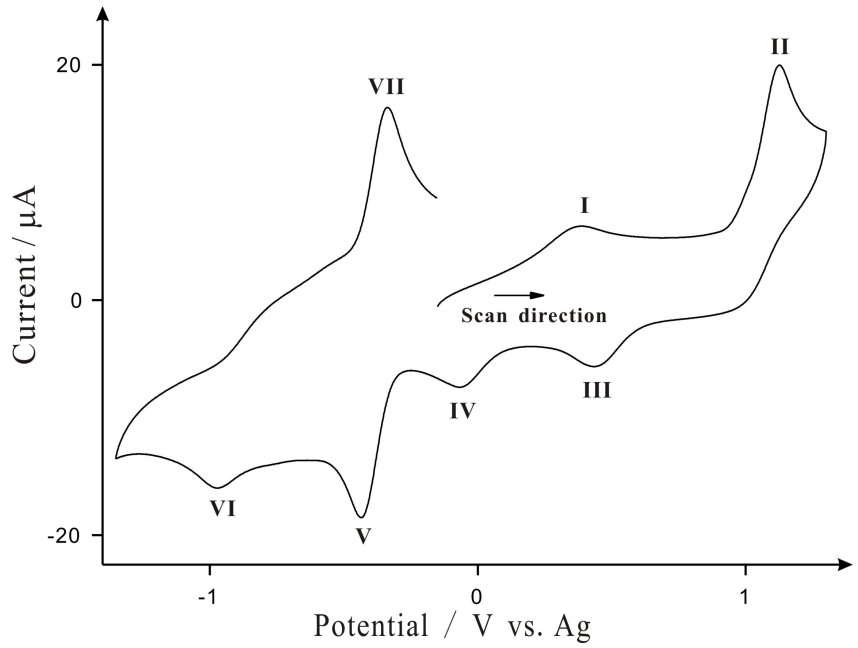


Figure 11.11 Cyclic voltammogram of 1 mM hydroquinone and 1 mM benzoquinone with bubbling 0.1% vol ammonia for 500 seconds in PC with 1M TBAP at GC.

It was found that there are four redox peaks appearing in the potential range. As we explored before, clearly peak I is due to the oxidation of hydroquinone, followed by the reduction of QH^{2+}, peak II. The redox reaction of BQ is two one-electron steps corresponding to peak V and VI. For the peak III and IV, these correspond to the redox

of the anion produced from reaction between hydroquinone and ammonia. Note that the redox potential of the anion formed from the homogeneous step does not overlay with that of BQ, suggesting that only one proton has been consumed by the homogeneous reaction between hydroquinone and ammonia molecule. As a result, we suggest the mechanism in scheme 1 for the electrochemical process of hydroquinone-benzoquinone and the deprotonated hydroquinone ion under our experimental conditions.

11.3.4 Analytical ability of this Homogeneous Reaction between Hydroquinone and Ammonia in PC

Cyclic voltammetric responses were obtained at a GC electrode in a propylene carbonate solution containing 0.5 mM hydroquinone with 0.1 M TBAP in the absence of ammonia and saturated with different concentrations of ammonia gas (10, 50, 100 ppm); the voltammetric responses are shown in Figure 11.12. In the absence of ammonia, the anodic wave is corresponding to the two-electron oxidation of hydroquinone. On the other hand, a new wave attributed to the oxidation of deprotonated hydroquinone appeared after bubbling ammonia into the working solution. A plot of this new oxidation peak current versus the ammonia concentration (see insert graph in Figure 11.12) shows an excellent linear relationship, giving a sensitivity 1.29 $\times 10^{-7}$ A ppm^{-1} ($r^2 = 0.999$) and limit-of-detection 4.91 ppm ammonia (based on 3s*b*), demonstrating the analytical ability of this homogeneous reaction.

The analytical utility above has shown that the propylene carbonate solution containing hydroquinone can be used to the working electrolyte in the ammonia gas sensor. Generally in the gas sensor design, the electrolyte employed is water based. The appreciable water vapour pressure inevitably means that the sensor will dry out over

time so limiting the lifetime at typical operating temperatures and restricting the sensor reliability.

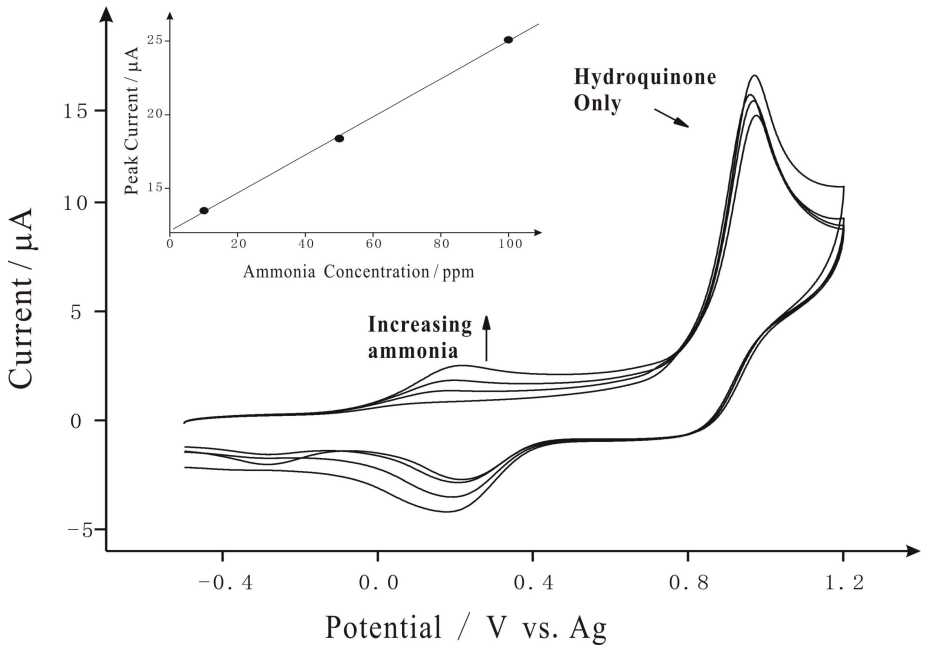


Figure 11.12 Cyclic voltammetric responses of 0.5mM hydroquinone to increasing ammonia concentration (10, 59 and 100 ppm) in PC (0.1M TBAP) at GC. Insert graph: a plot of the anodic peak current at +0.15V against concentration of ammonia (ppm).

The volatility of the water can be reduced by the use of high concentrations of sulphuric acid as an electrolyte but this places significant constraints on the voltammetry possible. In the context of direct amperometric ammonia sensing the ammonia will be irreversibly converted into the electro-inactive NH_4^+ ion: alternatives are clearly desirable. Propylene carbonate is likely a good choice for use as a solvent in commercial gas sensors given the the vapour pressure of propylene carbonate is 0.03 mm Hg (at 298 K) in contrast to the vapour pressure of water which is 17.5 mm Hg (at 298 K).[22] The consequence is that sensor lifetime maybe greatly extended as the tendency for the sensor to 'dry-out' is significantly reduced. At the same time, according to the equation 18, the deprotonation of the hydroquinone species in the

solvent propylene carbonate is expected to be reversible under the removal of ammonia. A 3mM hydroquinone in propylene solution containing 0.1M TBAP was selected to investigate this effect. Nitrogen gas was continuously bubbled into the solution after ammonia. Figure 11.13 shows the initial cyclic voltammetric response of hydroquinone is well overlaid with that from hydroquinone after nitrogen. It is clear that the addition of nitrogen make the ammonium decompose into ammonia and proton. And the proton combines with the hydroquinone anion to form the hydroquinone. The reversibility of the homogeneous step between hydroquinone and ammonia proves the ammonia sensor could be recycled with the removal of the ammonia from the solution.

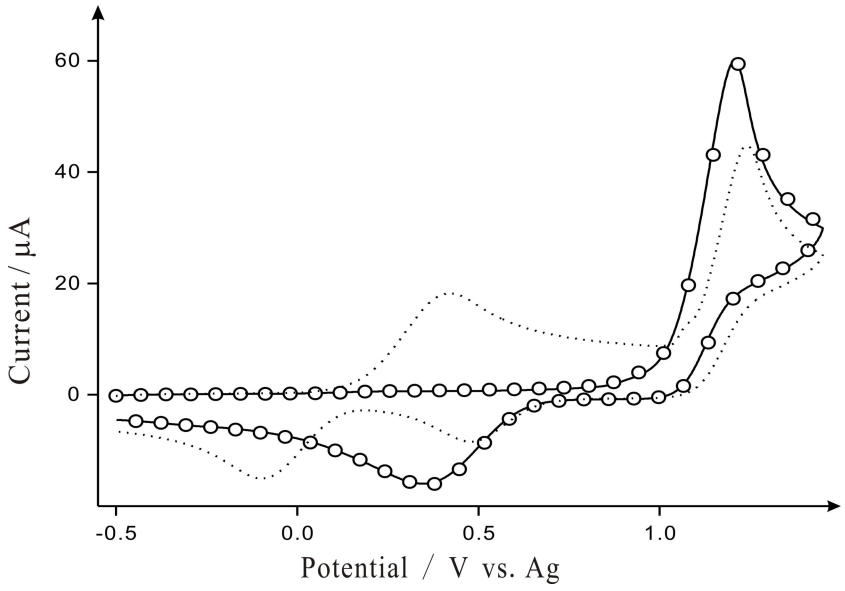


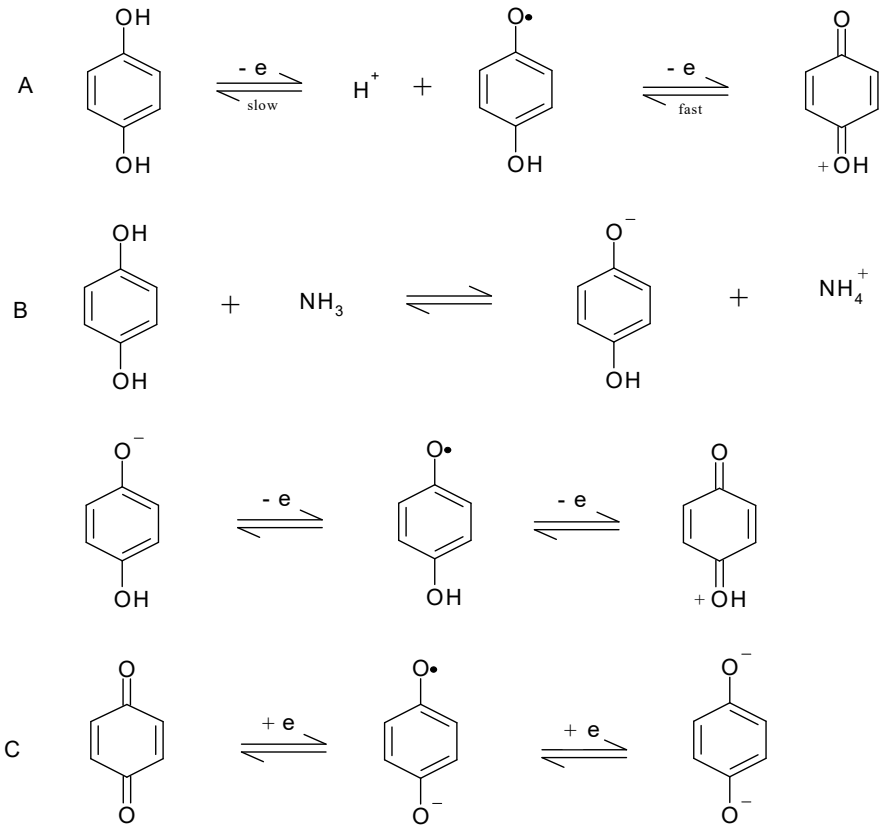
Figure 11.13 The cyclic voltammetric responses in PC (0.1M TBAP) for 3mM hydroquinone (—), after bubbling 0.1% ammonia time for 2000s (·) and the following addition of nitrogen (○)

11.4. Conclusion

The electrochemical processes of hydroquinone and benzoquinone have been investigated by cyclic voltammetry at glassy carbon electrodes in propylene carbonate. DigiSim® was employed to simulate the voltammetric responses and elucidate the

various mechanistic parameters. Futhermore, the response of hydroquinone in the presence of ammonia has been examined in the propylene carbonate. The above results detail a new oxidation wave observed at *ca.* + 0.15 V (vs. Ag wire) and can be attributed to the basic ammonia removing one proton from the hydroquinone species. Its analytical utility for ammonia sensing was examined in the range from 10 and 100 ppm by measuring the peak current of new wave as function of ammonia concentration with a detection limit of 4.9 ppm.

Scheme 1 The mechanisms for the electrochemical processes of hydroquinone-benzoquinone and the reaction between hydroquinone and ammonia.



11.5 References

(1) Tomilov, B. I.; Loshkarev, M. A. *Russ. J. Phys. Chem.* **1962**, *36*, 1027.

(2) Peover, M. E.; Davies, J. D. *J. Electroanal. Chem.* **1963**, *6*, 46.

(3) Bochkov, Y. G.; Aboimov, A. M.; Gorbachev, S. V. *Russ. J. Phys. Chem.* **1966**, *40*, 618.

(4) Eggins, B. R. *Chem. Commun.* **1969**, 1267.

(5) Eggins, B. R. *Chem. Commun.* **1969**, 232.

(6) Clark, B.; Evans, D. H. *J. Electroanal. Chem.* **1976**, *69*, 181.

(7) Wilford, J. H.; Archer, M. D. *J. Electroanal. Chem.* **1985**, *190*, 271.

(8) Gamage, R. S. K. A.; Umapathy, S.; Mcquillan, A. J. *J. Electroanal. Chem.* **1990**, *284*, 229.

(9) Uchiyama, S.; Hasebe, Y.; Ishikawa, T.; Nishimoto, J. *Anal. Chim. Acta.* **1997**, *351*, 259.

(10) Pletcher, D.; Thompson, H. *J. Chem. Soc.* **1998**, *94*, 3445.

(11) Lehmann, M. W.; Evans, D. H. *J. Electroanal. Chem.* **2001**, *500*, 12.

(12) Pastor-Moreno, G.; Riley, D. J. *Electrochem. Commun* **2002**, *4*, 218.

(13) Andrieux, C. P.; Saveant, J. M. *J. Electroanal. Chem.* **1970**, *28*, 339.

(14) Zhang, R. F.; Evans, D. H. *J. Electroanal. Chem.* **1995**, *385*, 201.

(15) Giovanelli, D.; Buzzeo, M. C.; Lawrence, N. S.; Hardacre, C.; Seddon, K. R.; Compton, R. G. *Talanta* **2004**, *62*, 904.

(16) Fernandez, H.; Zon, M. A. *J. Electroanal. Chem.* **1992**, *332*, 237.

(17) Dall'Antonia, L. H.; Vidotti, M. E.; Cordoba, S. I.; Torresi, C.; Torresi, R. M. *Electroanal* **2002**, *14*, 1577.

(18) Bendahan, M.; Lauque, P.; Seguin, J.-L.; Aguir, K.; Knauth, P. *Sens. Act. B* **2003**, *95*, 170.

(19) Buzzeo, M. C.; Giovanelli, D.; Lawrence, N. S.; Hardacre, C.; Seddon, K. R.; Compton, R. G. *Electroanal* **2004**, *16*, 888.

(20) Timmer, B.; Olthuis, W.; van den Berg, A. *Sens. Act. B* **2005**, *107*, 666.

(21) Ji, X.; Banks, C. E.; Compton, R. G. *Electroanal.* **2006**, *18*, 449.

(22) Lide, D. R. *CRC Handbook of Chemistry and Physics.* **1999-2000**.

(23) Sharp, P. *Electrochim. Acta.* **1983**, *28*, 301.

(24) Jacob, S. R.; Qi, H.; Coles, B. A.; Compton, R. G. *J. Phys. Chem. B.* **1999**, *103*, 2963.

(25) Wain, A. J.; Streeter, I.; Thompson, M.; Fietkau, N.; Drouin, L.; Fairbanks, A. J.; Compton, R. G. *J. Phys. Chem. B.* **2006**, *110*, 2681.

(26) Weil, J. A.; Bolton, J. R.; Wertz, J. E. *Electron Paramagnetic Resonance, Elementary Theory and Practical Applications.* **1994**.

(27) Parker, V. D. *Chem. Commun.* **1969**, *16*, 716.

(28) Eggins, B. R.; Chambers, J. Q. *J. Electrochem. Soc.* **1970**, *117*, 186192.

(29) Parker, V. D.; Eberson, L. *Chem. Commun.* **1970**, *12*, 1290.

(30) Parker, V. D. *Electrochim Acta.* **1973**, *18*, 519.

(31) Keyes, T. E.; Forster, R. J.; Bond, A. M.; Miao, W. *J. Am. Chem. Soc.* **2001**, *123*, 2877.

(32) Shoup, D.; Szabo. *J. Electroanal. Chem.* **1982**, *140*, 237.

(33) Evans, R. G.; Compton, R. G. *ChemPhysChem.* **2006**, *7*, 488.

(34) Silvester, D. S.; Wain, A. J.; Aldous, L.; Hardacre, C.; Compton, R. G. *J. Electroanal. Chem.* **2006**, *7*, 2162.

(35) Eggins, B. R. *Chem. Commun.* **1972**, 427.

(36) Russell, C.; Janicke, W. *J. Electroanal. Chem.* **1986**, *199*, 139.

(37) Rosanske, T. W.; Evans, D. H. *J. Electroanal. Chem.* **1976**, *72*, 277.

(38) Rees, N. V.; Clegg, A. D.; Klymenko, O. V.; Coles, B. A.; Compton, R. G. *J. Phys. Chem. B.* **2004**, *108*, 13047.

(39) Nicholson, R. S. *Anal. Chem.* **1965**, *37*, 1351.

(40) Evans, R. G.; Klymenko, O. V.; Price, P. D.; Davies, S. G.; Hardacre, C.; Compton, R. G. *ChemPhysChem.* **2005**, *6*, 526.

CHAPTER 12

Mechanistic Studies of the Electro-oxidation Pathway of Ammonia in Several Room Temperature Ionic Liquids

In this chapter a mechanistic study of the direct oxidation of ammonia is reported in several room temperature ionic liquids (RTILs) on a 10 μm diameter Pt microdisk electrode. In all five RTILs, both HA and NH_4^+ are reduced at the electrode surface, forming hydrogen gas, which is then oxidised. The effect of changing the RTIL anion is discussed, and this work also has implications in the possible amperometric sensing of ammonia gas. This work discussed in this chapter has been published as an article in *J. Phys. Chem. C*, **2007**, 111, 9562.

12.1 Introduction

Room temperature ionic liquids (RTILs) can be broadly defined as compounds composed entirely of ions that exist in their liquid state at or below 298 K.[1-3] They possess several characteristics, including wide potential electrochemical windows, low-volatility and good conductivity, which render them attractive alternatives as electrochemical solvents[2,4,5] and are also used in various electrochemical applications

such as solar cells, electrochemical sensors, fuel cells, capacitors, and lithium batteries.[6-9] The low-volatility and high thermal stability of RTILs render them potentially advantageous media for the detection of gases and for the development of stable and robust gas sensors.[6] The ability to detect such target gases is of great importance to both the medical profession as well as numerous industries, including brewing factories, gas exhaust analysis, fermentation, environmental and process control.

Given its high toxicity, the determination of ammonia is essential to a number of applications including environmental protection, clinical diagnosis, industrial processes, food processing and power plants.[10,11] Ammonia detection is also important for the diagnosis of diseases such as renal inadequacy and diabetes.[12] Another important arena for ammonia determination is in water samples where it indicates organic material decomposition, which can be harmful to human health, whilst higher ammonia levels are of analytical interest in industrial operations such as refrigeration or fertilizer manufacture.[13,14] The electrochemical oxidation of ammonia has been studied in alkaline solutions and has been the subject of continuous investigations.[15-23] As a result, several protocols based on its determination via its direct oxidation have been developed. However, to our knowledge, only a few studies have been reported in aprotic or RTIL solvents[24-26] and with relatively little mechanistic detail.

Buzzeo *et al.*[25] have examined the electrochemical oxidation of ammonia in dimethylformamide (DMF) and the room temperature ionic liquid 1-ethyl-3-methylimidazolium bis(trifluoromethylsulfonyl)imide ($[C_2mim][NTf_2]$) and observed similar voltammetric responses in each solvent, with a large oxidative wave seen initially and the appearance of a new reductive wave after the oxidation. It was shown that the ammonium cation was formed after oxidation of ammonia, followed by

deprotonation of ammonium to form ammonia and protons, which can then be oxidised at the electrode surface. The mechanism was suggested as follows:

$$4NH_3(g) \rightarrow 3NH_4^+ + \frac{1}{2}N_2(g) + 3e^- \quad (12.1)$$

$$NH_4^+ \rightleftharpoons NH_3(g) + H^+ \quad (12.2)$$

$$H^+ + e^- \rightarrow \frac{1}{2}H_2 \quad (12.3)$$

Very recently we have also investigated the electrochemical oxidation of ammonia at a glassy carbon electrode in propylene carbonate (PC)[26] and the electrochemical behavior of ammonia observed were similar to those reported above.

A substantial part of the work presented here will focus on the mechanistic studies of the electro-oxidation pathway of ammonia in a series of ionic liquids and the subsequent elucidation of the reaction pathway. As a result, the reduction of the ammonium ion was also studied in order to 'fingerprint' any peaks following the oxidation of ammonia. Martinez *et al.*[27] have studied the electrochemical reduction of the ammonium ion in the aprotic solvent dimethylsulfoxide (DMSO) on platinum electrodes, and shown that the ion can be electrochemically reduced to produce ammonia and hydrogen. They then proposed that these products could be oxidised at different potentials. Two of the possible mechanisms were suggested[27] as follows:

$$Pt + NH_4^+ + e^- \rightleftharpoons NH_3 + Pt(H) \quad (12.4)$$

$$Pt(H) + NH_4^+ + e^- \rightleftharpoons NH_3 + H_2 + Pt \quad (12.5)$$

Or

$$Pt + NH_4^+ + e^- \rightleftharpoons NH_3 + Pt(H) \quad (12.6)$$

$$Pt(H) + Pt(H) \rightleftharpoons 2Pt + H_2 \quad (12.7)$$

The reduction of NH_4^+ was also studied by Buzzeo *et al.*[25] in the RTIL $[C_2mim][NTf_2]$ and in the aprotic solvent DMF, and it was found that the reduction peak of NH_4^+ was at the same potential as the reduction peak following the oxidation of ammonia.

In this chapter we have carried out a detailed study of the mechanism of the oxidation of ammonia in several room temperature ionic liquids with different anions, namely $[C_4mim][BF_4]$, $[C_4mim][OTf]$, $[C_2mim][NTf_2]$, $[C_4mim][NTf_2]$ and $[C_4mim][PF_6]$ (for structures, see Figure 12.1). The cyclic voltammetry obtained has allowed the proposal of a revised mechanism for ammonia oxidation in RTILs. This work also has implications in helping to define a pKa scale in ionic liquids (following on from a previous study on the oxidation of hydrogen in RTILs),[28] and in the possible analytical sensing of ammonia gas.

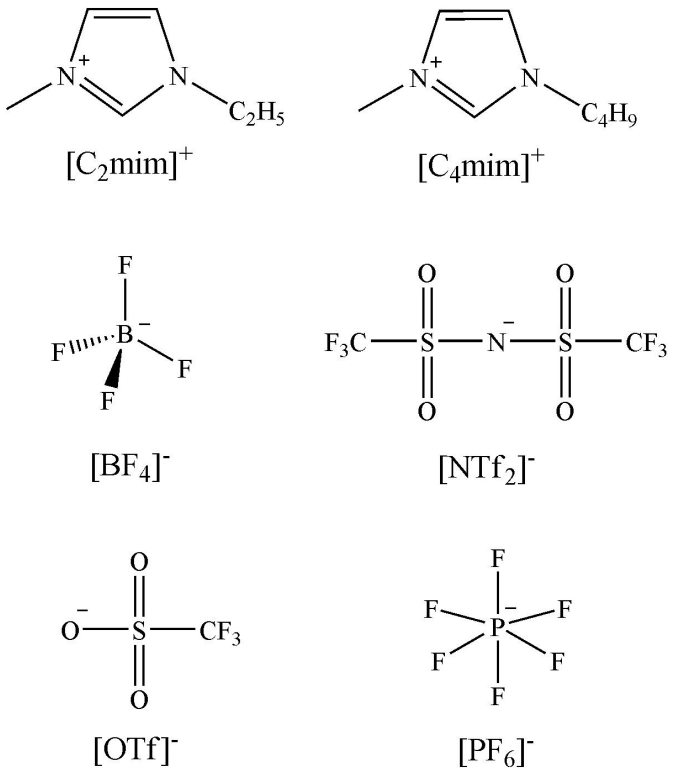


Figure 12.1 Molecular structures of the cations and anions employed in the RTILs in this study**.**

12.2 Experimental

12.2.1. Chemicals

1-Ethyl-3-methylimidazolium bis(trifluoromethylsulfonyl)imide ([C_2mim][NTf_2]), 1-butyl-3-methylimidazolium bis(trifluoromethylsulfonyl)imide ([C_4mim][NTf_2]) and their bromide salt precursors were prepared by standard literature procedures.[29,30] 1-Butyl-3-methylimidazolium tetrafluoroborate ([C_4mim][BF_4], high purity), 1-butyl-3-methylimidazolium hexafluorophosphate ([C_4mim][PF_6], high purity) and 1-butyl-3-methylimidazolium trifluoromethylsulfonate ([C_4mim][OTf], high purity) were kindly donated by Merck KGaA. [C_4mim][BF_4] and [C_4mim][PF_6] were used as without further purification. 'High purity' means a halide content of less than 100 ppm. [C_4mim][OTf] was first diluted with CH_2Cl_2 and passed through a column consisting of alternating layers of neutral aluminium oxide and silica gel in order to remove residual acidic impurities. All ILs were dried for 72 hours at 70 ºC before use. Ferrocene (Aldrich, 98%), Cobaltocenium hexafluorophosphate ($Co(C_5H_5)_2PF_6$, Acros Organics, 98%), ammonium nitrate (NH_4NO_3, BDH, 98%), ammonium hexafluorophosphate (NH_4PF_6, Aldrich, >95%), tetra-*n*-butylammonium perchlorate (TBAP, Fluka, Puriss electrochemical grade, >99%) and acetonitrile (Fischer Scientific, dried and distilled, >99.99%) were used as received, without further purification. Ammonia gas (10% NH_3, the remainder nitrogen, N_2) and hydrogen gas (H_2, 99.995% pure) were purchased from BOC gases, Manchester, UK.

12.2.2. Instrumental

Electrochemical experiments were performed using a computer controlled μ-Autolab potentiostat (Eco-Chemie, Netherlands). A conventional two-electrode arrangement was employed, with a platinum electrode (10μm diameter) as the working

electrode, and a 0.5mm diameter silver wire as a quasi-reference electrode. The platinum microdisk electrode was polished on soft lapping pads (Kemet Ltd., UK) using alumina (Buehler, Illinois) of size 1.0μm and 0.3μm. The electrode diameter was calibrated electrochemically by analyzing the steady-state voltammetry of a 2mM solution of ferrocene in acetonitrile containing 0.1M TBAP, adopting a value for the diffusion coefficient of 2.3×10^{-5} $cm^2 s^{-1}$ at 298K.[31]

The electrodes were housed in a glass cell designed for investigating microsamples of ionic liquids under a controlled atmosphere, as reported previously[28,32] and shown as Figure 12.2. The working electrode was modified with a section of disposable micropipette tip to create a small cavity above the disk into which a drop (~20μL) of ionic liquid was placed. Prior to the addition of gas, the cell was purged using a vacuum pump (Edwards High Vacuum Pump, Model ES 50), which also served to remove impurities and trace atmospheric moisture naturally present in the IL. When the baseline showed little or no traces of impurities, ammonia or hydrogen gas was introduced via one arm of the cell. The gas was then allowed to diffuse through the sample of ionic liquid until equilibration was reached (typically after 30 minutes for ammonia and 10 minutes for hydrogen). Signals were monitored over a period of time to ensure true equilibration was obtained. An outlet gas line led from the other arm of the cell into a fume cupboard.

For experiments involving NH_4NO_3, saturated stock solutions were first made up in *ca.* 100 μL of the corresponding RTIL. The solutions were stirred for at least 4 hours to allow for full dissolution. 20 μL of this solution was then pipetted into the plastic collar above the working electrode, transferred into the T-cell and placed under vacuum. Cobaltocenium hexafluorophospate was added to the RTIL inside the T-cell by

pipetting 10 μL of a 20 mM $CcPF_6$ solution in acetonitrile, allowing evaporation of the acetonitrile to leave a final concentration of 10 mM $CcPF_6$ in the RTIL.

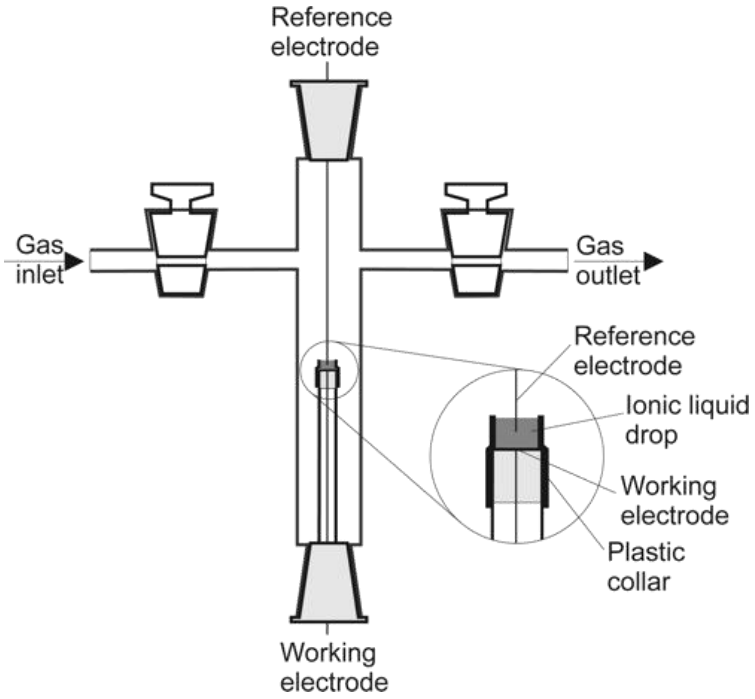


Figure 12.2 A cross section of the glass cell used to conduct electrochemical experiments on 20μL samples of RTILs under conditions of controlled atmosphere.

12.2.3 Chronoamperometric Transients

Chronoamperometric transients for the reduction of ammonium nitrate were recorded using a sample time of 0.01 seconds. The potential was stepped from 0V to a potential after the reduction peak (different for each RTIL). The experimental data was theoretically fitted using a nonlinear curve fitting function available in ORIGIN 7.0 (Microcal Software Inc.) following the Shoup and Szabo[33] expression (equations 12.8-10), as previously employed by Evans *et al*.[34]

$$I = -4nFDcr_d f(\tau) \tag{12.8}$$

$$f(\tau) = 0.7854 + 0.8863\tau^{-1/2} + 0.2146e^{-0.7823\tau^{-1/2}} \tag{12.9}$$

$$\tau = \frac{4Dt}{r_d^2} \tag{12.10}$$

Here, n represents the number of electrons transferred, F is the Faraday constant, D is the diffusion coefficient, c is the concentration, r_d is the radius of the microdisk electrode and t is the time. By fixing a value of the radius, it is possible to obtain the value for diffusion coefficient, D, of the species, and the product of the number of electrons multiplied by concentration, nc.

12.3 Results and Discussion

The electrochemistry of ammonia has been studied in a range of common ionic liquids with different anions, namely [C_4mim][BF_4], [C_4mim][OTf], [C_2mim][NTf_2], [C_4mim][NTf_2] and [C_4mim][PF_6], all of which showed a clean voltammetric baseline when fully vacuum purged. Initially, we will first describe the results obtained in one ionic liquid in detail, ([C_4mim][BF_4]), and then second report similar findings in the other four RTILs.

12.3.1 A Mechanistic Electrochemical Study of Ammonia in [C_4mim][BF_4]

12.3.1.1 Voltammetry of Ammonia in [C_4mim][BF_4]

The electrochemical oxidation of ammonia was first investigated by passing a positive pressure of ammonia gas (10%; 90% N_2) over 20 μL of [C_4mim][BF_4]. Maximum peak currents were obtained after *ca.* 30 minutes of gas diffusing into the liquid. The voltammetric responses of a saturated ammonia solution on a 10 μm platinum electrode are shown in Figure 12.3 at a range of scan rates from 100 mV s^{-1} to 10 V s^{-1} (solid lines), together with a blank cyclic voltammogram at 10 V s^{-1} (dotted line) for comparison. A single oxidative wave, peak I at *ca.* +1.36 V *vs* Ag (at 10 V s^{-1})

is observed, and is attributed to the direct oxidation of ammonia at the electrode surface, as previously reported by Buzzeo *et al.*[25] in the RTIL [C_2mim][NTf_2] and by Ji *et al.*[26] in propylene carbonate (PC). The peak potential of this wave becomes more negative when the scan rate is increased, indicating electrochemical irreversiblilty, as confirmed by tafel analysis of the linear region of the current peak, which gave a transfer coefficient, β, of 0.08. It can also be seen that a reductive wave emerges at *ca.* -0.75 V *vs* Ag (peak III) on the reverse scan, and a corresponding oxidative wave at -0.35 V (peak IV).

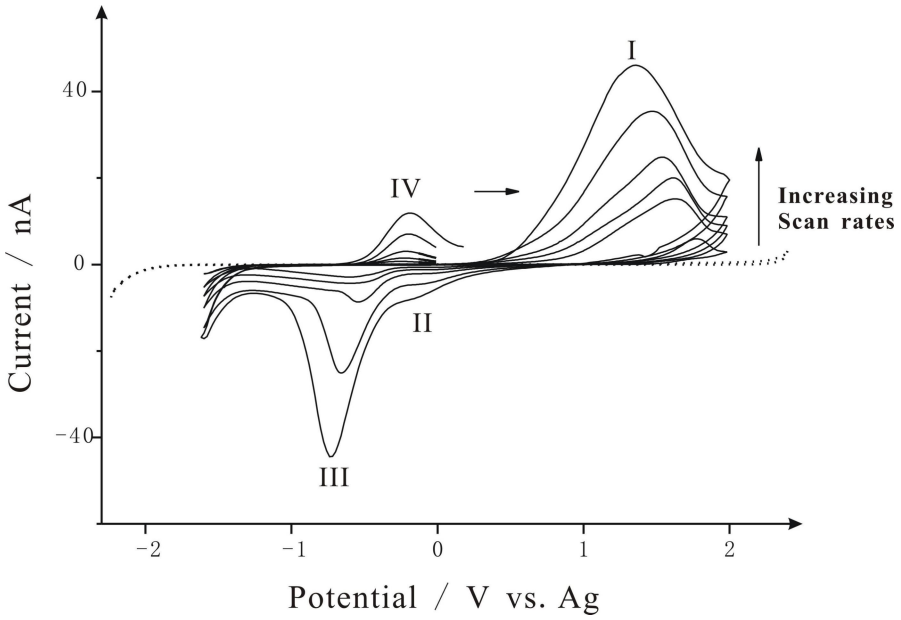


Figure 12.3 Cyclic voltammetric responses of [C_4mim][BF_4] saturated with 10 vol% ammonia on a 10 μm diameter platinum electrode, at scan rates from 0.1 to 10 Vs^{-1}. Dotted line = 0 vol% ammonia.

It is believed that peak III is the reduction of NH_4^+, as indicated by the investigation of the voltammetry of NH_4NO_3, (shown in section 12.3.1.2.) and by Buzzeo *et al.*[25] in

$[C_2mim][NTf_2]$ and Ji *et al.*[26] in PC. Since the appearance of peak IV has been reported previously,[25,26] but its identity is unconfirmed, a further experiment was then performed. A sample of $[C_4mim][BF_4]$ was saturated with ammonia for *ca.* 30 minutes and a typical voltammogram was obtained. Hydrogen gas was then introduced to the cell for *ca.* 10 minutes, and the resulting voltammogram (not shown here) showed a large increase in the size of peak IV, which allows us to confidently suggest that peak IV corresponds to the oxidation of bulk hydrogen.

As seen in Figure 12.3, there is also evidence of a small 'pre-wave' emerging at -0.20 V (peak II) on the reductive sweep. It is believed that after the reduction of NH_3, the H^+ is stabilized and solvated by the numerous anions of the RTIL. The exact nature and constitution of solvated protons in ILs are still not presently known. However, here the solvated proton is henceforth referred to as the 'protonated anion(s)', or HA, both for simplicity and in deference to the observed changes in the nature of the proton upon changing the RTIL anion. We believe that peak II is the reduction of the protonated anion(s), i.e. $H[BF_4]_x$, hereafter referred to as $H[BF_4]$, and this will be discussed later in section 12.3.1.3. Analysis of the oxidative peak current (for all peaks) as a function of scan rate showed a linear dependence with the square root of scan rate, suggesting that all electrochemical processes are diffusion-controlled.

The relative sizes of peaks II and III with increasing scan rate can shed light on the possible mechanism occurring in this system. At lower scan rates (100 mV s^{-1}), peak III is clearly evident, but peak II is not seen. As the scan rate increases (up to 10 V s^{-1}), the relative size of peak II increases. This indicates that the species giving rise to peak II (the protonated anion) is formed first, and can only be seen when the scan rate is sufficiently fast enough to outrun the kinetics of the follow-up chemistry. We therefore propose, in light of these findings, the following general reaction mechanism:

$$NH_3(g) + 3A^- \rightarrow \frac{1}{2}N_2(g) + 3HA + 3e^- \quad (12.11)$$

$$HA + NH_3(g) \rightleftharpoons NH_4^+ + A^- \quad (12.12)$$

$$HA + e^- \xrightarrow{rds} A^- + Pt(H) \rightarrow A^- + \frac{1}{2}H_2(g) \quad (12.13)$$

$$NH_4^+ + e^- \xrightarrow{rds} NH_3(g) + Pt(H) \rightarrow NH_3 + \frac{1}{2}H_2(g) \quad (12.14)$$

where A^- = the un-protonated anion(s), $[BF_4]^-$, and HA is the protonated anion(s), $H[BF_4]$. Note HA may in fact represent the interaction of H^+ with one or more anions, *e.g*. homoconjugation. In the mechanism, ammonia is initially oxidised (with net three-quarters of a mole of electrons per mole NH_3),[25,26] producing nitrogen gas and three protons, which readily (probably instantaneously) protonate, or are solvated by the anion(s). The protonated anion(s) then reacts with another ammonia molecule to form an ammonium ion, which is in equilibrium with the protonated anion(s). There are now two possible reduction steps; one is the reduction of the protonated anion(s) (equation (12.13), corresponding to peak II) and the second is the reduction of the ammonium ion (equation (12.14), corresponding to peak III). Both equations (12.13) and (12.14) produce hydrogen gas, further supporting the identity of peak IV as the oxidation of hydrogen. Depending on the position of equilibrium of equation (12.12), the relative sizes of peaks II and III are likely to change. It is believed that the position of equilibrium is determined by the thermodynamics of formation of the protonated anion(s), and will vary if the anion is changed. This is explored further in section 12.3.3.

Attempts to obtain a diffusion coefficient (and solubility) of ammonia in $[C_4mim][BF_4]$ by fitting the experimental data to the Shoup and Szabo[33] expression proved inadequate due to the complicated follow-up chemistry in the mechanism. However, the diffusion coefficient is expected to be one or two orders of magnitude

less than in conventional aprotic solvents such as acetonitrile and DMF, due to the higher viscosity of the RTIL (109 cP for $[C_4mim][BF_4]$[35] compared to 0.78 cP in DMF at 298 K).

12.3.1.2 Reduction of Ammonium Nitrate in $[C_4mim][BF_4]$

In order to further explore the electrochemical reaction mechanisms of ammonia, we next studied the reduction of NH_4^+ ion (present in this study as ammonium nitrate, NH_4NO_3). Figure 12.4 shows a typical cyclic voltammetric response of saturated NH_4NO_3 obtained at a 10 μm platinum electrode in $[C_4mim][BF_4]$ solution at a scan rate of 1 V s^{-1}. A large reductive wave, peak ii at –0.75 V *vs* Ag, due to the electrochemical reduction of ammonium ion is observed, followed by two resulting oxidative waves at –0.51 V (peak iii) and +0.06 V (peak iv). The oxidative wave, peak v, at +2.06 V, corresponds to the oxidation of nitrate.[36]

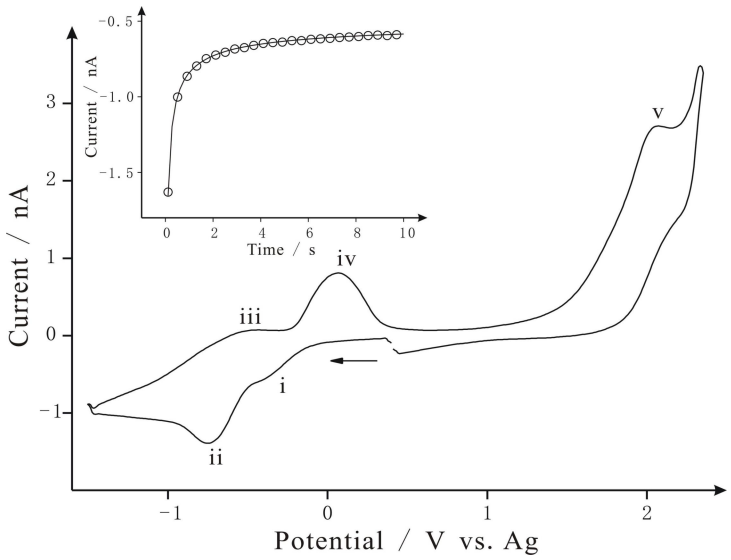


Figure 12.4 Cyclic voltammogram obtained at a platinum microdisk electrode (diameter 10 μm) for a saturated solution of NH_4NO_3 in $[C_4mim][BF_4]$ at a scan rate of 1 Vs^{-1}. The electrode was activated for 1 minute at +1.5V prior to the scan. The inset shows experimental (solid line) and fitted theoretical (circles) chronoamperometric transient obtained for the reduction of a saturated solution of NH_4NO_3 in $[C_4mim][BF_4]$ on a 10μm Pt electrode. The potential was stepped from 0 to -1V.

A potential step was performed on the reductive wave (peak ii) of NH_4NO_3 in $[C_4mim][BF_4]$ on a freshly polished electrode, allowing analysis of peak ii without the added complication of peak i. The potential was stepped from a region of no current flow at 0 V to a potential after the peak (-1.0 V) and the current response monitored as a function of time. The diffusion coefficient of ammonium in $[C_4mim][BF_4]$ was found to be 6.2 (±0.3) × 10^{-8} cm^2 s^{-1} (cf. 2.14 × 10^{-5} cm^2 s^{-1} [37] and 1.65 × 10^{-5} cm^2 s^{-1} [38] in water, consistent with much slower diffusion in the RTIL due to the higher viscosity; 110 cP in $[C_4mim][BF_4]$[35] *vs* 1.0 cP in water at 293 K).

It is interesting to note that the reductive peak at -0.37V (peak i, Figure 12.4) appears only under certain conditions; it is absent on the first reductive sweep, but after the scan is swept to positive potentials (i.e. above peak v), it is clearly evident. We believe that this is due to the reduction of the protonated anion(s), as shown by the addition of hydrogen gas to the solution. It is thought that the protonated anion is formed in an equilibrium reaction with NH_4^+, and scanning to a positive potential may cause a small number of ammonium ions to exchange a proton with the anion(s) of the ionic liquid. This phenomenon is also explored in more detail in Section 12.3.3. The appearance of peaks iii and iv in Figure 12.4 have been observed previously in $[C_2mim][NTf_2]$[25] and in the aprotic solvents DMF[25] and DMSO,[27] and were tentatively attributed to the oxidation of adsorbed hydrogen in two different oxidation states,[27] or to the oxidation of hydrogen to protons and then the direct oxidation of ammonia.[25] In the next section, we show that the second oxidation peak (iv) occurs due to the oxidation of bulk hydrogen, and we propose that the first oxidation peak (iii) is probably the oxidation of adsorbed hydrogen, which is unsurprising given the relatively broad shape of the peak. This is further supported by the observations made by Martínez *et al.*,[27] who reported the disappearance of the two oxidative peaks on gold

electrodes. As hydrogen was found to be inactive on gold in a previous study,[28] it suggests that both oxidative peaks (iii and iv) are probably due to hydrogen.

12.3.1.3. The Addition of Hydrogen Gas and Electrode "Activation"

In order to try to 'fingerprint' the peaks observed in Figure 12.4, the voltammetry of NH_4NO_3 in the presence of hydrogen gas was studied. In a recent study, a quasi-reversible peak was observed for the oxidation of hydrogen in a range of RTILs.[28] This peak was enhanced and became more electrochemically reversible when the electrode was pre-anodized ("activated") at a positive potential of +2.0 V, and was thought to be due to the formation of platinum oxides on the surface of the electrode as a result of the oxidation of trace water. Before activation, the oxidation wave of hydrogen was relatively broad and widely separated from the corresponding reduction peak, even at relatively fast scan rates (4 V s^{-1}).[28] A similar "activation" effect is observed here for the reduction of NH_4^+. The inset to Figure 12.5 shows two voltammograms observed for the reduction of NH_4NO_3 on a Pt microelectrode (d=10μm) at a scan rate of 10 V s^{-1}. The solid line shows the voltammetry obtained before the electrode is activated, and the dotted line shows the voltammetry after activating the electrode at +1.5V *vs* Ag for 1 minute. It is clearly seen that the shape of all voltammetric peaks become more defined, and the peak separations (between peaks ii and iii) are reduced upon activation, consistent with the electrode activation effect seen for hydrogen.[28] Figure 12.5 shows the reduction of NH_4NO_3 in the absence (dotted line) and presence (solid line) of hydrogen gas on a 10μm diameter Pt electrode at a scan rate of 10 V s^{-1}. The electrode was "activated" at +1.5 V for 1 minute in both cases. Clearly peaks i and iv are enhanced on addition of hydrogen gas, and correspond to the oxidation of hydrogen (peak iv) and the subsequent reduction of the protonated anion(s), $H[BF_4]$ (peak i).

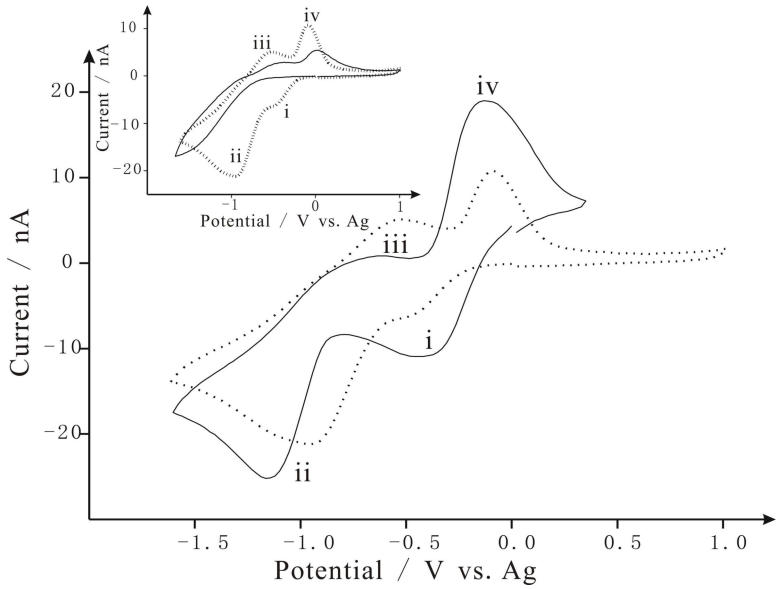


Figure 12.5 Cyclic voltammetry for the reduction of a saturated solution of NH_4NO_3 in the absence (dotted line) and presence (solid line) of 100 vol% H_2 in $[C_4mim][BF_4]$ at a scan rate of 10 V s^{-1} on a 10µm diameter Pt electrode. The electrode was electrochemically activated for 1 minute at 1.5 V (vs. Ag) before each scan. The inset shows the reduction of saturated NH_4NO_3 on a 10µm diameter Pt electrode in $[C_4mim][BF_4]$, at a scan rate of 10 V s^{-1}: (a) without activation (solid line), (b) with activation for 1 minute at +1.5 V (dotted line).

12.3.1.4 Using Cobaltocenium Hexafluorophosphate as An Internal Reference Couple

As a final test to 'fingerprint' further the peaks resulting from the oxidation of ammonia (Figure 12.3), an internal reference couple, Cobaltocenium Hexafluorophosphate ($Co(C_5H_5)_2PF_6$), was added to both the ammonia and ammonium ion solutions. It is expected that some shift in the peak potentials may be observed in these systems due to the Ag quasi-reference electrode used, as this can change its potential in the presence of certain species. $Co(C_5H_5)_2PF_6$ has been recommended by IUPAC as one of several stable reference couples in aprotic solvents, and has been used by Bond *et al.*[39] in RTILs in this context. Consequently, the voltammetry of the oxidation of ammonia and the reduction of NH_4NO_3 was studied on a 10 µm diameter Pt electrode in the presence of 10 mM $Co(C_5H_5)_2PF_6$ and is shown in Figures 12.6a and

12.6b at a scan rate of 10 V s^{-1}. The inset to Figure 12.6 shows the voltammetry of $Co(C_5H_5)_2PF_6$ before the addition of gas. For clarity, the reduction peaks corresponding to the reduction of cobaltocenium hexafluorophosphate:

$$[Co(C_5H_5)_2]^+ + e^- \rightleftharpoons [Co(C_5H_5)_2] \quad (12.15)$$

$$[Co(C_5H_5)_2] + e^- \rightleftharpoons [Co(C_5H_5)_2]^- \quad (12.16)$$

have been labelled as Cc(1) and Cc(2) respectively on all subsequent figures, and as Cc(1)′ and Cc(2)′ for the back peaks corresponding to the reverse of equations (12.15) and (12.16).

Figure 12.6a shows two repeat cyclic voltammograms obtained for the oxidation of ammonia in the presence of $Co(C_5H_5)_2PF_6$ at a Pt electrode (d=10μm) at a scan rate of 10 Vs^{-1}. The first scan was swept negatively to show the first $Co(C_5H_5)_2PF_6$ reduction peak clearly, and was then swept oxidatively over the ammonia oxidation peak. The second scan showed two reductive peaks (II and III) on the cathodic sweep, and peaks Cc(1)′ and IV on the anodic sweep. The same experiment was repeated with NH_4NO_3 in the presence of $Co(C_5H_5)_2PF_6$, and the peaks are labelled on the voltammogram (Figure 12.6b). The peak positions relative to Cc(1)′ can now be used to try to 'fingerprint' peaks II, III and IV.

All peak potentials relative to Cc(1)′ for the oxidation of ammonia in $[C_4mim][BF_4]$ are given in Table 1, and in Table 2 for the reduction of the ammonium ion. Relative to Cc(1)′, peaks III (Figure 12.6a) and ii (Figure 12.6b) are both *ca.* -100 mV, suggesting that peak III can be identified as the reduction of the protonated anion(s) (see section 12.3.1.3). Peaks II (Figure 12.6a) and i (Figure 12.6b) are both *ca.* +200 mV *vs* Cc(1)′, allowing the identification of peak III as the reduction of NH_4^+. Peak IV is *ca.* +300 mV, peak iii is *ca.* +450 mV, peak iv is *ca.* +900 mV (all *vs* Cc(1)′), which initially

suggests that they are all due to different species. However, as stated earlier, peaks IV and iv were identified as the oxidation of bulk hydrogen, so the 600 mV difference in their positions may be the result of a shift due to platinum oxide on the electrode surface. Peak iii (as suggested earlier) is most likely the oxidation of adsorbed hydrogen.

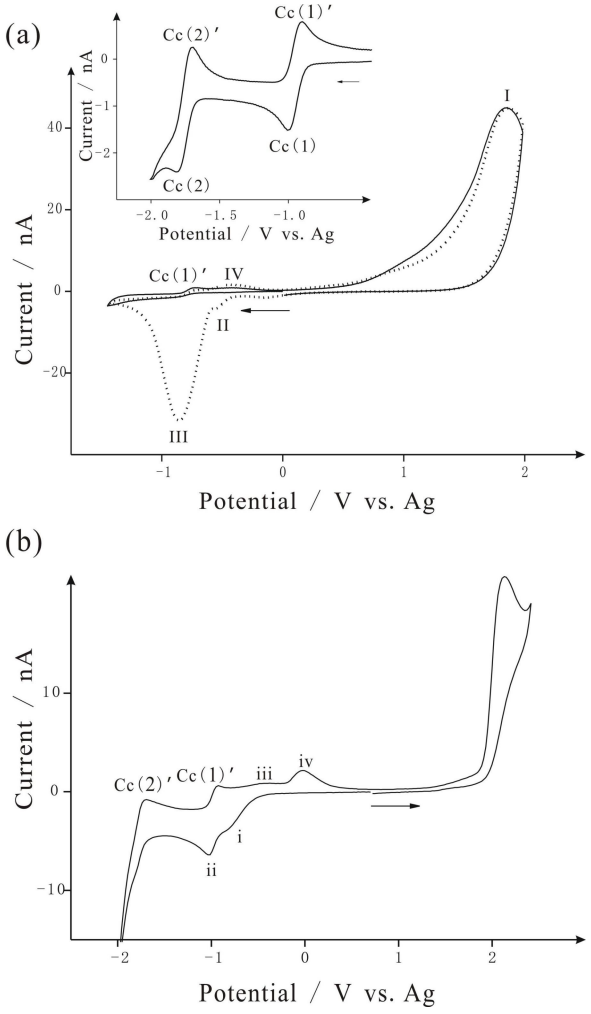


Figure 12.6 (a) Cyclic voltammetric responses of $[C_4mim][BF_4]$ saturated with 10 vol% ammonia obtained at a 10 μm diameter platinum electrode at a scan rate of 10 V s^{-1} with 10 mM cobaltocenium hexafluorophosphate ($Co(C_5H_5)_2PF_6$) added as an internal reference. The first (dotted line) and second (solid line) reductive scans are shown. The inset shows the voltammetry of $Co(C_5H_5)_2PF_6$ before the addition of ammonia gas. (b) Cyclic voltammetry obtained at a Pt microdisk electrode (diameter=10 μm) for a saturated solution of NH_4NO_3 in $[C_4mim][BF_4]$ containing 10 mM $Co(C_5H_5)_2PF_6$ at a scan rate of 10 V s^{-1}.

12.3.2 Electrochemical Study of Ammonia in Different RTILs

In order to investigate any difference in behaviour due to the solvent, the oxidation of ammonia and reduction of the ammonium ion was studied in a range of room temperature ionic liquids with different common anions, namely [C_4mim][OTf], [C_2mim][NTf_2], [C_4mim][NTf_2], [C_4mim][PF_6] (for structures, see Figure 12.1a). The voltammograms obtained over a range of scan rates for the oxidation of NH_3 on a *non-activated* platinum microdisk electrode (diameter=10μm) for these four RTILs are shown in Figure 12.7, at various scan rates from 100 mV s^{-1} to 10 V s^{-1}. The voltammetry obtained for the reduction of NH_4NO_3 (under the same conditions as Figure 12.7) is shown in Figure 12.8, and the voltammetry of NH_4NO_3 in the presence of H_2 is shown in Figure 12.9 (again under the same conditions). Each RTIL will be briefly discussed individually. Generally, (with the exception of [C_4mim][PF_6]) the conclusions are the same, and the oxidation mechanism of ammonia was found to follow the reaction scheme given by equations (12.11) to (12.14).

12.3.2.1 Voltammetry of Ammonia in [C_4mim][OTf]

Figure 12.7a shows the voltammetry for the oxidation of ammonia in [C_4mim][OTf] on a Pt microdisk electrode (d=10 μm) at scan rates from 100 mV s^{-1} to 10 V s^{-1}. The identity of all the peaks are as follows: Peak I is the direct oxidation of ammonia, peak II is the reduction of the protonated anion(s) (see section 12.3.4), peak III is the reduction of NH_4^+ (see section 12.3.4), and peak IV is the oxidation of bulk hydrogen (as confirmed by the growth of this peak in the presence of H_2). It can be clearly seen that the relative size of peak II increases with scan rate, indicating that the mechanism of ammonia oxidation follows the scheme given in equations (12.11) to (12,14); the protonated anion(s), H[OTf], is formed first, followed by the ammonium ion.

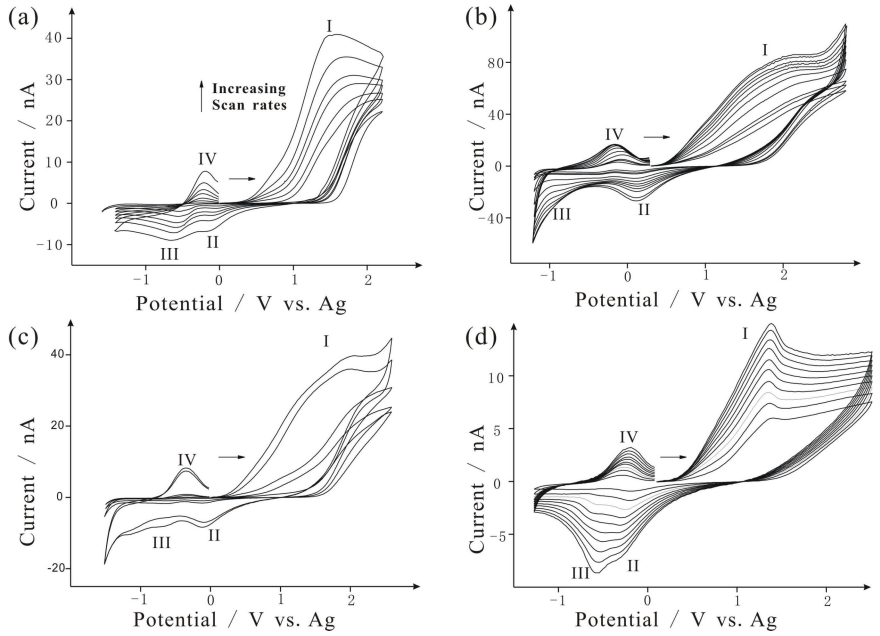


Figure 12.7 Cyclic voltammetry for the oxidation of 10 vol% ammonia on a non-activated 10μm diameter Pt electrode in: (a) $[C_4mim][OTf]$, (b) $[C_2mim][NTf_2]$, (c) $[C_4mim][NTf_2]$ and (d) $[C_6mim][PF_6]$ at various scan rates from 100 mV s^{-1} to 10 V s^{-1}.

Figure 12.8a shows the voltammetry for the reduction of NH_4NO_3 at a *non-activated* Pt electrode (diameter=10 μm) at scan rates of 100 mV s^{-1} to 10 V s^{-1}. Similar peaks were observed to Figure 12.4 (in $[C_4mim][BF_4]$), so we propose that the peaks in Figure 12.8a are identified as follows: peak ii is the reduction of NH_4^+, peak iii is the oxidation of adsorbed H_2, and peak iv is the oxidation of bulk H_2. The identity of peak iv is further confirmed by the addition of H_2 gas to the sample. Figure 12.9a shows the voltammetry obtained in the absence (dotted line) and the presence (solid line) of hydrogen on a Pt microdisk electrode (d=10 μm) at a scan rate of 10 V s^{-1}, and it is seen that peak iv grows significantly in the presence of hydrogen. The diffusion coefficient of NH_4^+ was found to be 7.1 (±0.5) × 10^{-8} cm^2 s^{-1} from fitting to chronoamperometric transients. A comparison of diffusion coefficients in the five studied RTILs is given in Table 3.

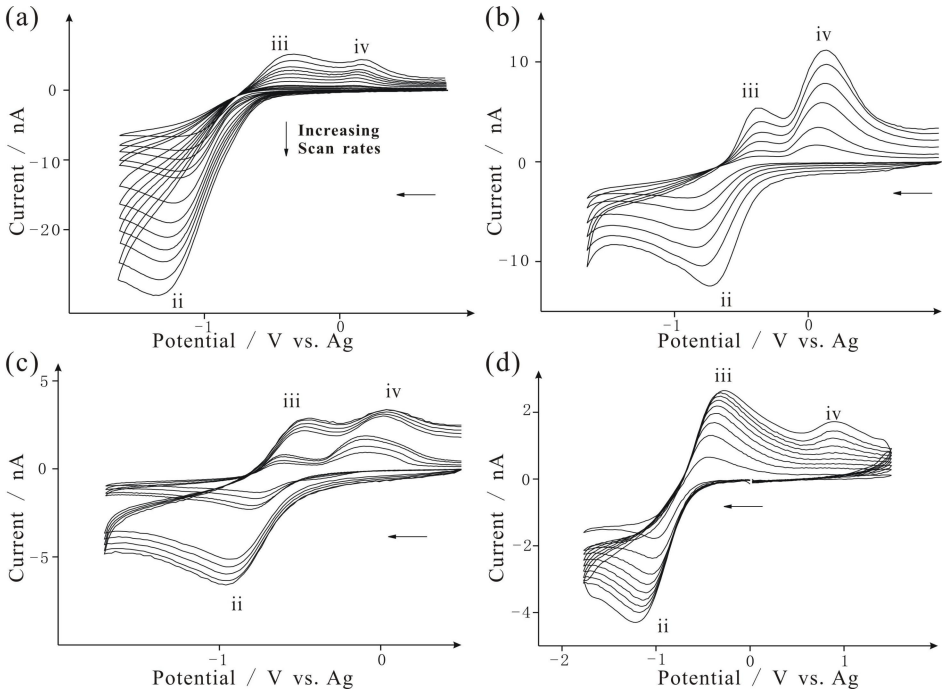


Figure 12.8 Cyclic voltammetry for the reduction of a saturated solution of NH_4NO_3 on a non-activated 10μm diameter Pt electrode in: (a) [C_4mim][OTf], (b) [C_2mim][NTf_2], (c) [C_4mim][NTf_2] and (d) [C_6mim][PF_6] at a range of scan rates from 100 mV s^{-1} to 10 V s^{-1}.

12.3.2.2 Voltammetry of Ammonia in [C_2mim][NTf_2]

The voltammetry for the oxidation of ammonia in [C_2mim][NTf_2] on a 10 μm diameter Pt electrode at various scan rates is shown in Figure 12.7b. Peak I is the oxidation of ammonia and peak II is the reduction of the protonated anion(s). Peak III is the reduction of NH_4^+, which becomes less defined as the scan rate increases, perhaps indicating that the position of equilibrium of equation (12.12) is shifted more towards the protonated anion(s), H[NTf_2]. This is not unexpected, since H[NTf_2] was shown to be more immediately formed (compared to H[OTf], H[BF_4], and H[PF_6]) in the study of the oxidation of hydrogen.[28] This is also discussed further in Section 12.3.3. Peak IV corresponds to the oxidation of bulk hydrogen (confirmed by an increase in peak height in the presence of hydrogen). It is noted that the relative size of peak II increases more

with scan rate than peak III, indicating again that the protonated anion(s) is formed first, followed by NH_4^+, as shown by in the scheme by equations (12.11) to (12.14).

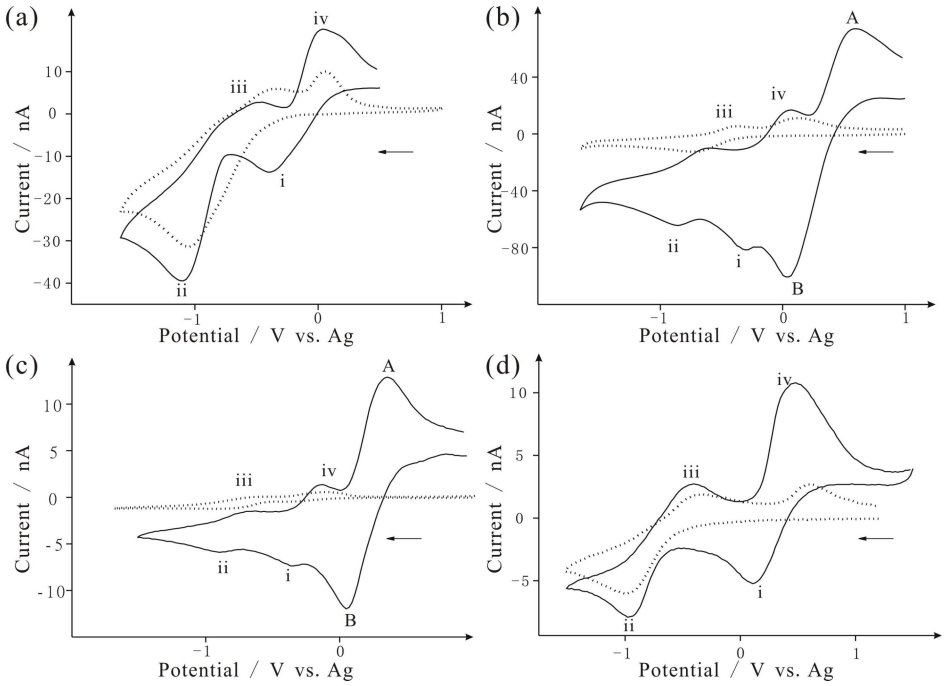


Figure 12.9 Cyclic voltammetry for the reduction of saturated NH_4NO_3 (dotted lines), and NH_4NO_3 in the presence of 100 vol % H_2 (solid lines) at a scan rate of 10 V s^{-1} on a 10μm diameter Pt electrode in: (a) [C_4mim][OTf], (b) [C_2mim][NTf_2], (c) [C_4mim][NTf_2] and (d) [C_6mim][PF_6]. The electrode was activated at +1.5V for 1 minute prior to the scans containing NH_4NO_3 and H_2.

Next, the reduction of the ammonium ion was studied. Cyclic voltammograms obtained at various scan rates on a *non-activated* Pt electrode (diameter 10 μm) for the reduction of NH_4NO_3 in [C_2mim][NTf_2] are shown in Figure 12.8b. Peak ii is identified as the reduction of the ammonium ion (see section 12.3.4), peak iii is most likely the oxidation of adsorbed hydrogen, and peak iv is probably the oxidation of bulk hydrogen. To further determine the identity of peak iv, hydrogen gas was added to a solution of [C_2mim][NTf_2] saturated in ammonia. Figure 12.9b shows the cyclic voltammetry obtained for the reduction of NH_4^+ in the absence (dotted line) and

presence (solid line) of hydrogen on a Pt microdisk electrode (d=10 μm) at a scan rate of 10 V s^{-1}. In the presence of hydrogen, peak i appears on the cathodic scan, and peak iv is slightly enhanced on the anodic scan, consistent with the observations in $[C_4mim][BF_4]$ (Figure 12.5) and $[C_4mim][OTf]$ (Figure 12.9a). However, the voltammetry shows the appearance of a new redox couple, labelled A and B. It is thought that both this new redox couple, A and B, as well as peaks i and iv, are all due to the oxidation of hydrogen, and the reduction of the protonated anion(s). The appearance of two peaks in $[NTf_2]^-$ based ionic liquids was noted previously[28] and is consistent with the new results. The reason for this phenomenon in $[NTf_2]^-$ based ionic liquids is still unclear, however, the voltammetry in Figure 12.9b suggests that peak i and iv are due to the reduction of the protonated anion(s) and the oxidation of bulk hydrogen, respectively. The diffusion coefficient of NH_4^+ in $[C_2mim][NTf_2]$ was found (from fitting to chronoamperometric transients) to be 13.0 (±0.2) × 10^{-8} cm^2 s^{-1}, and is given in Table 3.

12.3.2.3 Voltammetry of Ammonia in $[C_4mim][NTf_2]$

Figure 12.7c shows the oxidation of ammonia in $[C_4mim][NTf_2]$ on a 10 μm Pt microdisk electrode at various scan rates from 100 mV s^{-1} to 10 V s^{-1}. As with $[C_4mim][BF_4]$, $[C_4mim][OTf]$ and $[C_2mim][NTf_2]$, the peaks are defined as follows: peak I is the direct oxidation of ammonia, peak II is the reduction of the protonated anion(s) (see section 12.3.4), peak III is the reduction of NH_4NO_3 (less peak shaped than in $[C_4mim][BF_4]$ and $[C_4mim][OTf]$ probably due to the position of equilibrium of equation (8) being more in favour of the protonated anion(s), $H[NTf_2]$), and peak IV is the oxidation of bulk hydrogen (as shown by an increase in peak height in the presence

of hydrogen gas). The relative size of peak II increases more with scan rate than peak III, again suggesting that the protonated anion(s) is formed before NH_4^+, and that the mechanism follows equations (12.11) to (12.14).

The reduction of NH_4NO_3 was next studied. Cyclic voltammetry obtained on a 10 μm Pt electrode at various scan rates from 100 mV s^{-1} to 10 V s^{-1} is shown in Figure 12.8c. As shown previously for [C_4mim][BF_4], [C_4mim][OTf] and [C_2mim][NTf_2], peak ii is identified as the reduction of the ammonium ion and peak iii is probably the oxidation of adsorbed hydrogen. The identity of peak iv was then investigated by the addition of H_2 gas. Figure 12.9c shows the reduction of NH_4NO_3 in the absence (dotted line) and presence (solid line) of H_2 in [C_4mim][NTf_2] at a scan rate of 10 V s^{-1}. As with [C_2mim][NTf_2], an extra redox couple (labelled A and B) appears in the presence of hydrogen, and the appearance of peak i (corresponding to the reduction of the protonated anion(s), H[NTf_2]) is now evident. Peak iv is also slightly enhanced, suggesting that this corresponds to one of the two peaks (seen previously)[28] resulting from the oxidation of bulk hydrogen in $[NTf_2]^-$ based ionic liquids. From chronoamperometry, a diffusion coefficient of 9.8 ($\pm$0.6) $\times$ 10^{-8} cm^2 s^{-1} for NH_4^+ in [C_4mim][NTf_2] was calculated, and is given in Table 3.

12.3.2.4 Voltammetry of Ammonia in [C_4mim][PF_6]

Cyclic voltammograms for the oxidation of ammonia in [C_4mim][PF_6] at various scan rates from 100 mV s^{-1} to 10 V s^{-1} on a Pt electrode (d=10 μm) are shown in Figure 12.7d. The peaks are identified as follows: peak I is the oxidation of ammonia, peak II is the reduction of the protonated anion(s), H[PF_6], peak III is the reduction of NH_4^+ (see section 12.3.4) and peak IV is the oxidation of bulk hydrogen (as confirmed by an increase in peak height in the presence of H_2 gas). In this RTIL, in contrast to all others

studied, peak III increases with increasing scan rate to a greater extent than peak II. This suggests that the ammonium ion is formed first, followed by proton transfer to form the protonated anion(s). We therefore propose a revised mechanism for the oxidation of ammonia in $[C_4mim][PF_6]$:

$$4NH_3(g) \rightarrow 3NH_4^+ + \frac{1}{2}N_2(g) + 3e^- \quad (12.17)$$

$$NH_4^+ + A^- \rightleftharpoons NH_3(g) + HA \quad (12.18)$$

$$HA + e^- \xrightarrow{rds} A^- + Pt(H) \rightarrow A^- + \frac{1}{2}H_2(g) \quad (12.13)$$

$$NH_4^+ + e^- \xrightarrow{rds} NH_3(g) + Pt(H) \rightarrow NH_3 + \frac{1}{2}H_2(g) \quad (12.14)$$

where A^- = the un-protonated anion, $[PF_6]^-$, and HA is the protonated anion(s), $H[PF_6]$. It is also interesting to note that the peak potentials for the oxidation of ammonia (peak I) do not significantly shift with increasing scan rate (in contrast to all other RTILs studied), further suggesting that a different mechanism is taking place.

Figure 12.8d shows cyclic voltammograms at a range of scan rates from 100 mV s^{-1} to 10 V s^{-1} for the reduction of NH_4PF_6 (chosen because NH_4NO_3 was only sparingly soluble in $[C_4mim][PF_6]$) in $[C_4mim][PF_6]$. As with all other RTILs studied, peak ii is identified as the reduction of NH_4^+, peak iii is probably the oxidation of adsorbed hydrogen, and peak iv is the oxidation of bulk hydrogen (as shown by an increase in peak height in the presence of H_2 gas). Figure 12.9d shows the voltammetry for the reduction of NH_4^+ in the absence (dotted line) and presence (solid line) of H_2 in $[C_4mim][PF_6]$ on a Pt electrode (d=10 μm) at a scan rate of 10 V s^{-1}. It can clearly be seen that peak iv grows significantly with the addition of H_2, therefore confirming the identity of peak iv as the oxidation of bulk hydrogen, and the identity of peak i as the reduction of the protonated anion(s), $H[PF_6]$. From chronoamperometry, a diffusion

coefficient of 2.5 (±0.1) × 10^{-8} cm^2 s^{-1} for NH_4^+ in [C_4mim][PF_6] was calculated, and is given in Table 3.

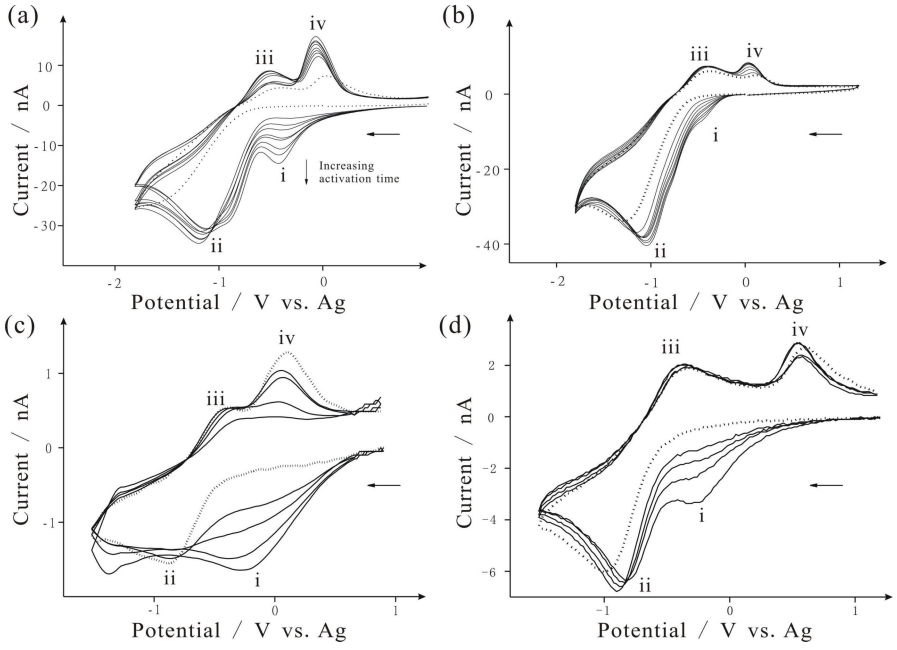


Figure 12.10 Cyclic voltammograms for the reduction of a saturated solution of NH_4^+ on a 10μm diameter Pt electrode at a scan rate of 10 Vs^{-1} in: (a) [C_4mim][BF_4], (b) [C_4mim][OTf], (c) [C_4mim][NTf_2] and (d) [C_4mim][PF_6]. The electrode was activated electrochemically at +1.5 V for the following times: (a) 0 (dotted line), 2, 5, 10, 30, 60, 120 and 240 seconds, (b) 0 (dotted line), 2, 5, 10, 30, 60, 120 and 240 seconds, (c) 0 (dotted line), 1, 2, 5 and 10 seconds, (d) 0 (dotted line), 30, 60, 120 and 240 seconds.

12.3.3 Effect of Electrode Activation on the Relative Ratios of Peaks i and ii

As mentioned previously in this study, the peak shapes and relative sizes of all peaks (i to iv) following the reduction of NH_4^+ were altered by electrochemically 'activating' the surface of the Pt electrode prior to the voltammetric scan. This was also seen for the oxidation of hydrogen in several RTILs on a Pt electrode,[28] and was attributed to the formation of Pt oxides on the electrode surface. As a result, the peak shape for the oxidation of hydrogen became sharper, and more electrochemically reversible.[28] This is now demonstrated for the reduction of the ammonium ion. Figure

12.10 shows the effect of activating the surface of the electrode prior to the reduction of NH_4^+ in four RTILs with different anions: (a) [C_4mim][BF_4], (b) [C_4mim][OTf], (c) [C_4mim][NTf_2] and (d) [C_4mim][PF_6], on a Pt electrode (d=10 μm) at a scan rate of 10 V s^{-1}. In the RTILs [C_4mim][BF_4], [C_4mim][OTf] and [C_4mim][PF_6] (Figures 12.10: a, b and d), the voltammetry shown in Figure 12.10 represents 'activating' the electrode from 0 (dotted line) to 240 seconds, which was necessary to show the appearance of the reduction of the protonated anion(s), peak i. In [C_4mim][NTf_2] (Figure 12.10c) and [C_2mim][NTf_2] (not shown), the maximum activation time was reduced to 10 seconds, since the size of peak i was already larger than the reduction of the ammonium ion, peak ii. As can clearly be seen in Figure 12.10, the relative size of peak i to peak ii is hugely affected by the nature of the anion. This is not unexpected, since it is thought that the relative sizes of peaks i and ii are thought to be dependent on the position of equilibrium of the following equation:

$$NH_4^+ + A^- \rightleftharpoons NH_3(g) + HA \qquad (12.18)$$

where A^- is the un-protonated anion, and HA is the protonated anion(s). It appears that the position of equilibrium is most shifted towards the right hand side in [C_4mim][NTf_2], suggesting a high stability of H^+ in $[NTf_2]^-$ based RTILs, hence giving-rise to a large peak i. On the other hand, peak i remains relatively small after 240 seconds activation in [C_4mim][OTf], suggesting that the position of the equilibrium remains in favour of NH_4^+ *i.e.* only a small amount of H[OTf] is formed in this system. In [C_4mim][BF_4] and [C_4mim][PF_6], the position of equilibrium is somewhere in-between, reflecting a balance between the formation of HA and NH_4^+. The findings compare quite well to a study on the reactivity in zeolite catalysed Friedel-Crafts reactions,[40] where cation exchange with the zeolite produces free acid, which catalyses the reaction. Reactivity for H[NTf_2] was higher than either H[OTf] or H[BF_4] where

poor reactions were seen. This may indicate that there is more acid produced in the case of $H[NTf_2]$ due to an increased solvation of H^+ with $[NTf_2]^-$ anions, as seen here. These results also seem to correspond well to those obtained for the oxidation of H_2 in the same RTILs,[28] with the exception of $[C_4mim][OTf]$, which, in contrast to the present results, showed almost fully reversible voltammetry for H_2, suggesting in this case that H^+ is more readily solvated with $[OTf]^-$ anions. This interesting difference suggests the need for further exploration into the pK_a properties of room temperature ionic liquids with different anions.

12.3.4 Comparison of Results Obtained in All Five RTILs

In order to fully 'fingerprint' the peaks resulting from the oxidation of ammonia and the reduction of NH_4^+, $Co(C_5H_5)_2PF_6$ was added as an internal reference. As with $[C_4mim][BF_4]$ above, the voltammetry of NH_3 and NH_4^+ in the other four RTILs was obtained in the presence of $Co(C_5H_5)_2PF_6$. A comparison of peak positions relative to the peak Cc(1)′ are given in Table 1 for the all peaks related to the oxidation of ammonia, and in Table 2 for all the peaks related to the reduction of NH_4^+. In all RTILs, peak II and i are at approximately the same potential, suggesting that these are both due to the reduction of the protonated anion(s) (as confirmed by addition of H_2 gas, shown earlier in Figure 12.9). Furthermore, the potentials of peak III and peak ii are the same, indicating that these peaks are both due to the reduction of NH_4^+. In all RTILs, the potential of peaks III and IV do not match up with either peak iii or peak iv. However, the addition of H_2 gas to the solutions in all RTILs suggest that peaks IV and iv are due to the oxidation of bulk hydrogen and the shift is likely due to the formation of platinum oxide on the electrode surface (noted earlier). Peak iii is most likely the oxidation of adsorbed hydrogen.

Table 1 Comparison of peak positions* of all peaks resulting from ammonia oxidation

RTIL	I	II	III	IV	A	B
$[C_4mim][BF_4]$	+ 2.59 V	200 mV	- 100 mV	300 mV	-	-
$[C_4mim][OTf]$	+ 2.79 V	500 mV	- 150 mV	250 mV	-	-
$[C_2mim][NTf_2]$	+ 2.90 V	600 mV	150 mV	400 mV	1600 §	1050
$[C_4mim][NTf_2]$	+ 2.87 V	650 mV	100 mV	400 mV	1500 §	1050
$[C_4mim][PF_6]$	+ 2.88 V	700 mV	200 mV	450 mV	-	-

*_vs_ Cc(1)′. Positions of peaks II, III, IV, A and B are given to the nearest 50 mV.
§ obtained from voltammetry of NH_4^+ with H_2 at 10 V s^{-1} (see Figure 12.9)

Table 2 Comparison of peak positions* of all peaks resulting from NH_4^+ reduction

RTIL	i	ii	iii	iv
$[C_4mim][BF_4]$	200 mV §	- 100 mV	450 mV	900 mV
$[C_4mim][OTf]$	500 mV §	- 150 mV	550 mV	1000 mV
$[C_2mim][NTf_2]$	-	150 mV	650 mV	1150 mV
$[C_4mim][NTf_2]$	600 mV §	100 mV	650 mV	1200 mV
$[C_4mim][PF_6]$	750 mV §	200 mV	700 mV	1900 mV

*_vs_ Cc(1)′. Positions of all peaks are given to the nearest 50 mV.
§ obtained from voltammetry of NH_4^+ with 1 min activation at 10 V s^{-1} (see Figure 12.10)

There appears to be only a small difference in the peak potentials for ammonia oxidation (peak I) over all RTILs studied, suggesting that this system is relatively insensitive to the identity of the RTIL. This is not surprising, since the mechanism was

shown to be highly electrochemically irreversible, and will likely be dependent on the energetics of the solvation of ammonia. For all other peaks reported in Tables 1 and 2, a small shift is observed in different RTILs, indicating that there may be some RTIL dependence, but is not significantly large, probably due to the highly irreversible nature of the electron transfer. The gradient obtained from Tafel plots for peaks II, III, i and ii was -787, -615, -291 and -556 mV dec^{-1} respectively. These relative large values further suggest that all the peaks are electrochemically very irreversible.

Table 3 Comparison of calculated diffusion coefficients and solubilities for NH_4^+ in five different ionic liquids

RTIL	Viscosity[§] / cP	Reference	D_{NH4+} [§] / 10^{-8} cm^2 s^{-1}	Saturated conc. NH_4NO_3 [§]/ mM
$[C_4mim][BF_4]$	110	[35]	6.2 ± 0.3	38.5 ± 1.5
$[C_4mim][OTf]$	90	[41]	7.1 ± 0.5	520 ± 30
$[C_2mim][NTf_2]$	28	[41]	13.0 ± 0.2	12.2 ± 1.0
$[C_4mim][NTf_2]$	44	[2]	9.8 ± 0.6	13.7 ± 0.5
$[C_4mim][PF_6]$	275	[2]	2.5 ± 0.1	122 ± 1 *

[§] at 298 K
*Present in solution as NH_4PF_6

The diffusion coefficients for NH_4^+ obtained in the five RTILs are compared in Table 3. The diffusion coefficient, *D*, is expected to be approximately inversely proportional to the viscosity, η, according to the Stokes-Einstein relation given in equation (19), and should pass through the origin.

$$D = \frac{kT}{6\eta\pi a} \tag{12.19}$$

Here, *k* is the Boltzmann constant, *T* is the temperature, and *a* is the hydrodynamic

radius of the diffusing species. A plot of D *vs* $1/\eta$ for the five RTILs is shown in Figure 12.11. The diffusion coefficients appear to be very approximately proportional to the inverse of viscosity. The solubility of NH_4^+ in the five RTILs was obtained from chronoamperometry and is also reported in Table 3. The values are relatively modest in $[C_4mim][BF_4]$, $[C_2mim][NTf_2]$, $[C_4mim][NTf_2]$, relatively large in $[C_4mim][PF_6]$ (perhaps due to fact that the counter anion of NH_4^+ was $[PF_6]^-$ in this case), and high in $[C_4mim][OTf]$ (520 mM), reflecting the solubility differences due to the nature of the RTIL anion.

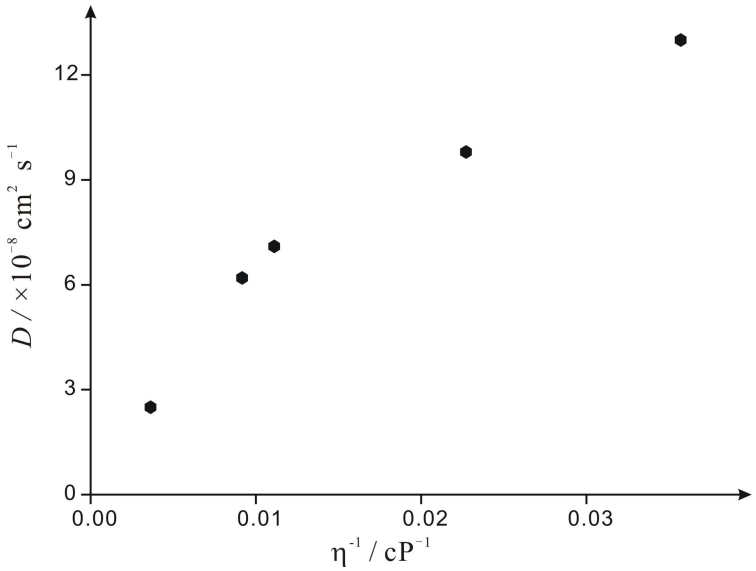


Figure 12.11 Plot of the diffusion coefficient, D, at 293 K of NH_4^+ (calculated from potential step chronoamperometry) against the inverse of viscosity, η^{-1}, for the five RTILs studied.

12.4 Conclusions

The oxidation of ammonia has been studied in a range of RTILs with different anions. In all RTILs studied, the cyclic voltammetry shows a broad oxidative peak, with two cathodic peaks and one anodic peak following the oxidation. The two cathodic peaks were identified as: (1) the reduction of the protonated anion(s), HA, and (2) the reduction of NH_4^+. The resultant anodic peak is likely the oxidation of bulk hydrogen. In four of the five RTILs studied, the mechanism is thought to follow the

scheme given in equations (11) to (14); the protonated anion(s) is formed first, followed by NH_4^+. In $[C_4mim][PF_6]$, NH_4^+ is formed prior to the formation of $H[PF_6]$. In all cases, the protonated anion(s), HA, and ammonium ion, NH_4^+, are thought to be in equilibrium, and the position of equilibrium can be altered by changing the nature of the RTIL anion. The formation of HA is most strongly favoured when $A^- = [NTf_2]^-$, and least favoured when $A^- = [OTf]^-$. Intermediate characteristics are seen when $A^- = [BF_4]^-$ or $[PF_6]^-$. In all RTILs, the formation of HA is enhanced by 'activating' (pre-anodising) the Pt electrode at positive potentials. This work has implications in defining pK_a in RTIL media, and in the possible amperometric sensing of ammonia gas.

12.5 References

(1) Marsh, K. N.; Deev, A.; Wu, A. C.-T.; Tran, E.; Klamt, A. *Korean J. Chem. Eng.* **2002**, *19*, 357.

(2) Buzzeo, M. C.; Evans, R. G.; Compton, R. G. *ChemPhysChem* **2004**, *5*, 1106.

(3) Earle, M. J.; Seddon, K. R. *Pure Appl. Chem.* **2000**, *72*, 1391.

(4) Silvester, D. S.; Compton, R. G. *Z. Phys. Chem.* **2006**, *220*, 1247.

(5) Endres, F.; Sein El Abedin, S. *Phys. Chem. Chem. Phys.* **2006**, *18*, 2101.

(6) Buzzeo, M. C.; Hardacre, C.; Compton, R. G. *Anal. Chem.* **2006**, *76*, 4583.

(7) Howlett, P. C.; MacFarlane, D. R.; Hollenkamp, A. F. *Electrochem. Solid State Lett.* **2004**, *7*, A97.

(8) McEwen, A. B.; Ngo, H. L.; LeCompte, K.; Goldman, J. L. *J. Electrochem. Soc.* **1999**, *144*, L84.

(9) Wang, P.; Zakeeruddin, A. M.; Moser, J. E.; Gratzel, M. *J. Phys. Chem. B* **2003**, *107*, 13280.

(10) Sazhin, S. G.; Soborover, E. I.; Tokarev, S. V. *Russian J. Nondestructive Testing* **2003**, *39*, 791.

(11) Timmer, B.; Olthuis, W.; vaan den Berg, A. *Sensors and Actuators B* **2005**, *107*, 666.

(12) Marcovici, E. *Wiener Klinische Wochenschrift* **1911**, *23*, 1037.

(13) Gallagher, J. T.; Tayler, F. M. *Education in Chem.* **1967**, *4*, 30.

(14) Wobst, E.; Homman, G.; Friedrich, H. *Brauindustrie* **1993**, *78*, 608.

(15) de Vooys, A. C. A.; Koper, M. T. M.; van Santen, R. A.; van Veen, J. A. R. *J. Electroanal. Chem.* **2001**, *506*, 127.

(16) Despić, A. R.; Dražić, D. M. R., P. M. *Electrochimica Acta.* **1966**, *11*, 997.

(17) Gerischer, H.; Mauerer, A. *J. Electroanal. Chem.* **1970**, *25*, 421.

(18) Katan, T.; Galiotto, R. J. *J. Electrochem. Soc.* **1963**, *110*, 1022.

(19) López de Mishima, B. A.; Lescano, D.; Molina Holgado, T.; Mishima, H. T. *Electrochimica Acta.* **1997**, *43*, 395.

(20) McKee, D. W.; Scarpellino, A. J.; Danzig, J., I. F.; Pak, M. S. *J. Electrochem. Soc.* **1969**, *116*, 562.

(21) Pignet, T.; Schmidt, L. D. *J. Catalysis* **1975**, *40*, 212.

(22) Sasaki, K.; Hisatomi, Y. *J. Electrochem. Soc.* **1970**, *117*, 758.

(23) Spetz, A.; Armgarth, M.; Lundström, I. *J. Appl. Phys.* **1988**, *64*, 1274.

(24) Barnes, K. K.; Mann, C. K. *J. Org. Chem.* **1967**, *32*, 1479.

(25) Buzzeo, M. C.; Giovanelli, D.; Lawrence, N. S.; Hardacre, C.; Seddon, K. R.; Compton, R. G. *Electroanalysis* **2004**, *16*, 888.

(26) Ji, X.; Banks, C. E.; Compton, R. G. *Electroanalysis.* **2006**, *18*, 449.

(27) Martínez, C.; Arvía, A. J.; Wargon, J. A. *Electrochimica Acta.* **1973**, *18*, 485.

(28) Silvester, D. S.; Aldous, L.; Hardacre, C.; Compton, R. G. *J. Phys. Chem. B* **2007**, In press.

(29) Bonhôte, P. A. D.; Papageorgiou, N.; Kalyanasundaram, K.; Grätzel, M. *Inorg. Chem.* **1996**, *35*, 1168.

(30) MacFarlane, D. R.; Meakin, P.; Sun, J.; Amini, N.; Forsyth, M. *J. Phys. Chem. B.* **1999**, *103*, 4164.

(31) Sharp, M. *Electrochimica Acta.* **1983**, *28*, 301.

(32) Silvester, D. S.; Wain, A. J.; Aldous, L.; Hardacre, C.; Compton, R. G. *J. Electroanal. Chem.* **2006**, *596*, 131.

(33) Shoup, D.; Szabo, A. *J. Electroanal. Chem.* **1982**, *140*, 237.

(34) Evans, R. G.; Klymenko, O. V.; Price, P. D.; Davies, S. G.; Hardacre, C.; Compton, R. G. *ChemPhysChem* **2005**, *6*, 526.

(35) Wang, J.; Tian, Y.; Zhao, Y.; Zhuo, K. *Green Chem.* **2003**, *5*, 618.

(36) Broder, T. L.; Silvester, D. S.; Aldous, L.; Hardacre, C.; Crossley, A.; Compton, R. G. *New J. Chem.* **2007**, *31*, 966.

(37) Hall, J. R.; Wishaw, B. F.; Stokes, R. H. *J. Am. Chem. Soc.* **1953**, *75*, 1556.

(38) Lutz, J. L.; Mendenhall, G. D. *J. Crystal Growth* **2000**, *217*, 183.

(39) Hultgren, V. M.; Mariotti, A. W. A.; Bond, A. M.; Wedd, A. G. *Anal. Chem.* **2002**, *74*, 3151.

(40) Hardacre, C.; Katdare, S. P.; Milroy, D.; Nancarrow, P.; Rooney, D. W.; Thompson, J. M. *J. Catalysis* **2004**, *227*, 44.

(41) Huddleston, J. G.; Visser, A. E.; Reichert, W. M.; Willauer, H. D.; Broker, G. A.; Rogers, R. D. *Green Chem.* **2001**, *3*, 156.